

Collision-induced intramultiplet mixing for the $\text{Ne}^{**}\{(2p)5(3p)\} + \text{He}$ or Ne system

Citation for published version (APA):

Manders, M. P. I. (1988). *Collision-induced intramultiplet mixing for the $\text{Ne}^{**}\{(2p)5(3p)\} + \text{He}$ or Ne system*. [Phd Thesis 1 (Research TU/e / Graduation TU/e), Applied Physics and Science Education]. Technische Universiteit Eindhoven. <https://doi.org/10.6100/IR285959>

DOI:

[10.6100/IR285959](https://doi.org/10.6100/IR285959)

Document status and date:

Published: 01/01/1988

Document Version:

Publisher's PDF, also known as Version of Record (includes final page, issue and volume numbers)

Please check the document version of this publication:

- A submitted manuscript is the version of the article upon submission and before peer-review. There can be important differences between the submitted version and the official published version of record. People interested in the research are advised to contact the author for the final version of the publication, or visit the DOI to the publisher's website.
- The final author version and the galley proof are versions of the publication after peer review.
- The final published version features the final layout of the paper including the volume, issue and page numbers.

[Link to publication](#)

General rights

Copyright and moral rights for the publications made accessible in the public portal are retained by the authors and/or other copyright owners and it is a condition of accessing publications that users recognise and abide by the legal requirements associated with these rights.

- Users may download and print one copy of any publication from the public portal for the purpose of private study or research.
- You may not further distribute the material or use it for any profit-making activity or commercial gain
- You may freely distribute the URL identifying the publication in the public portal.

If the publication is distributed under the terms of Article 25fa of the Dutch Copyright Act, indicated by the "Taverne" license above, please follow below link for the End User Agreement:

www.tue.nl/taverne

Take down policy

If you believe that this document breaches copyright please contact us at:

openaccess@tue.nl

providing details and we will investigate your claim.

COLLISION-INDUCED INTRAMULTIPLY MIXING
FOR THE
Ne {(2p)⁵(3p)} + He or Ne SYSTEM**

PROEFSCHRIFT

ter verkrijging van de graad van doctor aan de
Technische Universiteit Eindhoven, op gezag van
de Rector Magnificus, prof. dr. F.N. Hooge, voor
een commissie aangewezen door het College van
Dekanen in het openbaar te verdedigen op dinsdag
17 mei 1988 te 16.00 uur

door

MAARTEN PIETER IGNACE
MANDERS

geboren te Eindhoven

Dit proefschrift is goedgekeurd door de promotor

prof. dr. B.J. Verhaar

Co-promotor: dr. H.C.W. Beijerinck

aan mijn ouders

CONTENTS

| | | |
|-----|--|----|
| I | INTRODUCTION | 1 |
| | 1. Context of the work | 1 |
| | 2. This thesis | 3 |
| | 3. The excited neon states | 4 |
| II | POLARIZATION EFFECTS IN COLLISION-INDUCED INTRAMULTIPLY MIXING FOR $\text{Ne}^{**}\{(2p)^5(3p)\} + \text{He}$ (Phys. Rev. Lett. 57 (1986) 1577; <i>ibid.</i> 57 (1986) 2472) | 12 |
| III | A CROSSED-BEAM EXPERIMENT ON INTRAMULTIPLY MIXING COLLISIONS WITH SHORT-LIVED $\text{Ne}^{**}\{(2p)^5(3p)\}$ ATOMS (J. Chem. Phys., (1988), submitted for publication) | 16 |
| | 1. Introduction | 18 |
| | 2. Experimental signals and design considerations | 23 |
| | 3. Experimental setup | 27 |
| | 3.1. Overview | 27 |
| | 3.2. Optical detection system | 31 |
| | 3.3. Laser beam alignment | 35 |
| | 3.4. Pseudo-random laser chopper | 39 |
| | 3.5. Computer control | 40 |
| | 4. Calibration of the experiment | 43 |
| | 4.1. Measuring routine | 43 |
| | 4.2. Secondary-beam density | 51 |
| | 4.3. Transmission factor | 51 |
| | 4.4. Optimum collision-induced fluorescence signal | 53 |
| | 4.5. Center-of-mass energy | 55 |
| | 4.6. Optical detection efficiency | 57 |
| | 4.7. Alignment of three crossing beams | 61 |
| | 4.8. Optical pumping | 65 |
| | 5. Inelastic total cross sections | 72 |
| | 5.1. Deconvolution for finite scattering volume | 72 |
| | 5.2. Measurement of inelastic cross sections | 75 |
| | 5.3. Types of measuring runs | 78 |
| | 5.4. Polarized-atom cross sections | 81 |
| | 5.5. Energy dependence | 83 |
| | 5.6. System-related aspects | 87 |
| | 6. Concluding remarks | 88 |

| | | |
|----|--|-----|
| IV | COLLISION-INDUCED INTRAMULTIPLY MIXING FOR $\text{Ne}^{**}\{(2p)^5(3p)\} + \text{He}$: EXPERIMENT AND QUANTUM CALCULATIONS (Phys. Rev. A, (1987) accepted for publication) | 92 |
| | 1. Introduction | 94 |
| | 2. Collision dynamics | 97 |
| | 2.1. Scattering process | 97 |
| | 2.2. Model potential method for $\text{Ne}^{**}\text{-He}$ | 98 |
| | 3. Coupled-channels calculation | 105 |
| | 3.1. Coupled-channels theory | 105 |
| | 3.2. Ω -diabatic basis | 107 |
| | 3.3. Program performance | 111 |
| | 3.4. Polarized cross sections | 112 |
| | 4. Experimental setup | 117 |
| | 4.1. Design | 117 |
| | 4.2. Performance | 122 |
| | 4.3. Measuring routine | 125 |
| | 5. Experimental results for polarized cross sections | 127 |
| | 5.1. The $(\{\alpha\}_5, J_5=1)$ initial state | 128 |
| | 5.2. The $(\{\alpha\}_6, J_6=1)$ initial state | 135 |
| | 6. Energy dependence and absolute values | 137 |
| | 6.1. Energy dependence | 137 |
| | 6.2. Various other transitions | 139 |
| | 7. Concluding remarks | 142 |
| V | SEMICLASSICAL ANALYSIS OF POLARIZATION EFFECTS IN COLLISION-INDUCED INTRAMULTIPLY MIXING FOR $\text{Ne}^{**}\{(2p)^5(3p)\} + \text{He}$ (Phys. Rev. A, (1988) submitted for publication) | 146 |
| | 1. Introduction | 148 |
| | 2. New experimental results | 152 |
| | 3. Semiclassical model | 160 |
| | 3.1. Adiabatic representation | 160 |
| | 3.2. Radial coupling | 164 |
| | 3.3. Rotational coupling | 168 |
| | 3.4. The $\text{Ne}^{**}\text{-He}$ case: avoided crossings | 171 |
| | 3.5. The $\text{Ne}^{**}\text{-He}$ case: rotational coupling vs locking | 176 |

| | | |
|--|---|-----|
| 4. | Application to the $\{\alpha\}_{4,5,6,7}$ group | 181 |
| 4.1. | Single- and multiple-curve-crossing model | 181 |
| 4.2. | The $\{\alpha\}_5 \leftrightarrow \{\alpha\}_7$ transitions | 187 |
| 4.3. | The $\{\alpha\}_5 \leftrightarrow \{\alpha\}_4$ transitions | 191 |
| 4.4. | The $\{\alpha\}_7 \leftrightarrow \{\alpha\}_6$ transitions | 195 |
| 4.5. | The $\{\alpha\}_5 \leftrightarrow \{\alpha\}_6$, $\{\alpha\}_{7,6} \leftrightarrow \{\alpha\}_4$ transitions | 197 |
| 4.6. | General conclusions | 199 |
| 5. | Concluding remarks | 202 |
| VI COLLISION-INDUCED INTRAMULTIPLY MIXING FOR $\text{Ne}^{**}\{(2p)^5(3p)\} + \text{He}$: | | |
| | PRINCIPLES AND PRACTICE OF SYMMETRY EFFECTS (Phys. Rev. A, (1968) | |
| | submitted for publication) | 206 |
| 1. | Introduction | 208 |
| 2. | Role of inversion symmetry in core/valence electron separation for stationary nuclei | 211 |
| 3. | Inversion and identical-nuclei symmetry in $\text{Ne}^{**}\text{-Ne}$ scattering | 215 |
| 3.1. | Inversion symmetry and the coupled-channel equations | 215 |
| 3.2. | $\text{Ne}^{**}\text{-Ne}$ cross sections for non-identical nuclei | 217 |
| 3.3. | $\text{Ne}^{**}\text{-Ne}$ cross sections for identical nuclei | 220 |
| 4. | Experimental $^{20}\text{Ne}^{**}\text{-}^{20}\text{Ne}$ and $^{22}\text{Ne}^{**}\text{-}^{20}\text{Ne}$ cross sections | 223 |
| 4.1. | Experimental conditions | 223 |
| 4.2. | Experimental cross sections | 224 |
| 4.3. | Discussion | 231 |
| 5. | Preliminary coupled-channel results | 234 |
| 5.1. | The coupled-channels calculation | 234 |
| 5.2. | Results | 237 |
| 6. | Concluding remarks | 241 |
| VII CONCLUDING REMARKS | | 244 |
| SUMMARY | | 250 |
| SAMENVATTING | | 254 |
| DANKWOORD | | 258 |
| CURRICULUM VITAE | | 259 |

1. Context of the work

The Atomic Collisions and Spectroscopy group in the Physics Department of Eindhoven University of Technology has a long tradition in connection with noble gas atoms¹⁾. The first excited metastable $R^*\{([n-1]p)^5(ns)\}$ and short-lived $R^{**}\{([n-1]p)^5(np)\}$ states play an important role in various kind of plasmas and gas discharges, e.g. in lasers and lamps.

The group's attention was directed first at collisions (elastic^{2,3)}, inelastic^{4,5)} and reactive⁶⁻⁸⁾) between metastable noble gas atoms and various ground-state atoms and molecules. In the interest of creating well-defined experimental conditions, crossed-beam experiments have been the rule since then. For neon atoms, the transition from the metastable Ne^* -states to the short-lived Ne^{**} -states can be effected in a relatively simple way, with a laser operating in the visible wavelength region. With optical pumping techniques^{9,10)} being used already for state selection of Ne^* -atoms, the study of short-lived Ne^{**} -atoms has come about as a natural extension of earlier work.

The study of short-lived Ne^{**} -atoms was conceived from the first as covering as wide a range as possible. This means, first, that a multitude of possible processes are to be examined with a variety of techniques ("multi-observable" approach). Second, that both experimental and theoretical aspects are to receive attention ("complete" analysis).

In collisions of excited Ne^{**} -atoms with ground state atoms/molecules, several inelastic channels may be open, depending on the atom/molecule in question. The first of these comprise intramultiplet mixing transitions between Ne^* -states. If the collision partner's ionization threshold is sufficiently low, Penning and associative ionization can also take place. With molecules, the host of possible processes includes depolarization, rotational excitation, etc. This thesis has Ne^{**} -intramultiplet mixing as its subject. In a different project, a similar effort is now being devoted to Penning ionization with Ne^{**} -atoms¹¹).

Experimentally, the short lifetimes of the Ne^{**} -atoms and the small cross sections for intramultiplet mixing transitions pose considerable difficulties. The novel technique developed for the present study overcomes these and allows distinguishing intramultiplet mixing from other processes. As for theory, a description of the collision process requires information on the interaction, in the form of potential curves and coupling matrix elements. To provide a link between these and the experimental results, a fully quantummechanical calculation is the first choice. However, when it comes to insight in the collision dynamics, semiclassical considerations are known to offer advantages.

Among the possible collision partners for the short-lived Ne^{**} -atoms, He and Ne stand out. For the Ne^{**} -He and Ne^{**} -Ne systems, the process of intramultiplet mixing can be studied in isolation, since these are no disturbing processes. In addition, the availability of model potentials for these systems is very important¹²⁻¹⁵). (They are now available for Ar, too¹⁶.) Since for Ne^{**} -Ne the complication of possible symmetrization effects has to be considered, the Ne^{**} -He system is the prime candidate for a truly complete analysis. Next in line for attention is the Ne^{**} -Ar system, where only Penning ionisation is a disturbing factor.

In this thesis on intramultiplet mixing, emphasis is on the $\text{Ne}^{**}\text{-He}$ system. At the presently accessible thermal energies, no symmetrization effects have been experimentally observed for Ne. This has discouraged, for the moment, from devoting equal attention to the $\text{Ne}^{**}\text{-Ne}$ system.

It was recognized from the beginning that a project like the present "complete" study of the $\text{Ne}^{**}\text{-intramultiplet}$ mixing process in all its aspects, would be best served by the coordinated efforts of an experimental and a theoretical group. It has therefore been set up and run as a joint project of the Atomic Collisions and Spectroscopy group and the Theoretical Physics group.

2. This thesis

This thesis is based on five papers, each addressing a different aspect of our intramultiplet-mixing study. These constitute chapters 2 to 6.

Chapter 2¹⁷⁾ provides a bird's eye view of the experiment. Though of necessity rather superficial in places, it can serve as a general introduction. In chapter 3¹⁸⁾ the experiment is discussed in considerable detail. Both the experimental setup and experimental procedure are described. Chapter 4¹⁹⁾ deals with the $\text{Ne}^{**}\text{-He}$ case, confronting experimental data with quantum-mechanical calculations. After dwelling on the subject of model potentials, it goes into the matter of the quantum-mechanical coupled-channel calculations using these potentials as input. Subsequently, in chapter 5²⁰⁾ a semiclassical approach is presented, which provides for more physical insight than the purely quantum-mechanical calculations. This analysis in semiclassical terms, which incorporates all aspects of the collision process, proves successful in explaining a considerable part of the observed phenomena. Chapter 6²¹⁾ is devoted

exclusively to the $\text{Ne}^{**}\text{-Ne}$ system. Besides presenting a number of experimental results, it discusses the general principles involved in symmetrization. Finally, in chapter 7, some concluding remarks are offered. We also use the opportunity to mention some subjects that have been examined but not yet written up. This often amounts to a discussion of the possible future course of the project.

The format of the thesis, a collection of papers, brings with it a number of consequences. The experimental results, rather than being presented in a body, are scattered over the separate chapters. On the other hand, a certain amount of overlap between chapters is unavoidable, in the interest of each paper's self-consistence. The original paper's numbering of equations, figures and tables has been maintained throughout. Also, each chapter has its own list of references. On the whole, it was felt that the advantages of the present approach outweigh the disadvantages.

3. The Excited Neon states

Not only for its intrinsic interest, but also on account of its relevance to the molecular $\text{Ne}^{**}\text{-X}$ interaction, we will now give a succinct description of the Ne-atom. Neon is a noble gas, with a ground-state electron configuration of $(1s)^2(2s)^2(2p)^6$. In the lower excited states a single 2p core electron is excited to the 3s or 3p orbital. The resulting $\text{Ne}^*\{(1s)^2(2s)^2(2p)^5(3s)\}$ and $\text{Ne}^{**}\{(1s)^2(2s)^2(2p)^5(3p)\}$ configurations are split by Coulomb and spin-orbit interactions into four and ten fine-structure states, respectively. In the Paschen notation, the four Ne^* -states are called $1s_i$, with i running from 2 to 5 with decreasing energy. The ten Ne^{**} -states are denoted by $2p_k$, where k runs from 1 to 10.

In this thesis we will write $Ne^{***}\{(2p)^5(3p)\}_k \equiv \{\alpha\}_k$. For the metastable Ne^* -states we use the LS-notation $Ne^*(^3P_0)$, $(^3P_2)$. The Ne^* - and Ne^{***} -multiplets are shown in the level scheme of Fig. 1 in Chapter 3.

The Paschen notation, to a large extent, lacks a physical meaning. A notation allowing of a physical interpretation is for instance the LS-notation, which has its basis in the LS- or Russell-Saunders coupling scheme. This, like other possible coupling schemes, assumes a certain order of importance of the interactions perturbing the isotropic average Coulomb-potential field, in which each electron moves. The average Coulomb interaction gives rise to the principal quantum number n and to the quantum number l for the electron's orbital angular momentum. Of course, each electron also possesses a spin quantum number $s = \frac{1}{2}$. Now, for a coupling scheme to be completely valid, any previous perturbation must split levels to such an extent that subsequent coupling-disturbances will not substantially mix them again.

In the Russell-Saunders or LS-coupling scheme, the non-isotropic residual Coulomb interaction between the core electrons and the valence electron is the primary perturbing factor. The collective core orbital angular momentum \underline{L}_c couples with the valence electron's \underline{l} to a total orbital angular momentum \underline{L} . This implies an effective coupling (based on the anti-symmetry postulate) of the spins \underline{S}_c and \underline{s} to \underline{S} . With spin-orbit coupling next in strength, \underline{L} and \underline{S} couple to total angular momentum \underline{J} . Each of the resulting fine structure states has $(2J+1)$ -fold degeneracy, with the magnetic quantum number $M = -J, -J+1, \dots, J$. This degeneracy can be resolved in a magnetic field. The resulting states

$$\{ (L_c l)L, (S_c s)S \} J(M) \quad (1a)$$

are given in the LS-notation by

Table I. Survey of notations in use for the first two excited Ne-multiplets.

| Name | Principle | Coupling scheme | Notation |
|-------------------------|-------------------------------|------------------------------------|---|
| Paschen | order of energy | - | $1s_i$ (Ne^*) $2p_k$ (Ne^{**}) |
| LS, Russell-Saunders | LS-coupling | $\{(L_c \ell)L, (S_c s)S\}J(M)$ | $2S+1_{L_j}$ |
| jj | jj-coupling | $\{(L_c S_c)J_c, (\ell s)j\}J(M)$ | - |
| jl, intermediate | jl-coupling | $\{[(L_c S_c)J_c, \ell]K, s\}J(M)$ | $2S_c+1_{L_c J_c} n_l [K]_J$ |
| modified Racah | shorthand jl (core states) | (like jl) | $n_l (\cdot)_{K-\frac{1}{2}, J}$ |
| this thesis | pragmatic | - | $2S+1_{J_L}$ (Ne^*) $\{\alpha\}_k$ (Ne^{**}) |

$$2S+1_{LJ}$$

(1b)

where according to usage the states with $L = 0, 1, 2, \dots$ are denoted with S, P, D,

In the so-called jj-coupling scheme the interactions are, in order of strength, first, spin-orbit coupling for the core and spin-orbit coupling for the valence electron and, second, the residual Coulomb-interaction between core and valence electron. In the above self-evident notation, this gives rise to states

$$\{ (L_c S_c) J_c, (l s) j \} J(M) \quad (2)$$

For noble gases, with a single electron excited to an outer orbital, the jl- or intermediate coupling scheme might be more appropriate than either of the two above extremes. In this scheme, spin-orbit coupling of the core electrons comes first, implying orbital, spin, and total angular momentum quantum numbers L_c , S_c and J_c (based on either jj- or LS-coupling). Next in importance is the residual Coulomb interaction between core and valence electron, by which the latter's orbital angular momentum l is coupled with J_c to K , the total angular momentum apart from the valence electron spin s . The quantum number K can assume the values $K = |J_c - l|, |J_c - l| + 1, \dots, J_c + l$. The last and weakest interaction is spin-orbit coupling for the distant valence electron, which couples K and s to J . Thus, we arrive at states

$$\{ [(L_c S_c) J_c, l] K, s \} J(M) \quad (3a)$$

which in spectroscopic notation are given by

Table II. The Ne* and Ne** fine-structure states in the notations of Table I.

| This thesis | Paschen | LS, Russell-Saunders $2S+1L_J$ | jI, intermediate $2S_c+1L_c J_c \text{ nl}[K]_J$ | Modified Racah $nl'_{k-\frac{1}{2}, J}$ |
|--------------|-----------|-----------------------------------|---|--|
| $1P_1$ | $1s_2$ | $1P_1$ | $2P_{1/2} 3s [1/2]_1$ | $3s'_{01}$ |
| $3P_0$ | $1s_3$ | $3P_0$ | $2P_{1/2} 3s [1/2]_0$ | $3s'_{00}$ |
| $3P_1$ | $1s_4$ | $3P_1$ | $2P_{3/2} 3s [3/2]_1$ | $3s_{11}$ |
| $3P_2$ | $1s_5$ | $3P_2$ | $2P_{3/2} 3s [3/2]_2$ | $3s_{12}$ |
| $\{a\}_1$ | $2p_1$ | $1S_0$ | $2P_{1/2} 3p [1/2]_0$ | $3p'_{00}$ |
| $\{a\}_2$ | $2p_2$ | $3P_1$ | $2P_{1/2} 3p [1/2]_1$ | $3p'_{01}$ |
| $\{a\}_3$ | $2p_3$ | $3P_0$ | $2P_{3/2} 3p [1/2]_0$ | $3p_{00}$ |
| $\{a\}_4$ | $2p_4$ | $3P_2$ | $2P_{1/2} 3p [3/2]_2$ | $3p'_{12}$ |
| $\{a\}_5$ | $2p_5$ | $1P_1$ | $2P_{1/2} 3p [3/2]_1$ | $3p'_{11}$ |
| $\{a\}_6$ | $2p_6$ | $1D_2$ | $2P_{3/2} 3p [3/2]_2$ | $3p_{12}$ |
| $\{a\}_7$ | $2p_7$ | $3D_1$ | $2P_{3/2} 3p [3/2]_1$ | $3p_{11}$ |
| $\{a\}_8$ | $2p_8$ | $3D_2$ | $2P_{3/2} 3p [5/2]_2$ | $3p_{22}$ |
| $\{a\}_9$ | $2p_9$ | $3D_3$ | $2P_{3/2} 3p [5/2]_3$ | $3p_{23}$ |
| $\{a\}_{10}$ | $2p_{10}$ | $3S_1$ | $2P_{3/2} 3p [1/2]_1$ | $3p_{01}$ |

$$2S_c + 1 \quad L_c J_c \quad nl [K]_J \quad (3b)$$

with n the principal quantum number of the valence electron. Considering that singly-excited noble gas atoms (core configuration $\dots(np)^5$) have either a ${}^2P_{3/2}$ or a ${}^2P_{1/2}$ core, the modified Racah notation offers a short-hand form:

$$nl \left(\begin{array}{c} ' \\ K-\frac{1}{2}, J \end{array} \right) \quad (3c)$$

where the prime above ℓ is used in the case of a ${}^2P_{1/2}$ core. The various coupling schemes and notations are summarized in Table I.

The states of Eqs. (1), (2) and (3), of course, span the same part of Hilbert space. In practice, depending on the various coupling strengths, no coupling scheme may be absolutely valid, with some mixing of basis states occurring in all. Table II for the excited $Ne^* \{2p\}^5 \{3s\}$ and $Ne^{**} \{2p\}^5 \{3p\}$ states must be seen in this light. It gives the main components of each of the Paschen $1s_i$ and $2p_k$ states in the LS- and jl -bases. These may or may not be the only components. For example, according to calculations in Refs. 12 and 13, the $Ne^{**} \{\alpha\}_4$ -state is given in the LS-basis by

$$|\{\alpha\}_4\rangle = 0.414 |{}^3D_2\rangle + 0.532 |{}^1D_2\rangle - 0.738 |{}^3P_2\rangle \quad (4a)$$

and in the jl -basis by

$$|\{\alpha\}_4\rangle = 0.150 |{}^2P_{3/2} \ 3p[\frac{5}{2}]_2\rangle - 0.406 |{}^2P_{3/2} \ 3p[\frac{3}{2}]_2\rangle + \\ + 0.902 |{}^2P_{1/2} \ 3p[\frac{3}{2}]_2\rangle \quad (4b)$$

indicating a preference for the latter basis. In general, it is found²²⁾ that the Ne^* -states closely resemble LS-states. To the Ne^{**} -states, the following applies. Those with $J = 0$ favor the LS-coupling scheme. For the $J = 1$ states there is no clear-cut preference for either the LS- or the jl -coupling scheme. The $J = 2$ states, however, are more like jl -states. In keeping with these findings, we denote the Ne^* -states by their LS-symbols $2S+1L_J$. For the Ne^{**} -states we use the neutral symbol $\{\alpha\}_k$, in preference to the Paschen notation $2p_k$.

The limited applicability of the jl -coupling scheme to the first two excited Ne-multiplets is reflected in Table II by the incomplete separation between ${}^2P_{3/2}$ and ${}^2P_{1/2}$ core states. This has immediate relevance for our study of $\text{Ne}^{**}\text{-X}$ intramultiplet processes. We can never hope to completely isolate the parts played in the interaction by the Ne^+ -core and the e^- -valence electron. For that, we would have to go to, e.g., the $\text{Ne}\{(2p)^5(7p)\}$ configuration, where the core splitting is clearly evident²³⁾. However, of more direct consequence is the fact that this holds for the heavier noble gases, like krypton (Kr)²⁴⁾, as well. This must serve as a clear indication of the future course of the project.

References

- 1 H.C.W. Beijerinck, *Comm. At. Mol. Phys.* 19 (1987) 227.
- 2 E.R.T. Kerstel, C.P.J.W. van Kraysdijk, J.C. Vlugter, and H.C.W. Beijerinck, *Chem. Phys.*, (1988) accepted for publication.
- 3 E.R.T. Kerstel, M.F.M. Janssens, K.A.H. van Leeuwen, and H.C.W. Beijerinck, *Chem. Phys.* 119 (1988) 325.
- 4 R.J.F. van Gerwen, E.J.D. Vredendregt, E.R.T. Kerstel, and H.C.W. Beijerinck, *Chem. Phys.* 118 (1987)407.
- 5 E.J.W. van Vliembergen, E.J.D. Vredendregt, G.H. Kaashoek, J.P.M.J. Jaspar, M.M.M. van Lanen, M.F.M. Janssens, M.J. Verheijen, and H.C.W. Beijerinck, *Chem. Phys.* 114 (1987)117.

- 6 J.P.C. Kroon, A. Cottaar-Haverkorn, and H.C.W. Beijerinck, *Chem. Phys.* **103** (1986) 119.
- 7 M.J. Verheijen and H.C.W. Beijerinck, *Chem. Phys.* **102** (1986) 225.
- 8 F.T.M. v.d. Berg, J.H.M. Schonenberg, and H.C.W. Beijerinck, *Chem. Phys.* **115** (1987) 359.
- 9 J.P.C. Kroon, H.C.W. Beijerinck, B.J. Verhaar, and N.F. Verster, *Chem. Phys.* **90** (1984) 195.
- 10 J.P.C. Kroon, H.A.J. Senhorst, H.C.W. Beijerinck, B.J. Verhaar, and N.F. Verster, *Phys. Rev. A* **31** (1985) 3724.
- 11 a) J.P.J. Driessen, F.J.M. v.d. Weijer, and H.C.W. Beijerinck, *Conference Proceedings, XIth Int. Symp. on Mol. Beams, Edinburgh 1987* (1987); b) H.C.W. Beijerinck, J.P.J. Driessen, and F.J.M. v.d. Weijer, *Conference Proceedings 1988 DAMOP/APS Meeting, Baltimore*, to be published.
- 12 D. Hennecart and F. Masnou-Seeuws, *J. Phys. B* **18** (1985) 657.
- 13 D. Hennecart, Ph.D. Thesis, Université de Caen (1987), unpublished.
- 14 J.S. Cohen and B. Schneider, *J. Chem. Phys.* **61** (1974) 3230.
- 15 I. Dabrowski and G. Herzberg, *J. Mol. Spectr.* **73** (1978) 183
- 16 a) W. Buszert, T. Bregel, R.J. Allan, M.-W. Ruf, and H. Hotop, *Z. Phys. A* **320** (1985) 105; b) W. Buszert, Ph.D. Thesis, Universität Kaiserslautern (1985), unpublished.
- 17 M.P.I. Manders, J.P.J. Driessen, H.C.W. Beijerinck, and B.J. Verhaar, *Phys. Rev. Lett.* **57** (1986) 1577; *ibid.*, **57** (1986) 2472.
- 18 M.P.I. Manders, W.M. Ruyten, F. v.d. Beucken, J.P.J. Driessen, W.J.T. Veugelers, P.H. Kramer, E.J.D. Vredenburgt, W.B.M. van Hoek, G.J. Sandker, H.C.W. Beijerinck, and B.J. Verhaar, *J. Chem. Phys.*, submitted for publication
- 19 M.P.I. Manders, J.P.J. Driessen, H.C.W. Beijerinck, and B.J. Verhaar, *Phys. Rev. A*, (1988) accepted for publication.
- 20 M.P.I. Manders, W.B.M. van Hoek, E.J.D. Vredenburgt, H.C.W. Beijerinck, and B.J. Verhaar, *Phys. Rev. A*, submitted for publication.
- 21 M.P.I. Manders, W. Boom, H.C.W. Beijerinck, and B.J. Verhaar, *Phys. Rev. A*, submitted for publication.
- 22 J. Martens, *Int. Rep. TUE* (1984) (in Dutch).
- 23 S. Bashkin and J.O. Stoner, "Atomic Energy Levels and Grotrian Diagrams", North Holland, Amsterdam (1975), Vol. I
- 24 V. Kaufman and C.J. Humphreys, *J. Opt. Soc. Am.* **59** (1970) 1614

Polarization Effects in Collision-Induced Intramultiplet Mixing for $Ne^{} \{ (2p)^5(3p) \} + He$**

M. P. I. Manders, J. P. J. Driessen, H. C. W. Beijerinck, and B. J. Verhaar
Physics Department, Eindhoven University of Technology, Eindhoven, The Netherlands
 (Received 27 December 1985)

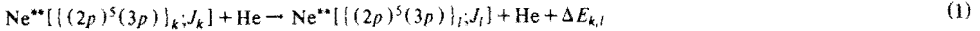
High-quality polarized-emission cross sections for the $\{ \alpha \}_5 = |J=1, M_J\rangle \rightarrow \{ \alpha \}_7$ and $\{ \alpha \}_5 \rightarrow \{ \alpha \}_4$ transitions in the $\{ \alpha \} = \{ (2p)^5(3p) \}$ multiplet (lifetime 20 ns) have been measured in a crossed-beam experiment. For the $\{ \alpha \}_5 \rightarrow \{ \alpha \}_7$ transition we observe a strong preference for the $|M_J|=0$ orientation. The small cross section for the $|M_J|=1$ orientation can be understood qualitatively from the model potentials of Hennecart and Masnou-Seeuys by the strong coupling to the $\{ \alpha \}_4$ and $\{ \alpha \}_6$ states (avoided crossings), which is absent for the $\Omega = |M_J|=0^-$ molecular potentials because of the constraint of reflection symmetry.

PACS numbers: 31.50.+w, 34.50.Pi, 34.50.Rk

Inelastic collisions of atoms in short-lived, electronically excited states presently are in the focus of attention of both theorists¹⁻⁴ and experimentalists.⁵⁻¹¹ A recent review of the field has been given by Hertel.¹² The dependence of the outcome of the collision process on the initial orientation of the electronic angular momentum with respect to the initial relative velocity of the collision partners has proven to reveal many interesting features of the potential surfaces and collision dynamics.^{2,6,7} So far, most experiments have

been performed in bulk. Only recently have crossed-beam experiments with a much better defined initial relative velocity been reported,^{6,7} resulting in more reliable results on these polarization effects. Until now, the rather simple one-electron alkali-metal^{4-6,13-15} and two-electron alkaline-earth^{3,7-9} systems have received most attention.

In this paper we report the first crossed-beam study of inelastic, fine-structure-changing collisions for the system



involving beams that are well characterized with respect to direction, velocity, and excited-state polarization. Strong, interesting polarization effects have been detected and absolute values of cross sections have been determined with a high accuracy of 25%.

Typical lifetimes of the $\{ \alpha \}_k = \{ (2p)^5(3p) \}_k$ states, with k running from 1 to 10 with decreasing energy, are $\tau = 20$ ns. The total energy spread of the multiplet is $\Delta E_{1,10} = 584$ meV. Although a large number, $\sum_{k=1}^{10} (J_k + 1) = 23$, of molecular states is involved, which complicates the analysis of the observed transitions, this system has two major advantages. First, the process of intramultiplet mixing has been investigated in detail in the afterglow of gas discharges, resulting in a suitable set of reference rate constants for Ne and He as collision partners.^{11,16-18} Second, model potentials are available for the Ne^{**} -He system, allowing a direct comparison of theory and experiment by means of full quantum-mechanical coupled-channels calculations.

A schematic view of the crossed-beam apparatus is given in Fig. 1. The short-lived $Ne^{**} \{ (2p)^5(3p) \}$ atoms are produced by laser excitation of one of the metastable $Ne^* \{ (2p)^5(3s) \}$ states. The primary beam of metastable atoms originates in a discharge-excited supersonic expansion. Downstream of the skimmer all charged particles are removed by condenser plates. A

laser beam from a cw single-mode dye laser crosses the primary beam at a point 90 mm downstream of the source. This crossing point is located near the focus of

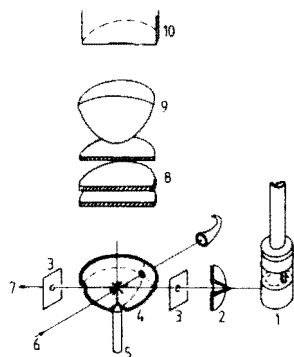


FIG. 1. Schematic view of the experimental setup. (1) primary-beam source; (2) skimmer; (3) beam collimators, 1 mm i.d.; (4) parabolic mirror; (5) secondary beam; (6) laser beam; (7) primary beam; (8) cutoff and interference filters; (9) lens; (10) photomultiplier in cooled housing.

a parabolic mirror. A skimmerless supersonic expansion, with a typical nozzle-to-primary beam distance $z_p = 2$ mm, provides a high-density secondary beam. The parabolic mirror focuses a large fraction (40% solid-angle efficiency) of the fluorescence radiation into a nearly parallel beam. Narrow-band interference filters (2 nm FWHM, 10 nm at 10^{-6} transmission) are used to select a single line of either the direct fluorescence from the initial state k or the collision-induced fluorescence from the final state l . These signals yield the number of atoms in the k and l states, respectively. Additional suppression of background light is achieved by the use of cutoff filters. The transmitted photons are focused on the 9-mm cathode of an S20 photomultiplier in a cooled housing. When we are measuring direct fluorescence radiation, gray filters are added to the optical system in order to guarantee a linear response of the photomultiplier.

The detection efficiency of the optical system is typically 10^{-3} per photon ($\lambda = 650$ nm) produced in the scattering volume. With primary- and secondary-beam densities of the order of $n_1 = 10^{13} \text{ m}^{-3}$ and $n_2 = 5 \times 10^{20} \text{ m}^{-3}$, the overall figure of merit in the thermal energy range is about $2 \text{ kHz}/\text{\AA}^2$ for the number of counts per unit of inelastic total cross section. The background counting rate ranges from 2 to 15 kHz and is mainly due to the line emission from the discharge in the primary-beam source.

In this Letter we report the polarization and energy dependence of the inelastic total cross section Q_{7-5} for the collision-induced transition $\text{Ne}^{**}(\{ \alpha \}_5; J_5 = 1) \rightarrow \text{Ne}^{**}(\{ \alpha \}_7; J_7 = 1)$, with He as the collision partner. Using a linearly polarized laser beam and with the metastable $\text{Ne}^*[\{(2p)^2(3s)\}; J = 0]$ state as lower level we excite the $|\{ \alpha \}_5; J m_j\rangle_E = |\{ \alpha \}_5; 1 0\rangle_E$ magnetic substate, with the electric field vector \mathbf{E} as quantization axis at an angle β with the relative velocity vector \mathbf{g} . Scattering theory then predicts for the observed polarized cross section $Q_{7-5}^{\beta}(E)$

$$Q_{7-5}^{\beta}(E) = Q_{7-5}^{01}(E) \cos^2 \beta + Q_{7-5}^{11}(E) \sin^2 \beta, \tag{2}$$

with $Q_{7-5}^{M_j}(E)$ the polarized-emission cross section for a well defined initial asymptotic quantum number $|M_j\rangle_g$ with respect to the relative velocity, i.e., the asymptotic Ω value.

In Fig. 2 we show the experimental results Q_{7-5}^{β} for the $\{ \alpha \}_5 \rightarrow \{ \alpha \}_7$ transition with $\Delta E_{5,7} = 80.7$ meV, at a center-of-mass energy $E = 100$ meV. The measurements have been performed by variation of the angle θ between the primary-beam velocity \mathbf{v}_1 and \mathbf{E} , yielding extrema at angles $\theta = \theta_0$ and $\theta = \theta_0 + \pi/2$. By considering the Newton diagram of the collision process and taking into account that extrema occur at $\beta = 0$ and

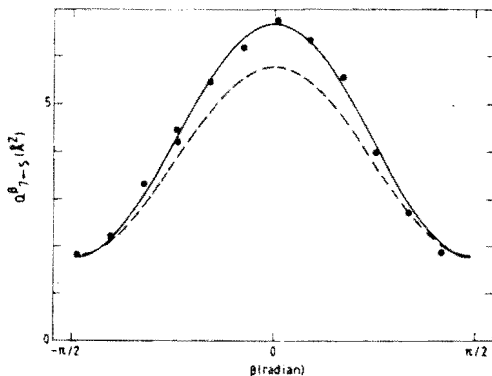


FIG. 2. Experimental results for the observed polarized-emission cross section Q_{7-5}^{β} as a function of the angle β between the electric field \mathbf{E} of the laser and the relative velocity \mathbf{g} , at a center-of-mass energy $E = 100$ meV. The statistical error is less than the size of the data points. The solid line is a curve fit according to Eq. (2). The dashed line is the prediction of the model potential of Hennecart and Masnou-Seeuws.

$\beta = \pi/2$, we can determine which of these extrema in θ corresponds to $\mathbf{E} \parallel \mathbf{g}$, i.e., $\theta = \theta_g$ and $\beta = 0$. From the orientation θ_g of the relative velocity vector in the laboratory system, the absolute value of the relative velocity and thus the collision energy may be readily calculated, with the well known values of the laboratory velocities \mathbf{v}_1 and \mathbf{v}_2 as input. Together with the nozzle-to-primary beam distance z_p , the angle $\theta = \theta_g$ also yields the effective position of the collision volume on the primary-beam axis. This information may then be used to determine the secondary-beam density and the acceptance of the optical system. At present we estimate the overall accuracy of the resulting absolute cross sections at 25%.

In Fig. 3 we show the observed energy dependence of the polarized-emission cross sections Q_{7-5}^{01} and Q_{7-5}^{11} . The datum point at energy $E = 165$ meV has been obtained with a 90% He/10% Ne seeded primary beam. The He^* metastable atoms are converted with approximately 50% efficiency into Ne^* atoms by the He^*-Ne excitation-transfer reactions. The other data points have been measured by variation of the position of the laser beam along the primary-beam axis, which results in different center-of-mass energies. We observe a good agreement between the two experimental methods. Errors in the energy are typically 5%, due both to the uncertainty and spread of the measured (Ne^*) or calculated (He) velocity distributions of the colliding atoms, and to the uncertainty of the angle θ_g .

To obtain insight into the mechanisms underlying

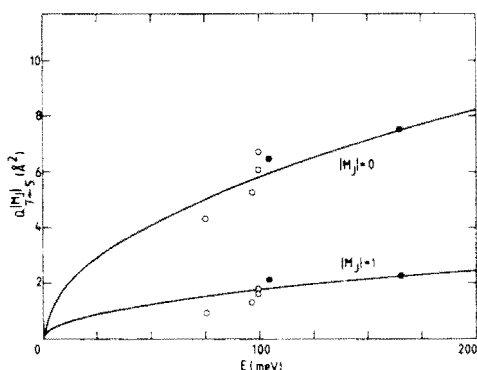


FIG. 3. Energy dependence of the polarized-emission cross sections $Q_{7-5}^{0|}$ and $Q_{7-5}^{1|}$, with E the center-of-mass energy. The full points have been obtained by varying the magnitude of the primary-beam velocity v_1 ; the open points by varying the direction of v_1 by scanning the laser beam along the primary-beam axis. The solid lines indicate the functional behavior $Q_{7-5}^{M_j} \sim E^{1/2}$.

the surprisingly large polarization effects, we have to consider the salient features of the adiabatic potential curves involved, as calculated by Hennecart and Masnou-Seeuws^{1,11} with a model potential method. We first discuss the $\{\alpha\}_5 \rightarrow \{\alpha\}_7$ transition. Both the initial and the final states show only a small splitting between the $\Omega = 0$ and $\Omega = 1$ molecular potentials. To indicate the range of internuclear distances R that is probed, at $E = 100$ meV the classical turning point for both Ω potentials of the $\{\alpha\}_5$ state is $R_t = 6a_0$ for an impact parameter $b = 0$ and $R_t = 7.1a_0$ for $b = 6a_0$. For $\Omega = 0$ the adiabatic electronic states are divided into 0^+ and 0^- classes, depending on the reflection symmetry. The $\Omega = 0^-$ class contains the $\{\alpha\}_{2,5,7,9,10}$ states and there is a strong coupling of the $\{\alpha\}_5$ and $\{\alpha\}_7$ states. This coupling can be identified as an avoided crossing at $R_c = 7.0a_0$ with a Landau-Zener-type coupling matrix element $H_{57} = 22$ meV (equal to half of the smallest separation of the potential curves), which is very large in comparison with the energy difference $\Delta E_{57} = 80.7$ meV of the $\{\alpha\}_5$ and $\{\alpha\}_7$ states at infinity. For $\Omega = 1$ there is no symmetry constraint and the intermediate $\{\alpha\}_6$ state disturbs the coupling of the $\{\alpha\}_5$ with the $\{\alpha\}_7$ state. We now observe an avoided crossing of the $\{\alpha\}_6$ and $\{\alpha\}_7$ states at $R_c = 7.5a_0$ with $H_{67} = 3.5$ meV. Moreover, the initial $\{\alpha\}_5$ state is now coupled to the $\{\alpha\}_4$ state by an avoided crossing with $H_{45} = 1.0$ meV at $R_c = 8.5a_0$. The small contribution of the $\Omega = 1$ orientation to the $\{\alpha\}_5 \rightarrow \{\alpha\}_7$ transition is due to the strong coupling of both the initial and final states to the $\{\alpha\}_4$ and $\{\alpha\}_6$ states, respectively, which is absent for the

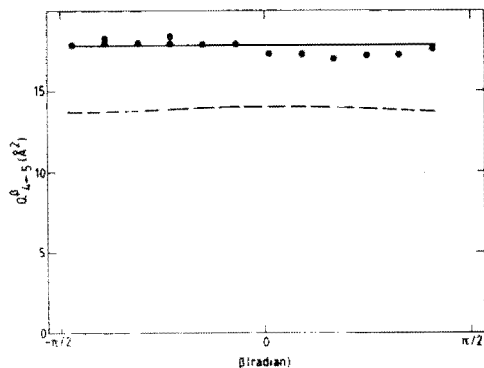


FIG. 4. Experimental results for the observed cross section $Q_{7-5}^{0|}$ at $E = 100$ meV (the solid line indicates the average value), in comparison with the predictions of the model potentials of Hennecart and Masnou-Seeuws (dashed line). The data points have not been corrected for the nonisotropic distribution of collision-induced fluorescence radiation.

$\Omega = 0^-$ adiabatic potentials. The large coupling matrix element H_{57} for $\Omega = 0^-$ is consonant with a main contribution to the cross section from small impact parameters, where radial velocities are large. Even without "locking" of the initial $\Omega = |M_j|$ orientation to the internuclear axis, this orientation will then be largely conserved at the crossing radius. This results in the large polarization effect $Q_{7-5}^{0|} \gg Q_{7-5}^{1|}$.

The picture that thus emerges is confirmed by the $\{\alpha\}_5 \rightarrow \{\alpha\}_4$ transition, for which the results are shown in Fig. 4. We note the absence of a significant polarization effect. This is in apparent contradiction with the simultaneous presence of an avoided crossing of the $\{\alpha\}_5$ and $\{\alpha\}_4$ states for the $\Omega = 1$ orientation, and the absence of any coupling at all for $\Omega = 0$ where initial and final states are in different symmetry classes. However, because of the small splitting of the $\{\alpha\}_5$ state between the $\Omega = 0$ and $\Omega = 1$ adiabatic potentials, the "locking" of the initial orientation to the internuclear axis constitutes only a minor effect. The asymptotic $|M_j| = 0$ orientation will thus be partially rotated at the crossing radius into a local $\Omega = 1$ state, which does couple with the final $\{\alpha\}_4$ state. This effect will be most pronounced for large impact parameters. Because of the very small coupling matrix element H_{45} , which requires small values of the radial velocity for optimum coupling, we indeed expect a predominant contribution from impact parameters $b \approx R_c$. Hence, the absence of a polarization effect, $Q_{4-5}^{0|} \approx Q_{4-5}^{1|}$, is qualitatively understood.

The total inelastic cross sections for the $\{\alpha\}_4 \rightarrow \{\alpha\}_5$ transition, as measured by Hennecart¹¹ in a

gas discharge, show a temperature dependence that is in agreement with a curve-crossing mechanism. This is supported by his calculation of the matrix elements of the radial coupling operator $\delta/\delta R$, which shows a localized coupling at $R = 8.5a_0$.

We have also performed a fully quantum-mechanical coupled-channels calculation using a diabatic basis $\{| \alpha \rangle_k; J_k \Omega \pi P M_P \}$, where the basis vectors have a well defined parity π , well defined quantum numbers P and M_P for the total angular momentum in the space-fixed frame, and well defined quantum numbers J and $\Omega = |M_J|_z$ for the total electronic angular momentum in the body fixed frame, with z' along the internuclear axis. On this basis we have a maximum of 18 coupled equations for each value of P and $\pi = \pm 1$, because depending on parity the $\Omega = 0^-$ or 0^+ class is absent. We limit the calculation to P values corresponding to impact parameters $b \approx P\lambda \leq 15a_0$, with λ the de Broglie wavelength in the incoming channel. For an energy $E = 100$ meV this comes down to $P \leq 100$.

The results of these calculations are given in Figs. 2 and 4. Because the model potentials of Hennecart and Masnou-Seeuws,^{1,11} which have been used as input, are available only for $R \geq 4.5a_0$, a hard-sphere core has been added. However, this does not influence the results. We observe that theoretical predictions for both transitions are in fair agreement with the measurements.

In conclusion, we can state that the model potentials of Hennecart and Masnou-Seeuws provide a sufficient basis for both a simple qualitative description and a quantitative coupled-channels calculation.

The localized radial couplings in the $\{ \alpha \}_{4,5,6,7}$ group and the absence of "locking" phenomena open up the prospect of a semiclassical description in terms of the Landau-Zener formalism for avoided crossings and a simple geometrical interpretation of rotational coupling. Future measurements of the energy dependence of all transitions in this group of four levels will have to show whether this is possible. The available

center-of-mass energies are $0.1 \text{ eV} \leq E \leq 5 \text{ eV}$, where a hollow-cathode arc¹⁹ will be used for the high energy range.

¹D. Hennecart and F. Masnou-Seeuws, *J. Phys. B* **18**, 657 (1985).

²W. Buszert, T. Bregel, R. J. Allan, M. W. Ruf, and H. Hotop, *Z. Phys. A* **320**, 105 (1985).

³M. H. Alexander, T. Orlikowski, and J. E. Straub, *Phys. Rev. A* **28**, 73 (1983).

⁴G. Nienhuis, *Phys. Rev. A* **26**, 3137 (1982).

⁵J. G. Kircz, R. Morgenstern, and G. Nienhuis, *Phys. Rev. Lett.* **48**, 610 (1982).

⁶H. A. J. Meyer, H. P. van der Meulen, and R. Morgenstern, to be published.

⁷D. Neuschäfer, M. O. Hale, I. V. Hertel, and S. R. Leone, to be published.

⁸M. O. Hale, I. V. Hertel, and S. R. Leone, *Phys. Rev. Lett.* **53**, 2296 (1984).

⁹M. O. Hale and S. R. Leone, *Phys. Rev. A* **31**, 103 (1985).

¹⁰A. Bähring, I. V. Hertel, E. Meyer, W. Meyer, N. Spies, and H. Schmidt, *J. Phys. B* **17**, 2859 (1984).

¹¹D. Hennecart, *J. Phys. (Paris)* **39**, 1065 (1978), and thesis, Université de Caen, 1982 (unpublished).

¹²I. V. Hertel, *Rep. Prog. Phys.* **48**, 375 (1985).

¹³J. M. Mesdagh, J. Berlande, P. de Pujo, J. Cuvallier, and A. Binet, *Z. Phys. A* **304**, 3 (1982).

¹⁴E. Düren, E. Hasselbrink, and H. Tischen, *Phys. Rev. Lett.* **50**, 1983 (1983).

¹⁵L. Hüwel, J. Maier, and H. Pauly, *J. Chem. Phys.* **76**, 4961 (1982).

¹⁶M. J. Webster and M. J. Shaw, *J. Phys. B* **12**, 3521 (1979).

¹⁷F. C. M. Coolen, N. van Schaik, R. M. M. Smits, M. Prins, and L. W. G. Steenhuysen, *Physica (Amsterdam)* **93B+C**, 131 (1978); R. M. M. Smits, thesis, Eindhoven University of Technology, 1977 (unpublished).

¹⁸R. S. F. Chang and D. W. Setser, *J. Chem. Phys.* **72**, 4099 (1980).

¹⁹P. G. A. Theeuwes, H. C. W. Beyerinck, D. C. Schram, and N. F. Verster, *J. Phys. E* **15**, 573 (1982).

1580

Polarization Effects in Collision-Induced Intramultiplet Mixing for $\text{Ne}^{}\{(2p)^3(3p)\} + \text{He}$.** M. P. I. MANDERS, J. P. J. DRIESSEN, H. C. W. BEIJERINCK, and B. J. VERHAAR [*Phys. Rev. Lett.* **57**, 1577 (1986)].

Throughout the paper, the phrase "polarized-emission cross sections" should be replaced by "polarized-atom cross sections."

2472

Chapter III.

A CROSSED-BEAM EXPERIMENT ON INTRAMULTIPLY MIXING COLLISIONS
WITH SHORT-LIVED $\text{Ne}^{**}\{(2p)^5(3p)\}$ ATOMS

M.P.I. Manders, W.M. Ruyten, F. v.d. Beucken, J.P.J. Driessen,
W.J.T. Veugelers, P.H. Kramer, E.J.D. Vredenbregt, W.B.M. van Hoek,
G.J. Sandker, H.C.W. Beijerinck, and B.J. Verhaar

Physics Department, Eindhoven University of Technology
P.O. Box 513, 5600 MB Eindhoven, The Netherlands

Abstract

We describe the design, operation and calibration of a crossed-beam experiment for the study of intramultiplet mixing collisions of short-lived electronically excited $\text{Ne}\{(2p)^5(3p)\} \equiv \{a\}$ atoms with ground-state atoms/molecules. The excellent performance of almost $1 \text{ kHz}/\text{\AA}^2$ (number of counts per unit of inelastic cross section) enables us to measure, with good accuracy, absolute total $\text{Ne}^{**}\text{-X}$ cross sections $Q_{l \leftarrow k}^{M_k}$, for the $\{a\}_k \rightarrow \{a\}_l$ transition. Here M_k is the magnetic quantum number of the electronic angular momentum \underline{J} of the initial $\{a\}_k$ state with respect to the asymptotic relative velocity. The polarized $\{a\}_k$ state is produced with a polarized laser. Narrow-band interference filters are used to detect the fluorescence radiation from the short-lived $\{a\}_k$ and $\{a\}_l$ states.

An extensive series of measurements has been undertaken to calibrate the experiment. These are related to, e.g., beam properties, the optical-pumping process, and the optical detection system. The basic principles of the collision experiment itself have been thoroughly examined as well.

We discuss the kinds of experiments it is possible to perform. These have yielded absolute (within 30%) cross sections between 0.05 and 50 \AA^2 . Very strong polarization effects have been observed, with $0.1 \lesssim Q_{l \leftarrow k}^{0} / Q_{l \leftarrow k}^{1} \lesssim 10$. The average collision energy has been varied between 50 and 250 meV (depending to some extent on the collision partner), by using a seeded primary beam and by manipulating the Newton diagram of primary- and secondary-beam velocity vectors. Time-of-flight measurements with a laser chopper have been performed as well. The wide range of Ne^{**} -collision partners offers the option of studying intramultiplet mixing pure (He, Ne), and in conjunction with Penning ionization (noble gas atoms Ar, Kr, Xe) or even angular-momentum coupling and anisotropy effects (molecules, from H_2 to CO_2 , N_2O).

1. Introduction

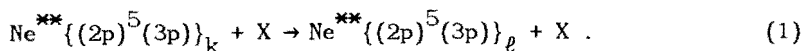
The study of inelastic collisions of atoms in short-lived, electronically excited states offers both great potential rewards and considerable practical difficulties. The latter have made this subject a relatively new entry in the atomic-collisions field. The former have caused a sizeable body of literature to appear in recent years, both of a theoretical¹⁻⁴⁾ and of an experimental nature⁵⁻¹⁷⁾. Hertel et al. have reviewed the subject in depth¹⁸⁾. Our own work¹⁹⁻²²⁾ concerns the short-lived Ne^{**} $\{(2p)^5(3p)\}$ atoms.

Experiments with ground state and metastable atoms pose considerably fewer experimental problems than similar experiments with short-lived atoms. For the latter cross sections are usually smaller. More significant, though, are the low effective particle densities associated with short lifetimes. This does not apply to atoms in a short-lived level that on excitation with a laser constitutes a two-level system with the metastable level from which it is produced. Hence the relative abundance of experiments with two-level systems. As an expedient solution to the low-density problem, bulk experiments have enjoyed considerable favor. Their large sensitivity, however, necessarily implies a low resolution. In a study of cross-section polarization effects and energy dependence, a crossed-beam experiment is much to be preferred. The relative velocity of the collision partners is well-defined, both as to orientation and as to magnitude. The energy range is much larger, as well. In spite of these obvious advantages, experiments of this type have been reported only recently^{6,7)}.

We have constructed a novel crossed-beam apparatus that makes possible a variety of experiments with short-lived (neon-)atoms that are not part of a two-level system. To a significant extent, it can be said to combine the high resolution of a crossed-beam experiment with the high sensitivity of bulk experiments.

In the short-lived atoms under discussion (be they the rather simple one-electron alkali-metal^{4-6,12-14}) and two-electron alkaline-earth^{3,7-9,15}) systems or, as in the present paper, noble gas atoms) the examination of polarization effects, in particular, is worthwhile. The outer electron occupies a relatively outlying (np) orbital. This, as opposed to the closer (ns) orbital of the corresponding metastable atoms. With an electron so far out, the initial orientation of the electronic angular momentum with respect to the asymptotic relative velocity of the collision partners may be expected to have a correspondingly large effect on the outcome of the collision process. The core hole in noble gas atoms has less direct influence on the potential surfaces. However, its orientation, which of course is coupled to that of the valence electron, will be of importance in a process like Penning ionization where the empty core orbital plays an active role. From polarization effects many interesting features of the potential surfaces and collision dynamics of the systems in question can be deduced. It is possible to prepare the short-lived atoms in a well-defined asymptotic orientation by use of a polarized laser.

The crossed-beam experiment which is the subject of this paper is concerned with the study of the inelastic intramultiplet mixing process



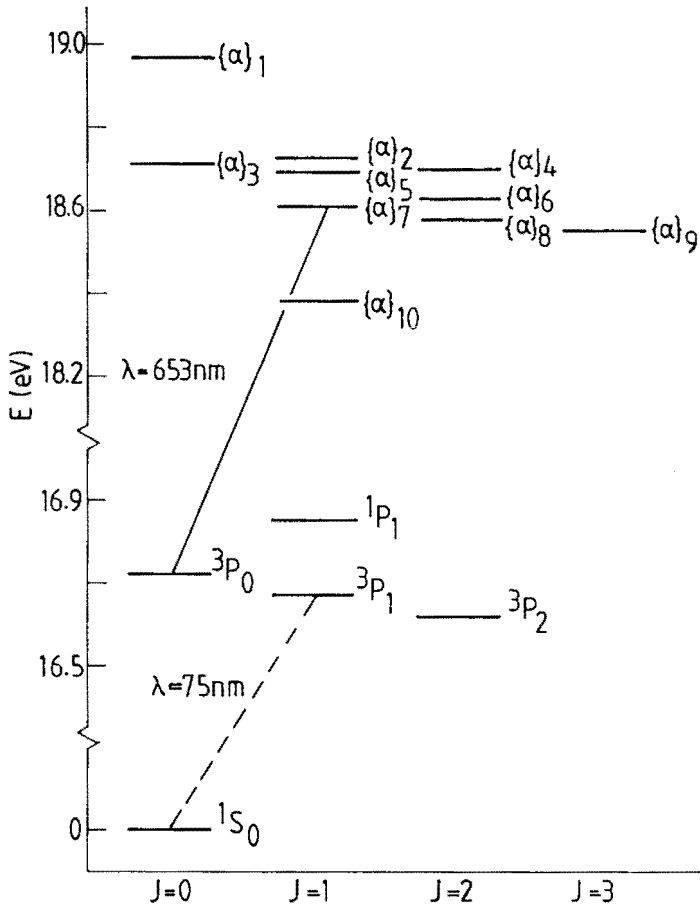


Fig. 1. Energy-level diagram of the $\text{Ne}^*\{(2p)^5(3s)\}$ (Russell-Saunders notation) and $\text{Ne}^{**}\{(2p)^5(3p)\}$ (Paschen numbering) excited states, grouped by their electronic angular momentum quantum number J .

Here X may in principle be any atom/molecule in the electronic ground state. So far, for reasons explained in Ref. 20, the Ne^{**}-He system has received most attention. The Ne^{**} $\{(2p)^5(3p)\}_k \equiv \{\alpha\}_k$ states, with k running from 1 to 10 with decreasing energy (as in the Paschen notation), are shown in Fig. 1. Their lifetimes are on the order of $\tau \approx 20$ ns. The total energy spread of the multiplet is $\Delta E_{1,10} = 584$ meV. Also shown in the figure is the Ne^{*} $\{(2p)^5(3s)\}_i$ multiplet, of which the Ne^{*} (3P_0) and Ne^{*} (3P_2) states are metastable. Excitation by laser from these to one of the short-lived Ne^{**}-states occurs at wavelengths $\lambda_{ik} \approx 600$ -700 nm. Radiative decay from the short-lived states is in the same visible wavelength-region. The Ne^{*} (3P_2) and Ne^{**} $\{\alpha\}_9$ states form a two-level system at $\lambda_{ik} = 640.2$ nm.

While the present paper will go into substantially more detail, a general overview of the crossed-beam experiment has been given already in Ref. 20. Both here and in Ref. 21 absolute polarized-atom Ne^{**}-He cross sections $Q_{\rho \leftarrow k}^{|M_k|}$ have been presented for a number of $\{\alpha\}_k \rightarrow \{\alpha\}_\rho$ transitions at thermal energies. Here M_k is the magnetic quantum number of the electronic angular momentum J of the initial $\{\alpha\}_k$ state along the asymptotic relative velocity \underline{g} , i.e. the z-axis. Cross-section data for the Ne^{**}-Ne system are given in Ref. 22. Large polarization effects have been observed, as well as considerable variation in cross-section magnitude.

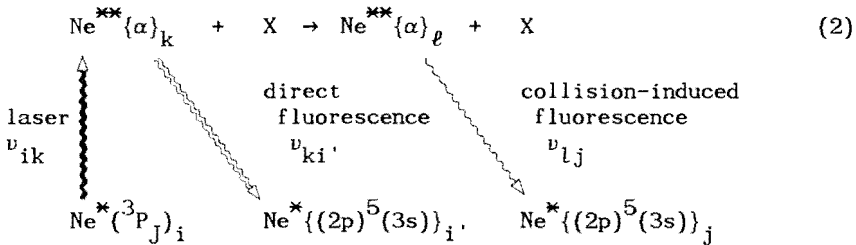
From a theoretical point of view, in our analysis of the experimental results we have made use of the Ne^{**}-He model potentials of Hennecart^{1,11)} and Masnou-Seeuws¹⁾. As accurate information on coupling potentials is indispensable for an explanation of polarization effects, their availability is very fortunate. Reference 20 describes our fully quantum-mechanical coupled-channels calculations on the Ne^{**}-He inelastic scattering problem, which use the above potentials as input. The Ne^{**}-Ne problem, which is complicated by the presence of additional symmetries not present for Ne^{**}-He, is discussed in Ref. 22. At the present thermal

energies these coupled-channels calculations (requiring several hours on a Burroughs B7900 mainframe computer for each energy value) yield cross sections that generally agree well with the experimental results²⁰⁻²¹). Regrettably, however, this constitutes basically a "black box" approach, in that the link between input (model potentials) and output (cross sections) is rather remote. This problem is addressed in Ref. 21, which offers a semiclassical analysis of transitions between states in the $\{a\}_{k=4,5,6,7}$ group. The presence of several avoided crossings between their adiabatic potentials, with its implication of strong localized radial coupling, both emphasizes the group's relatively isolated position within the larger Ne^{**} -multiplet and suggests the relevancy of a description in semiclassical terms. The semiclassical calculations turn out to provide superior insight in the Ne^{**} -He interaction and collision dynamics.

In this paper, we describe the design, operation and calibration of a crossed-beam experiment for the study of total cross sections for the $\text{Ne}^{**} + X$ intramultiplet mixing process of Eq. (1). We start out, in section 2, by considering the signals expected from this kind of experiment. This inevitably leads to a number of experimental requirements, that have heavily influenced the design of the apparatus. In section 3, the ultimate experimental setup is described, first in general terms, then in more detail. There follows section 4 on the calibration of the experiment, i.e. the way in which physically meaningful results may be obtained and subsequently analyzed. Section 5 deals first with data-analysis in general and then with the various experiments it is possible to perform in the present setup. Examples are given of each. Lastly, some concluding remarks are given in section 6. All in all, we aim to provide as complete an overview of the experiment as possible.

2. Experimental signals and design considerations

The design of a crossed-beam experiment for the investigation of inelastic collision processes with short-lived electronically excited atoms has to be considered very carefully. The more so when the reaction products can only be detected through their radiative decay. Let us assume a configuration of three crossing beams: the primary beam of metastable Ne^* -atoms, the laser beam tuned to a $\text{Ne}^* \rightarrow \text{Ne}^{**}$ transition, and the secondary beam of electronic ground state particles X. The experiment can be summed up in the reaction equation



Through optical pumping the metastable $\text{Ne}^{**}(^3P_J)_i$ atoms are excited to the initial short-lived $\text{Ne}^{**}\{\alpha\}_k$ state. Nearly all of the $\{\alpha\}_k$ atoms will be deexcited by spontaneous emission of what is to be called "direct" fluorescence radiation. With the secondary beam passing through the intersection of primary- and laser-beam, however, a small fraction of the $\{\alpha\}_k$ atoms will undergo an inelastic collision. This gives rise to population of the $\text{Ne}^{**}\{\alpha\}_\ell$ state, among others. This state, too, exhibits spontaneous decay within its natural lifetime $\tau \approx 20$ ns, generating "collision-induced" fluorescence radiation. The latter usually comprises several frequencies, like the direct fluorescence. By measuring a single line of both types of fluorescence, we obtain a measure for the number of atoms in the k and ℓ states, respectively, and thus ultimately for the

$\{a\}_k \rightarrow \{a\}_\ell$ cross section. The major experimental problems encountered follow directly from the expressions for the count rates $I_k(s^{-1})$ for the direct fluorescence from the initial state $\{a\}_k$, and $I_\ell(s^{-1})$ for the collision induced fluorescence from the final state $\{a\}_\ell$. These are given by

$$I_k = \eta_k \dot{N}_k R_k \quad (3a)$$

$$I_\ell = \eta_\ell \dot{N}_k R_k \frac{g}{v_1} n_2 \ell_\tau Q_{\ell \leftarrow k} \quad (3b)$$

with η_k and η_ℓ the photon detection efficiency for the direct and collision induced fluorescence, $\dot{N}_k(s^{-1})$ the flow of initial state particles through the scattering volume, v_1 the primary-beam velocity, g the relative velocity of the collision partners, n_2 the secondary-beam density, $\ell_\tau = v_1 \tau_k = v_1/A_k$ the "lifepath" of the initial state particles, and $Q_{\ell \leftarrow k}$ the total inelastic cross section for the $\{a\}_k \rightarrow \{a\}_\ell$ transition. Through the recycling factor $R_k \simeq 1/(1-A_{ki}/A_k)$ we take into account that a fraction A_{ki}/A_k of the atoms in the initial short-lived $\{a\}_k$ state is recycled via the metastable $Ne^*(^3P_J)$ lower level of the optical pumping transition. With appropriate laser power almost all of the $Ne^*(^3P_J)$ atoms in the primary beam are excited to the $\{a\}_k$ state, resulting in $\dot{N}_k = C_J \dot{N}_{Ne^*(J)}$, with C_J the relative population for the metastable state used for the $Ne^{**}\{a\}_k$ production. In Eq. (3b) for the collision-induced fluorescence signal we recognize the usual "n ℓ Q" product of a crossed-beam experiment, modified by the use of the "lifepath" instead of the length of the scattering volume. Of course, Eq. (3) does not apply to the two-level $Ne^*(^3P_2)$ - $Ne^{**}\{a\}_g$ system. Here the Ne-atom oscillates between the metastable and short-lived levels all through the scattering volume, with much larger signals as a result.

Strictly speaking, on its way to the scattering center the primary beam will be attenuated by secondary-beam particles; if not in the secondary beam itself, then in the form of residual gas. This implies, that the \dot{N}_k of Eq. (3) are related to the output of the primary-beam source through a transmission factor T_k , with

$$T_k = \dot{N}_k / \dot{N}_k^{(-\infty)} . \quad (4)$$

The importance of this phenomenon will become apparent soon; for the moment we will disregard it.

From Eq. (3) we can deduce the practical problems which our particular experiment presents. Both the lifepath ℓ_τ of the short-lived atoms and the transition cross section $Q_{\ell \leftarrow k}$ are very small: $\ell_\tau \simeq 20 \mu\text{m}$, $Q_{\ell \leftarrow k} \simeq 1 \text{ \AA}^2$. This implies that considerable effort will be required to obtain a measurable collision-induced fluorescence signal, i.e. a signal that can be separated from the inevitable background. Firstly, we must maximize primary-beam flow \dot{N}_{Ne}^* and secondary beam density n_2 . Secondly, extremely efficient detection of fluorescence photons is needed, that is to say large values of the optical detection efficiency η_ρ . As to background radiation, from Eqs. (3a) and (3b) it follows that at all times the direct fluorescence radiation will be several orders of magnitude larger than the collision-induced fluorescence. This calls for almost complete suppression of the former. Of course, the same holds for other sources of background radiation.

Because both factors R_k and g/v_1 in Eq. (2.2) are on the order of unity, the product of remaining factors must measure

$$\eta_\rho \dot{N}_k n_2 \gtrsim 5 \cdot 10^{27} \text{ m}^{-3} \text{ s}^{-1} \quad (5)$$

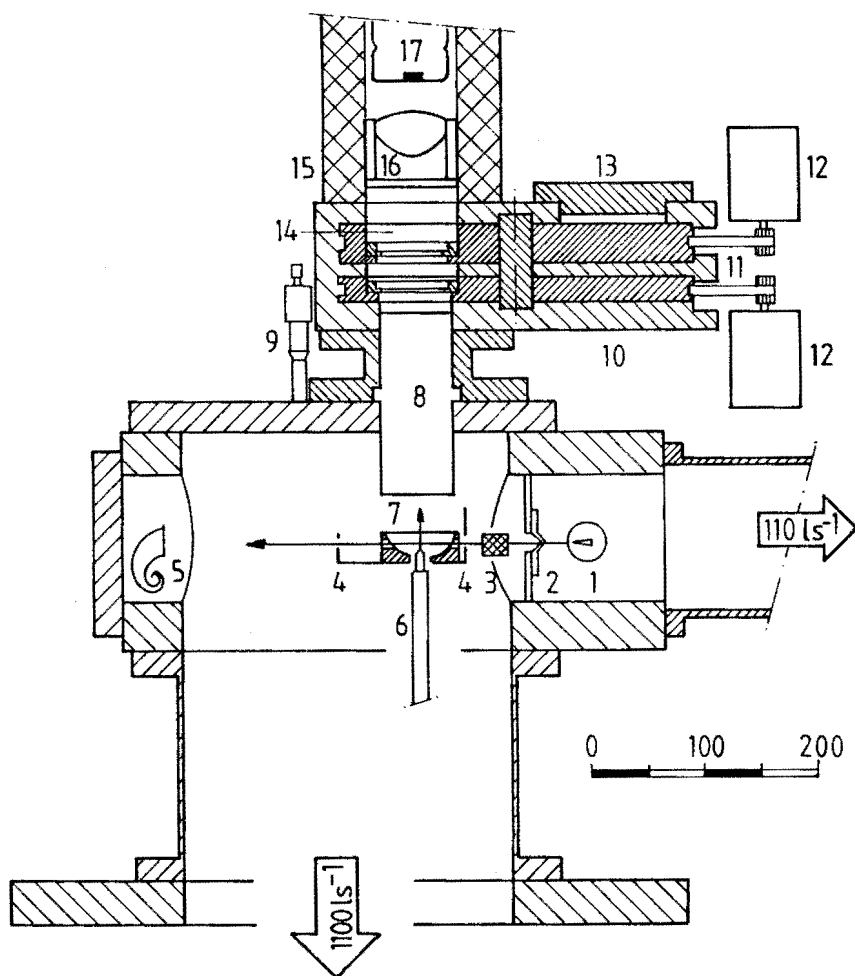


Fig. 2. Schematic drawing of the crossed-beam apparatus. The scale is in mm. To improve visibility, the size of e.g. diaphragm- and mirror-openings has been exaggerated.

(1) Primary beam source; (2) skimmer; (3) condenser plates; (4) primary-beam diaphragms; (5) primary-beam light-trap; (6) vertically adjustable secondary-beam nozzle; (7) parabolic mirror; (8) plexiglass light-guide; (9) micrometer for nozzle adjustment; (10) filter-assembly; (11) belt-driven rotatable filter disks; (12) stepper motors; (13) filter loading-gate; (14) interference and cut-off filters in filter-holders; (15) cooled photomultiplier-housing; (16) no-dew aspherical lens-assembly; (17) photomultiplier.

to obtain a count rate $I_\ell \gtrsim 10^3 \text{ s}^{-1}$, for ℓ_τ and $Q_{\ell+k}$ as given above. In a non-optimized, standard crossed-beam experiment²³⁾, we find typical values $\eta_\ell \simeq 10^{-4}$, $n_2 \simeq 5 \cdot 10^{17} \text{ m}^{-3}$ and $\dot{N}_k = 10^8 \text{ s}^{-1}$ (for a primary-beam center-line intensity of $10^{14} \text{ s}^{-1} \text{ sr}^{-1}$ and 10^{-6} sr^{-1} solid angle). This results in

$$\eta_\ell \dot{N}_k n_2 \simeq 5 \cdot 10^{21} \text{ m}^{-3} \text{ s}^{-1} \quad (6)$$

and a completely impractical count rate of $I_\ell \simeq 10^{-3} \text{ s}^{-1}$!

3. Experimental setup

3.1. Overview

The special requirements of the present experiment have led us to design a novel crossed-beam apparatus, of which a schematic view is given in Fig. 2. Figure 3 offers a more general overview of the experimental setup.

The primary beam of metastable Ne^* -atoms originates in a discharge-excited supersonic expansion, or thermal metastable source (TMS)²⁴⁾. The source chamber, pumped by a 110 ℓ/s turbo-molecular pump, is connected by a 0.5 mm ϕ skimmer to the main vacuum chamber. The latter was machined from a solid block of aluminum. It is pumped by an oil-diffusion pump with an effective pumping speed of 1200 ℓ/s , for a pressure, with no secondary beam, of $p \simeq 2 \cdot 10^{-7}$ Torr. The maximum center-line $\text{Ne}^*(^3P_2)$ intensity for the TMS, operated with pure neon, is about $j_{i,0} \simeq 10^{14} \text{ s}^{-1} \text{ sr}^{-1}$; the $\text{Ne}^*(^3P_2) : \text{Ne}^*(^3P_0)$ ratio is roughly statistical, i.e. 5 : 1. Downstream of the skimmer, all charged particles are removed by condenser plates. The required high density of metastable Ne^* -atoms in the collision region is

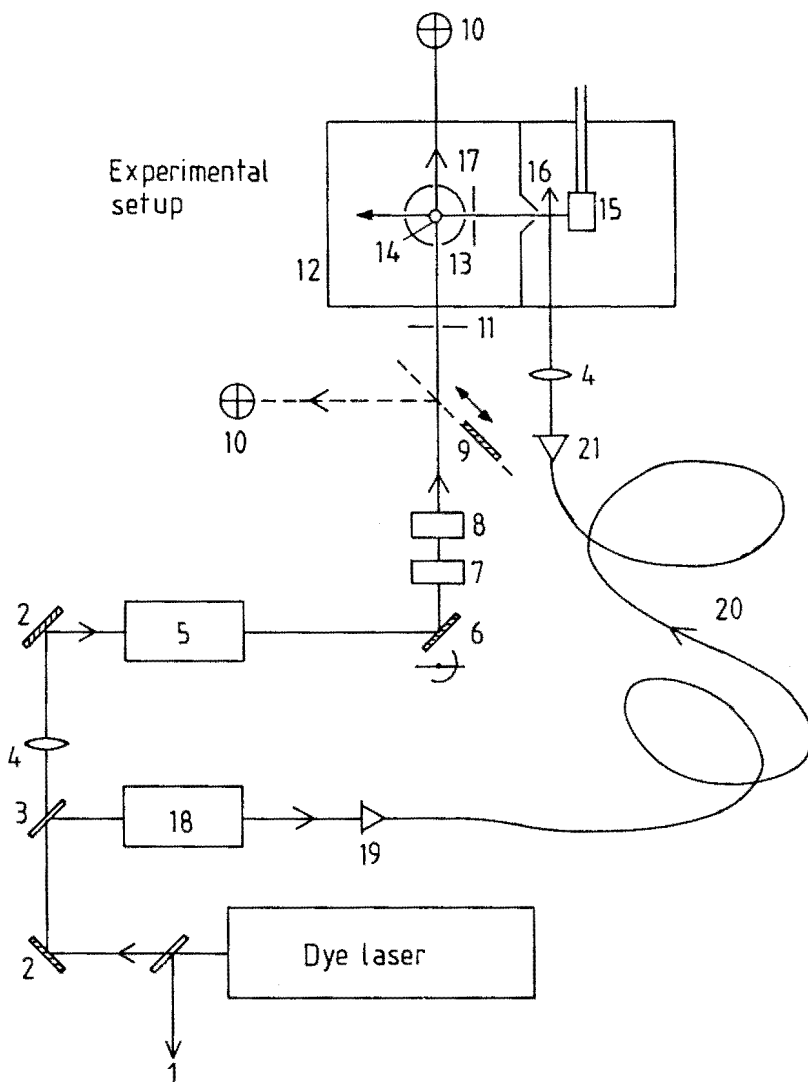


Fig. 3. Overview of the experimental set-up. A separate atomic-beam set-up controls the laser-frequency stabilization.

(1) To laser-frequency stabilization set-up; (2) mirror; (3) beam-splitter; (4) lens; (5) laser-power stabilization; (6) rotatable/translatable mirror; (7) rotatable planparallel plate; (8) laser polarization rotator; (9) movable mirror; (10) quadrant detector; (11) diaphragm; (12) vacuum chamber; (13) parabolic mirror; (14) secondary-beam nozzle; (15) primary-beam source; (16) skimmer; (17) primary-beam diaphragm; (18) laser-chopper; (19) optical-fibre entrance; (20) optical fibre; (21) optical-fibre exit.

obtained by virtue of its small distance to the TMS. With the collision region situated about 90 mm from the TMS, the primary beam density is $n_{\text{Ne}^*} \approx 10^{13} \text{ m}^{-3}$. Metastable particle flow \dot{N}_{Ne^*} through the collision region is determined by the 1 mm ϕ primary-beam defining diaphragm at 60 mm from the skimmer. This geometry results in $\dot{N}_{\text{Ne}^*} \approx 2 \cdot 10^{10} \text{ s}^{-1}$. A 2 mm ϕ diaphragm downstream of the collision region is used for primary-beam alignment. Still further on, a light-trap collects the light from the TMS.

The secondary beam is formed by a skimmerless supersonic expansion (nozzle diameter $2 R_n = 50 \mu\text{m}$). This allows a very small distance from the nozzle to the collision region and a correspondingly high secondary-beam density. In our apparatus the distance may be adjusted from 0 - 12 mm by a micrometer outside the vacuum chamber, through a pin-lever construction. Typically, the distance is 2 mm. For noble gas atoms at a reservoir-pressure $p_{2,0} = 120 \text{ Torr}$ and -temperature $T_2 = 300 \text{ K}$, the secondary-beam density is then given by both theory and experiment²⁵⁾ as $n_2 \approx 3 \cdot 10^{20} \text{ m}^{-3}$. Secondary-beam gas flow is controlled by two pneumatic valves. Upon closure with one valve of the gas-supply, the other valve allows pumping of the gas-leads. From a working pressure of about $4 \cdot 10^{-6} \text{ Torr}$, it takes about 10 s for the pressure to be restored to $2 \cdot 10^{-7} \text{ Torr}$. Depending on the secondary-beam gas, a longer waiting period may be necessary. In summary, we have fulfilled the first experimental requirement of high primary- and secondary-beam densities by situating both primary- and secondary-beam sources as close to the collision region as possible.

The laser beam, linearly polarized, from a Spectra Physics 580A cw single mode dye laser system crosses the primary beam of metastable Ne^* atoms at right angles. The required 590-660 nm range is covered by the easy-to-use Rhodamine 6G, Rhodamine 6B and DCM dyes. The laser frequency is stabilized to within 0.5 MHz rms deviation of the transition frequency ν_{ik} ²⁶⁾. In addition, the frequency is continuously tunable under computer

control within a range of $\nu_{ik} \pm 200$ MHz, in steps as small as 0.1 MHz. Laser power (typically maintained at $P \lesssim 0.2$ mW in the collision region) is controlled and stabilized ($\pm 2\%$) with an electro-optical modulator. Two lenses ($f_1 = 500$ mm, $f_2 = 2000$ mm) are used to obtain a waist in the collision region ($1/e^2$ radius $W \approx 0.4$ mm). The laser polarization can be rotated by means of a stepper-motor driven $\lambda/2$ -plate.

Because of the short lifetimes of the $\text{Ne}^{**}\{\alpha\}_k$ atoms produced in the optical pumping process, it is the laser beam that determines the lateral position of the collision region. The secondary beam has to pass through the crossing point of the laser and primary beams. In view of the vital importance of proper laser beam alignment, two quadrant diodes defining the laser beam axis have been incorporated in the setup. Alignment itself is effected, in the horizontal plane containing the primary-beam axis, by means of a stepper-motor driven rotatable and translatable mirror. For vertical movement of the laser beam we use a rotatable planparallel plate, stepper-motor actuated as well.

The dependence of the optical pumping process on the presence of low-strength magnetic fields²⁷⁾ has necessitated surrounding the vacuum chamber with a set of six rectangular Helmholtz-like coils. With these any field $B \lesssim 2$ G in the scattering center can be nullified, the earth's field ($B \lesssim 0.5$ G) in particular.

In order to perform time-of-flight measurements, part of the laser beam from the dye laser may be branched off with a beam splitter. This second beam is directed through a fiber to the primary beam, between the nozzle of the TMS and the skimmer. An electro-optical modulator in combination with a polarizer allows rapid switching on and off of the laser beam. With the laser attuned to a $\text{Ne}^*(^3P_{0,2}) \rightarrow \text{Ne}^{**}\{\alpha\}_k$ transition, the Ne^* -density in the primary beam will then be modulated accordingly. A laser power of $P \approx 0.5$ mW suffices for nearly 100% modulation of the primary beam.

The optical detection system uses a parabolic mirror for the collection of fluorescence radiation, and narrow-band interference filters for wavelength selection. Additional suppression of background light is achieved through cut-off filters. All filters are housed in a separate filter-assembly. The transmitted photons are focussed on the cathode of a photomultiplier. For a more detailed discussion of the optical system, we refer to the next section. Ultimately, a high detection efficiency is achieved: typically, $\eta_l \simeq 10^{-3}$ per photon produced in the collision region. Like the primary-beam defining diaphragms, the secondary-beam nozzle, and the quadrant diodes used for laser beam alignment, the parabolic mirror has been rigidly attached to the top flange of the vacuum chamber. The latter can therefore be removed without compromising the alignment of these components. The vital performance characteristics of the crossed-beam apparatus have been summarized in Table I. A look at the $\eta_l \dot{N}_k n_2$ -product shows that the tentative requirement of Eq. (6) has been all but satisfied. The overall figure of merit in the thermal energy range is about $1 \text{ kHz}/\text{\AA}^2$, for the number of counts per unit of inelastic cross section. The background count rate ranges from 2 to 15 kHz and is due mainly to the line-emission from the discharge in the TMS.

3.2. Optical detection system

The demands made on the optical detection system, i.e. a large detection efficiency η and effective suppression of background radiation, have been met by employing narrow-band interference filters for wavelength selection. As the interference filters require perpendicular incidence, the collision region is situated near the focal point of a parabolic mirror. Thus a substantial portion of the fluorescence radiation is imaged into a (nearly) parallel beam. Solid-angle efficiency of the parabolic mirror is

Table I. Performance characteristics of the crossed-beam apparatus. The symbols have been defined in the text. The value of the "performance number" is to be compared with that given in Eq. (5).

| Name | Quantity | Typical value |
|----------------------------------|--|---------------|
| optical detection efficiency | η_e (counts/photon) | 1 10^{-3} |
| primary-beam flux | \dot{N}_{Ne^*} (s^{-1}) | 2 10^{10} |
| primary-beam transmission | T_k | 0.35 |
| optical pumping recycling factor | R_k | 1.5 |
| lab-c.m. conversion | g/v_1 | ~ 1 |
| secondary-beam density | n_2 (m^{-3}) | 3 10^{20} |
| life path | l_τ (m) | 2 10^{-5} |
| inelastic cross section | Q_{e+k} (m^2) | 1 10^{-20} |
| "performance number" | $\eta_e \dot{N}_k n_2$ ($m^{-3} s^{-1}$) | 3 10^{27} |
| count rate | I_e (s^{-1}) | 0.63 10^3 |

approximately 0.40, i.e. a solid angle of 1.6π is collected. The condition of (nearly) perpendicular incidence on the interference filters poses no serious limitation on the acceptance of the optical system. The optical phase volume of the parabolic mirror - interference filter combination is very much larger than can be attained with a monochromator. Originally, a Melles Griot parabolic mirror ($f = 10.2$ mm) was used, with a rhodium coating on a nickel substrate. Entrance and exit ports for the primary and laser beams have been added. An opening in the bottom for the secondary-beam nozzle was present already. This mirror has now been replaced by a non magnetic all-aluminum specimen of the same specifications and with a comparable reflection coefficient $R \approx 0.80$. To interchange filters during the experiment, they have been positioned outside the vacuum chamber. To minimize the loss due to divergence of the light from the parabolic mirror, a plexiglass cylinder has been used as a transparent vacuum seal. This acts as a light guide, on account of complete internal reflection.

The interference filters (peak transmission $T_{\max} \approx 0.70$, 2 nm full-width-at-half-maximum (FWHM), 10 nm FW at 10^{-6} transmission) (see Fig. 12, in the next section) allow us to monitor a single line of either the collision-induced fluorescence from the final state $\{\alpha\}_p$, or the direct fluorescence from the initial state $\{\alpha\}_k$. Generally, we have ample background suppression. In some cases the wavelength spacing to a nearby direct fluorescence line is simply too small. Where necessary, additional suppression of background light is achieved by the use of colored glass cut-off filters. When measuring direct fluorescence radiation, neutral density filters are added to the optical system in order to guarantee a linear response of the counting system.

Given the important role that filters (interference filters in particular) play in the experiment, a special filter assembly has been designed, that combines easy interchangeability of the filters with

hermetic optical sealing. It is shown in Fig. 4. The two flat disks, which are its major constituents, have five filter chambers each. The lower and upper disks accommodate one and two filters per chamber, respectively. For this purpose, the filters have all been mounted in standard filter-holders. The disks may be rotated independently, so as to bring any combination of the 2×5 filter positions into the light path of the optical system. The filters may be rearranged in the disks through a cover in the assembly, diagonally opposite the photomultiplier housing. One filter position in the upper disk has been sacrificed to give access to the filters in the lower disk. Through the use of various fabrics, sandwiched between moving and non-moving parts, it has been ensured that no light from the surroundings can penetrate into the optical system. Likewise, heavily compressed fabric sealing between both filters and filter-holders and filter-holders and filter-chambers prevents light from the experiment from circumventing the filters. With a metal disk replacing the filters in front of the photomultiplier, no rise in the dark-count number of the photomultiplier (about 12 s^{-1}) is observed under any circumstances.

The filter-disks can be rotated by hand. However, the experiment requires the filters in front of the photomultiplier to be changed at short time-intervals. Therefore, a pair of stepper motors has been mounted, each driving a disk through a belt around its circumference. These stepper motors are under computer control. The computer checks for proper positioning of the disks by reading out an array of four micro-switches, actuated by notches cut into each disk. One of the notches serves for indexing purposes only, the other three are needed to unambiguously identify each of the five filter positions per disk. Of course, at all times the direction of rotation is chosen so as to minimize the number of steps to the next filter position. Through parallel processes in the experiment computer, the disks are made to rotate simultaneously. Lastly,

lest during the filter change the photomultiplier is unintentionally exposed to excessive light-intensity, the laser beam is interrupted by a computer-actuated shutter.

After passing through the filters, the photons are focussed by an aspherical lens ($f = 39$ mm) onto the 9 mm ϕ cathode of a selected red-sensitive EMI 9862 S20 photomultiplier in a housing cooled to -20° C. Quantum efficiency of the photomultiplier is a low 3-5%, depending on the wavelength. Finally, pulses from the photomultiplier are converted into TTL pulses by a EG&G PARC model 1182 amplifier/discriminator. As mentioned before, in the present configuration the overall detection efficiency of the optical system is typically $\eta_1 \approx 10^{-3}$ counts per photon produced in the collision region.

3.3. *Laser-beam alignment*

The crucial importance of proper laser-beam alignment has already been indicated and will be reexamined later. Laser-beam diameter is on the order of 1 mm ($1/e^2$ contour) and an accuracy of better than 0.05 mm in both the horizontal and the vertical position of the laser beam - primary beam intersection is required. Because of this it was found necessary to establish both a way to fix the true laser-beam axis in space, and to maneuver the laser beam into the proper position. In view of the desired accuracy and in order to minimize the time spent on alignment, an automated procedure is preferred. The heart of the alignment system are two light-sensitive quadrant diodes. As shown in Fig. 5, these are divided into four equal parts, each of which will yield a signal proportional to the amount of incoming light. From the right-left and up-down differences in signal magnitude, the position of a laser beam striking the detector can be determined. As an example, Fig. 5 shows the result of a horizontal scan of

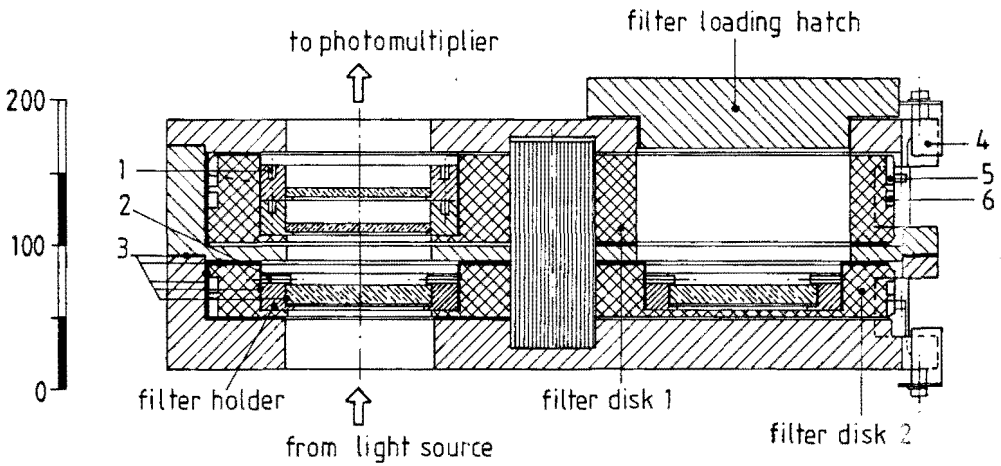


Fig. 4. Schematic drawing of the filter assembly. Its major components have been indicated. The scale is in mm. The thickness of the fabric sealing between the parts has been exaggerated.

(1) Threaded hole for filter-holder removal; (2) lock-screw securing interference filter; (3) fabric sealing between moving and non-moving parts; (4) micro-switch (one of four per filter disk); (5) activating notch for micro-switch; (6) groove for belt driving filter disk.

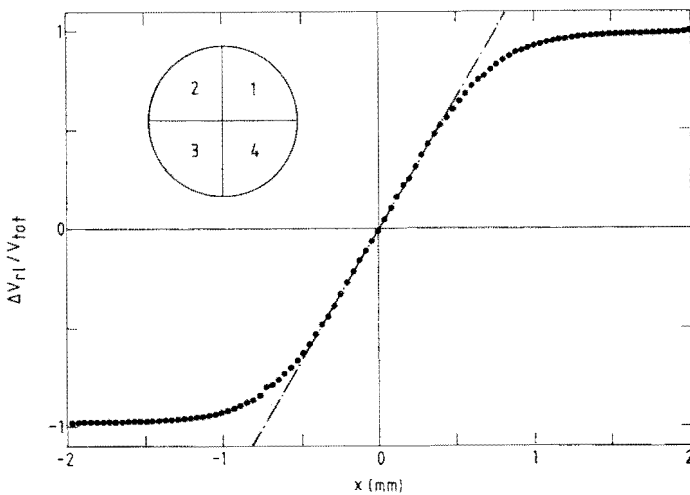


Fig. 5. The scaled differential right-left signal $\Delta V_{rl} = (V_1 + V_4) - (V_2 + V_3)$, for a 1.3 mm diameter ($1/e^2$) approximately Gaussian laser beam moving horizontally over a quadrant detector. The signal displays linear behavior about the center-position. This allows positioning of the laser beam by the fast and accurate method of interpolation.

the laser beam across the detector surface. The linear behavior of the right-left signal about the origin allows a highly accurate estimate of the laser beam position.

Two quadrant diodes are needed to fix a line in space. The second of these has been situated for the laser beam to hit upon its exit from the vacuum chamber. The first has been placed at right angles to the laser beam. An angled mirror moving into and out of the laser beam makes it possible to illuminate the first and second detector in turn. This setup has been pictured in Fig. 3. A linear bearing allows one-dimensional movement of the mirror only, answering all demands regarding positioning accuracy. Having the detector itself return again and again to the same position in the beam would require considerably more effort. The signals from the detectors are fed through a multiplexer to four gates of an ADC converter and read by the computer. Moving the mirror is done by stepper motor, under computer control. Both detectors and mirror are mounted on a yoke, which is fixed rigidly to the lid of the vacuum chamber. Thus their position with respect to the primary-beam - defining diaphragms and the secondary-beam nozzle is fixed, as well. Initial alignment of the detectors is done both visually and by, for instance, maximizing the direct fluorescence signal with respect to the angle between laser and primary beam. Horizontal and vertical positioning of the detector is possible in 0.01 mm increments, with a micrometer.

With the quadrant detectors in place, it remains to devise an automated alignment procedure. For this, use was made of the translator/rotator module²⁸⁾ mentioned earlier, whose mirror can be translated and rotated independently by stepper motors. Thus the laser beam can be moved at will in the horizontal plane. In particular, by using both stepper motors under computer control, rotation about any given point, within limits, becomes feasible. At present translation is in 0.01 mm steps and rotation in

0.2 mrad steps, over a total range of 15 mm and 200 mrad, respectively. This is commensurate with the requirements of the experiment. In a more simple module, a stepper motor rotating a planparallel plate can move the laser beam up and down in steps of approximately 0.01 mm. There is at present no provision for rotating the laser beam in the vertical plane. This is least critical to a proper outcome of the experiment, however, and alignment by hand to within 2 mrad prior to starting the automated alignment procedure suffices.

Horizontal alignment is performed first. To begin with, the laser beam is rotated about the *first* detector into alignment with the *second*. Subsequently this is repeated the other way around, the laser beam now being aligned with the *first* detector, while alignment is maintained on the *second* detector. This procedure is iterated, if necessary. In the end, the laser beam can thus be aligned to within 0.1 mrad. This corresponds to a horizontal position error of less than 0.05 mm on the two detectors, well within their linear range (see Fig. 5). By *translating* the laser beam a scan can then be made over the two detectors, akin to the one in Fig. 5, though over a smaller range and in fewer steps. Since the position of the scattering center between the two detectors is known, the laser beam can in principle be made to pass within approximately 0.005 mm, while maintaining its smaller than 0.1 mrad misalignment. In the vertical direction, the alignment procedure essentially duplicates the last stage of the horizontal alignment. Now, the *translation* is performed by rotating the planparallel plate. The whole laser beam alignment process, apart from the initial positioning by hand which is needed only intermittently, takes the computer about 15 minutes.

3.4. Pseudo-random laser chopper

In the present mini-beam setup, the metastable primary-beam atoms traverse only a short distance $L \approx 90$ mm from the thermal metastable beam source to the collision region. Average beam velocity is about $v_1 \approx 1000$ m s⁻¹. For time-of-flight (TOF) measurements to yield a properly resolved velocity spectrum with, say, $\Delta v_1/v_1 \lesssim 0.5 - 5\%$, channel times $t_k < 0.5 - 5$ μ s with correspondingly short burst times t_b are required. In addition, the low signal strengths associated with the collision-induced fluorescence in particular, indicate the use of a pseudo-random chopper function which has a much larger open time-fraction than the more usual single-burst chopper function²⁹). However, it is very difficult to synchronize a pseudo-random mechanical chopper with the multichannel scaler counting the signal in its time-channels. Furthermore, the short burst times required rule out a mechanical chopper, for reasons of mechanical strength alone³⁰). This means, that an optical laser-chopper presents the only viable option for TOF-measurements. Of course, the limited amount of room available in our very compact apparatus also favors this technique, wherein the metastable $\text{Ne}^*(^3P_{0,2})$ density in the primary beam is modulated by a laser beam attuned to a $\text{Ne}^*(^3P_{0,2}) \rightarrow \text{Ne}^{**}\{\alpha\}_k$ transition.

The chopper laser beam is branched off with a beam splitter from the laser beam that produces the initial short-lived $\text{Ne}^{**}\{\alpha\}_k$ -atoms in the scattering volume. A Coherent model 28 electro-optical crystal is used together with a fast high voltage amplifier driven by TTL pulses, to rotate the laser's polarisation over 90° , and back. In combination with a polarizer, this effectively turns the beam off and on. With the laser beam directed through a fiber to the space between the nozzle of the TMS and the skimmer, the primary beam of metastable $\text{Ne}^*(^3P_{0,2})$ atoms is consequently turned "on" and "off". Up to 98% modulation of the relevant Ne^* -flux can be achieved in this way, with a laser power $P \approx 0.5$ mW.

The fast multiscaler³¹⁾ has 255 time-channels, with a minimum channel time $t_k = 500$ ns. It is able to store a pre-programmed pseudo-random or single-burst series in its memory. This may be administered in the form of TTL pulses to the high voltage amplifier controlling the electro-optical modulator. The fluorescence signals from the collision volume are accumulated in the multiscaler's time channels. This arrangement ensures the proper synchronisation of chopper and multiscaler. Channel times t_k are derived from an external 20 MHz clock. It is possible to select burst times $t_b = i/5 * t_k$, with $i = 1, \dots, 5$.

The multiscaler was designed to function as an intelligent interface in a computer-controlled measuring system. Prior to measuring, the computer loads the desired pseudo-random or single-burst series of an arbitrary length $N \leq 255$ into the multiscaler's memory. Then, after a starting signal from the computer, the multiscaler accumulates data in its time channels for a maximum of 65000 chopper periods. Overflow errors and the like are reported back to the computer. In the meantime, the computer is free to perform other tasks, such as checking the status of the experiment or performing a calculation upon the data already collected. After its final period, the multiscaler notifies the computer which samples the accumulated data and restarts the cycle.

3.5. Computer control

The complexity and required accuracy of the experiment are such, that it could hardly be run without the aid of a computer. This applies both to the actual measuring process and to the data-gathering and -analysis. As will be detailed in section 4, every basic cross-section measurement requires the frequent tuning and detuning of the laser, the rotation of filters for direct and collision-induced fluorescence, and the turning on

and off of the secondary beam. A complete cross section measurement (section 5) requires that e.g. the laser polarisation be rotated, or the laser beam moved, or the secondary-beam gas changed. With the exception, at present, of the latter, all of the above can be performed by computer. So can, as we have seen already, the alignment of the laser beam.

The experiment computer was developed in the Physics Department on the basis of the Motorola M68000 microprocessor³²⁾. It is programmed in the Pascal-related language PEP (Program Editor and Processor)³³⁾, which is an interpreter-based language and thus especially suited to an experimental environment. The computer's capacity to handle several parallel processes at a time is also very useful in this respect. Experiment-control and data-gathering procedures are collected in libraries in the micro-computer's memory (1 Mbyte, at present) and are accessed by the measuring program.

The computer's connection to the experimental setup is through the modular Eurobus interface system³⁴⁾. A number of interfaces is available. For data gathering, multiple channel ADC's, scalers and preset-scalers are used (the latter two combine with a 20 MHz clock into a frequency counter). The multiscaler mentioned above also adheres to the Eurobus protocol. Basic functions of the experimental setup (associated with stepper motors, micro-switches, relays, etc.) are handled by stepper-motor interfaces, input-/output-registers and DAC's. The input-/output-register also provides a hardware-based communication's link with the separate LSI 11/02 micro-computer controlling the laser system. In addition information is exchanged through a common file on background memory.

Both experiment- and laser-computer are connected, through the departmental network Budgetnet³⁵⁾, to a central MicroVax II computer, which acts as host in a file-server capacity. After preliminary analysis, data gathered by the experiment computer are sent to the host computer, along

Table II. Typical background signals for the crossed-beam apparatus.

| Background source | Signal without interference filter (s^{-1}) | Signal with interference filter ^{a)} (s^{-1}) |
|-----------------------------------|---|--|
| PM dark count | 12 | 12 |
| surroundings ^{b)} | $40 \cdot 10^3$ | 55 |
| laser ^{c)} | $50 \cdot 10^6$ ^{d)} | 200 |
| TMS | $30 \cdot 10^3$ | 1000 |
| direct fluorescence ^{e)} | -- | 4000 |

a) 703 nm

b) normal lighting

c) 0.1 mW, 633 nm

d) extrapolated value

e) 633, 650, 717 nm

Budgetnet's 2.5 Mbaud serial line. From the host, data can be sent to the computing center's Burroughs B7900 mainframe computer over the university's 9600 baud TUE-network, for further analysis. Once the group's network of PC/AT compatible microcomputers has been connected to Budgetnet, these will largely supersede the B7900 as a tool for full data-analysis.

4. Calibration of the experiment

4.1. Measuring routine

Our aim is to determine the collision-induced and direct fluorescence signals I_ℓ and I_k , as defined in Eq. (3). Ideally, this would involve two measurements only, with different interference filters. In practice, however, we will have to correct for background light which cannot be entirely suppressed by the optical system. The main sources of background are light from the surroundings, stray light from the laser, direct fluorescence from the initial $Ne^{**}\{\alpha\}_k$ level, and stray light from the primary beam source (TMS). While with some effort the first two may be reduced to an extent that the interference filters are capable of suppressing them almost entirely, this does not hold for the other two. Of course, light from the TMS contains the very wavelengths that we are investigating. For the relative importance of the various sources of background in our apparatus, see Table II.

In order to correct for background contributions, two further diagnostics are employed in addition to the use of different filters for direct and collision-induced fluorescence. The first of these is modulation of the optical pumping process by which the initial $Ne^{**}\{\alpha\}_k$ atoms are produced. Rather than simply turning the laser "on" and "off", which allows

Table III. The settings used for signal-diagnostics, and the corresponding experimental signals. See the text for explanation.

| Filters for | Secondary beam | Laser beam | Collision- induced Signal = fluorescence ⁺ | Direct fluorescence ⁺ | Back- ground | "Real" signal |
|--|----------------|--------------------------------|--|-------------------------------------|-----------------------------|--|
| collision- induced fluorescence from { α }_l-level (L) | on | ν_0 $\nu_0 + \Delta\nu$ | $L^{\text{on}}(\nu_0) = T_k \dot{N}_\ell \eta_\ell^l + T_k \dot{N}_k \eta_\ell^k$ | $+ T_k \dot{N}_k \eta_\ell^k$ | $+ \mathcal{R}_\ell B_\ell$ | $L^{\text{on}} = L^{\text{on}}(\nu_0) - L^{\text{on}}(\nu_0 + \Delta\nu)$ |
| | off | ν_0 $\nu_0 + \Delta\nu$ | $L^{\text{off}}(\nu_0) =$ $L^{\text{off}}(\nu_0 + \Delta\nu) = \epsilon\{\dots\dots\dots\}$ | $\dot{N}_k \eta_\ell^k$ | $+ B_\ell$ | $L^{\text{off}} = L^{\text{off}}(\nu_0) - L^{\text{off}}(\nu_0 + \Delta\nu)$ |
| direct fluorescence from { α }_k-level (K) | on | ν_0 $\nu_0 + \Delta\nu$ | $K^{\text{on}}(\nu_0) = T_k \dot{N}_\ell \eta_k^l + T_k \dot{N}_k \eta_k^k$ | $+ T_k \dot{N}_k \eta_k^k$ | $+ \mathcal{R}_k B_k$ | $K^{\text{on}} = K^{\text{on}}(\nu_0) - K^{\text{on}}(\nu_0 + \Delta\nu)$ |
| | off | ν_0 $\nu_0 + \Delta\nu$ | $K^{\text{off}}(\nu_0) =$ $K^{\text{off}}(\nu_0 + \Delta\nu) = \epsilon\{\dots\dots\dots\}$ | $\dot{N}_k \eta_k^k$ | $+ B_k$ | $K^{\text{off}} = K^{\text{off}}(\nu_0) - K^{\text{off}}(\nu_0 + \Delta\nu)$ |

for no easy correction for stray laser light, the laser is tuned and detuned sufficiently (about 100 MHz) to preclude excitation of the metastable $\text{Ne}^*(^3\text{P}_{0,2})$ atoms. The slight accompanying wavelength change makes no difference to the optical system. The second additional diagnostic is modulation of the *secondary beam*, by simply turning it on and off. Of course this also influences the attenuation of the primary beam by secondary-beam particles. By combining these three modulation techniques, we can devise a tactic to eliminate all background contributions.

Table III lists all possible diagnostic combinations together with the corresponding experimental signals. These consist of varying contributions from the direct fluorescence from the initial level, the collision-induced fluorescence from the final level, and background light. The "net" direct and collision-induced fluorescence signals I_ℓ and I_k of Eq. (3) have been emphasized. The transmission factor T_k has been defined in Eq. (4). The factors \mathcal{A}_k and \mathcal{A}_ℓ formally take into account the effects on the background signal B of Rayleigh scattering of background light by the high-intensity secondary beam. We also nominally allow for imperfect detuning of the laser, whereby a fraction $\epsilon > 0$ of the metastable atoms will still be pumped. Lastly, a superscript ℓ/k used in connection with the detection efficiency $\eta_{k/\ell}$ indicates a radiation wavelength $\lambda_{\ell/k}$ at odds with the normal transmission wavelengths $\lambda_{k/\ell}$ of the filter combination in question.

It is evident, that the additional measurements with detuned laser allow us to correct for background contributions other than those from the direct fluorescence radiation. Hence, the phrase "real" signals in Table III. In the short-hand notation of this table, we have for the averaged transmission factor T_k of Eq. (4):

$$T_k = \frac{K^{\text{on}}}{K^{\text{off}}} \tag{7}$$

Table IV. Typical signal count rates and measuring times. These apply to the $\{a\}_7 \rightarrow \{a\}_5$ transition for $|M_7| = 0$.

| | Signal | Count rate (s^{-1}) | Measuring time (s) |
|--|--------------------------------|-------------------------|--------------------|
| collision- induced fluorescence (L) | $L^{\text{on}}(v_0)$ | 9460 | 180 |
| | $L^{\text{on}}(v_0+\Delta v)$ | 8940 | 180 |
| | $L^{\text{off}}(v_0)$ | 8930 | 50 |
| | $L^{\text{off}}(v_0+\Delta v)$ | 8840 | 50 |
| direct fluorescence (K) a) | $K^{\text{on}}(v_0)$ | 4440 | 50 |
| | $K^{\text{on}}(v_0+\Delta v)$ | 590 | 50 |
| | $K^{\text{off}}(v_0)$ | 11200 | 30 |
| | $K^{\text{off}}(v_0+\Delta v)$ | 520 | 30 |
| cross section $Q_{\ell \leftarrow k} \frac{ M_k }{I_k}$ $= 0.70 \text{ \AA}^2$ | $\frac{I_\ell}{I_k}$ | 0.127 ± 0.07 | 620 |

a) Including neutral density filter ($7 \cdot 10^{-5}$ transmission).

where the collision-induced contribution to the K^{on} -signal has been neglected. The ratio I_ℓ/I_k of collision-induced and direct fluorescence signals, from which the total cross section $Q_{\ell k}$ may ultimately be determined, follows from

$$\frac{I_\ell}{I_k} = \frac{L^{\text{on}}}{K^{\text{on}}} - \frac{L^{\text{off}}}{K^{\text{off}}} \quad (8)$$

The second term corrects for the "leakage" of direct fluorescence radiation through the filters meant for collision-induced fluorescence. If there were no such leakage, we would of course have $L^{\text{off}} = 0$ (no secondary beam, therefore no inelastic process).

In practice, tuning and detuning of the laser (by piezo-element), turning the secondary beam on and off (by pneumatic valves), and exchanging the filters for direct and collision-induced fluorescence (by stepper motors) are under computer control. Thus, the whole sequence can easily be incorporated into the measuring program and be executed automatically. Composite time for the set of 8 measurements, needed to determine a single transition cross section $Q_{\ell k}$, is generally 10-40 minutes, depending on cross-section magnitude. Typical signals are given in Table IV. These apply to the $\{a\}_7 \rightarrow \{a\}_5$ transition with asymptotic orientation $|M_5|=0$.

From Eq. (3), the ratio I_ℓ/I_k of collision-induced and direct fluorescence signals follows as

$$\left[\frac{I_\ell}{I_k} \right]_{\text{ideal}} = \frac{\eta_\ell}{\eta_k} \frac{g}{v_1} n_2 e_\tau Q_{\ell \leftarrow k}(g) \quad (9)$$

In anything other than the ideal case of a vanishing scattering volume, combining Eq. (9) with the experimental ratio I_ℓ/I_k of Eq. (8) yields an

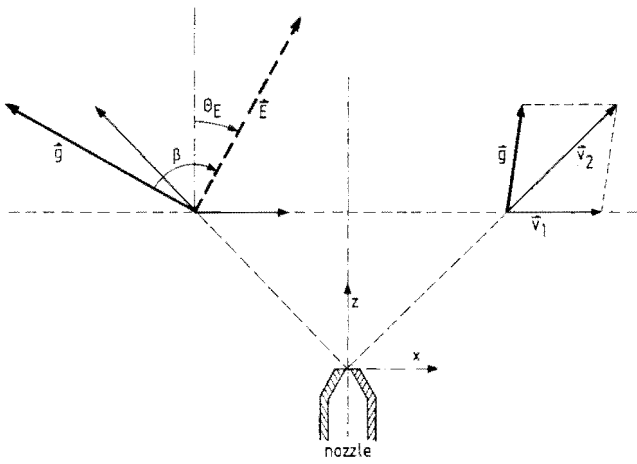


Fig. 6. Newton diagram of the collision process, with \underline{v}_1 and \underline{v}_2 the primary- and secondary-beam velocities. The laser beam is in the y-direction. The laser electric field vector \underline{E} makes an angle β with the relative velocity \underline{g} .

averaged cross section value $Q_{\ell \leftarrow k}$. Taking the convolution effects due to a finite scattering volume V into consideration, we have in more specific terms than offered by Eq. (9):

$$\frac{I_{\ell}}{I_k} = \frac{\int_V n_1(\underline{r}) T_k(\underline{r}) n_k(\underline{r}) n_2(\underline{r}) g(\underline{r}) Q_{\ell \leftarrow k}(g) d\underline{r}}{A_k \int_V \eta_k(\underline{r}) T_k(\underline{r}) n_k(\underline{r}) d\underline{r}}. \quad (10)$$

The optical detection efficiencies η_{ℓ} and η_k have been mentioned already in connection with Eq. (3), as have the primary-beam transmission factor T_k , the secondary-beam density n_2 and, of course, the inelastic transition cross section $Q_{\ell \leftarrow k}$. Equation (10) now also takes explicit account of the density profile n_k of the initial short-lived $Ne^{**}\{\alpha\}_k$ atoms. The Einstein coefficient $A_k = \tau_k^{-1}$ of spontaneous emission links the number of $\{\alpha\}_k$ -atoms with the number \dot{N}_k of photons produced, in Eq. (3). We recall, that the lifepath ℓ_{τ} is given by $\ell_{\tau} = v_1 \tau_k$. The small size of the scattering volume V , as determined by the density profile $n_k(\underline{r})$, ensures that Eq. (9) is indeed a fair approximation of Eq. (10).

In the experiment we have no detailed knowledge of primary-beam densities and therefore of absolute values n_k . However, since we are concerned only with the ratio I_{ℓ}/I_k , this does not preclude the possibility of obtaining absolute cross-section values. With equal force, this applies to the optical detection efficiencies η_{ℓ} and η_k , absolute values for which would be very hard to determine. Again, any unknown *common* factors are eliminated from Eq. (10). Even the potentially troublesome attenuation phenomenon factors out, to first order. We will now discuss, separately, the various quantities in Eq. (10) and the way in which the experiment has been calibrated with regard to each of them.

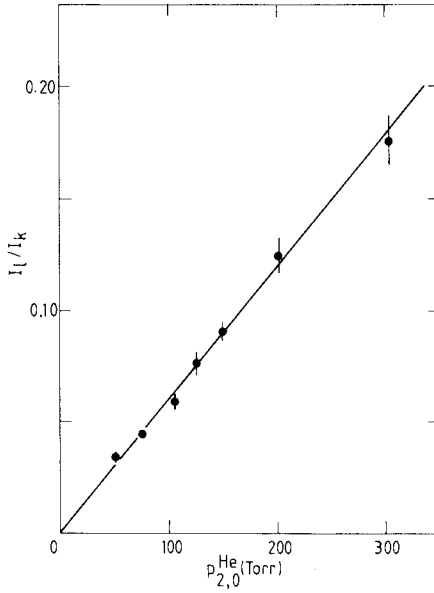


Fig. 7. Collision-induced to direct fluorescence ratio I_l/I_k as a function of the secondary-beam reservoir-pressure $p_{2,0}^{\text{He}}$. In accordance with Eq. (9), I_l/I_k does not depend on the primary-beam transmission factor T_k , but is proportional to $n_2 \sim p_{2,0}$.

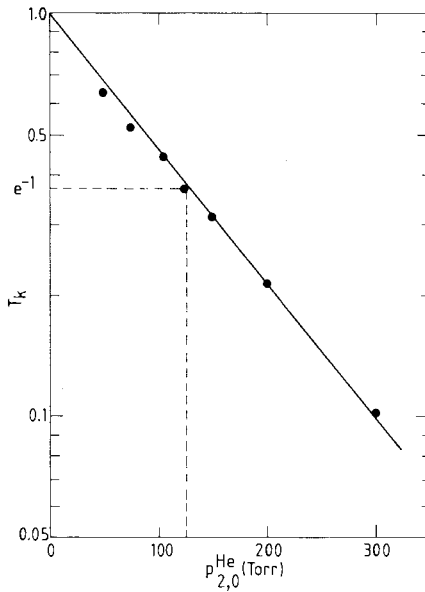


Fig. 8. The primary-beam transmission factor T_k as a function of the secondary-beam reservoir pressure $p_{2,0}^{\text{He}}$. The observed exponential attenuation conforms to Eq. (12). The $1/e$ point corresponds to the optimum of I_l in Fig. 10.

4.2. Secondary beam density n_2

The secondary-beam density n_2 is directly related to the source density $n_{2,0}$ through the shape of the radially expanding flow field of the supersonic expansion. For mono-atomic gases, with the nozzle shape used in our setup, experiment and theory are in excellent agreement²⁵⁾. For a nozzle radius R_2 , we have in spherical coordinates relative to the nozzle:

$$n_2(r,\theta) = n_{2,0} \left(a R_n / r \right)^2 \cos^3 \theta \quad (11)$$

with $a = 0.806$. (For a view of the coordinate system used in relation with the experiment, see Fig. 6.) The source density may be expressed in terms of the reservoir-pressure $p_{2,0}$ and -temperature $T_{2,0}$ by the ideal gas law.

In Fig. 7 we have plotted the ratio I_ℓ/I_k of collision-induced and direct fluorescence signals, as a function of secondary-beam reservoir pressure $p_{2,0}^{\text{He}}$. The linear dependence of $I_\ell/I_k \sim n_2 \ell_\tau Q_{\ell \leftarrow k}$ on $p_{2,0}^{\text{He}}$ provides convincing evidence of the soundness of the principles embodied in our experiment. In addition, of course, the linear dependence of n_2 itself on $p_{2,0}$ is demonstrated in this way, indicating our control of secondary-beam properties. In practice, at large distance from the nozzle, the effect of residual pressure (due to limited pumping capacity) is bound to make itself felt.

4.3. Transmission factor T_k

The attenuation of the primary beam, travelling in the x-direction, by secondary-beam particles can be described by a transmission factor $T_k(x) = n_{\text{Ne}^*}(x)/n_{\text{Ne}^*}(-\infty)$, of the form (compare Eq. (3))

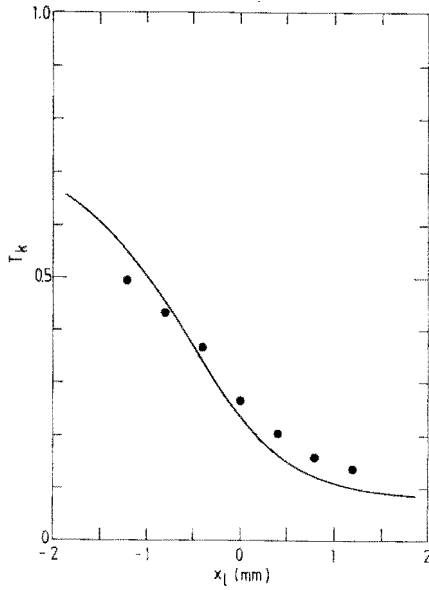


Fig. 9. The primary-beam transmission factor T_k as a function of the laser-beam position x_l along the primary-beam axis. The agreement with the calculated transmission is less than usual for this measurement. This has a negligible effect on calculated cross sections, however.

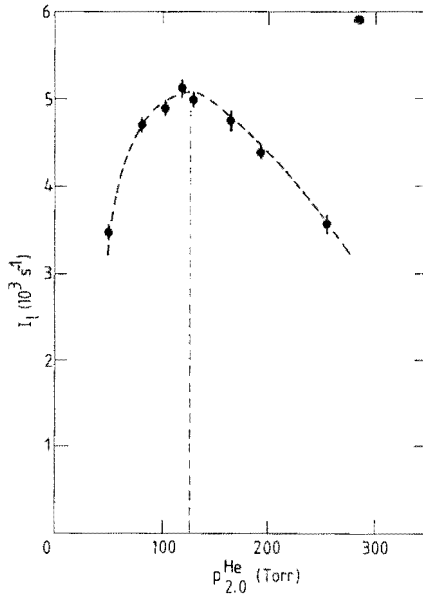


Fig. 10. The collision-induced fluorescence signal I_ℓ as a function of secondary-beam reservoir pressure $p_{2,0}^{He}$. Due to the opposite effect of $p_{2,0}^{He}$ on the secondary-beam density n_2 and the primary-beam transmission factor T_k , an optimum pressure is found. This roughly satisfies Eq. (14) and corresponds to $T_k \approx 1/e$ in Fig. 8.

$$T_k(\underline{r}) = \exp \left[- \int_{-\infty}^x \frac{g(\underline{r}')}{v_1} n_2(\underline{r}') Q^{el} dx' \right]. \quad (12)$$

Here Q^{el} is the effective total cross section for elastic scattering of Ne^* -atoms. Assuming mono-energetic particle beams and with the secondary-beam density given by Eq. (11), Eq. (12) can be solved analytically in the xz -plane, determined by the primary-beam axis (x) and the center-line (z) of the secondary-beam expansion (see Fig. 6)³⁶). Of course, at any given position we are bound to find:

$$- \ln(T_k) \sim n_{2,0} \sim p_{2,0}.$$

This behaviour of T_k as a function of the secondary-beam pressure $p_{2,0}$ is indeed demonstrated in Fig. 8. Figure 9 shows T_k as a function of the position x_l of the laser beam along the primary-beam axis. A curve fit on the basis of Eq. (12) to Ne^{**} -He transmission data for a variety of pressures and positions (x, z) yields a value $Q_{Ne^*-He}^{el} \approx 100 \text{ \AA}^2$. This is a reasonable value for hard-sphere scattering, as shown by comparison with $\pi R_m^2 \approx 75 \text{ \AA}^2$, with R_m the position of the potential-well³⁷). The residual gas pressure within the parabolic mirror, found from these measurements as $p_{r,He} \approx 4 \cdot 10^{-4}$ Torr for $p_{2,0} = 120$ Torr, corresponds closely with the value $p_{r,He} = 7 \cdot 10^{-4}$, calculated on the basis of pumping speed considerations.

4.4. Optimum collision-induced fluorescence signal I_ℓ

For a given position of the scattering volume, the collision-induced fluorescence signal I_ℓ is determined by the product $T_k n_2$ of primary-beam transmission and secondary-beam density (see Eq. (10), or Eqs. (3) and (4)). As an increase in n_2 automatically results in a decrease in T_k , there is bound to be an optimum reservoir density $n_{2,0}$, for which I_ℓ

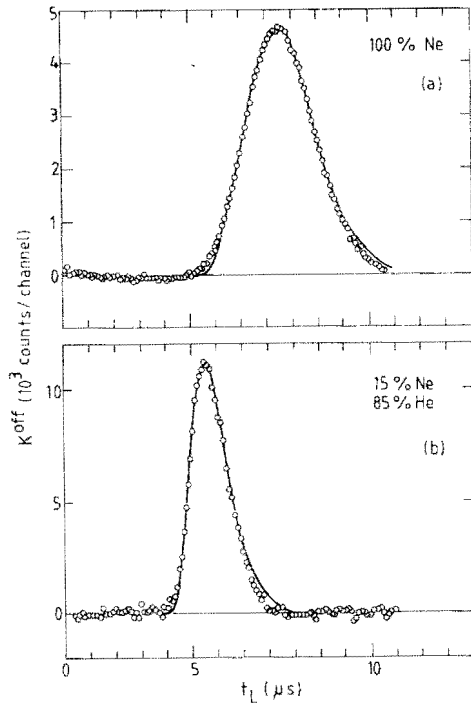


Fig. 11. Time-of-flight distributions of a 100% Ne (a) and a 15% Ne - 85% He (b) beam from the thermal metastable beam source. The flight-path is $L \approx 86$ mm. Both spectra were obtained with the laser-chopper operating in single-burst mode, with channel-time $t_k = 1 \mu\text{s}$. Peak velocities are $v_1^{\text{pure}} \approx 1010 \text{ ms}^{-1}$ and $v_1^{\text{seeded}} \approx 1495 \text{ ms}^{-1}$.

attains a maximum value. This occurs, when

$$\frac{\partial I_\ell}{\partial n_{2,0}} = \frac{\partial(T_k n_2)}{\partial n_{2,0}} = 0 . \quad (13)$$

Behavior of this kind can be observed in Fig. 10 of I_ℓ versus the secondary-beam reservoir pressure $p_{2,0}^{\text{He}} \sim n_{2,0}$. If in Eq. (12) for T_k the factor g/v_1 is neglected, it can be readily verified that for $x = 0$ the optimum reservoir density is given by

$$n_{2,0}^{\text{opt}} = \frac{3z_n}{2(aR_n)^2 Q e^1} . \quad (14)$$

At room temperature this corresponds with $p_{2,0}^{\text{opt}} = 110$ Torr for $Q^{e1} = 100 \text{ \AA}^2$ and $R_n = 25 \text{ \mu m}$. Figure 10 which shows the optimum to lie at $p_{2,0}^{\text{opt}} \simeq 120$ Torr bears this out. For the above value of $n_{2,0}^{\text{opt}}$, we have $T_k^{\text{opt}} \simeq e^{-1}$. This is confirmed by Fig. 8 of $T_k(p_{2,0}^{\text{He}})$!

4.5. Center-of-mass energy E

The center-of-mass energy is given by $E = \frac{1}{2}\mu g^2$, with μ the reduced mass and g the relative velocity of the colliding particles. Into g enter both the primary-beam velocity v_1 and the secondary-beam velocity v_2 .

As to v_2 , the velocity distribution in our supersonic expansion is given by Ref. 25. It is approximately Gaussian, peaked at the final value of the flow velocity:

$$v_2 = u_\infty (1 - \frac{1}{2} S^{-2}) \quad (15)$$

$$u_\infty = \left[\frac{\gamma}{\gamma-1} \right]^{\frac{1}{2}} \left[\frac{2kT_{2,0}}{m_2} \right]^{\frac{1}{2}}$$

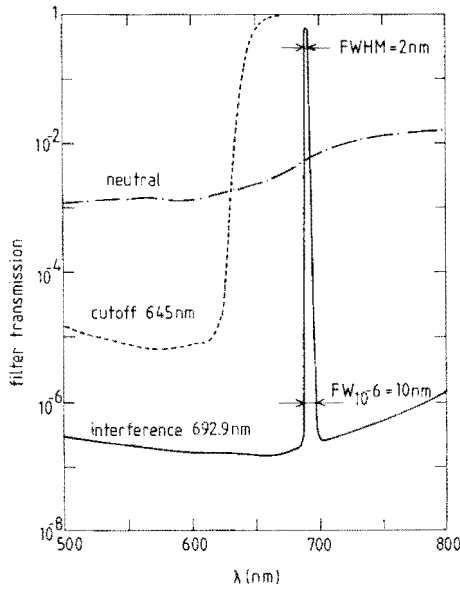


Fig. 12. Transmission as a function of wavelength for a 692.9 nm interference filter, a 645 nm red glass cut-off filter, and a neutral density filter. These filters are typical of the filters used in the experiment.

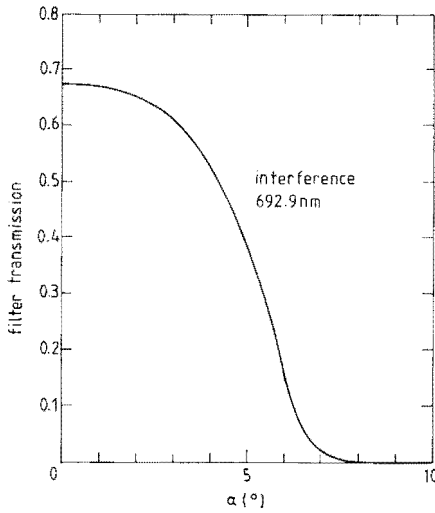


Fig. 13. Transmission of the 692.9 nm signal line through the 692.9 nm interference filter of Fig. 12, as a function of the off-normal angle of incidence α . In effect, the transmission peak shifts to lower wavelengths with increasing α .

where γ represents the specific heat ratio $\gamma = c_p/c_v$ (5/3 for mono-atomic gases). At a typical pressure $p_{2,0}^{\text{He}} = 120$ Torr and temperature $T_{2,0} = 300$ K, the speed ratio for He is $S_2^{\text{He}} = 4.4$, resulting in $v_2^{\text{He}} = 0.97 u_\infty = 1715$ m s⁻¹. For Ne, at $p_{2,0}^{\text{Ne}} = 160$ Torr, we find $S_2^{\text{Ne}} = 6.5$, so that $v_2^{\text{Ne}} = 0.99 u_\infty = 775$ m s⁻¹.

Equation (15) will not serve for the primary beam velocity v_1 , for lack of an appropriate temperature $T_{1,0}$ in the discharge excited source. Therefore, time-of-flight (TOF) measurements were performed to determine the primary-beam velocity distribution. For a pure 100% Ne-discharge, the result is given in Fig. 11a. A 15% Ne - 85% He seeded beam yields the TOF-spectrum of Fig. 11b. In both cases the TOF-spectrum was fitted with a Gaussian velocity distribution. The peak velocity v_1 and speed ratio S_1 are found to be $v_1 = 1010$ m s⁻¹ and $S_1 = 4.7$ for the pure beam, while $v_1 = 1495$ m s⁻¹ and $S_1 = 5.7$ for the seeded beam.

We note that the position dependence of the direction of \underline{v}_2 causes both magnitude and direction of the relative velocity to be position dependent, as well. This is illustrated in Fig. 6 by the xz -diagram of velocity vectors in the laboratory system.

4.6. Optical detection efficiency η

The optical detection system and its components have been described above. The detection efficiency η_ℓ (defined as pulses counted per photons produced) may be written as

$$\eta_\ell = \sum_j \frac{A_{\ell j}}{A_\ell} \eta_j^0(\lambda_j) \eta_j(\underline{r}, \theta_E) . \quad (16)$$

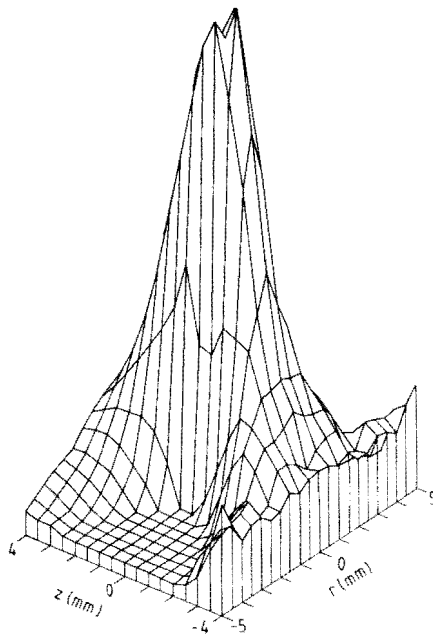


Fig. 14. Calculated detection efficiency $\eta(r,z)$ of the optical system with the interference filter of Figs. 12 and 13. Isotropic emission of fluorescence radiation has been assumed. The axial symmetry about the vertical z -axis then makes η a function of $r = (x^2 + y^2)^{1/2}$ and z only, where the origin is in the focus of the parabolic mirror.

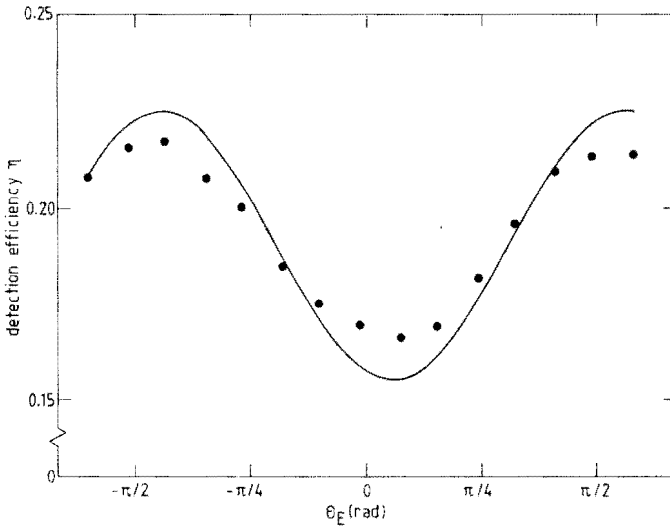


Fig. 15. The direct fluorescence signal K^{off} for the $(\{\alpha\}_5; J_5=1)$ state excited from the metastable $(^3P_0)$ state, as a function of the laser polarisation angle θ_E with the z -axis (the symmetry axis of the optical system). Taking account of the anisotropy of the fluorescence radiation, the less than 4π solid-angle detection efficiency, and the off-axis laser-beam position, the calculated drawn curve reproduces the signal well.

Here $A_{\ell j}/A_{\ell}$ is the branching ratio for a particular fluorescence line j . In addition to the quantum efficiency of the photomultiplier, the total transmission along the optical axis of all elements is featured in η_j^0 . Position-dependent deviations from the optical axis (associated, for example, with non-normal incidence on the interference filters), as well as the effect of non-isotropic light production by polarized atoms, are incorporated in η_j . With an interference filter in the optical system, the sum in Eq. (16) is usually reduced to a single term $j = \ell$, the only one for which $\eta_j^0 \neq 0$.

We have calibrated each optical component separately. Subsequently, the geometric function η_j is calculated numerically. Typical transmission curves for a three-cavity interference filter (692.9 nm, corresponding to the $\{\alpha\}_G \rightarrow ({}^1P_1)$ transition), a red glass cut-off filter (645 nm), and a neutral density filter, are given in Fig. 12. They have been measured using a standard light source, a Jarrell-Ash 1.0 m double (Czerny-Turner) monochromator and a Keithley Instruments 610 CR electrometer. The curve for the interference filter was obtained under conditions of normal incidence. For non-normal angles of incidence, the transmission profile is shifted to lower wavelengths. This means, that the nominal wavelength will be transmitted to a lesser degree. The latter effect is exemplified by Fig. 13 of the transmission of the 692.9 nm signal line (from a neon spectral lamp) through the interference filter of Fig. 12, as a function of the off-normal angle of incidence α . Taking the other optical components (parabolic mirror, light-guide, lens) into account as well, we find the calculated position dependence $\eta(r,z)$ of the detection efficiency for this interference filter to be as in Fig. 14. In the calculation, isotropic emission of light was assumed.

The anisotropy of the detection efficiency becomes apparent, when measuring I_k for varying angles θ_E of the laser polarisation. Then the influence of the non-isotropic emission of dipole radiation by the

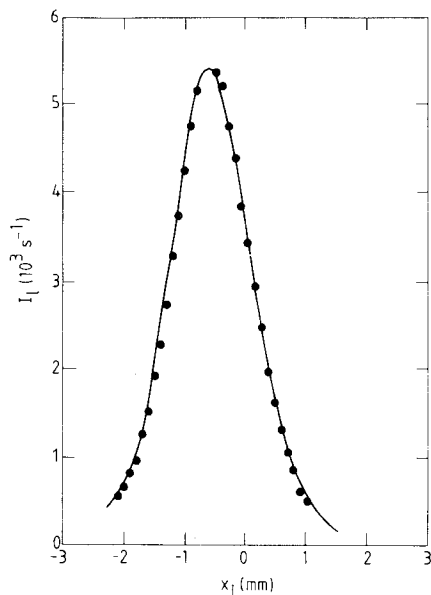


Fig. 16. The collision-induced fluorescence signal I_p resulting from the $\text{Ne}^{**}\text{-He}$ $\{\alpha\}_5 \rightarrow \{\alpha\}_4$ transition, as a function of the laser-beam position x_l along the primary-beam axis. The drawn curve was calculated according to Eq. (10) and normalized to the maximum of the experimental data. The lack of a significant polarization effect in the $\{\alpha\}_5 \rightarrow \{\alpha\}_4$ cross section (see Fig. 27) obviates the need for a correction for the changing angle β between the laser electric field \underline{E} and the relative velocity \underline{g} . What small polarization effect there is tends to compensate the effect of the energy change associated with a change in x_l (compare Fig. 17).

polarized initial state $\{\alpha\}_k$ (see section 4.8) causes I_k to vary. For a $\text{Ne}^*(^3P_0)$ metastable state, this is shown in Fig. 15. Again, the effect is largely reproduced by the appropriate calculation.

4.7. Alignment of three crossing beams

The experiment requires that the primary-beam axis and the center-line of the secondary-beam expansion cross at right angles, at or near the focal point of the parabolic mirror. The laser beam must cross the primary beam, once more at right angles, in a spot well-determined with respect to the secondary-beam nozzle. It is relatively straightforward to first align the two primary-beam defining diaphragms with the focal point of the mirror, and then the skimmer of the primary-beam source with the diaphragms; also, to make the secondary-beam nozzle axis coincide with that of the mirror. All these components may then be fixed in place semi-permanently. Laser-beam alignment, however, is another matter.

As a characteristic of our use of a free-jet secondary-beam expansion, the laser beam ultimately determines the position of the collision volume. As the relative velocity g and the secondary-beam density n_2 in particular are strongly position dependent, laser-beam alignment takes on a critical importance. This is evidenced by Fig. 16 of an I_l -signal as a function of the laser-beam position x_l along the primary-beam axis, and likewise by Fig. 17 of the ratio I_l/I_k .

In the interest of accuracy and reproducibility, the laser line has been fixed with two quadrant detectors, as described earlier. Theoretical accuracy of the horizontal laser beam alignment is $\Delta x = 0.005$ mm and $\Delta\phi = 0.1$ mrad, as determined by the step size (0.01 mm and 0.2 mrad, respectively) of the stepper-motor - gearing combination selected for the laser-beam translator/rotator module. By the automated alignment procedure

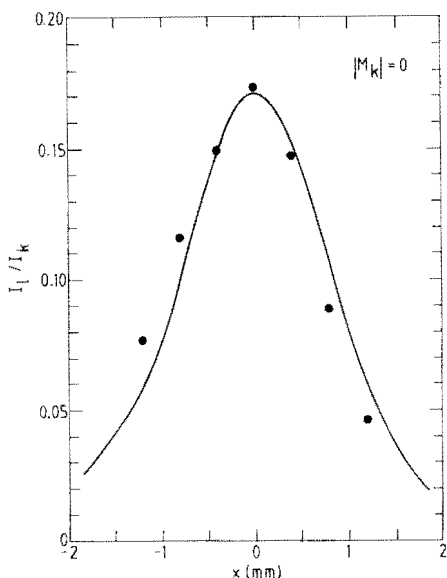


Fig. 17. Collision-induced to direct fluorescence ratio I_l/I_k for the $\text{Ne}^{**}\text{-He}$ $(\alpha)_5 \rightarrow (\alpha)_7$ transition for $|M_5| = 0$, as a function of the laser-beam position x_l along the primary-beam axis. The drawn curve was calculated according to Eq. (10) and normalized to the maximum of the experimental data. The result reflects the energy dependence of $Q_{7\leftarrow 5}^{[0]}$ that is shown in Fig. 32. The higher energy upstream of the secondary-beam nozzle corresponds to a larger cross section and thus to a larger fluorescence signal. Downstream of the nozzle the reverse is true.

of section 3 the stepper-motor setting for the angle φ is reproduced perfectly every time, that for the position x within two steps ($\Delta x = 0.02$ mm). Figures for the vertical z -position are similar to those for the x -position.

In the matter of the initial laser-beam alignment, i.e. the positioning of the quadrant detectors, the top of the nozzle provides both a vertical and (to a lesser degree) a horizontal visual reference. Perpendicularity of laser- and primary-beam can be easily achieved by measuring the direct fluorescence signal I_k over a wide range of angles φ , with a figure like Fig. 18 as the result. The correct setting corresponds to the maximum signal (minimum Doppler shift). In a similar way the vertical laser beam position may be checked for maximum overlap with the primary beam.

In a somewhat more elaborate procedure, the experiment itself provides an additional check on the horizontal position. We can perform a so called polarization measurement of the cross section $Q_{\ell \leftarrow k}^\beta$ for an $|\alpha_k^{J_k=1}\rangle$ initial state, excited from the (3P_0) metastable state. Here β is the angle between the electric field vector \underline{E} of the linearly polarized laser and the asymptotic relative velocity. Theory²¹⁾ predicts that the observed cross section will behave according to

$$Q_{\ell \leftarrow k}^\beta = C_0^1 + C_1^1 \cos 2\beta . \quad (17)$$

In principle, any transition of the above description will do. In practice, the Ne^{**}-He $\{\alpha\}_5 \rightarrow \{\alpha\}_7$ transition is a most convenient candidate, due to its large polarization effect combined with a considerable cross-section magnitude.

The cross section $Q_{\ell \leftarrow k}^\beta$ is measured by variation of the angle θ_E between the primary-beam velocity \underline{v}_1 and \underline{E} . As may be seen in Fig. 6 of the diagram of velocity vectors in the laboratory system, the relation between θ_E and β

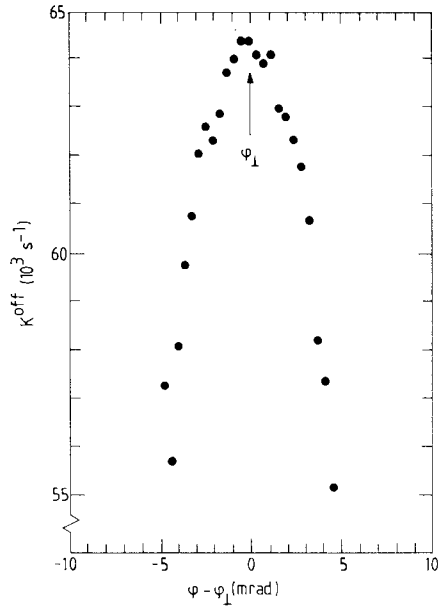


Fig. 18. The direct fluorescence signal K^{off} as a function of the angle φ between laser- and primary-beam. With the laser tuned to the frequency of a Doppler-free atomic transition, the signal's maximum corresponds to perpendicular alignment. For increasing misalignment the Doppler shift grows and the fluorescence signal decreases.

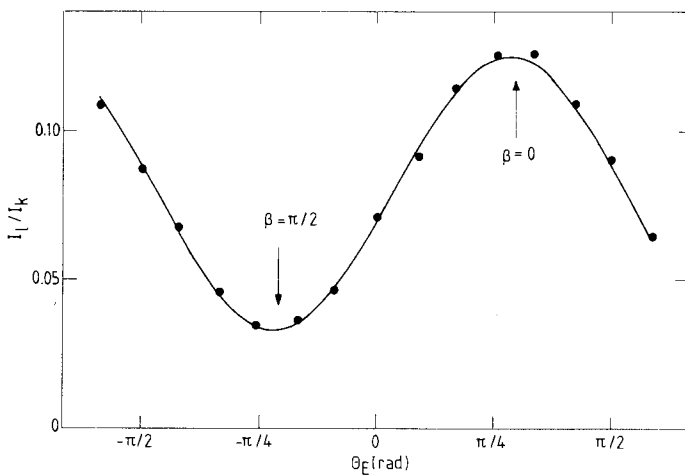


Fig. 19. The ratio I_{\perp}/I_k of collision-induced and direct fluorescence signals for the $\text{Ne}^{**}\text{-He } \{\alpha\}_5 \rightarrow \{\alpha\}_7$ transition, as a function of the laser-polarisation angle θ_E . The drawn curve results from a least-squares fit of the data to Eq. (17). This offers a way of determining the position of the scattering center along the primary-beam axis.

depends on the position x_s of the scattering center. In accordance with Eq. (17), extrema will occur at angles $\theta_E = \theta_0$ and $\theta_E = \theta_0 + \pi/2$. This we observe in Fig. 19. These extrema correspond to $\beta = 0$ and $\beta = \pi/2$. We only need to identify the extremum belonging to $\beta = 0$, for which $\theta_E = \theta_g$, i.e. $\underline{g} \parallel \underline{E}$. This problem can be solved unequivocally by measuring $Q_{\ell \leftarrow k}$ for some different positions x_s and, if necessary, primary-beam velocities v_1 .

Referring to Fig. 6, the absolute value of the relative velocity vector \underline{g} can be readily calculated from the orientation θ_g , using the well-known values of v_1 and v_2 as input. So can the orientation of \underline{v}_2 . The latter, in combination with the nozzle-to-primary-beam distance z_n , gives us the effective position x_s of the collision volume on the primary-beam axis. The laser-beam position x_l then follows from the off-set $\Delta x_{\ell s} = x_\ell - x_s$, specific to the optical pumping process. Over a number of such tests, the x-scale is permanently coupled to the scale of the laser-beam translator or, in our case, to the quadrant detectors.

4.8. Optical pumping

Because the distribution of the initial $\{\alpha\}_k$ atoms ultimately determines the position and extent of the collision region, its calculation is of prime importance. We have numerically solved a set of rate equations for the upper $Ne^{**}\{\alpha\}_k$ and lower $Ne^*(^3P_{0,2})$ level densities, taking into account absorption, stimulated emission, and spontaneous emission (the latter to all $Ne^*\{(2p)^5(3s)\}$ levels). The different upper and lower magnetic sublevels m_J , with respect to the laser polarisation \underline{E} , are treated separately. Also, it is possible to postulate a magnetic field.

Among the simplifications of our model are: (1) the divergence of the Ne^* and laser beams is neglected; (2) they are taken to be perpendicular; (3) the laser is tuned exactly to the optical transition. Thus, with the

Ne^* -atoms moving in the x-direction, we have essentially a one-dimensional problem. For every value of z, we find a number of J_k+1 density profiles $n_k^{m_k} |E(x)$. We usually assume a perfectly Gaussian two-dimensional laser-field, very slightly collimated. Figure 20 of a laser-intensity profile, with a Gaussian fit, bears out this assumption. Disregarding in the present context both magnetic sublevels and magnetic fields (which are discussed below), we find for instance a profile $n_k(x)$ such as shown in section 5.1. With the laser beam used in the experiment (power $P \simeq 0.1$ mW, waist-radius $[1/e^2]$ $W_x = W_z \simeq 0.5$ mm) and at thermal velocities, the short-lived $\text{Ne}^{**}\{a_k\}$ atoms are confined to a considerably smaller space than the laser-beam profile itself. Also, note the upstream shift of the n_k -profile. (All this, of course, does not hold for the two-level $\text{Ne}^*(^3P_2)$ - $\text{Ne}^{**}\{a\}_9$ system.) A comparison between scattering volume positions, determined from polarisation measurements (section 4.7) on the one hand, and calculated from laser-beam positions on the other, confirms that these calculations basically represent reality well.

A magnetic field exerts a certain influence on the effective scattering center position. Much more important, though, is its effect on the observed cross sections $Q_{\ell \leftarrow k}^\beta$. We recall that the ultimate purpose of the experiment is to determine single- M_k -state polarized cross sections $Q_{\ell \leftarrow k}^{|M_k|}$, where M_k is the magnetic quantum number of the initial electronic angular momentum J along the asymptotic relative velocity \underline{g} . Now, the observed cross section Q^β , with β the angle between \underline{E} and \underline{g} , has the general form

$$Q_{\ell \leftarrow k}^\beta = \sum_{n=0}^{J_k} C_n^{J_k} \cos 2n\beta . \quad (18)$$

In detail²⁰⁾,

$$Q_{\ell \leftarrow k}^{\beta} = \sum_{m_k = -J_k}^{J_k} g_{m_k} \sum_{M_k = -J_k}^{J_k} \{d_{m_k M_k}^{J_k}(\beta)\}^2 Q_{\ell \leftarrow k}^{|M_k|} \quad (19)$$

where the rotation matrices or reduced Wigner-D-functions $d^{38)}$ transform the initial distribution g_{m_k} over magnetic substates $|\alpha_k J_k m_k\rangle_{\underline{E}}$ to a distribution over substates $|\alpha_k J_k M_k\rangle_{\underline{g}}$. The calculation of the distribution g_{m_k} provides the final calibration of the experiment.

The general principles involved have been mentioned already in our discussion of the initial-state density profile $n_k^{m_k}(\underline{r})$. In the present experiment, the distribution parameter g_{m_k} may be linked to the time-integral of $n_k^{m_k}$ over the collision region. Here, the presence or absence of a magnetic field makes a crucial difference²⁷⁾. With a linearly polarised laser, only $\Delta m = 0$ transitions are allowed. The case of an $|\alpha_k J_k = 1\rangle$ initial state being excited from the $|^3P_0, J_1 = 0\rangle$ metastable state is straightforward. Only the $m_k = 0$ substate is populated. Due to the upper state's short lifetime, no appreciable precession of J_k about a magnetic field \underline{B} of earth-field's strength can take place. As a result, we find:

$$\begin{aligned} g_{m_k=0}^{J_k=1} &= 1 \\ g_{|m_k|=1}^{J_k=1} &= 0 \end{aligned} \quad (20)$$

For Eq. (19) this implies, simply, that

$$Q_{\ell \leftarrow k}^{\beta} = \frac{1}{2} (Q_{\ell \leftarrow k}^{|0|} + Q_{\ell \leftarrow k}^{|1|}) + \frac{1}{2} (Q_{\ell \leftarrow k}^{|0|} - Q_{\ell \leftarrow k}^{|1|}) \cos 2\beta . \quad (21)$$

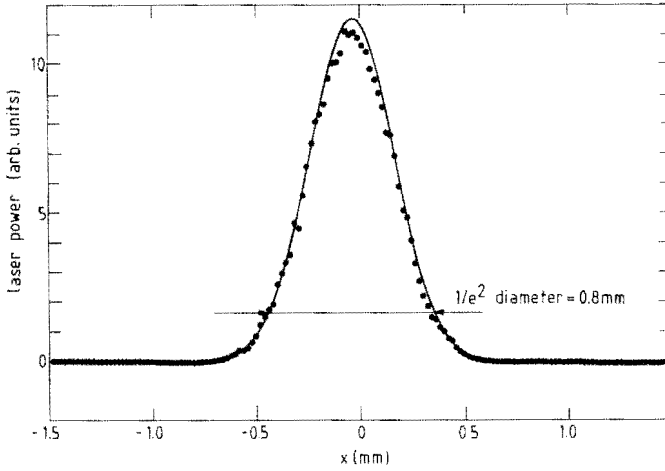


Fig. 20. Horizontal intensity profile of the laser-beam in the scattering center. The drawn curve represents a Gaussian profile of 0.8 mm waist diameter ($1/e^2$).

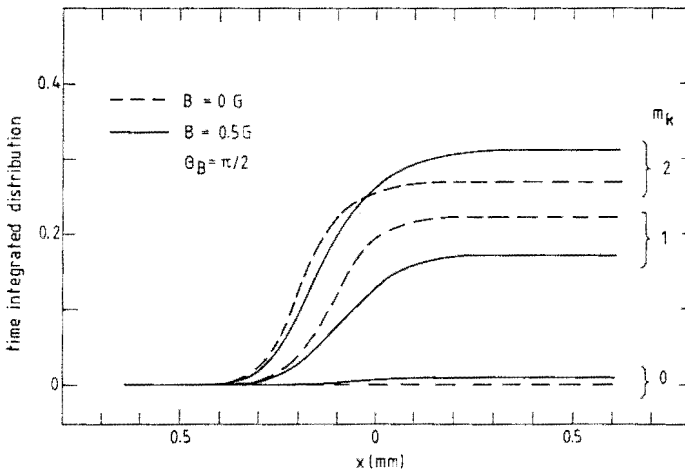


Fig. 21. The time-integrated upper-state density $n_g^{m_g}(t)$, resulting from the $(^3P_2) \rightarrow (\alpha)_g$ excitation process, calculated with and without a magnetic field \underline{B} . Here θ_B is the angle between \underline{B} and the laser electric field \underline{E} . The influence of B , when not compensated for, carries over directly into observed cross sections!

For $|\alpha_k J_k=2\rangle$ and $|^3P_2, J_i=2\rangle$, the $\Delta J = 0, \Delta m = 0$ transition is forbidden. However, while the upper short-lived state is quite impervious to the presence of a magnetic field \underline{B} , the metastable lower state is not. Mixing of the metastable $m_i = 0$ substates takes place, and the distribution $g_{m_k}^{J_k=2}$ over short-lived m_k -substates depends on the field's magnitude and its direction with respect to the laser polarisation \underline{E} :

$$\begin{aligned}
 g_{m_k=0}^{J_k=2} &= 0 \\
 g_{|m_k|}^{J_k=2} &= g_{|m_k|}^{J_k=2}(\underline{B})
 \end{aligned}
 \tag{22}$$

This is demonstrated by Fig. 21 of the evolution in time of $n_k^{|m_k|}$ for the $\{\alpha\}_4$ state, with and without a magnetic field. To judge the extent to which a magnetic field complicates the analysis of Q^β , it must be kept in mind that during the experiment the angle between \underline{B} and \underline{E} changes continuously. The distribution $g_{m_k}^{J_k=2}$ will vary accordingly. This produces the asymmetry in, for example, the Q_{7+8}^β cross section of Fig. 22, contrary to Eq. (18)! Evidently, while for some states $|\alpha_k J_k=2\rangle$ it matters less than for others, the absence of a magnetic field offers much the best starting point for the analysis of observed cross sections.

In our experiment the conditions are very favorable for the successful compensation of whatever magnetic field is present. First, the size of the scattering volume is so small ($\approx 1 \text{ mm}^3$), that only limited demands are made of the compensating field's homogeneity. More importantly, the optical pumping process itself offers an inbuilt verification method for the success of the compensating efforts.

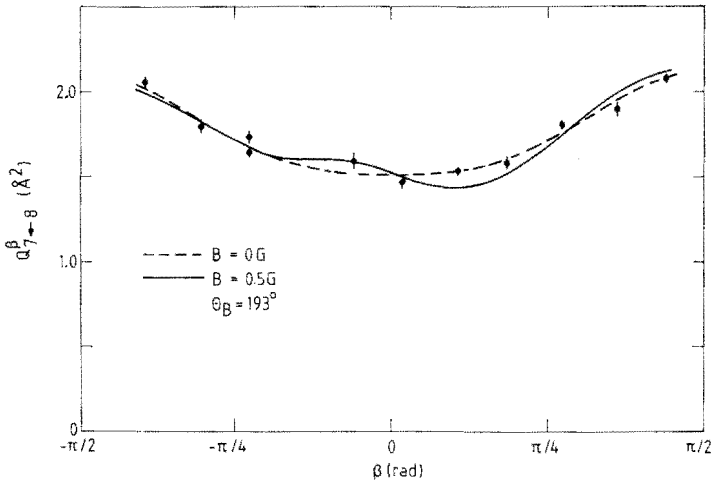


Fig. 22. For varying orientation θ_E of the laser electric field vector \underline{E} , the angle θ_B of the magnetic field \underline{B} with \underline{E} varies also. This causes the distribution over magnetic substates $\{(\alpha)_k J_k m_k \rangle_E$ to change continuously. In the observed $\text{Ne}^{**}\text{-He}$ cross section $Q_{10 \rightarrow 8}^\beta$ as a function of the angle β between \underline{E} and the relative velocity \underline{g} , a marked deviation from Eq. (18) is the result.

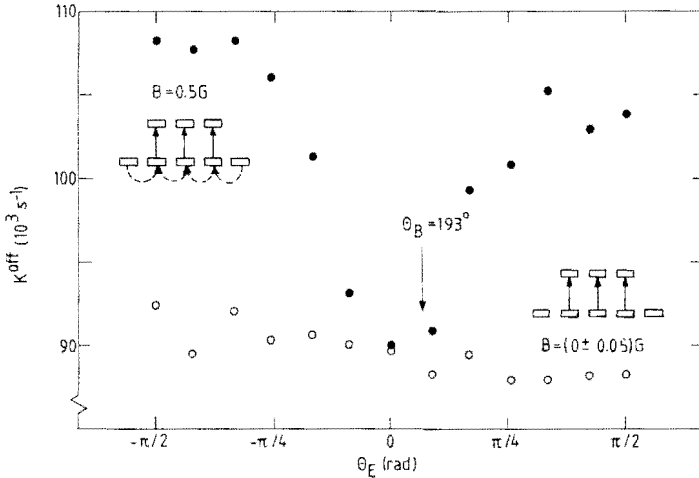


Fig. 23. The direct fluorescence signal K^{off} for the $(\{\alpha\}_5, J_5=1)$ state excited from the metastable $({}^3P_2)$ state, as a function of the laser-polarisation angle θ_E . A magnetic field in the scattering center causes the signal to vary, due to the admixture of the $\{({}^3P_2), J=2, m_J = \pm 2 \rangle_E$ sublevels. The nearly constant signal testifies to the absence of a magnetic field. Note the enlargement of the vertical scale.

For this, an $|\alpha_k J_k=1\rangle$ state is excited from the metastable $|^3P_2, J_1=2\rangle$ state. With the laser linearly polarized, as ever, only the lower level's $m_i = -1, 0, 1$ magnetic substates are pumped. In the absence of a magnetic field, the $m_i = -2, 2$ substates will be unaffected. Under those circumstances and sufficiently close to saturation, an isotropic distribution over the upper level's magnetic substates will be the result:

$$\begin{aligned} g_{m_k=0}^{J_k=1} &\simeq 1/3 \\ g_{|m_k|=1}^{J_k=1} &\simeq 1/3 \end{aligned} \tag{23}$$

An unpolarized initial short-lived state must of course lead to an unpolarized cross section:

$$Q_{\ell \leftarrow k}^{\beta} = 1/3 (Q_{\ell \leftarrow k}^{|0\rangle} + 2 Q_{\ell \leftarrow k}^{|1\rangle}) . \tag{24}$$

Now, any mixing of the $m_i = -2, 2$ substates due to a magnetic field is bound to give rise to a larger observed direct fluorescence signal I_k . Of course, if the magnetic field happens to be along the laser electric field \underline{E} , no mixing will take place.

As mentioned in section 3, we have installed three sets of rectangular Helmholtz-like coils around the major x-, y-, and z-axes of the experiment. They have been placed outside the vacuum chamber. Spatial limitations have forced us to deviate from the coils' ideal dimensions. Given the small scattering volume, this is of little significance.

Magnetic field compensation is best performed at a laser power sufficiently close to saturation that nearly all the relevant metastable atoms are pumped. Care must be taken that the laser polarization is not

along the field's component being compensated at the time. Successive and iterative minimization of the direct fluorescence signal I_k then yields the correct compensating field. The ultimate test for this procedure is provided by the comparison, shown in Fig. 23, of the signal I_k for the $\{a\}_5$ state (excited from the $(^3P_2)$ state), measured with and without activated coils, as a function of the laser polarization angle θ_E . Whereas the fluorescence yield is seen to vary strongly (about 20%) under the local field conditions, it is much more constant (to within 4%) when the compensating field is turned on, in accordance with Eq. (24). Moreover, the minimum signals are the same in both cases! At the time of this measurement the local field's strength was about $B \simeq 0.5$ G.

5. Inelastic total cross sections

5.1. Deconvolution for finite scattering volume

We can express Eq. (10) for the ratio I_ℓ/I_k of collision-induced and direct fluorescence signals in terms of the ideal first-order expression of Eq. (9), through a convolution factor ξ_V :

$$\frac{I_\ell}{I_k} = \xi_V \left[\frac{I_\ell}{I_k} \right]_{\text{ideal}} \quad (25)$$

Here $(I_\ell/I_k)_{\text{ideal}}$ is to be calculated in the scattering center \underline{r}_{sc} , for which we take the center-of-gravity of the $\{a\}_\ell$ transition. The various elements making up I_ℓ/I_k have been treated more or less extensively in section 4, with the exception of the cross section $Q_{\ell \leftarrow k}(g)$ itself. In general, we have

$$Q_{\ell \leftarrow k}(g) = f(g) Q_{\ell \leftarrow k}(g_{sc}) \quad (26)$$

$$f(g) = 1 + (g - g_{sc}) \left[\frac{dQ_{\ell \leftarrow k}}{dg} \right]_{sc} + \dots$$

The model function $f(g)$ is of less than critical importance, though, because of the small size of the collision region. Well-suited for Ne^{*k} -He transitions at thermal energies appears to be

$$f(g) = \frac{g}{g_{sc}} \quad (27)$$

With $f(g)$ figuring in ξ_V , we find from Eq. (25):

$$Q_{\ell \leftarrow k}(g_{sc}) = \left[\frac{I_\ell}{I_k} \right]_{\text{expt}} / \left\{ \xi_V \left[\frac{\eta_\ell}{\eta_k} n_2 \frac{g}{v_1} \ell_\tau \right]_{sc} \right\}. \quad (28)$$

The I_ℓ and I_k integrals of Eq. (10) are now approximated by means of a two-dimensional integration over the plane, which contains the primary beam axis and is normal to the laser beam, i.e. the xz -plane of Fig. 6. The primary and laser beams are presupposed to be cylindrical and exhibit maximum overlap. The effects of the primary beam extending in the laser beam's y -direction are taken into account only through the primary-beam width itself, i.e. through a z -dependent weight factor. Since the secondary beam density n_2 typically varies by less than 15% over the whole primary-beam width, the resulting overestimation of I_ℓ is limited. Ultimately, of course, the integration area is determined by the position x_ℓ of the laser beam.

The detection-efficiency profiles $\eta_\ell(x, z_f)$ (relative to the focal point $z_f = 0$ of the parabolic mirror) need be calculated only once, for each of the available interference filters (disregarding, of course, possible

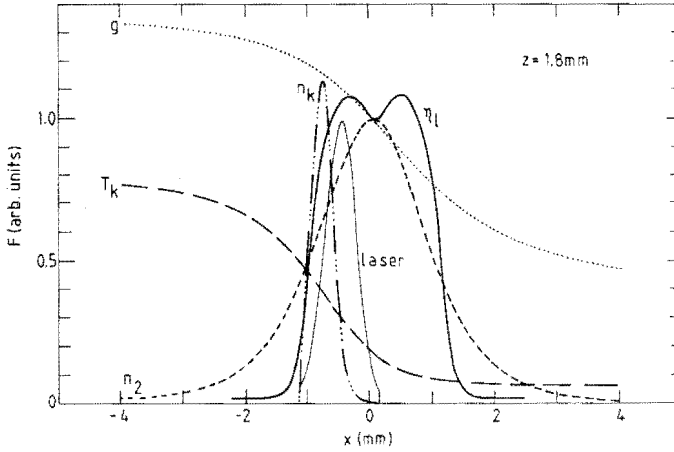


Fig. 24. The variation with the horizontal coordinate x of Fig. 6, for a fixed value $z = 1.8$ mm, of the two-dimensional model functions for the secondary-beam density n_2 (Eq. (11)), the primary-beam transmission T_k (Eq. (12)), the $\{\alpha\}_k$ -density n_k (section 4.8, disregarding magnetic sublevels), the relative velocity g (section 4.5) and the optical detection efficiency η (section 4.6, for isotropic light).

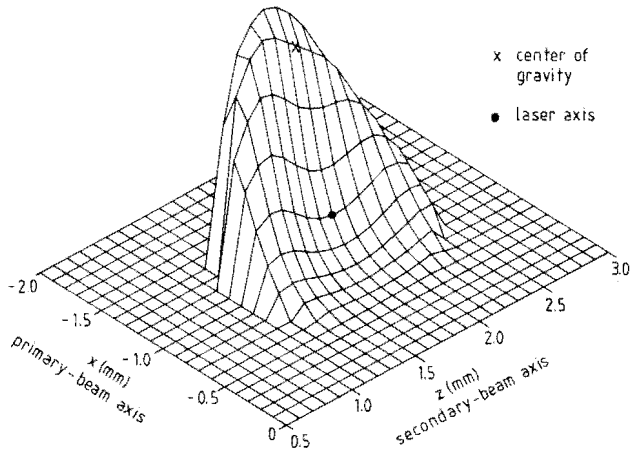


Fig. 25. Two-dimensional shape of the calculated collision-induced $\{\alpha\}_7$ -distribution $n_7(x,z)$ for the $\text{Ne}^{**}\text{-He } \{\alpha\}_5 \rightarrow \{\alpha\}_7$ transition, obtained from Eq. (10) with a supposed 1.3 mm diameter laser beam of 0.1 mW power. The distribution's center-of-gravity $(x_{sc}, z_{sc}) = (-0.30, 1.77)$, indicated with a cross (x), is seen to be situated upstream of the central position $(x_\ell, z_n) = (0.0, 1.8)$ of the laser beam, indicated with a dot (•).

variations in the anisotropy of the fluorescence radiation. For a grid of (x, z_f) values, the $\eta_\rho(x, z_f)$ have been permanently stored for use in the calculations. Likewise, the calculation of the density profile $n_k(x, z)$ of the initial short-lived $\{\alpha\}_k$ -atoms is independent of the laser beam position x_ρ . Its results can be used for any combination of x_ρ , nozzle distance z_n and final state $\{\alpha\}_\rho$.

Figure 24 gives an example of the behavior of the various quantities in Eq. (10) as a function of x in the xz -plane, for a given value of z . In Fig. 25, we show the shape of a calculated $\{\alpha\}_\rho$ -distribution. It is confined to a relatively small region. The center-of-gravity (x_{sc}, z_{sc}) generally does not lie on the laser-beam axis (x_ρ, z_n) .

The ultimate result of the I_ρ/I_k calculation (Eq. (10)) on the one hand, and the I_ρ/I_k measurement (Eq. (8)) on the other, is taken to be an absolute total cross section $Q_{\rho \leftarrow k}(E)$, with the energy $E = \frac{1}{2}\mu g^2(x_{sc}, z_{sc})$ pertaining to the point (x_{sc}, z_{sc}) , all in accordance with Eq. (26). A typical value of the convolution factor ξ_V of Eqs. (25) and (28) would be $\xi_V \approx 0.8$.

5.2. Measurement of inelastic cross sections

The nucleus of any of the experiments of the preceding section is the I_ρ/I_k measurement with its eight component measurements, as discussed in section 3. The inherent calibration method, implied by the measurement of ratios I_ρ/I_k only, goes a long way towards eliminating any long-term drift effects, to which the thermal metastable source in particular is prone. In addition, as a measure against linear drift during the I_ρ/I_k measurement itself, it pays to adopt a symmetrical order of basic measurements. In the notation of section 3, an example would be: $K^{off}_{-K}{}^{on}_{-L}{}^{on}_{-L}{}^{off}_{-L}{}^{on}_{-K}{}^{on}_{-K}{}^{off}$

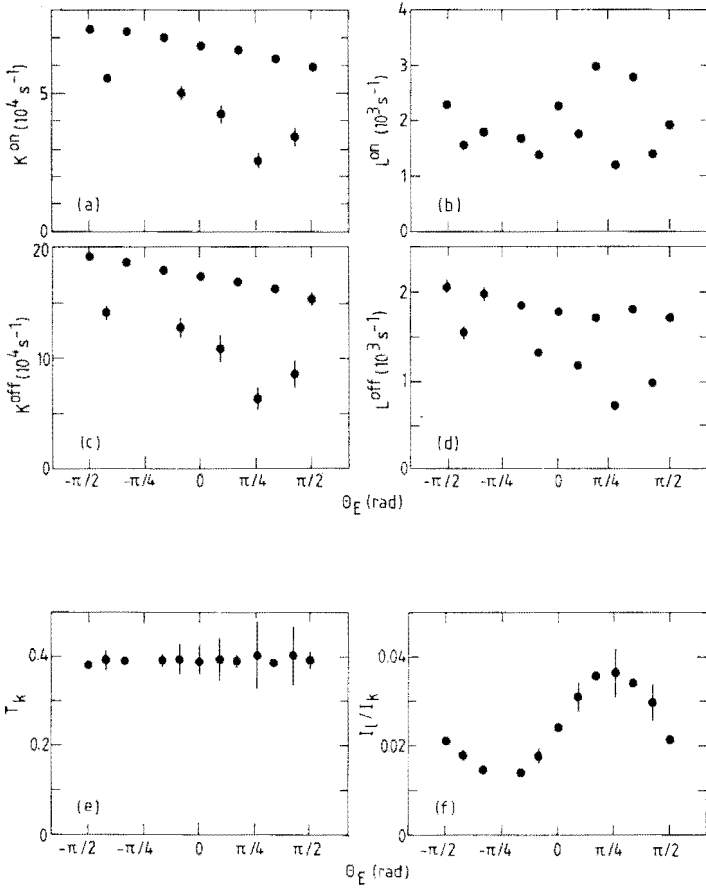


Fig. 26. The basic fluorescence signals K^{on} (a), L^{on} (b), K^{off} (c), and L^{off} (d) of subsection 4.1 as a function of the laser polarization angle θ_E . These were measured with a stepsize of 30° in two series starting at -105° and -90° , respectively. The observed atypically large drift in time is seen to leave the derived results for the transmission T_k (e) of Eq. (7) and the ratio I_l/I_k (f) of Eq. (8) largely unaffected.

(with each of these consisting of a measurement with tuned and detuned laser). In this respect, it saves time to minimize the number of filter changes and secondary-beam on/off transitions.

The efficacy of these measures is demonstrated by Fig. 26 of a complete Ne^{**}-He polarisation measurement for the $\{\alpha\}_9 - \{\alpha\}_7$ transition. By way of a standard extra precaution, the range of laser polarization angles has been covered in two series: $105^\circ, -75^\circ, \dots, 105^\circ$ and $-90^\circ, -60^\circ, \dots, 90^\circ$. The measurement is atypical in that the observed drift is unusually large. Still, the net I_ℓ/I_k signal is nearly unaffected by this. In addition, the constant value of the transmission factor $K^{\text{on}}/K^{\text{off}}$ is a guarantee of a constant secondary-beam density.

In practice, it is the measuring program executed by the experiment computer that supervises a complete run of the experiment. Beforehand, it prompts for and stores a table of the experimental parameters: order, number and length of the basic measurements; the filters required; the nature of the main experimental variable; its range etc. These, and others, are all saved in a data file on disk. Then the experiment runs its course, with the computer initiating changes in the laser frequency, actuating stepper motors, and so on. Before going to a new setting of, e.g. the polarization angle, the data from the previous I_ℓ/I_k measurement are saved in the datafile. An overview of the data is printed out, together with the results of a preliminary analysis. A complete run is usually scheduled to take about three hours. This is roughly the length of time, that the laser system can be counted on to maintain its stabilization on the transition frequency without a mode-hop. If the laser were to fail during the experiment, or e.g. a filter could not be located, the experimentalist is summoned to correct the problem. Of course, an entirely independent system of pressure-, temperature- and coolant-water-flow-monitors checks for problems of a different nature.

5.3. Types of measuring runs

The present "mini-beam" experiment is concerned with the behavior of inelastic collision-induced cross sections $Q_{\ell \leftarrow k}$ as a function of the initial state $\{\alpha\}_k$, the final state $\{\alpha\}_\ell$, the collision energy E , the laser polarisation angle θ_E and the secondary-beam gas (He, Ne, N_2 , ...). A change of the initial state requires that the laser be tuned to a different transition frequency ν_{ik} , which takes time and calls for a human operator. An automated secondary-beam gas exchange system is being considered, but not operational. With these exceptions, all of the above variables can be changed during the measurements, by computer. However, in the interest of the subsequent analysis, it is generally wise to change only one variable at a time. Also, the more variables there are, the more prolonged a measurement will be, with a proportionally larger chance of a problem developing.

We can distinguish between several basic types of measuring runs, examples of which will be given later in this section:

- 1) *Polarization measurement*: I_ℓ/I_k as function of the polarization angle θ_E . The most fundamental measurement of all. In the case of an $|\alpha_k J_k=1\rangle$ initial state, Eq. (21) indicates that two measurements suffice.
- 2) *Absolute scaling measurement*: I_ℓ/I_k for various final states $\{\alpha\}_\ell$, through a change of filters. The filter assembly takes up to four filter combinations at a time, in addition to the filters for the direct fluorescence. This type of measurement is very useful for calibrating a series of separate measurements.
- 3) *Energy measurement*: I_ℓ/I_k for different collision energies E . The change in energy is brought about by scanning the laser beam along the primary-beam axis. This results in a different direction of the

secondary-beam velocity v_2 , and therefore in a different relative velocity g . The accessible energy range is limited, of course. A different, more laborious, means of changing the collision energy is through the use of a seeded primary beam, which directly affects the magnitude of the primary-beam velocity v_1 . We have used various Ne/He mixtures.

- 4) *Time-of-flight measurement*: I_e/I_k , resolved as to primary-beam velocity v_1 . These measurements are very time-consuming, even when using the pseudo-random correlation method mentioned in section 3. They are therefore best suited to strong transitions. Also, transitions with an $|\alpha_{k J_k=1}\rangle$ initial state are favored over those with an $|\alpha_{k J_k=2}\rangle$ initial state.

Used mainly for calibration purposes and therefore occupying a somewhat separate place is the following type of measurement:

- 5) *K-polarization measurement*: the direct fluorescence signal K^{off} of Table V as a function of the polarisation angle θ_E . This allows a check on the absence of a magnetic field. Also, it gives an idea of the sensitivity of the optical detection efficiency to the anisotropy of the fluorescence radiation emitted by polarized $\{\alpha\}_k$ atoms.

We repeat, that for measurements with a variety of a secondary-beam gases (providing yet another cross section through variable-space) to be in the same category as the above kinds of experiment, an adaptation of the gas-handling system would be required. A change in laser frequency, for another initial state $\{\alpha\}_k$, not only takes time in itself but may also affect laser-beam alignment. This calls for a repetition of the alignment procedure of section 3.

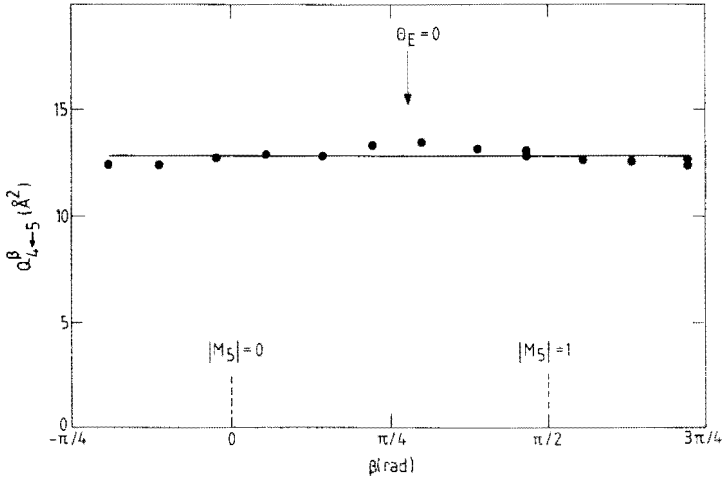


Fig. 27. Experimental results for the observed $\text{Ne}^{**}\text{-He}$ cross section $Q_{4\leftarrow 5}$ as a function of the angle β between the electric field \underline{E} of the laser and the relative velocity \underline{g} , at a center-of-mass energy $E_5 \approx 100$ meV. The statistical errors are smaller than the size of the data points. The observed dependence on β reflects the non-isotropic distribution of collision-induced fluorescence radiation, which we have not corrected for here. The drawn curve therefore indicates the average value of the data points and does not represent a curve fit according to Eq. (21).

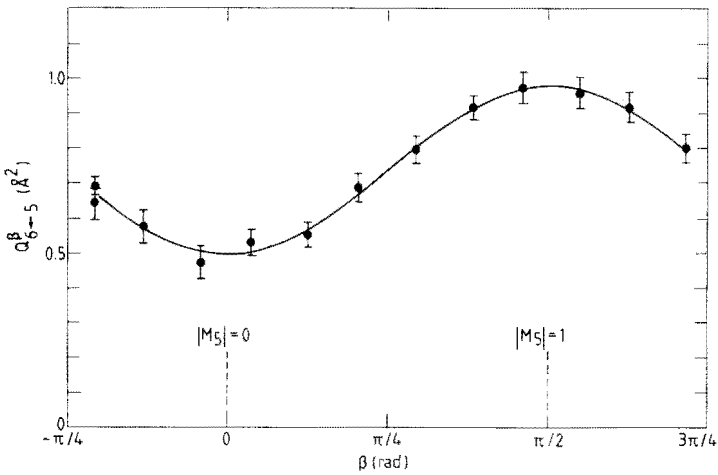


Fig. 28. Experimental results for the observed $\text{Ne}^{**}\text{-He}$ cross section $Q_{6\leftarrow 5}^{\beta}$ as a function of the angle β between the electric field \underline{E} of the laser and the relative velocity \underline{g} , at a center-of-mass energy $E_5 \approx 100$ meV. Statistical errors only have been indicated. The drawn curve represents a fit of the data points according to Eq. (21).

We will now present some results for the major types of experiments being performed. This is mostly by way of example only. For a detailed analysis we refer to Refs. 20-22.

5.4. Polarized-atom cross sections

In Figs. 27 - 29 we show the experimental results $Q_{\ell \leftarrow k}^{\beta}$ for the $\text{Ne}^{**}\text{-He}$ $\{a\}_5 \rightarrow \{a\}_4$, $\{a\}_6$ and $\{a\}_7$ transitions, at center-of-mass energy $E \approx 100$ meV^{20}). The experiments were performed by pumping the $\{a\}_5$ level through the $(^3\text{P}_0) \rightarrow \{a\}_5$ transition at $\lambda = 626$ nm. The $\{a\}_5$ state has $J_5 = 1$. We note that the whole gamut of possible polarisation effects is observed. The $Q_{6 \leftarrow 5}^{\beta}$ and $Q_{7 \leftarrow 5}^{\beta}$ closely conform to the $\cos 2\beta$ -expression of Eq. (21), as shown by the results of a least-squares fit of the data points. The somewhat deviating behaviour of the $Q_{4 \leftarrow 5}^{\beta}$ cross section is caused by the non-isotropic distribution of collision-induced fluorescence radiation, which takes on importance in the absence of a real polarisation effect. It is possible to correct for this. We find that $Q_{\ell \leftarrow 5}^{|0\rangle} / Q_{\ell \leftarrow 5}^{|1\rangle} = 1.06, 0.52$ and 3.5 for $\ell = 4, 6$ and 7 , respectively. As to cross section magnitude, the variation there is considerable as well, with $Q_{4 \leftarrow 5}$ and $Q_{6 \leftarrow 5}$ at opposite ends of the scale. Figure 30 of $Q_{8 \leftarrow 9}^{\beta}$ at $E \approx 100$ meV illustrates the presence of the higher order terms of Eq. (18). The data points were fitted with the model function of Eq. (18) for $n \leq 3$.

The largest polarization effects observed so far are those for the $\text{Ne}^{**}\text{-He}$ $\{a\}_7 \rightarrow \{a\}_{4,5}$ transitions at $E \approx 100$, with $Q_{\ell \leftarrow 7}^{|0\rangle} / Q_{\ell \leftarrow 7}^{|1\rangle} \approx 0.1$ and 9 for $\ell = 4$ and 5 , respectively²¹⁾. For the $\{a\}_7 \rightarrow \{a\}_4$ transition we find a very small cross section $Q_{4 \leftarrow 7}^{|0\rangle} \approx 0.05 \text{ \AA}^2$. Compare this with the much larger $\text{Ne}^{**}\text{-CO}_2$ cross sections ($\approx 50 \text{ \AA}^2$) shown in section 5.6.

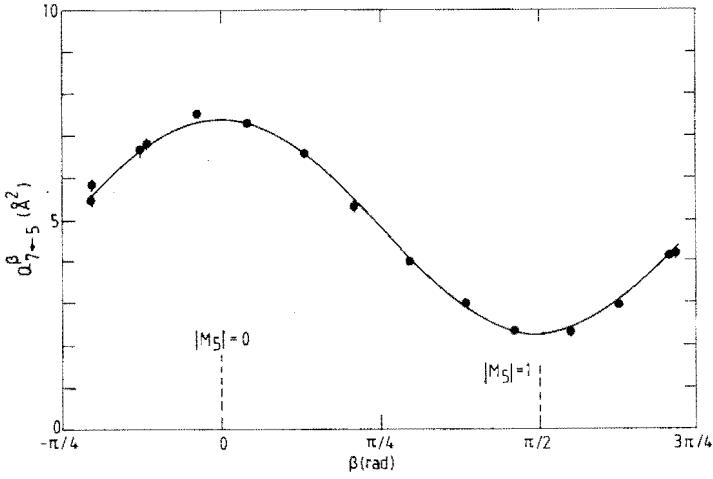


Fig. 29. Experimental results for the observed $\text{Ne}^{***}\text{-He}$ cross section $Q_{7\leftarrow 5}^\beta$. See caption of Fig. 28 for further detail.

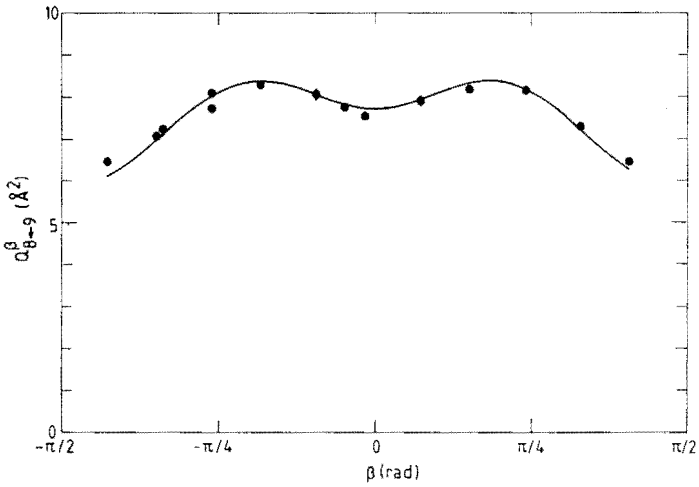


Fig. 30. Experimental results for the observed $\text{Ne}^{***}\text{-He}$ cross section $Q_{8\leftarrow 9}^\beta$. Curve fit of data points according to Eq. (18) with $n \leq 3$. See caption of Fig. 28 for further detail.

5.5. Energy dependence

The observed energy dependence of the $Q_{4\leftarrow 5}^{|M_5|}$ and $Q_{7\leftarrow 5}^{|M_7|}$ cross sections for Ne^{**}-He is shown in Figs. 31 and 32^{20,21}). The measurements have been performed both by varying the magnitude of the primary beam velocity v_1 (by using a 15% Ne - 85% He seeded primary beam) and by varying the direction of the secondary beam velocity v_2 (by scanning the laser beam along the primary-beam axis). In general, the energy range that is accessible by these means is $50 \text{ meV} \lesssim E \lesssim 250 \text{ meV}$ (depending to some extent on the secondary-beam gas).

Velocity-averaged results only are presented here. The actual velocity distribution in the scattering center matters relatively little for these transitions, but plays an important role in e.g. the highly endothermic $\{\alpha\}_7 \rightarrow \{\alpha\}_5$ transition, where the energy threshold is $\Delta E_{57} = 81 \text{ meV}$. This effect becomes progressively less important at higher energies.

In time-of-flight (TOF) measurements, the separate TOF-spectra of the K^{off} , K^{on} , L^{off} and L^{on} signals (see section 4) can be combined into an I_e/I_k spectrum in the usual fashion (i.e. in accordance with Eq. (8)). In theory, continuous coverage of the thermal velocity range is possible by performing TOF-measurements at various laser-beam positions (as in the energy measurements, discussed earlier). Some preliminary results, applying to the Ne^{**}-He $\{\alpha\}_5 \rightarrow \{\alpha\}_7$ transition for $|M_5| = 0$, can be seen in Fig. 33. The pseudo-random correlation method was employed here, with a channel-time $t_k = 5 \mu\text{s}$, at three different laser positions. Unfortunately, deconvolution along the lines of section 4 (Eq. (10)), undertaken separately for each primary-beam velocity, not quite succeeds in achieving the desired overlap of cross section values, yet.

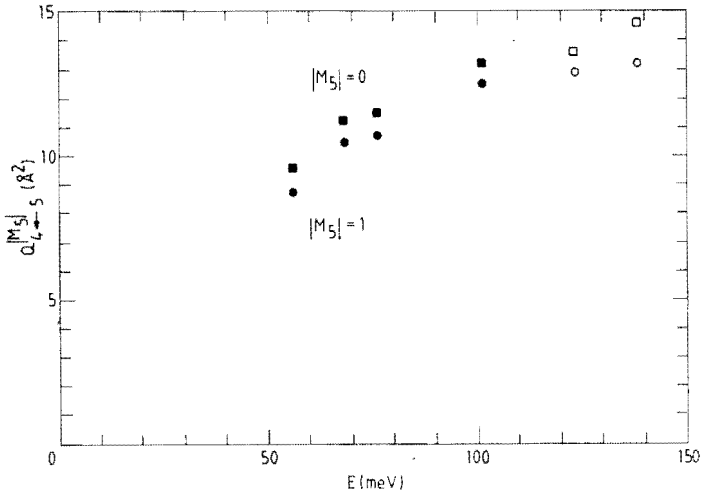


Fig. 31. Energy dependence of the polarized $\text{Ne}^{**}\text{-He}$ cross sections $Q_{4\leftarrow 5}^{0|}$ and $Q_{4\leftarrow 5}^{1|}$, with E the center-of-mass energy. The open points have been obtained by varying the magnitude of the primary-beam velocity v_1 ; the full points by varying the position of the laser beam along the primary-beam axis, and thus the direction of v_2 .

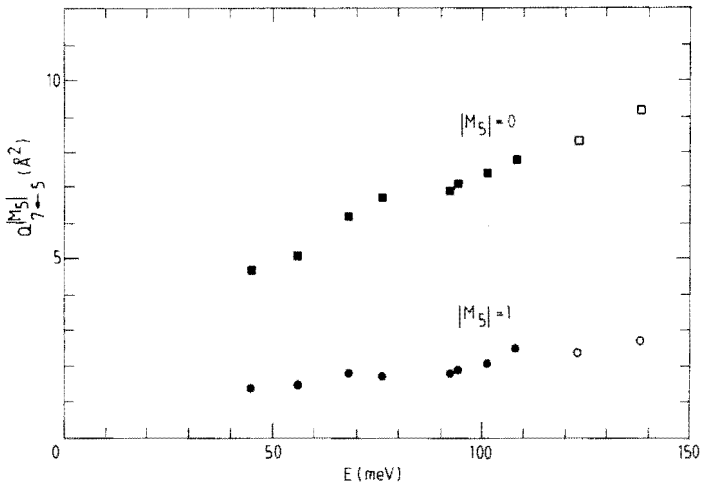


Fig. 32. Energy dependence of the polarized $\text{Ne}^{**}\text{-He}$ cross sections $Q_{7\leftarrow 5}^{0|}$ and $Q_{7\leftarrow 5}^{1|}$. See caption of Fig. 31 for further detail.

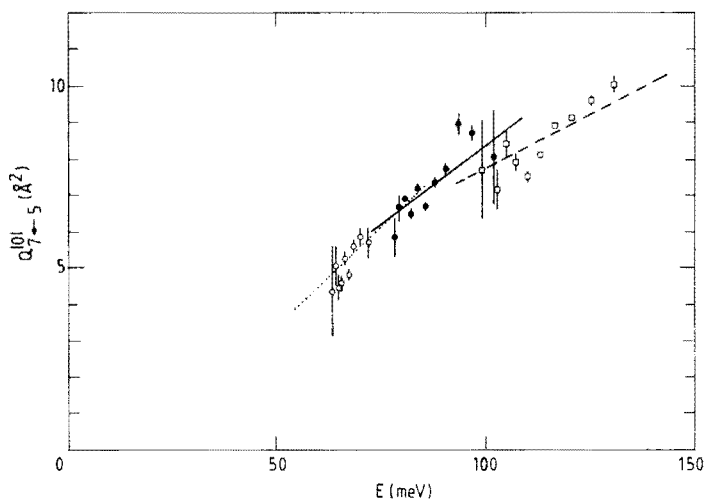


Fig. 33. Energy dependence of the polarized $\text{Ne}^{*} - \text{He}$ cross sections $Q_{7+5}^{(0)}$, obtained from time-of-flight measurements at three different laser-beam positions. Together these measurements span the $60 \text{ meV} \lesssim E \lesssim 140 \text{ meV}$ energy range. The TOF-data were obtained using the pseudo-random correlation method, with a channel time $t_k = 5 \mu\text{s}$. The lines in the figure are the result of the velocity-dependent deconvolution. Their overlap still leaves something to be desired.

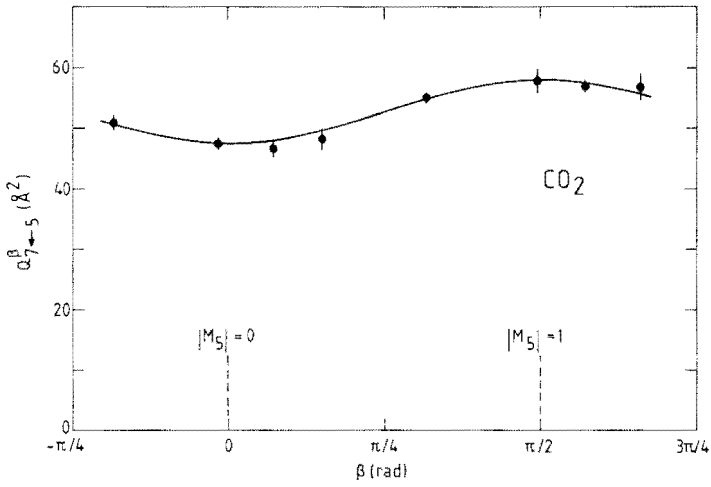


Fig. 34. Experimental results for the observed $\text{Ne}^{***}\text{-CO}_2$ cross section Q_{7+5}^{β} , at energy $E_5 \approx 160$ meV. See caption of Fig. 28 for further detail. Note the differences with Fig. 35.

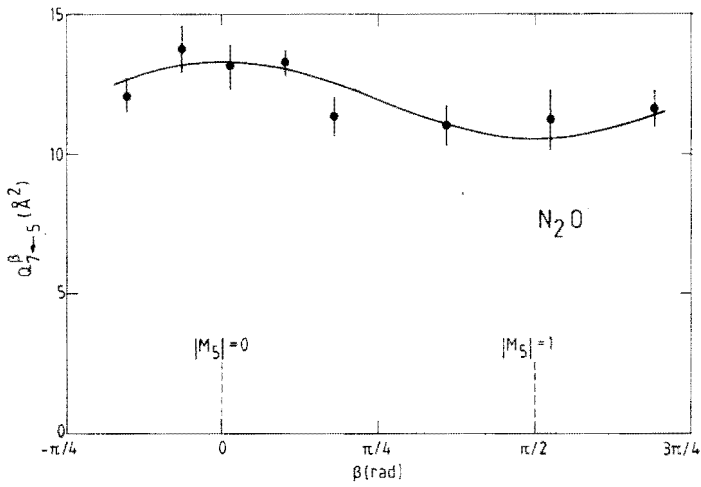


Fig. 35. Experimental results for the observed $\text{Ne}^{***}\text{-N}_2\text{O}$ cross section Q_{7+5}^{β} , at energy $E_5 \approx 160$ meV. See caption of Fig. 28 for further detail. Note the differences with Fig. 34.

5.6. System-related aspects

The mini-beam apparatus described in the present paper was set up specifically for experiments with short-lived Ne^{**} -atoms. A change to a different noble-gas atom such as Ar^{**} or Kr^{**} , while highly interesting, entails certain practical difficulties.

The production of metastable atoms is not one of these. The metastable beam source will accommodate a variety of noble gases. As to the optical detection system, this would require at least a new set of interference filters and probably a different type of photomultiplier as well. It is, however, the need for a laser operating in a different wavelength region that presents the major (financial) problem. In our laboratory, work on diode lasers is in progress, which will perhaps make the transition to Ar^{**} or Kr^{**} a viable option.

As opposed to the situation for the short-lived atom, there is a wide choice in ground-state collision partners. Generally speaking, only corrosive gases are excluded, for obvious reasons. Noble gas atoms from Ar upwards offer the chance of an indirect view of Penning ionization, a process not occurring for the Ne^{**} -He and Ne^{**} -Ne systems we have so far concentrated on. In Ne^{**} -molecule collisions, processes like angular momentum coupling and rotational excitation must be considered (as they must in e.g. Ne^* - H_2 collisions³⁹⁾), in addition to intramultiplet mixing and Penning ionization.

We have performed preliminary measurements for Ne^{**} -Ar, Kr, Xe and for Ne^{**} - H_2 , CH_4 , N_2 , CO_2 , N_2O . By way of example, Figs. 34 and 35 show the observed cross sections $Q_{7\leftarrow 5}^\beta$ for Ne^{**} - CO_2 and Ne^{**} - N_2O , respectively, at approximate energy $E = 160$ meV. We note first that in both cases the polarization effect is smaller than for Ne^{**} -He (compare Fig. 29). This is part of a general trend. Remarkably, the polarization effect is reversed

for Ne^{**}-CO₂. Also, there is a large difference in cross section magnitude. Anisotropy effects are expected to play an important role here. To derive from experimental data such as these information about the interactions constitutes a major challenge.

6. Concluding remarks

The mini-beam experiment, described in these pages, has proven to be a valuable instrument for the study of inelastic collisions of short-lived Ne^{**}-atoms. With some exaggeration, it can be said to combine the sensitivity of a beam-gas cell experiment with the resolution of a full-size crossed-beam experiment. The disadvantages attached to the use of a free-jet secondary-beam expansion (alignment problems on the one hand, convolution difficulties in the calibration on the other) are surmountable. The possibility of varying the collision energy by moving the scattering center position is a bonus in this respect.

In the near future we will install a hollow cathode arc metastable beam source⁴⁰⁾, thus opening up the superthermal energy range $0.5 \text{ eV} < E < 5 \text{ eV}$, as well. At the same time, cooling and/or heating of the secondary-beam nozzle should be relatively easy to achieve. In this regard, we note that a laterally movable nozzle assembly would significantly enhance the capacity for energy variation by manipulation of the Newton diagram of the primary- and secondary-beam velocity vectors. In the longer term, the availability of diode-lasers operating in the infrared raises the prospect of experiments with short-lived Ar^{**}- or Kr^{**}-atoms.

Diode lasers might also be used in combination with the present dye laser in a two-photon-excitation experiment. In this, the short-lived two-level system $\{a\}_g$ state, produced by the dye laser in a saturated

transition from the metastable (3P_2) state, would be excited by the diode laser to the lowest Rydberg-type states.

The large polarization effects that are observed attest to the interest of the Ne^{**}-atom/molecule systems. For a system like Ne^{**}-He in particular, the experiment provides the invaluable first ingredient for a complete analysis of interaction and collision dynamics. The fortunate availability of Ne^{**}-He model potentials is another such ingredient. Using quantum-mechanical coupled-channels calculations²⁰⁾, supplemented where possible by semiclassical calculations²¹⁾, a direct confrontation between theory and experiment has become possible.

References

- 1 D. Hennecart and F. Masnou-Seeuws, J. Phys. B 18, 657 (1985).
- 2 a) W. Buszert, T. Bregel, R.J. Allan, M.-W. Ruf, and H. Hotop, Z. Phys. A 320, 105 (1985); b) W. Buszert, T. Bregel, J. Ganz, K. Harth, A. Siegel, M.-W. Ruf, H. Hotop and H. Morgner, J. Phys. (Paris) 46 C19 (1985).
- 3 M.H. Alexander, T. Orlikowski, and J.E. Straub, Phys. Rev. A 28, 73 (1983).
- 4 G. Nienhuis, Phys. Rev. A 26, 3137 (1982).
- 5 J.G. Kircz, R. Morgenstern, and G. Nienhuis, Phys. Rev. Lett 48, 610 (1982).
- 6 H.A.J. Meyer, H.P. van der Meulen, and R. Morgenstern, Z. Phys. D 5, 299 (1987).
- 7 D. Neuschäfer, M.O. Hale, I.V. Hertel and S.R. Leone, in "Electronic and Atomic Collisions", Eds. D.C. Lorents, W.E. Meyerhof, and J.R. Peterson, Elsevier (1986)
- 8 a) M.O. Hale, I.V. Hertel, and S.R. Leone, Phys. Rev. Lett. 53, 2296 (1984); b) M.O. Hale and S.R. Leone, Phys. Rev. A 31, 103 (1985).
- 9 J.M. Parson and T. Ishikawa, J. Chem. Phys. 80, 3137 (1984)
- 10 A. Bähring, I.V. Hertel, E. Meyer, W. Meyer, N. Spies, and H. Schmidt, J. Phys. B 17, 2859 (1984).

- 11 a) D. Hennecart, *J. Phys. (Paris)* **39**, 1065 (1978); b) D. Hennecart, Ph.D. Thesis, Université de Caen, 1982 (unpublished).
- 12 J.M. Mestdagh, J. Berlande, P. de Pujo, J. Cuvallier, and A. Binet, *Z. Phys. A* **304**, 3 (1982).
- 13 E. Düren, E. Hasselbrink, and H. Tischen, *Phys. Rev. Lett.* **50**, 1983 (1983).
- 14 L. Hüwel, J. Maier, and H. Pauly, *J. Chem. Phys.* **76**, 4961 (1982).
- 15 H.J. Yuh and P.J. Dagdigan, *Phys.Rev. A* **28**, 63 (1983).
- 16 a) N.Böwering, M.R. Bruce and J.W. Keto, *J. Chem. Phys.* **84**, 709 (1986);
b) N.Böwering, M.R. Bruce and J.W. Keto, *J. Chem. Phys.* **84**, 715 (1986).
- 17 J.K. Kuh and D.W. Setser, *J. Chem. Phys.* **84**, 4304 (1986).
- 18 I.V. Hertel, H. Schmidt, A. Bähring and E. Meyer, *Rep. Prog. Phys.* **48**, 375 (1985).
- 19 M.P.I. Manders, J.P.J. Driessen, H.C.W. Beijerinck and B.J. Verhaar, *Phys. Rev. Lett.* **57**, 1577 (1986); *ibid.*, **57**, 2472 (1986).
- 20 M.P.I Manders, J.P.J. Driessen, H.C.W. Beijerinck and B.J. Verhaar, *Phys. Rev. A*, (1988) accepted for publication.
- 21 M.P.I. Manders, W.B.M. van Hoek, E.J.D. Vredenburg, G.J. Sandker, H.C.W. Beijerinck and B.J. Verhaar, to be published.
- 22 M.P.I. Manders, W. Boom, H.C.W. Beijerinck and B.J. Verhaar, to be published.
- 23 J.P.C. Kroon, Ph.D. Thesis, Eindhoven University of Technology (1985).
- 24 M.J. Verheijen, H.C.W. Bijerinck, L.H.A.M. van Moll, J.P.J. Driessen and N.F. Verster, *J.Phys. E* **17** (1984) 904.
- 25 H.C.W. Beijerinck and N.F. Verster, *Physica* **111C** (1981) 327.
- 26 M.J. Verheijen, H.C.W. Beijerinck and N.F. Verster, *J. Phys. E* **15** (1982) 1198.
- 27 J.P.C. Kroon, H.C.W. Beijerinck, B.J. Verhaar and N.F. Verster, *Chem.Phys.* **90** (1984) 195.
- 28 M.J. Verheijen, H.C.W. Beijerinck and N.F. Verster, *Rev.Sci.Instr.* **56** (1985) 62.
- 29 a) H.C.W. Beijerinck, R.J.G.M. Moonen and N.F. Verster, *J.Phys. E* **7** (1974) 31; b) H.C.W. Beijerinck, Ph.D. Thesis, Eindhoven University of Technology (1975).
- 30 S.M. Trujillo, P.K. Rol and E.W. Rothe, *Rev.Sci.Instr.* **33** (1962) 841.
- 31 A.W.F. van Gerven, *Int.Rep. TUE VDF/NO 86-16* (1986) (in Dutch).
- 32 F.C. van Nijmegen, *Int.Rep. TUE VDF/CO 84-09* (1984) (in Dutch).

- 33 P.W.E. Verhelst and N.F. Verster, *Software Practice and Experience* 14 (2) (1984) 119.
- 34 F.C. van Nijmegen, *Int.Rep. TUE FTI/BA 87-03* (1987) (in Dutch).
- 35 J.H. Voskamp, F.C. van Nijmegen, and J.M.P. van Erum, *Conference Proceedings "Computing in High Energy Physics"*, ed. L.O. Hertzberger and W. Hoogland (1986) 222.
- 36 I.S. Gradshteyn and I.M. Ryzhik, *"Tables of Integrals, Series, and Products"*, Academic Press, New York (1965)
- 37 H.C.W. Beijerinck, *Comments At. Mol. Phys.* 19 (1987) 227
- 38 A. Messiah, *"Quantum Mechanics"*, Vol. I + II, North Holland, Amsterdam (1981).
- 39 J. Robert, V. Bocvarski, B. Stern, J. Reinhardt and J.Baudon, to be published.
- 40 P.G.A. Theuws, H.C.W. Beijerinck, D.C. Schram and N.F. Verster, *J.Phys. E* 15 (1982) 573.

C h a p t e r I V.

COLLISION-INDUCED INTRAMULTIPLY MIXING FOR $\text{Ne}^{**}\{(2p)^5(3p)\} + \text{He}$:
EXPERIMENTS AND QUANTUM CALCULATIONS

M.P.I. Manders, J.P.J. Driessen, H.C.W. Beijerinck and B.J. Verhaar

Physics Department, Eindhoven University of Technology,

P.O. Box 513, 5600 MB Eindhoven, The Netherlands.

Abstract

We have investigated fine-structure-changing collisions of short-lived (20 ns) Ne^{**} atoms in the $\{\alpha\} \equiv \{(2p)^5(3p)\}$ multiplet with ground state He atoms. A newly-designed crossed-beam apparatus allows the measurement of accurate polarized cross sections $Q_{l \leftarrow k}^{|M_k|}$ for the $\{\alpha\}_k \rightarrow \{\alpha\}_l$ transition. In the experiment, the initial $\{\alpha\}_k$ -state is prepared with a well-defined asymptotic orientation M_k of its electronic angular momentum J , through excitation of metastable Ne^* atoms with a polarized laser. The reported transitions are mainly between states in the $\{\alpha\}_{4,5,6,7}$ group (Paschen numbering), at approximately 100 meV center-of-mass energy. Some of these exhibit very strong polarization effects, with differences between $Q_{l \leftarrow k}^{|M_k|}$ and $Q_{l \leftarrow k}^{|M'_k|}$ of up to a factor 4.

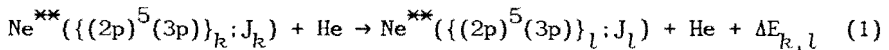
Fully quantum-mechanical coupled-channels calculations on a diabatic basis, with the Ne^{**} -He model potentials of Hennecart and Masnou-Seeuws as input, prove successful in reproducing experimental results.

Cross section behavior may be qualitatively understood from the presence of avoided crossings between the adiabatic potentials, indicative of strong radial coupling. The restraint of reflection symmetry is strongly felt here. In addition, the effects of rotational coupling can be readily identified.

1. Introduction

Inelastic collisions of atoms in short-lived, electronically excited states presently are in the focus of attention of both theorists¹⁻⁴⁾ and experimentalists⁵⁻¹⁷⁾. A recent review of the field has been given by Hertel¹⁸⁾. The dependence of the outcome of the collision process on the initial orientation of the electronic angular momentum with respect to the initial relative velocity of the collision partners has proven to reveal many interesting features of the potential surfaces and collision dynamics^{2,6,7)}. So far, most experiments have been performed in bulk. Only recently crossed-beam experiments with a much better defined initial relative velocity have been reported^{6,7)}, resulting in more reliable results on these polarisation effects. Until now, the rather simple one-electron alkali metal^{4-6,12-14)} and two-electron alkaline earth^{3,7-9,15)} systems have received most attention, with less emphasis being put on noble gas atoms^{16,17)}.

In this paper we report the first crossed beam study of inelastic, fine-structure changing collisions for the system



involving beams that are well-characterised with respect to direction, velocity and excited state polarisation. Strong, interesting polarisation effects have been observed and absolute values of cross sections have been determined with a high accuracy of 25 %. We have touched upon this subject already in an earlier letter¹⁹⁾.

In a study of this sort, He is a "natural" choice as a collision partner for the short-lived Ne^{**} atoms. Some of the reasons for this may be deduced from the energy level scheme in Fig. 1, which shows the first and second excited multiplets, plus the ionisation limit, of the rare gas atoms from He to Xe. It will be apparent that, at other than very high energies, a collision partner of either lighter or equal mass precludes the possibility of processes like Penning ionisation or excitation transfer obscuring the intramultiplet mixing picture. So, for $\text{Ne}^{**} + \text{He}$ (and $\text{Ne}^{**} + \text{Ne}$), the ground state atom can be assumed to remain in the ground state. Likewise, there will be no chance of other than the short-lived Ne^{**} states playing a part.

Typical lifetimes of the $\{a\}_i \equiv \{(2p)^5(3p)\}_i$ states, with i running from 1 to 10 with decreasing energy, are $\tau \approx 20$ ns. The total energy spread of the multiplet is $\Delta E_{1,10} = 584$ meV. The Ne states are shown in Fig. 2. Although a large number $\sum_{i=1}^{10} (J_i + 1) = 23$ of molecular states is involved, which complicates the analysis of the observed transitions, the $\text{Ne}^{**} - \text{He}$ system has two major advantages, besides the ones already cited. Firstly, the process of intramultiplet mixing has been investigated in detail in the afterglow of gas discharges, resulting in a suitable set of reference rate constants for Ne and He as collision partners^{11,20-23}). Secondly, model potentials are available for the $\text{Ne}^{**} - \text{He}$ system¹), allowing a direct comparison of theory and experiment by means of fully quantum-mechanical coupled-channels calculations. In the $\text{Ne}^{**} - \text{Ne}$ case such a calculation is complicated by the presence of additional symmetries, due to equal charges for $^{22}\text{Ne}^{**} - ^{20}\text{Ne}$, and to both equal charges and identical particles for $^{20}\text{Ne}^{**} - ^{20}\text{Ne}$. For the present, we limit our discussion to the $\text{Ne}^{**} - \text{He}$ case.

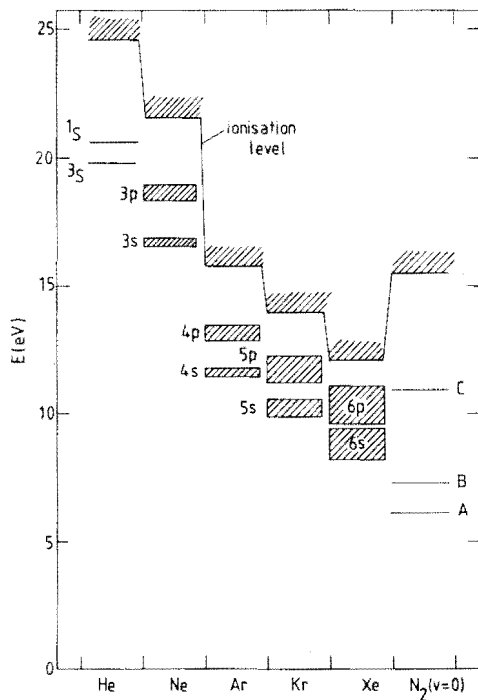


Fig. 1. Energy levels of the rare gases from He through Xe, plus N_2 as a typical molecule. Indicated are the first (ns) and second (np) excited multiplets, as well as the ionisation limit.

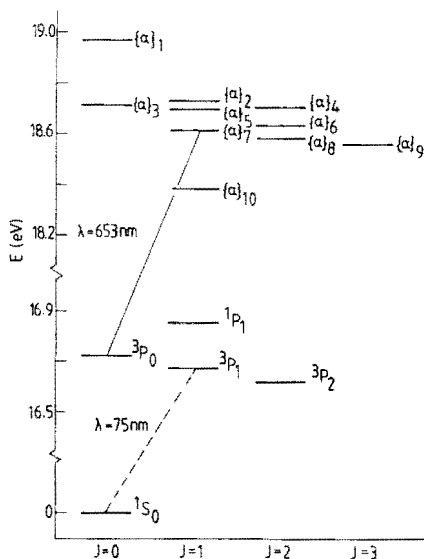


Fig. 2. Energy-level diagram of the $Ne^* \{ (2p)^5(3s) \}$ (Russell-Saunders notation) and $Ne^{**} \{ (2p)^5(3p) \} \equiv \{ \alpha \}$ (Paschen numbering) excited states, grouped by their electronic angular momentum quantum number J .

2. Collision dynamics

2.1. Scattering process

The Hamiltonian governing the process of Eq. (1) consists of the kinetic energy operator of nuclear motion T_n , with radial and rotational components T_{rad} and T_{rot} , and the electronic molecular Hamiltonian H^{mol} , which contains the atomic Hamiltonians $H^{Ne^{***}}$ and H^{He} as well as the molecular interaction $V^{Ne^{***}-He}$:

$$H = T_{rad} + T_{rot} + H^{Ne^{***}} + H^{He} + V^{Ne^{***}-He} \quad (2)$$

The relative motion of the nuclei results in a rotational angular momentum \underline{N} . At the same time, both the Ne^{***} atom and its collision partner may in principle possess an intrinsic angular momentum \underline{J} . In fact, as we have seen, the He atom remains in the ground state, and we will at all times have total electronic angular momentum $\underline{J} = \underline{J}_{Ne^{***}}$. Electronic and rotational angular momentum couple to total angular momentum $\underline{P} = \underline{N} + \underline{J}$, which is a conserved quantity. The initial and final Ne^{***} atomic states may have different \underline{J} . Within the limits posed by $\underline{P} = \underline{N} + \underline{J}$, \underline{N} will change accordingly. Due to inversion symmetry, the total parity π is a conserved quantity as well.

At the present collision energies of less than 0.5 eV, relative velocities of the colliding atoms are small, compared to electron velocities. In consequence, the electronic wave function will be able to adapt itself more or less adiabatically to the orientation of the inter-nuclear axis. The picture that thus emerges is that of a quasi-molecular system. The interaction between the collision partners is apt to be

governed by the molecular potential curves. However, other than in the completely adiabatic Born-Oppenheimer approach, the molecular states are still coupled by the nuclear motion.

It is apparent from the above that the molecular quantum number $\Omega = |M_{J_{z'}}|$, with $M_{J_{z'}}$, the magnetic quantum number with respect to the body-fixed internuclear axis z' , will have relevance at small distances. We note that the $J_{z'}$ operator does not commute with \underline{N} , so that a description in terms of the quantum number N of nuclear rotational motion then becomes infeasible. Naturally, the above adiabatic, i.e. molecular, picture does not rule out a description in diabatic, i.e. atomic, terms, as long as a sufficient number of basis states is included in either description. Indeed, atomic terms are naturally associated with the asymptotic state of the system, which ultimately decides the outcome of the scattering experiment.

2.2. Model potential method for $Ne^{**}-He$

The atoms in our collision experiment constitute a quasi-molecular system. The experiment may be interpreted through the relevant molecular potential curves, i.e. eigenvalues of the molecular Hamiltonian H^{mol} . With regard to these, ab initio²⁴⁾ and configuration-interaction²⁵⁾ calculations for the Ne^*-Ne system have met with limited success.

For the case of the Na-Ne interaction, the model potential method, which solves a one-electron Schrödinger equation for the motion of the valence electron in the effective potential of the two cores, gives fairly accurate results²⁶⁾.

To extend the model potential method to the Ne^{**} -rare gas systems, the coupling of angular momentum (orbital and spin) of the (3p)-valence electron and the (2p)⁻¹ open shell core has to be included, and may be

expected to have considerable effect²⁷⁾. The definition of an effective potential takes proportionally more effort. This problem has been solved by Hennecart^{1,11)} and Masnou-Seeuws¹⁾ for Ne^{**}-He at internuclear distances $R \geq 4.5 a_0$, using an iterative, first order perturbation treatment. For a start, they solve the one-electron problem for an effective zero order molecular interaction potential V_{int} , that contains only the spherical part H_a of the atomic electron-core interaction, as well as the molecular electron-He and electron-core-He interactions. This results in eigenvalues $V_\sigma(R)$ and $V_\pi(R)$ for the $(3p), |m_l| = 0$ and $(3p), |m_l| = 1$ molecular states, respectively, with m_l the magnetic subquantum number for the orbital angular momentum of the valence electron. Comparison of calculated atomic and molecular electron orbitals indicates that the $(2p)^{-1}$ core orbital is not modified by the presence of the perturbing rare gas atom and that the modification of the $(3s)$ and $(3p)$ valence electron wave functions is limited to a small region around the perturber. For internuclear distances $R \geq 4.5 a_0$, which is the lower limit of the $V_\sigma(R)$ and $V_\pi(R)$ calculation by Hennecart and Masnou-Seeuws, this places the modification well outside the core region.

The spin-orbit coupling and the non-spherical part of the electron-core interaction can thus be calculated by first order perturbation theory in an atomic $|LSJM_J\rangle$ basis, with L , S and J the orbital, spin and total Ne angular momentum quantum numbers. In the same $|LSJM_J\rangle$ basis, the matrix elements of V_{int} have been calculated by Hennecart^{1,11)} and Masnou-Seeuws¹⁾ through the method of representing V_{int} in terms of irreducible tensor operators. The matrix elements are given by linear combinations of $V_\sigma(R)$ and $V_\pi(R)$.

Hennecart and Masnou-Seeuws then assume a diagonal charge-induced dipole core-He interaction $V^{core}(R) = -C_4/R^4$. Thereby, the electronic Hamiltonian H^{mol} for $R \geq 4.5 a_0$ is completely determined. With the

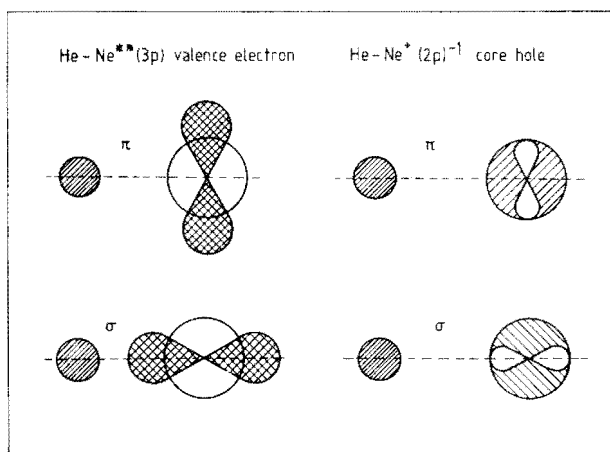


Fig. 3. The Ne (3p) valence electron (#) and (2p) core hole (//) charge distributions associated with the π and σ states of the e^- -He and Ne^+ -He systems. The attractive/repulsive character of the valence electron π/σ -orientation potentials is reversed in the case of the core hole.

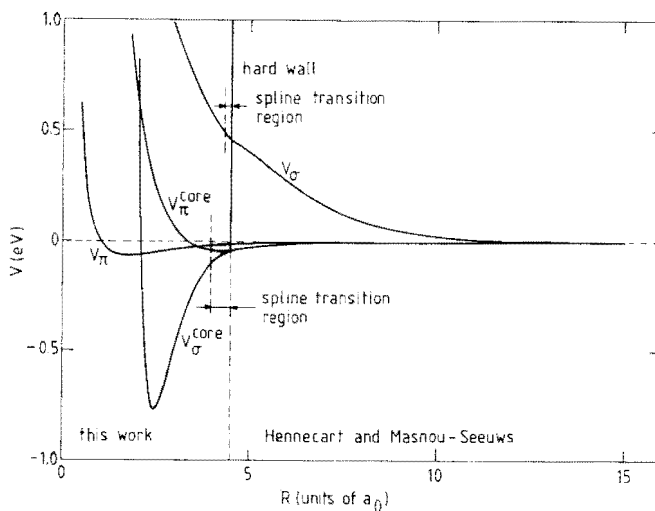
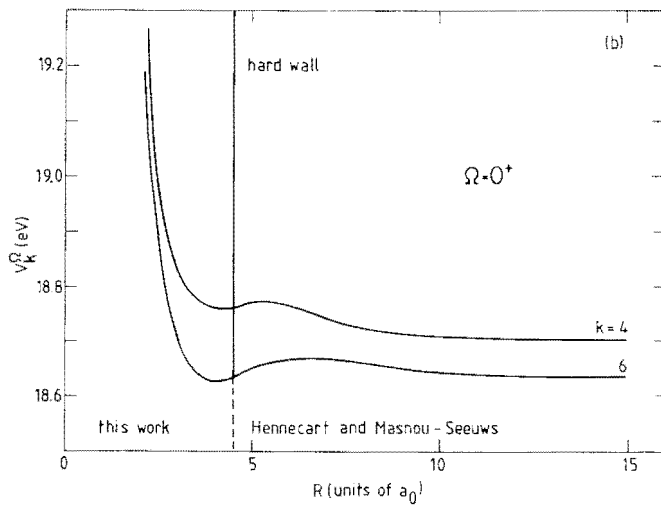
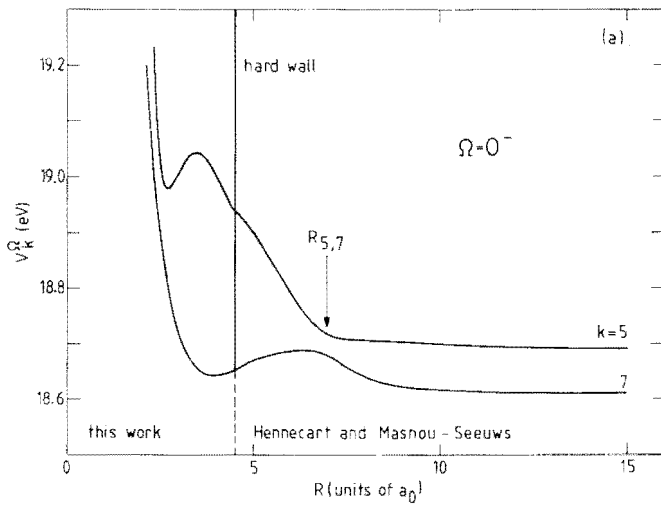


Fig. 4. Potentials resulting from the e^- -He and Ne^+ -He interaction, for the π and σ orientations. For internuclear distances $R > 4.5 a_0$ these follow the prescription of Hennecart and Masnou-Seeuws. At smaller distances they result from the extension procedure described in section 2.2. In each case the cubic spline transition region has been indicated.

expansion of the $\{\alpha\}_k$ atomic states in the $|LSJM_J\rangle$ -basis known, H^{mol} may be transformed to the $|\alpha JM_J\rangle$ representation. Diagonalisation yields the molecular, adiabatic, eigenstates $|\alpha J\Omega(R)\rangle$ and potential curves $V_k^\Omega(R)$. The 23 adiabatic potential curves are, of course, divided into Ω -manifolds. Additionally, for $\Omega = 0$ the constraint of reflection symmetry generates distinct + and - classes, containing the even and odd J states, respectively.

The above potentials, given for $R \geq 4.5 a_0$, can only be used as input for a full coupled-channels calculation through the addition of a hard wall at the cutoff distance. In the case of an adiabatic potential curve of a repulsive nature, this is a reasonable assumption, especially at low energies. For the curves which are attractive at $R = 4.5 a_0$, this procedure is more debatable. To investigate the importance of the inner potential regions for the calculated inelastic cross sections, we have extended the potentials to smaller distances. This was done, both for the valence electron-He interaction (in a simple empirical way) and for the core-He interaction.

We first consider the general character of the valence electron and core potentials at small distances. As was the case for the valence electron, different core orientations will result in different core-He potentials: $V_\sigma^{\text{core}}(R)$ and $V_\pi^{\text{core}}(R)$ for the $(2p)^{-1}, |m_l| = 0$ and $(2p)^{-1}, |m_l| = 1$ molecular states (see Fig. 3). For the $(3p)$ valence electron, the repulsive forces arising from the overlap of wave functions will be more important at a given separation for the σ -state than for the π -state, due to the σ -wave function being oriented towards the ground state atom. For the $(2p)^{-1}$ core hole this situation is reversed: the π -potential will be more repulsive than the σ -potential. Moreover, due to the smaller spatial extension of the $(2p)^{-1}$ wave function, the corresponding repulsive forces will be of shorter range. At large distances, where the weakly



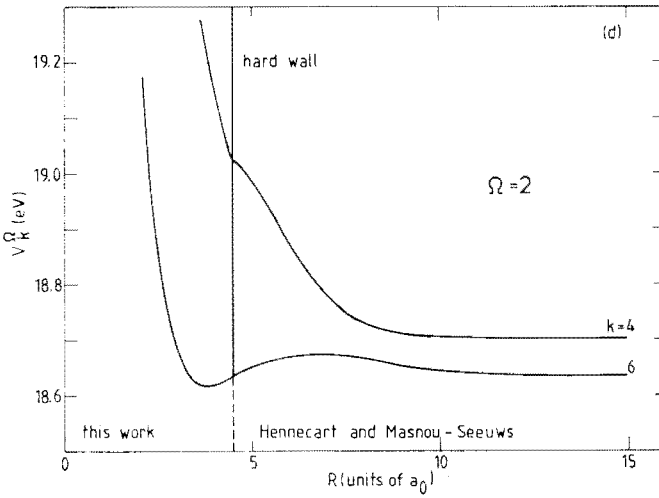
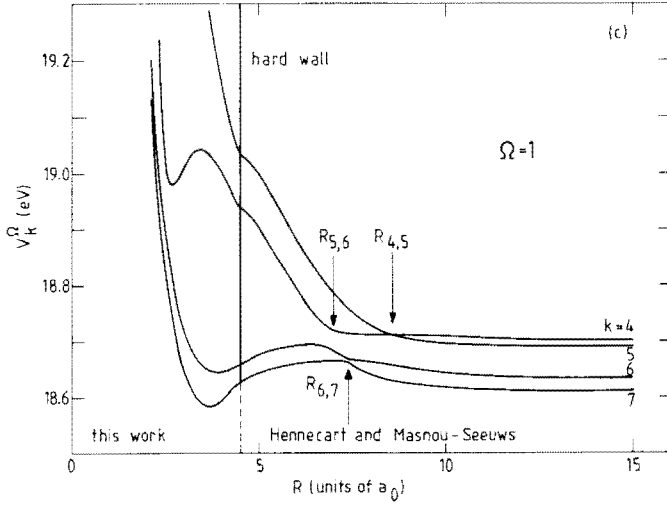


Fig. 5. Adiabatic potential curves $V_k^\Omega(R)$ for the $\{\alpha\}_{k=4,5,6,7}$ multiplet of special interest, as derived from the basic potentials of Fig. 4. The arrows point to the position $R_{k,l}$ of unmistakable avoided crossings.

attractive dispersion interaction becomes dominant, V_σ will be slightly more attractive than V_π , due to the greater polarizability of the σ -orbital. At these distances, any effect of the core orientation will be negligible. The potentials of Hennecart and Masnou-Seeuws for the valence electron, given for $4.5 a_0 \leq R \leq 15 a_0$, indeed display the expected short-range behaviour, while V_σ is still slightly repulsive at $R = 15 a_0$.

The extension of the V_π and V_σ valence electron potentials was performed in the following way. To V_σ we added a repulsive exponential core; V_π was extrapolated on the basis of an electrostatic model for the contribution of the two lobes of the π -orbital to the charge-induced dipole electron-He interaction. The core-He potential²⁸⁾ may be derived from the spectroscopy of the $(\text{NeHe})^+$ ion²⁹⁾. From a certain internuclear distance $R \geq 6a_0$, it equals the diagonal charge-induced dipole core-He interaction $-C_4/R^4$, mentioned earlier. Apart from an additional phase factor $(-1)^{L-L'}$, the V_σ^{core} and V_π^{core} contributions to the $\text{Ne}^{**}\text{-He}$ interaction matrix in the $|\text{LSJM}_J\rangle$ representation can be calculated in the same way as the V_σ and V_π valence electron contributions, i.e. by using the formalism of irreducible tensor operators. The potentials resulting from this approach are shown in Fig. 4 (for $R < 4.5 a_0$), together with the original potentials of Hennecart and Masnou-Seeuws (for $R \geq 4.5 a_0$). We observe that the general behavior of the various potentials is in agreement with our discussion of the different character of the σ and π states of the valence electron and the core hole.

In Fig. 5 we show some adiabatic potential curves $V_k^\Omega(R)$, of relevance to this paper. They were calculated from the potentials of Fig. 4. The states $\{\alpha\}_k$ with $k = 4,5,6,7$ that appear in Fig. 5, form a multiplet of special interest, on account of the presence of a number of unmistakable avoided crossings between their adiabatic potentials. It is important to note, that only at fairly small internuclear distances the Ω -splitting

$V_k^\Omega - V_k^{\Omega'}$ between the potential curves for a given $\{\alpha\}_k$ state grows large, compared to the rotational coupling strength. Therefore, at larger distances, there will be no "locking" of the electronic angular momentum J to the internuclear axis, i.e. no Ω -conservation.

3. Coupled-channels calculation

3.1. Coupled-channels theory

The stationary state $Ne^{**}He$ wave function $\psi(\underline{r}, \underline{R})$, where \underline{r} represents all electron coordinates and \underline{R} is the internuclear radius vector, satisfies the time-independent Schrödinger equation

$$H \psi(\underline{r}, \underline{R}) = E \psi(\underline{r}, \underline{R}) \quad (3)$$

with E the total energy in the center-of-mass system, and the Hamiltonian H being given by Eq. (2). Solutions to Eq. (3) must of course obey the usual asymptotic outgoing wave boundary conditions³⁰⁾.

In coupled-channels theory, $\psi(\underline{r}, \underline{R})$ is expanded in an orthonormal basis of channel functions $|\varphi_i\rangle$, characterized by the collective quantum number i , resulting in

$$\psi(\underline{r}, \underline{R}) = \sum_i \frac{F_i(R)}{R} |\varphi_i\rangle \quad (4)$$

From Eqs. (3) and (4), by bracketing with $\langle\varphi_i|$, a set of coupled second-order radial differential equations is obtained for the radial wave

functions of nuclear motion $F_i(R)$. For the basis set $\{|\varphi_i\rangle\}$ we choose diabatic basis functions that are eigenfunctions of the atomic part $H^{Ne^{**}+He}$ of the Hamiltonian H of Eq. (2).

The coupled equations are then given by

$$\frac{d^2 F_i(R)}{dR^2} + \frac{2\mu}{\hbar^2} \{E - E^{Ne^{**}} - E^{He}\} F_i(R) = \sum_j \frac{2\mu}{\hbar^2} \{ \langle \varphi_i | V^{Ne^{**}-He}(R) | \varphi_j \rangle + \langle \varphi_i | T_{rot} | \varphi_j \rangle \} F_j(R) \quad (5)$$

The operator T_{rot} provides rotational coupling; "physical" coupling occurs by the interaction $V^{Ne^{**}-He}$. This is in contrast to the adiabatic approach of Hennecart and Masnou-Seeuws, where coupling is caused by the operators T_{rad} and T_{rot} .

The adiabatic and diabatic approaches of course yield equivalent results for equivalent basis sets. Generally speaking, however, where coupling is limited to a few (quasi)molecular states, a fair description is possible with a smaller number of adiabatic states than diabatic states. Where this is not so, no preference exists for either basis in terms of the number of coupled equations to be solved. However, in terms of numerical stability, the adiabatic approach has the disadvantage of involving the calculation of the radial coupling matrix elements by numerical differentiation. This is especially troublesome near so-called avoided crossings of adiabatic potentials. In addition, a diabatic basis set obviates the need for the calculation of adiabatic eigenfunctions.

3.2. Ω -diabatic basis

We will now discuss our diabatic basis set, as well as its implementation in our coupled-channels code. Asymptotically, an obvious choice of electronic basis functions is that of atomic eigenfunctions $|\alpha JM_{J_z}\rangle^{\text{Ne}^{**}} |^1S_0\rangle^{\text{He}} \equiv |\alpha JM_{J_z}\rangle$, with the magnetic quantum number M_{J_z} taken with respect to the space-fixed z-axis (i.e. the asymptotic relative velocity). These may be coupled with the space-fixed eigenfunctions $|NM_N\rangle$ of the rotational energy operator $T_{\text{rot}} = \frac{N^2}{2\mu R^2}$, to form N -diabatic basis functions with total angular momentum quantum number P and well-defined parity $\pi = (-1)^N$:

$$|\varphi_i\rangle^N = |\pi\alpha JNPM_P\rangle$$

For smaller values of the internuclear distance R , a *body-fixed* coordinate system, with the z' -axis along the internuclear axis, is more appropriate ($V^{\text{Ne}^{**}\text{-He}}$ being known in the $|\alpha J\Omega\rangle$ representation). We repeat that the quantum number N is not compatible with M_{J_z} , essentially because a rotation of the internuclear axis implies a change of the quantization axis for M_{J_z} . We therefore go to a new basis of common eigenfunctions $|PM_P M_{J_z'}\rangle$ of the \underline{P}^2 , P_z and $P_{z'} = J_z$, operators, coupled with atomic eigenfunctions $|\alpha JM_{J_z'}\rangle$. This gives basis states $|\alpha JM_{J_z'} PM_P\rangle$. To also provide for definite parity, we subsequently combine opposite $M_{J_z'}$ to form Ω -diabatic basis functions, where $\Omega \equiv |M_{J_z'}|$:

$$|\varphi_i\rangle^\Omega = |\pi\alpha J\Omega PM_P\rangle$$

Our coupled-channels calculations are performed in the Ω -basis. Leaving out the superscript Ω for simplicity, the coupled equations of Eq. (5) are in this representation

$$\frac{d^2 F_i(R)}{dR^2} + \left\{ k_i^2 - \frac{P(P+1) + J(J+1) - 2\Omega^2}{R^2} \right\} F_i(R) = \sum_j \frac{2\mu}{\hbar^2} \left\{ \langle \varphi_i | V^{\text{Ne}^{***}\text{-He}}(R) | \varphi_j \rangle - \frac{1}{2\mu R^2} \langle \varphi_i | P_+ J_- + P_- J_+ | \varphi_j \rangle \right\} F_j(R) \quad (6)$$

with $|\varphi_i\rangle \equiv |\pi\alpha J\Omega P M_p\rangle$ the channel functions used, k_i the asymptotic wave number (given by $k_i^2 = 2\mu/\hbar^2 \{E - E_i^{\text{Ne}^{***}\text{-He}}\}$), and $P_{\pm} = P_x \pm iP_y$, and $J_{\pm} = J_x \pm iJ_y$, the body-fixed ladder operators for the total and electronic angular momenta. The differential equations of Eq. (6) are uncoupled with respect to P and parity π . For the 10 states $|\alpha_k J_k\rangle$ of the Ne^{***} -multiplet (with $k = 1, \dots, 10$) it follows directly from $\Omega = 0, \dots, J$ that we have 23 basis function $|\varphi_i\rangle$. In the region where the non-diagonal elements of the physical coupling matrix become zero, i.e. $V^{\text{Ne}^{***}\text{-He}} = 0$ for $i \neq j$, it is profitable to switch to the N -representation, with basis functions $|\pi\alpha J N P M_p\rangle$, so that the rotational coupling matrix elements also vanish. In this basis the equations of Eq. (5) become completely uncoupled, and we have the usual radial equations for elastic scattering off a spherical long range potential, namely the diagonal elements of the $V^{\text{Ne}^{***}\text{-He}}$ matrix. When these too disappear, the radial equations yield the analytical solutions of spherical Hankel-functions of the first and second kind. They make the matching to the asymptotic boundary condition a simple matter.

An interesting aspect of our description of the scattering of Ne^{***} by ground state He is its analogy to the scattering of particles from an axially symmetric rigid rotor³¹). Coupling of the particle angular momentum

with the angular momentum of the rotor to a total angular momentum leads to a coupling of particle and rotor motion, in the same way that the coupling of \underline{J} and \underline{N} to \underline{P} results in the coupling of electron and nuclear motion in the $\text{Ne}^{***}\text{-He}$ case.

In the actual coupled-channels program, the calculation of S-matrix elements proceeds in several stages. Firstly, for a total number of M channels $|\varphi_j\rangle = |\pi\alpha J\Omega P M_p\rangle$ in the Ω -diabatic representation, we have M linearly independent "mathematical" solution vectors $\underline{F}_i(R)$, which vanish at the origin. In practice, these are obtained by starting up \underline{F}_i in channel i at a radius R_0 , ideally in the classically forbidden region (hard wall at R_0). The coupled differential equations are numerically integrated with a modified Numerov method³²⁾ to a point R_1 , where the physical coupling has disappeared: $V_{ij}^{\text{Ne}^{***}\text{-He}} = 0$ ($i \neq j$) for $R \geq R_1 - \Delta R$. The Ω -diabatic solutions at R_1 and $R_1 - \Delta R$ are transformed to the N -diabatic $|\varphi_i\rangle \equiv |\pi\alpha J N P M_p\rangle$ representation. From there on the components of each vector behave independently, as described by the decoupled equations in the N -representation. Rather than integrating the latter outward to the asymptotic matching radius R_2 , where $V^{\text{Ne}^{***}\text{-He}} = 0$, we adopt the more stable procedure of integrating inward from R_2 starting with spherical Bessel- and Neumann-like functions. This allows us to express each component of \underline{F}_i as a linear combination of basis solutions $I_i(R)$ and $O_i(R)$ with ingoing and outgoing spherical wave behavior at infinity, respectively. The M mathematical solution vectors \underline{F}_i are finally combined linearly to construct M "physical" solution vectors \underline{f}_i , such that

$$(\underline{f}_i)_j = I_j(R) - S_{ji} O_j(R) \quad (7)$$

The open-channel matrix of "reflection" coefficients is the desired S-matrix.

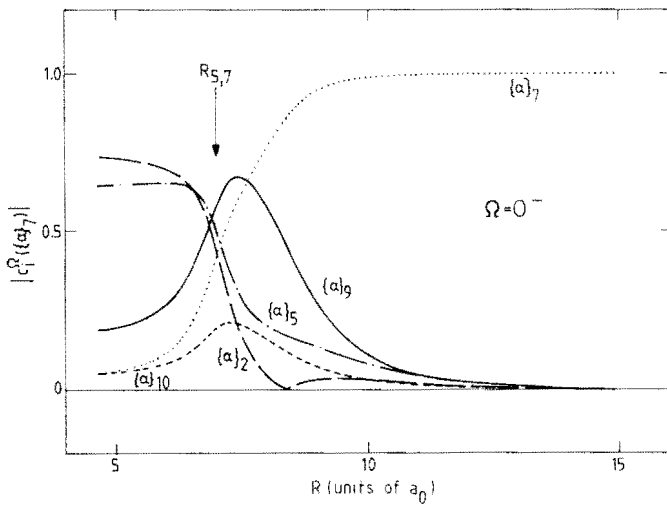


Fig. 6. Coefficients $|C_i^\Omega|$ of the $\{a\}_i$ components of the adiabatic $\text{Ne}^{**}\text{-He}$ eigenstate $|\{a\}_7, \Omega = 0^-\rangle$, as a function of the internuclear distance R . The position $R_{5,7}$ of the avoided crossing between the $V_5^{\Omega=0}$ and $V_7^{\Omega=0}$ adiabatic potentials coincides with a significant change in character of the adiabatic eigenstate.

3.3. Program performance

In any coupled channels calculation a choice has to be made concerning starting point, stepsize and basis set. Bernstein gives an exposé on this subject³⁰⁾. As to the starting point, the model potentials of Hennecart and Masnou-Seeuws discussed earlier are given for $R \geq 4.5 a_0$ only. The posting of a hard wall at $R = 4.5 a_0$ is the obvious answer to this problem. This has been done, even though from Fig. 5 it is clear that $R = 4.5 a_0$ is not yet inside the classically forbidden region. However, for the transitions of interest (mainly those within the $\{\alpha\}_{4,5,6,7}$ group), it has been verified by varying the starting point that the solutions are quite insensitive to this. Calculations with our extended potentials, made for the explicit purpose of evaluating the importance of the inner potential regions, confirm this. As will be seen, relevant cross sections differ by at most 25 % from the hard-wall results. In this connection, it is worth noting that especially for small R-values a problem arises. Without specific precautions, part of the S-matrix elements obtained would be highly unreliable, due to the tendency to linear dependence of solution vectors within the numerical noise level which builds up as a function of R. To avoid this, we form M new suitable linear combinations of mathematical solution vectors at one or more values of R³³⁾.

The stepsize, which is of course related to the wavelength λ for the lowest significant $\{\alpha\}_k$ state, was arrived at empirically by evaluating cross section precision and S-matrix symmetry for a limited number of P-values. A stepsize $\Delta R = 0.02 a_0$ was chosen.

The Ne^{**}-He system comprises $\sum_{i=1}^{10} (J_i+1) = 23$ molecular states $|\alpha J \Omega\rangle$. If all 10 fine-structure levels in the Ne^{**} $(\{\alpha\}_i; J_i)$ multiplet are included, we have a maximum of 18 coupled equations for each value of total angular

momentum P and parity $\pi = \pm 1$. Energy distance to the states of interest being no reliable criterion for the omission of basis states³⁰⁾, we have expanded every molecular state $|\alpha J \Omega(R)\rangle$ in its atomic component states $|\alpha J\rangle$. An example of this is given in Fig. 6. The relative un-importance of the $\{\alpha\}_1$ and $\{\alpha\}_3$ components of the $\{\alpha\}_{4,5,6,7}$ molecular states might lead one to drop these from the calculation. Since these are $J = 0$ states, only two Ω -diabatic basis states are saved, which is hardly worthwhile.

The question of the number of P -values to be included in the calculation is more straightforward. We can limit the calculation to those values of P corresponding to impact parameters $b \simeq P\lambda \leq 15 a_0$ (where $v^{\text{Ne}^{**}\text{-He}} \simeq 0$), with λ the de Broglie wave length in the incoming channel. For an energy $E = 100$ meV this amounts to $P \leq 100$. A complete coupled channels calculation with appropriate integration stepsize $\Delta R = 0.02 a_0$ then requires about 2 hours on a Burroughs B7900 mainframe computer.

3.4. Polarized cross sections

Solving the coupled-channels equations yields the S -matrix elements, which in the N -representation are defined as

$$S_{lk} \equiv \langle \pi \alpha_l J_l N_l P M_P | S | \pi \alpha_k J_k N_k P M_P \rangle.$$

A representative S -matrix element is displayed in Fig. 7. In general, we have $S(P) = |S(P)| \exp \{i\varphi[S(P)]\}$. Here, the phase $\varphi(S)$ has been plotted as a continuous function of the total angular momentum quantum number P , rather than being limited to $-\pi \leq \varphi(S) \leq +\pi$. We note that "zero points" of the norm $|S|$ of an S -matrix element correspond to π -jumps of the phase $\varphi(S)$. A passage of $S(P)$, between P and $P+1$, almost through the origin of the complex plane into the opposing quadrant implies a phase change $\Delta\varphi(S) = +\pi$ or $-\pi$.

The single- M_k state polarised cross section $Q_{l \leftarrow k}^{M_k}$ for the $|\alpha_k J_k M_k\rangle \rightarrow |\alpha_l J_l\rangle$ transition is given by

$$Q_{l \leftarrow k}^{M_k} = \frac{\pi}{k_k^2} \sum_P (2P+1) q_{l \leftarrow k}^{M_k}(P)$$

$$q_{l \leftarrow k}^{M_k}(P) = \sum_{N_l} \sum_{N_k} \sum_{N_k'} i^{(N_k - N_k')} \quad (8)$$

$$\times (J_k M_k P - M_P | N_k 0) (J_k M_k P - M_P | N_k' 0)$$

$$\times \{S_{lk} - \delta_{\alpha_l \alpha_k} \delta_{N_l N_k}\} \{S_{lk'} - \delta_{\alpha_l \alpha_k} \delta_{N_l N_k'}\}^*$$

with $q_{l \leftarrow k}^{M_k}(P)$ the transition probability for a certain P -value. From $P = J+N$, it follows directly that the summation over N -values is between $|P-J|$ and $P+J$. Of course, this is implied by the Clebsch-Gordan coefficients $(J_k M_k P - M_k | N_k 0)$ and $(J_k M_k P - M_k | N_k' 0)$. Also, $M_P \equiv M_k$. Because of the conjugation $*$ in Eq. (8), both phase and absolute value of the complex S -matrix elements are of importance for the polarised cross sections. This is contrary to the unpolarized case, where summation over all orientations $|M_k|$ of the initial state yields

$$Q_{l \leftarrow k} = \frac{\pi}{k_k^2} \sum_P (2P+1) q_{l \leftarrow k}(P)$$

$$q_{l \leftarrow k}(P) = \frac{1}{2J_k+1} \sum_{M_k=-J_k}^{J_k} q_{l \leftarrow k}^{M_k}(P)$$

$$= \sum_{N_l} \sum_{N_k} (2P+1) |S_{lk} - \delta_{\alpha_l \alpha_k} \delta_{N_l N_k}|^2 \quad (9)$$

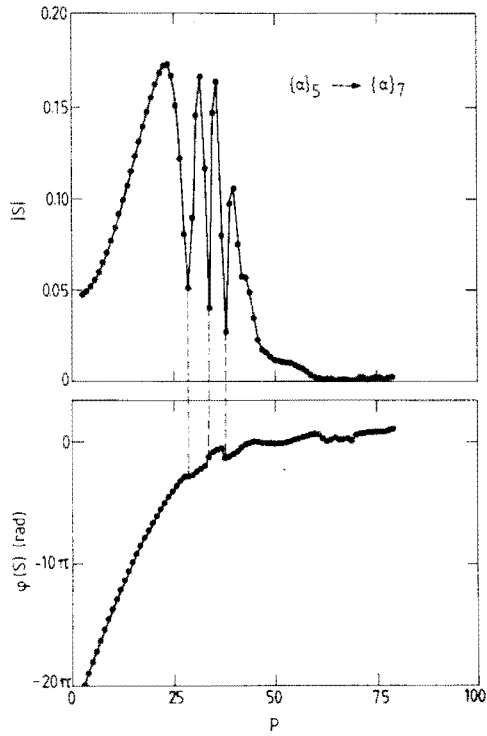


Fig. 7. Absolute value $|S(P)|$ and phase $\varphi[S(P)]$ of an S-matrix element for the $\{a\}_5 \rightarrow \{a\}_7$ transition, over the full range of total angular momentum quantum numbers P [calculation I(a) of Table III]. The phase has been plotted as a continuous function. The dotted lines connect the "zeros" of $|S|$ with the " π -jumps" in $\varphi(S)$.

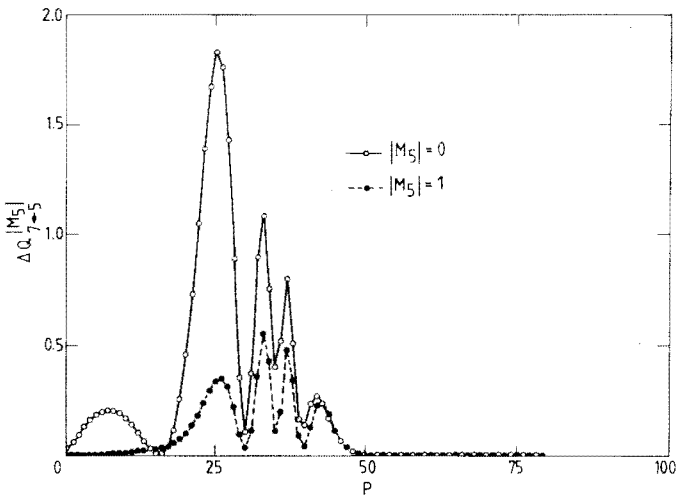


Fig. 8. Contributions $\Delta Q_{7 \leftarrow 5}^{M_5}$ to the pure-state polarised cross section $Q_{7 \leftarrow 5}^{M_5}$ for the $\{a\}_5 \rightarrow \{a\}_7$ transition (calculation Ia of Table II).

It is for this reason, that polarisation experiments are ultimately more informative. In Fig. 8 we show the inelastic $\{\alpha\}_5 \rightarrow \{\alpha\}_7$ cross section contribution per P-value, $\Delta Q_{7 \leftarrow 5}^{|M_5|}$ (P), for $|M_5| = 0$ and $|M_5| = 1$. The asymptotic orientation of the Ne^{***}-atom is seen to have great influence.

In their two-channel coupled-channels calculations, performed in an adiabatic basis as opposed to our diabatic basis, Hennecart^{1,11)} and Masnou-Seeuws¹⁾ do not take into account the rotational coupling (nor the diagonal $(J(J+1)-\Omega^2)/R^2$ term of the coupling matrix in the Ω -diabatic basis). This prototypical Ω -conserving approach is equivalent to "locking" the electronic angular momentum \underline{J} to the body-fixed internuclear axis. However, we observe a tendency of \underline{J} to remain space-fixed down to intermediate R-values. Furthermore, of course, in this way it becomes impossible to explain transitions like the $\{\alpha\}_3 \rightarrow \{\alpha\}_5$ transition¹¹⁾.

In an effort to quantify the differences between the two approaches, we have juxtaposed some results for both types of calculation in Table I. Comparing our calculation at $E_6 = 100$ meV (all-states, all-couplings, hard-wall) with the calculations of Hennecart and Masnou-Seeuws for the $\{\alpha\}_3 \rightarrow \{\alpha\}_4$ and $\{\alpha\}_4 \rightarrow \{\alpha\}_5$ transitions at the appropriate energies, we find fair agreement. We note that $Q_{4 \leftarrow 3}^{\text{ours}} > Q_{4 \leftarrow 3}^{\text{theirs}}$, while for the other transition the situation is reversed: $Q_{5 \leftarrow 4}^{\text{ours}} < Q_{5 \leftarrow 4}^{\text{theirs}}$. To determine to what extent this must be attributed to the presence or absence of rotational coupling, or to the implicit difference in basis sets, an additional full coupled-channels calculation would be required. We have limited ourselves to less extensive calculations with a basis set consisting of $\{\alpha\}_3$, $\{\alpha\}_4$, $\{\alpha\}_5$, $\{\alpha\}_6$ and $\{\alpha\}_7$ only. With this basis set and leaving out rotational coupling, the results of Hennecart and Masnou-Seeuws for the $\{\alpha\}_3 \rightarrow \{\alpha\}_4$ transition are reproduced quite well. This is true over the energy range $0 < E < 250$ meV. The same cannot be said for the $\{\alpha\}_4 \rightarrow \{\alpha\}_5$ transition. Even the much larger cross section value, obtained with rotational coupling, is somewhat

Table I. Rudimentary comparison between the calculations of the present work and those of Hennecart and Masnou-Seeuws, illustrating the large influence of rotational coupling on cross section values.

| Reference | Input _a | E_k (meV) | | Q_{l+k} (\AA^2) | |
|---|---|----------------|----------------|---|---|
| | | $\{\alpha\}_3$ | $\{\alpha\}_4$ | $\{\alpha\}_3 \rightarrow \{\alpha\}_4$ | $\{\alpha\}_4 \rightarrow \{\alpha\}_5$ |
| Hennecart and Masnou-Seeuws _b this work _c | two adiabatic states, no rotational coupling | 25 | 32 | 28 | 8.7 |
| | all states all couplings | 25 | 32 | 41 | 5.3 |
| Hennecart and Masnou-Seeuws _b this work this work | two adiabatic states, no rotational coupling | 25 | 32 | 28 | 8.7 |
| | $\{\alpha\}_{3,4,5,6,7}$ only no rotational coupling | 25 | 32 | 35 | 0.5 |
| | $\{\alpha\}_{3,4,5,6,7}$ only, all couplings | 25 | 32 | 51 | 4.2 |

- a) All calculations with hard wall at $R = 4.5 a_0$.
 b) Interpolated values ¹¹⁾.
 c) Calculation II(a).

too small. Rotational coupling causes the $\{\alpha\}_3 \rightarrow \{\alpha\}_4$ transition to be larger as well, but to a lesser degree. Whereas, of course, the material at hand is too slight to warrant a general conclusion, the above is at least indicative of the importance of rotational coupling. A similar remark can be made concerning the difference in results obtained from our calculations with full and truncated basis sets.

4. Experimental setup

4.1. Design

The design of a crossed-beam experiment for the investigation of inelastic collision processes with short-lived, electronically excited atoms has to be considered very carefully. The more so, when the reaction products can only be detected through their radiative decay. We assume a configuration of primary beam, secondary beam and laser beam crossing at right angles. The major experimental problems encountered follow directly from the expressions for the count rates I_k for the direct fluorescence from the initial state $\{\alpha\}_k$, without a secondary beam, and I_l for the collision-induced fluorescence from the final state $\{\alpha\}_l$, respectively. These are given by

$$I_k = \eta_k \dot{N}_k R_k \tag{10a}$$

$$I_l = \eta_l \dot{N}_k R_k \frac{g}{v_1} n_2 l_T Q_{l \leftarrow k} \tag{10b}$$

with η_k and η_l the photon detection efficiency for the direct and collision induced fluorescence, \dot{N}_k (s^{-1}) the flow of initial state particles through

the scattering volume, v_1 the primary beam velocity, g the relative velocity of the collision partners, n_2 the secondary beam density, $l_\tau = v_1 \tau_k = v_1 / A_k$ the lifepath of the initial state particles, and $Q_{l \leftarrow k}$ the total inelastic cross section for the $\{\alpha\}_k \rightarrow \{\alpha\}_l$ transition. Through the factor $R_k \simeq 1/(1-A_{ki}/A_k)$ we take into account, that a fraction A_{ki}/A_k of the atoms in the initial short-lived $\{\alpha\}_k$ state is recycled via the metastable $\text{Ne}^*(^3P_J)$ lower level of the optical pumping transition. With appropriate laser power, almost all of the $\text{Ne}^*(^3P_J)$ atoms in the primary beam are excited to the $\{\alpha\}_k$ state, resulting in $\dot{N}_k = C_J \dot{N}_{\text{Ne}^*(J)}$, with C_J the relative population of the metastable state used for the $\text{Ne}^{**}\{\alpha\}_k$ production. In Eq. (10b) for the collision-induced fluorescence signal we recognize the usual "nlQ" product of a crossed beam experiment, modified by the use of the lifepath l_τ instead of the length of the scattering volume.

From Eq. (10) we can deduce the practical problems which our particular experiment presents. Both the lifepath l_τ of the short-lived atoms, and the transition cross section $Q_{l \leftarrow k}$ are very small: $l_\tau \simeq 20 \mu\text{m}$; $Q_{l \leftarrow k} \simeq 1\text{\AA}^2$. This means, that it takes considerable effort to obtain a measurable collision-induced fluorescence signal, i.e. a signal that can be separated from the inevitable background. Firstly, we must maximize primary beam flow \dot{N}_{Ne^*} and secondary beam density n_2 . Secondly, extremely efficient detection of fluorescence photons is needed, that is to say, high values of the optical detection efficiency η_l . As to background radiation, from Eqs. (10a) and (10b) it follows, that at all times the direct fluorescence radiation \dot{N}_k will be several orders of magnitude larger than the inelastic fluorescence \dot{N}_l . This calls for almost complete suppression of \dot{N}_k . Of course, the same goes for other sources of background radiation.

The above experimental requirements have led us to design a novel crossed-beam apparatus, of which a schematic view is given in Fig. 9. The primary beam of metastable Ne^* -atoms originates in a discharge excited

supersonic expansion, or thermal metastable source (TMS)³⁴). The differentially-pumped source chamber is connected to the main vacuum chamber by a 0.5 mm ϕ skimmer. The maximum centerline $\text{Ne}^*(^3P_2)$ intensity for the TMS, operated with pure neon, is about $j_{i,0} \approx 10^{14} \text{ s}^{-1} \text{ sr}^{-1}$; the $^3P_2: ^3P_0$ ratio is roughly 5:1. Downstream of the skimmer, all charged particles are removed by condenser plates. A high density of metastable Ne^* atoms in the collision region is obtained by virtue of the small distance to the TMS. The collision region being situated about 90 mm downstream of the TMS, we have a primary beam density $n_{\text{Ne}^*} \approx 10^{13} \text{ m}^{-3}$. Metastable particle flow \dot{N}_{Ne^*} through the collision region is determined by the 1 mm ϕ primary beam defining diaphragm at 60 mm from the skimmer. This geometry results in $\dot{N}_{\text{Ne}^*} \approx 2 \cdot 10^{10} \text{ s}^{-1}$.

The primary beam of metastable Ne^* atoms is crossed at right angles by the laser beam from a cw single mode dye laser system. The laser frequency is stabilised to within 0.5 MHz rms deviation of the transition frequency ν_{ik} ³⁵). Laser power ($P \leq 0.2 \text{ mW}$ in the collision region) is controlled and stabilised with an electro-optical modulator. The laser beam has a waist in the collision region ($1/e^2$ radius, $W = 0.5 \text{ mm}$). Because of the short lifetimes of the $\text{Ne}^{**} \{ \alpha \}_k$ atoms, produced in the optical pumping process, it is the laser beam that determines the lateral position of the collision region. The secondary beam has to pass through the crossing point of the laser and primary beams.

A skimmerless supersonic expansion (nozzle diameter $2R_n = 50 \mu\text{m}$) forms the secondary beam. This allows a very small distance from the nozzle to the collision region, and a correspondingly high secondary beam density. In our apparatus the distance may be adjusted from 0-12 mm, but is typically 2 mm. In that case, for noble gas atoms, the secondary beam density is given by supersonic expansion theory³⁶) as $n_2 \approx 3 \cdot 10^{20} \text{ m}^{-3}$, at reservoir pressure $P_{2,0} = 120 \text{ Torr}$ and temperature $T_{2,0} = 300 \text{ K}$. In summary, we have fulfilled

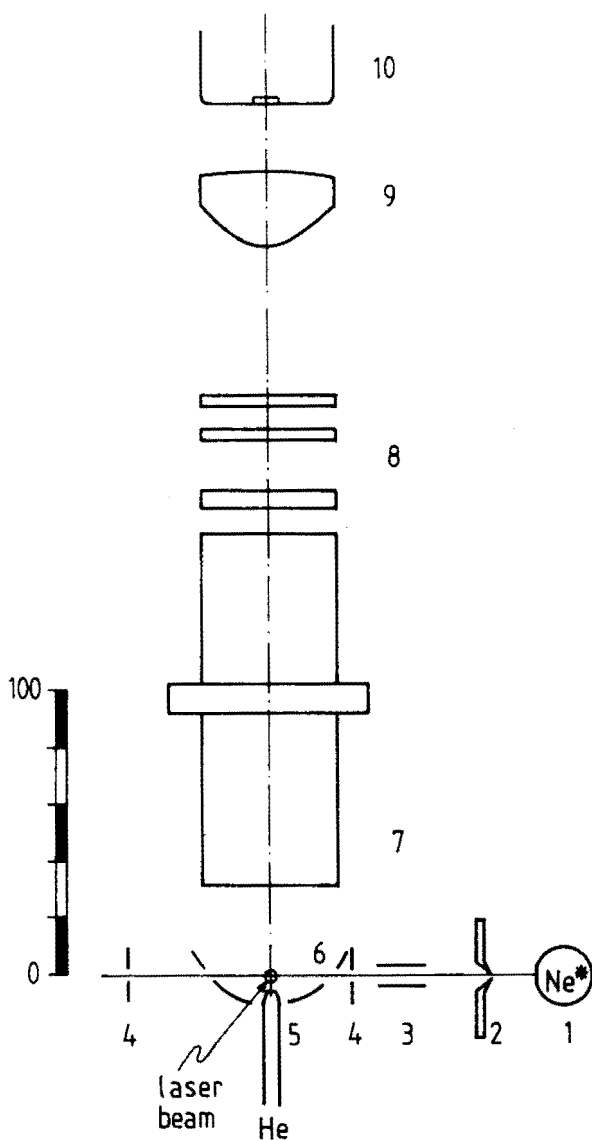


Fig. 9. Schematic view of the experimental set-up. The scale is in mm.

(1) Primary-beam source; (2) skimmer; (3) condenser plates; (4) primary-beam diaphragms; (5) secondary-beam nozzle; (6) parabolic mirror; (7) plexiglass light-guide; (8) interference and cutoff filters; (9) lens; (10) photomultiplier.

the first experimental requirement of high primary and secondary beam densities by situating both primary and secondary beam sources as close to the collision region as possible.

The demands made on the optical detection system, i.e. a large detection efficiency η and effective suppression of the direct fluorescence radiation, have been met by employing narrow-band interference filters for wavelength selection (2 nm FWHM, 10 nm FW at 10^{-6} transmission). With these we may monitor a single line of either the collision-induced fluorescence from the final state $\{a\}_l$, or the direct fluorescence from the initial state $\{a\}_k$. More in particular, as the interference filters require perpendicular incidence, the collision region is situated near the focal point of a parabolic mirror. Thus a substantial portion of the fluorescence radiation is imaged into a (nearly) parallel beam. Solid angle efficiency of the parabolic mirror is approximately 0.40, i.e. a solid angle of 1.6π is collected. The condition of (nearly) perpendicular incidence on the interference filters poses no serious limitation on the acceptance of the optical system. The optical phase volume of the parabolic mirror - interference filter combination is very much larger than may be attained with a monochromator. Additional suppression of background light is achieved by the use of colored glass cutoff filters. After passing through the filters, the photons are focussed onto the 9 mm ϕ cathode of an S20 photomultiplier in a cooled housing. Quantum efficiency of the photomultiplier is a low 3-5%, depending on the wavelength. When measuring direct fluorescence radiation, neutral density filters are added to the optical system in order to guarantee a linear response of the photomultiplier. In the present configuration the overall detection efficiency of the optical system is typically $\eta = 10^{-3}$ per photon ($\lambda=650$ nm) produced in the collision region. The overall figure of merit in the thermal energy

is about $1 \text{ kHz}/\text{\AA}^2$, for the number of counts per unit of inelastic total cross section. The background count rate ranges from 2 to 15 kHz and is due mainly to the line-emission from the discharge in the TMS.

4.2. Performance

Of the several noteworthy features of this experiment we here note only two, both related to the use of a free-jet expansion for our secondary beam. Firstly, before the primary beam ever reaches the scattering center, it is attenuated up to 70% by secondary beam particles, both in the expansion itself and in the form of residual gas. This results in a transmission factor T_k , depending upon the position x along the primary beam axis, that is given by

$$T_k(x) = \dot{N}_k(x) / \dot{N}_k(-\infty) = \exp\left(-\int_{-\infty}^x \frac{g(x')}{v_1} n_2(x') Q dx'\right) \quad (11)$$

Here Q is the effective total cross section for elastic scattering of Ne^* -atoms by He-atoms. Of course, this factor enters into both signals I_l and I_k for collision-induced and direct fluorescence, respectively. For the ratio of these two signals we have, in more specific terms than offered by Eq.(10):

$$\frac{I_l}{I_k} = \frac{\int_V \eta_l(\underline{r}) n_k(\underline{r}) n_2(\underline{r}) g(\underline{r}) Q_{l \leftarrow k}(g) d\underline{r}}{A_k \int_V \eta_k(\underline{r}) n_k(\underline{r}) d\underline{r}} \quad (12)$$

the integral being taken over the scattering volume V . To first order, and in keeping with Eq. (10), this reduces to

$$\frac{I_l}{I_k} \approx \frac{\eta_l}{\eta_k} \frac{g}{v_1} n_2 l_\tau Q_{l \leftarrow k} \quad (13)$$

The small size of the scattering region, as determined by the density profile $n_k(\underline{r})$ of the short-lived $\{\alpha\}_k$ atoms, ensures that Eq. (13) is indeed a fair approximation of Eq. (12).

Since we are concerned only with the ratio I_l/I_k , neither the potentially troublesome attenuation phenomenon nor a number of other unknown *common* factors preclude the possibility of obtaining absolute cross section values. This is illustrated by Figs. 10 and 11. Figure 10 shows T_k , measured by looking at the direct fluorescence signal I_k as a function of secondary beam reservoir pressure p_{He} . Agreement with Eq. (11) is very good. By inserting into Eq. (11) the secondary-beam density profile, we find from these and other measurements that $Q \approx 100 \text{ \AA}^2$, which is a reasonable value for hard-sphere scattering. In Fig. 11 we have plotted the ratio I_l/I_k of collision-induced and direct fluorescence signals, as a function of the pressure p_{He} . The linear dependence of $I_l/I_k \sim n_2 l_\tau Q_{l \leftarrow k}$ on p_{He} , in contrast to the behaviour of T_k , provides convincing evidence of the soundness of the principles embodied in our experiment.

As a second characteristic of our present setup, the scattering center position is ultimately determined by laser beam alignment. Since secondary-beam density, among others, does not factor out from the ratio of fluorescence signals, this alignment takes on a critical importance, as evidenced by Fig. 12 of the ratio I_l/I_k versus laser beam position along the primary-beam axis.

Given the position of the scattering center, either Eq. (12) or Eq. (13) can be used to obtain absolute cross section values. Of the quantities in these equations, the secondary-beam density n_2 is directly related to the source density n_{He} through the shape of the radially

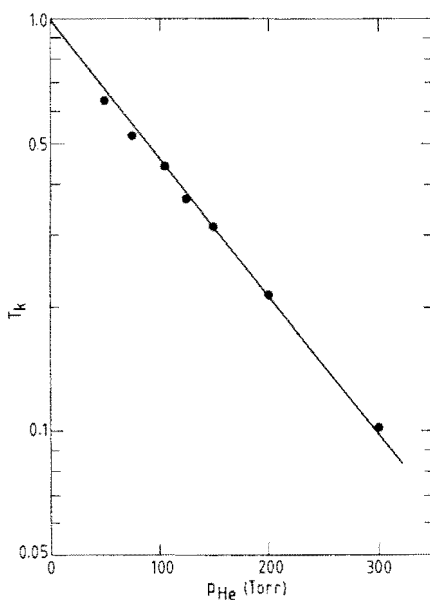


Fig. 10. The primary-beam transmission factor T_k as a function of secondary-beam reservoir-pressure p_{He} . The observed exponential attenuation is conform Eq. (11), with a cross section $Q \approx 100 \text{ \AA}^2$ for $Ne^*(^3P_0)$ -He collisions.

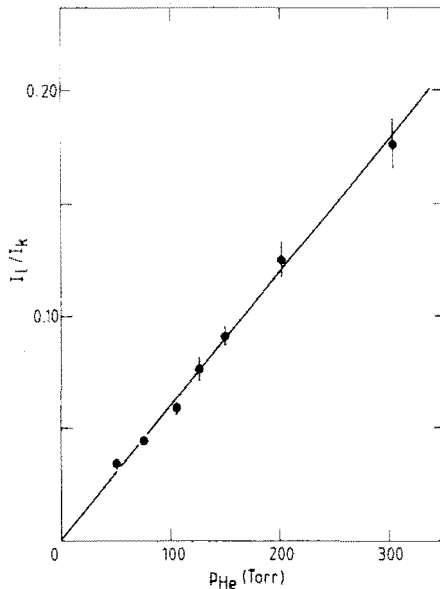


Fig. 11. Collision-induced to direct fluorescence ratio I_l/I_k as a function of secondary-beam reservoir-pressure p_{He} . As expected from Eq. (12), the ratio I_l/I_k does not depend on the primary-beam transmission factor T_k , but is proportional to $n_2 \sim p_{He}$.

expanding flow field. For mono-atomic gases, with the nozzle shape used in our setup, experiments and theory are in good agreement³⁶⁾. The position dependence of the detection efficiency η was calculated, following a separate calibration of the optical system's various components. To our advantage, only the ratio η_l/η_k is of importance. Under the simplifying assumption of mono-energetic particle beams, the position dependence of the relative velocity g is purely a matter of geometry. For use in Eq. (13), model calculations for the optical pumping process yield the distribution n_k of the short-lived atoms over the scattering volume. We find that cross sections, calculated with Eq. (13), differ by typically 20 % from those following from Eq. (12).

4.3. Measuring routine

Our aim is to determine the collision-induced and direct fluorescence signals I_l and I_k , as defined in Eq. (12). Ideally, this would involve two measurements only, with different optics (interference filters). In practice, however, we will have to correct for background light which cannot be entirely suppressed by the optical system.

In order to correct for background contributions, two further diagnostics are employed in addition to the use of different *filters* for direct and collision-induced fluorescence. The first of these is modulation of the optical pumping process by which the initial $Ne^{**}\{\alpha\}_k$ atoms are produced. Rather than simply turning the laser "on" and "off", which allows for no easy correction for stray laser light, the laser is tuned and detuned sufficiently (about 100 MHz) to preclude excitation of the metastable $Ne^*(^3P_J)$ atoms. The slight accompanying wavelength change makes no difference to the optical system. The second additional diagnostic is modulation of the *secondary beam*, by simply turning it on and off. Of

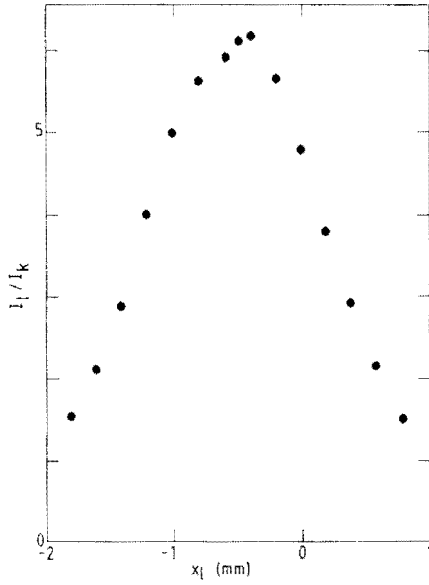


Fig. 12. Collision-induced to direct fluorescence ratio I_l/I_k as a function of laser-beam position x_l along the primary-beam axis. The result reflects mainly the secondary beam density profile.

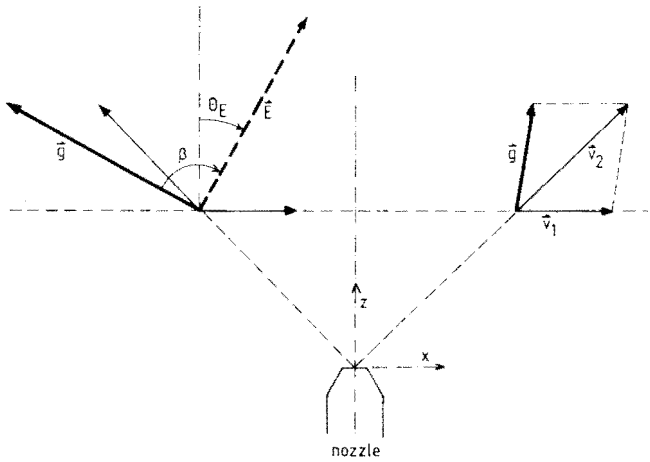


Fig. 13. Newton diagram of the collision process, with \underline{v}_1 and \underline{v}_2 the primary- and secondary-beam velocities. Upstream of the secondary-beam nozzle, the relative velocity \underline{g} is high; downstream, it is low. The angle β between the relative velocity \underline{g} and the laser electric field vector \underline{E} has been indicated.

course, this also influences the attenuation of the primary beam by secondary beam particles. By combining these three modulation techniques, which are all under computer control, we can easily design a strategy to eliminate all background contributions.

A paper, offering a more detailed description of the design of the apparatus and the execution of the measurements, is forthcoming³⁷⁾.

5. Experimental Results for Polarised Cross Sections

In our experiment, the short-lived $\text{Ne}^{**}\{\alpha\}_k$ atoms are prepared in a polarised state, consisting of an incoherent distribution over substates $|\alpha_k J_k m_k\rangle$ with respect to the excitation process quantisation axis. The associated probabilities are g_{m_k} . As a linearly polarised laser is used to excite the metastable Ne^* atoms, the natural excitation axis for the optical-pumping process is along the laser electric field \underline{E} . The quantisation axis for the collision process is the asymptotic relative velocity \underline{g} of the collision partners. For a given angle β between \underline{E} and \underline{g} , and suitable orientations of the remaining axes perpendicular to the quantisation axis, the initial state $|\alpha_k J_k m_k\rangle_{\underline{E}}$ can be written as

$$|\alpha_k J_k m_k\rangle_{\underline{E}} = \sum_{M_k} d_{m_k M_k}^{J_k}(\beta) |\alpha_k J_k M_k\rangle_{\underline{g}} \quad (14)$$

with d the usual rotation matrices or reduced Wigner D-functions³⁸⁾. The observed total cross section $Q_{l \leftarrow k}^{\beta}$ is now found to be an incoherent sum over the single M_k -state polarized cross sections $Q_{l \leftarrow k}^{|M_k|}$ of Eq. (7):

$$Q_{l \leftarrow k}^{\beta} = \sum_{m_k} g_{m_k} \sum_{M_k} \left\{ d_{m_k M_k}^{J_k}(\beta) \right\}^2 |M_k| \quad (15)$$

This incoherence with respect to M_k is essentially due to the fact that the final atomic polarization and direction of motion are not observed. The unpolarized cross section

$$Q_{l \leftarrow k} = \frac{1}{2J_k + 1} \sum_{M_k} |M_k| \quad (16)$$

is of course independent of the quantisation axis.

5.1. The $(\{a\}_5, J_5=1)$ initial state

We will first discuss a number of transitions which have in common the $\{a\}_5$ initial state, as produced from the $\text{Ne}^*(^3P_0)$ metastable state. For this $J_5 = 1$ state, distribution over the magnetic substates will be according to

$$\begin{cases} g_{m_k=0} & = 1 \\ g_{|m_k|=1} & = 0 \end{cases} \quad (17)$$

The cross section $Q_{l \leftarrow k}^{\beta}$ of Eq. (15) now becomes

$$Q_{l \leftarrow k}^{\beta} = \frac{1}{2} (Q_{l \leftarrow k}^{0|0|} + Q_{l \leftarrow k}^{1|1|}) + \frac{1}{2} (Q_{l \leftarrow k}^{0|0|} - Q_{l \leftarrow k}^{1|1|}) \cos 2\beta \quad (18)$$

where ultimately the polarized cross sections $Q_{l \leftarrow k}^{|M_k|}$ are of interest. As may be seen from Eq. (18), for $J_k = 1$, measurement of $Q_{l \leftarrow k}^{\beta=0}$ and $Q_{l \leftarrow k}^{\beta=\pi/2}$ suffices to determine $Q_{l \leftarrow k}^{0|0|}$ and $Q_{l \leftarrow k}^{1|1|}$. Both from the standpoint of detecting unfore-

seen physical effects and for the additional check it provides in the crucial matter of laser beam alignment, the coverage of a more extensive range of β -values is desirable.

In Fig. 13 we show the diagram of velocity vectors in the laboratory system. The relation between β and the laser polarisation angle θ_E depends on the scattering center position x_s , relative to the center-line of the secondary beam. Equation (18) can help us calibrate the zero of the x-scale. For a given position, the extrema of $Q_{l \leftarrow k}$ as a function of θ_E correspond to $\beta = 0$ and $\beta = \pi/2$, with only the identification of the extremum belonging to $\beta = 0$ left open. This problem can be solved unequivocally by measuring $Q_{l \leftarrow k}$ for some different positions x_s and primary beam velocities v_1 . Once this calibration has been performed, the x-scale is permanently coupled to the scale of the laser beam translator³⁹.

The experiments under discussion have been performed by pumping the $\{\alpha\}_5$ level through the $\text{Ne}^*(^3P_0) \rightarrow \{\alpha\}_5$ transition at $\lambda = 626.6$ nm. The $\{\alpha\}_4$, $\{\alpha\}_6$ and $\{\alpha\}_7$ states have been detected by observing the radiative decay at $\lambda = 667.8$ nm, 693.2 nm and 653.3 nm, respectively. In Figs. 14, 15 and 16 we show the experimental results $Q_{l \leftarrow k}^\beta$ for the $\{\alpha\}_5 \rightarrow \{\alpha\}_4$, $\{\alpha\}_6$ and $\{\alpha\}_7$ transitions, obtained by scanning the angle θ_E over the full range $-105^\circ \leq \theta_E \leq 105^\circ$.

Among the pictured transitions with $\{\alpha\}_5$ as an initial state, the whole gamut of possible polarisation effects is observed. At the present energy, we find that $Q_{4 \leftarrow 5}^{0|0} \simeq Q_{4 \leftarrow 5}^{0|1}$, $Q_{6 \leftarrow 5}^{0|0} < Q_{6 \leftarrow 5}^{0|1}$ and $Q_{7 \leftarrow 5}^{0|0} > Q_{7 \leftarrow 5}^{0|1}$. The polarisation effect in the $\{\alpha\}_5 \rightarrow \{\alpha\}_7$ transition is particularly pronounced. The $Q_{6 \leftarrow 5}^\beta$ and $Q_{7 \leftarrow 5}^\beta$ clearly conform to the $\cos 2\beta$ expression of Eq. (18). The somewhat deviating behavior of the $Q_{4 \leftarrow 5}^\beta$ cross section appears to be caused by the non-isotropic distribution of collision-induced fluorescence radiation, for which at present we do not correct and which takes on importance in the absence of a real polarisation effect. The shifted extrema at approximately

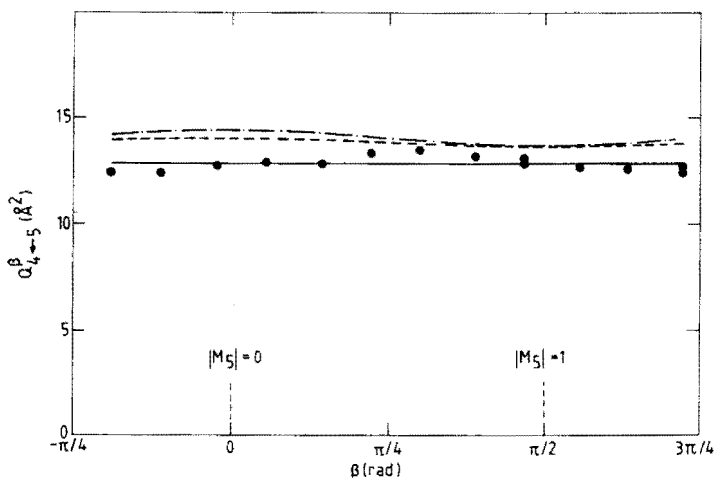


Fig. 14. Experimental results for the observed cross section Q_{4+5}^{β} as a function of the angle β between the electric field \underline{E} of the laser and the relative velocity \underline{g} , at a center-of-mass energy $E_6 = 100$ meV. The statistical errors are smaller than the size of the data points. The observed dependence on β reflects the non-isotropic distribution of collision-induced fluorescence radiation. The solid line (—) therefore indicates the average value of the data points and does not represent a curve fit according to Eq. (18). The other lines are the results of calculations with the model potentials of Hennecart and Masnou-Seeuws (---) and the extended potentials (-.-) of section 2.2 as input.

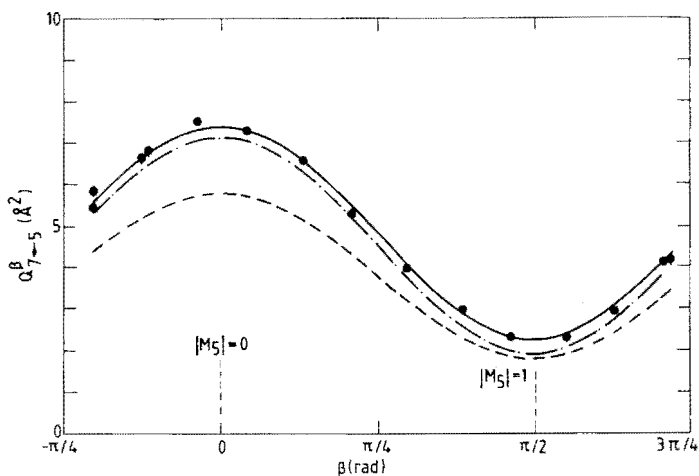


Fig. 16. Experimental results for the observed cross section Q_{7+5}^{β} . See caption of Fig. 15 for further detail.

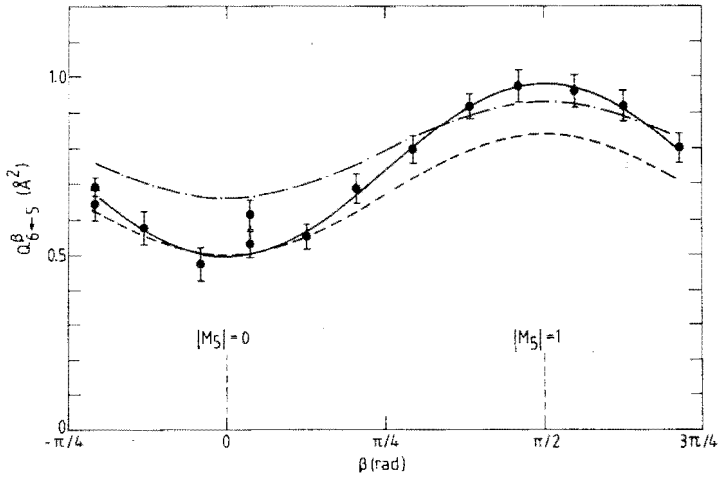


Fig. 15. Experimental results for the observed cross section $\sigma_{6 \leftarrow 5}^\beta$, as a function of the angle β between the electric field \underline{E} of the laser and the relative velocity \underline{g} , at a center-of-mass energy $E_S = 100$ meV. Statistical errors only have been indicated. The solid line (—) represents a curve fit of the data points according to Eq. (18). The other lines are the results of calculations with the model potentials of Hennecart and Masnou-Seeuws (---) and the extended potentials of section 2.2 (---) as input.

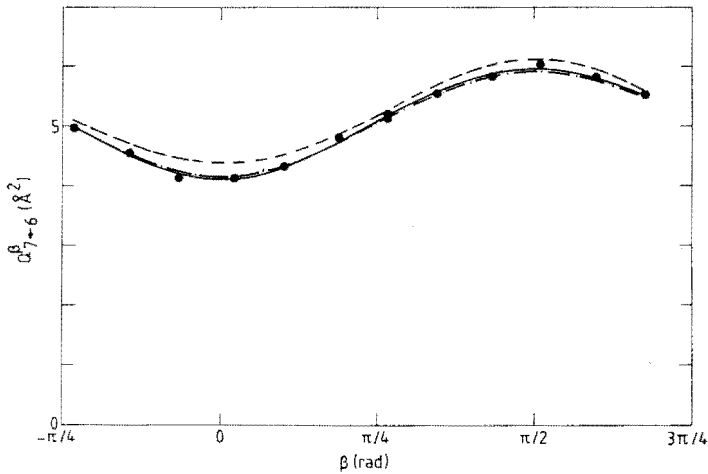


Fig. 17. Experimental results for the observed cross section $\sigma_{7 \leftarrow 6}^\beta$. Curve fit of data points (—) according to Eq. (19). See caption of Fig. 15 for further detail.

Table II. Observed and calculated polarized cross sections $Q_{l \leftarrow k}^{|\mathcal{M}_k|}$ at center-of-mass energy $E = 100$ meV. The potentials used in the calculations [I(a), I(b), II(a), and II(b)] are described in Table III.

| $\{\alpha\}_k \rightarrow \{\alpha\}_l$ | $ \mathcal{M}_k $ | $Q_{l \leftarrow k}^{ \mathcal{M}_k } (\text{\AA}^2)$ | |
|---|-------------------|---|---|
| | | experimental | calculated [I(a), I(b)] [II(a), II(b)] |
| $\{\alpha\}_5 \rightarrow \{\alpha\}_4$ | 0 | 13.2 | 14.0 14.4 |
| | 1 | 12.5 | 13.7 13.7 |
| $\{\alpha\}_5 \rightarrow \{\alpha\}_6$ | 0 | 0.50 | 0.50 0.66 |
| | 1 | 0.97 | 0.84 0.93 |
| $\{\alpha\}_5 \rightarrow \{\alpha\}_7$ | 0 | 7.0 | 5.8 7.1 |
| | 1 | 2.0 | 1.8 1.9 |
| $\{\alpha\}_6 \rightarrow \{\alpha\}_7$ | 0 | 8.3 | 7.3 7.8 |
| | 1 | 6.3 | 7.1 6.0 |
| | 2 | 3.1 | 3.0 3.1 |

Table III. Characteristics of the coupled-channel calculations, performed in this work.

| Calculation | Energy (meV) | Potentials |
|-------------|-----------------|------------|
| I(a) | $E_5 = 100$ | hard wall |
| I(b) | $E_6 = 100$ | hard wall |
| II(a) | $E_5 = 100$ | extended |
| II(b) | $E_6 = 100$ | extended |

$\theta_E = 0$ and $\theta_E = \pi/2$ are traceable to the symmetry axis of the apparatus at $\theta = 0$ and not to the initial J_k orientation. As to cross section magnitude, the variation there is considerable as well, with $Q_{4\leftarrow 5}$ and $Q_{6\leftarrow 5}$ at opposite ends of the scale. The resulting experimental polarized cross sections $Q_{l\leftarrow k} \frac{|M_k|}{|M_l|}$, derived from a least squares fit of the data points to Eq. (18), have been summarized in Table II.

With our coupled-channels code, we have computed polarized cross sections $Q_{l\leftarrow k} \frac{|M_k|}{|M_l|}$ at energies $E_5 = 100$ meV [calculation I(a)] and $E_6 = 100$ meV [calculation I(b)], relative to the indicated initial state. The model potentials of Hennecart^{1,11)} and Masnou-Seeuws¹⁾ were used. Of necessity, a hard wall at $R = 4.5a_0$ was introduced. In additional calculations at $E_5 = 100$ meV [II(a)] and $E_6 = 100$ meV [II(b)], the extended potentials of Fig. 4 were used. The characteristics of the coupled-channels calculations have been summarized in Table III. The results of these calculations are given in Figs. 14-16, as well as in Table II.

As far as the $\{\alpha\}_5 \rightarrow \{\alpha\}_l$ transitions are concerned, there is excellent agreement between theory and experiment: not only the polarization effect $Q_{l\leftarrow k}^{[0]} / Q_{l\leftarrow k}^{[1]}$, but even the absolute cross section values are reproduced well. Cross sections from the preliminary calculation with model potentials extended down to $R = 2a_0$ differ from the hard-wall results by 30% at most, which is on the order of the experimental errors. We have thus explicitly verified the relative unimportance of the inner region ($R \leq 4.5a_0$) of the $\text{Ne}^{**}\text{-He}$ potentials, for the above transitions and energies.

To obtain a qualitative insight into the mechanisms underlying the surprisingly large polarization effects, we have to consider the salient features of the adiabatic potential curves involved, as calculated by Hennecart^{1,11)} and Masnou-Seeuws¹⁾ with a model potential method. Indeed,

the choice of the $\{\alpha\}_{4,5,6,7}$ states as objects of our primary interest was dictated by the presence of several clear-cut avoided crossings between their adiabatic potentials.

We first discuss the $\{\alpha\}_5 \rightarrow \{\alpha\}_7$ transition of Fig. 16. Both the $\{\alpha\}_5$ and $\{\alpha\}_7$ states, but the former in particular, show only a small splitting between the $\Omega = 0$ and $\Omega = 1$ molecular potentials. To indicate the probed range of internuclear distances R : at $E = 100$ meV the classical turning point for both Ω potentials of the $\{\alpha\}_5$ state is $R_t = 6a_0$ for an impact parameter $b = 0$ and $R_t = 7.1a_0$ for $b = 6a_0$. For $\Omega = 0$ the adiabatic electronic states are divided into 0^+ and 0^- classes, depending on the reflection symmetry. The $\Omega = 0^-$ class contains the $\{\alpha\}_{2,5,7,9,10}$ odd- J states and there is a strong coupling of the $\{\alpha\}_5$ and $\{\alpha\}_7$ states. This coupling can be identified as an avoided crossing at $R_c = 7.0a_0$, with a Landau-Zener type coupling matrix element $H_{57} = 22$ meV (half the smallest separation of the potential curves), which is very large in comparison with the energy difference $\Delta E_{57} = 80.7$ meV of the $\{\alpha\}_5$ and $\{\alpha\}_7$ states at infinity. For $\Omega = 1$ there is no symmetry constraint and the intermediate $\{\alpha\}_6$ state disturbs the coupling of the $\{\alpha\}_5$ to the $\{\alpha\}_7$ state. We now observe an avoided crossing of the $\{\alpha\}_6$ and $\{\alpha\}_7$ states at $R_c = 7.5a_0$, with $H_{67} = 3.5$ meV. Moreover, the initial $\{\alpha\}_5$ state is now coupled to the $\{\alpha\}_4$ state by an avoided crossing with $H_{45} = 1.0$ meV at $R_c = 8.5a_0$. The contribution of the $\Omega = 1$ orientation to the $\{\alpha\}_5 \rightarrow \{\alpha\}_7$ transition is small due to the strong coupling of both the initial and final state to the $\{\alpha\}_4$ and $\{\alpha\}_6$ states, respectively, which is absent for the $\Omega = 0^-$ adiabatic potentials. The large coupling matrix element H_{57} for $\Omega = 0^-$ is consistent with a main contribution to the cross section from small impact parameters, where radial velocities are large. Even without "locking" of the initial $\Omega = |M_J|$ orientation to the internuclear axis, this orientation will then be largely conserved at the crossing radius. This explains the large polarization effect $Q_{7 \leftarrow 5}^{|0|} \gg Q_{7 \leftarrow 5}^{|1|}$.

The picture, that thus emerges, is confirmed by the $\{\alpha\}_5 \rightarrow \{\alpha\}_4$ transition, for which the results are shown in Fig. 14. We note the absence of a significant polarization effect. This is in apparent contradiction with the simultaneous presence of an avoided crossing of the $\{\alpha\}_5$ and $\{\alpha\}_4$ states for the $\Omega = 1$ orientation, and the absence of any coupling at all for $\Omega = 0$, where initial and final states are in different symmetry classes. However, because of the small splitting of the $\Omega = 0$ and $\Omega = 1$ adiabatic potentials for the $\{\alpha\}_5$ state, the "locking" of the initial orientation to the internuclear axis constitutes only a minor effect. The asymptotic $|M_J| = 0$ orientation will thus be partially rotated at the crossing radius into a local $\Omega = 1$ state, which does couple with the final $\{\alpha\}_4$ state. This effect will be most pronounced for large impact parameters. Because of the very small coupling matrix element H_{45} , which requires small values of the radial velocity for optimum coupling, we indeed expect a predominant contribution from large impact parameters. Hence, the absence of a polarization effect, $Q_{4+5}^{0|} \approx Q_{4+5}^{1|}$, is qualitatively understood. A similar reasoning may be applied to the other transitions within the $\{\alpha\}_{4,5,6,7}$ group.

5.2. The $(\{\alpha\}_6, J_6=2)$ initial state

As opposed to the $\{\alpha\}_5$ state, where $J_5 = 1$, the $\{\alpha\}_6$ state has $J_6 = 2$, and must be excited from the $\text{Ne}^*(^3P_2)$ state. From the metastable $\text{Ne}^*(^3P_2)$ state we may in principle excite states $\{\alpha\}_k$ with either $J_k = 1, 2$ or 3 . For $J_k = 1$, however, an isotropic distribution over m_k -substates will result. For $J_k = 2$, in the assumed absence of a magnetic field, we find

$$\begin{cases} g_{m_k=0} = 0 \\ g_{|m_k|=1} \approx 1/6 \\ g_{|m_k|=2} \approx 2/6 \end{cases} \quad (19)$$

for the (time-integrated) distribution over magnetic substates in the scattering volume, to be substituted in the general formula

$$Q_{l \leftarrow k}^\beta = \frac{1}{64} \times \quad (20)$$

$$\begin{aligned} & \left\{ [(22g_0 + 24g_1 + 18g_2)Q_{l \leftarrow k}^{0|} + (24g_0 + 64g_1 + 40g_2)Q_{l \leftarrow k}^{1|} + (18g_0 + 40g_1 + 70g_2)Q_{l \leftarrow k}^{2|}] \right. \\ & + [(24g_0 - 24g_2)Q_{l \leftarrow k}^{0|} + (32g_1 - 32g_2)Q_{l \leftarrow k}^{1|} + (-24g_0 - 32g_1 + 56g_2)Q_{l \leftarrow k}^{2|}] \cos 2\beta \\ & \left. + [(18g_0 - 24g_1 + 6g_2)Q_{l \leftarrow k}^{0|} + (-24g_0 + 32g_1 - 8g_2)Q_{l \leftarrow k}^{1|} + (6g_0 - 8g_1 + 2g_2)Q_{l \leftarrow k}^{2|}] \cos 4\beta \right\} \end{aligned}$$

The experimental results for the $\{\alpha\}_6 \rightarrow \{\alpha\}_7$ transition are displayed in Fig. 17. The $\{\alpha\}_6$ state was excited from the $\text{Ne}^*(^3P_2)$ state at $\lambda = 614.3$ nm. Detection took place at $\lambda = 692.3$ nm and 653.3 nm for the $\{\alpha\}_6$ and $\{\alpha\}_7$ states, respectively. The center-of-mass energy was approximately $E_6 = 95$ meV, rather than 100 meV as in the $\{\alpha\}_5$ measurements, due to a small difference in laser beam alignment. We observe, that in $Q_{7 \leftarrow 6}^\beta$ the presence of the higher order $\cos 4\beta$ -term of Eq. (20) is not immediately apparent. The experimental polarized cross section $Q_{7 \leftarrow 6}^{|M_6|}$ derived from Eqs. (19) and (20) are given in Table II.

Comparison with the results of the coupled-channels calculations, also given in Table II, again shows excellent agreement. This is true both for the calculation using the hard wall potentials [I(b)] and for that using the extended potentials [II(b)], but for the latter in particular. Strictly

speaking, of course, for a more balanced judgement a detailed examination of the distribution parameters g_{m_k} of Eq. (19) is needed. Developments which will enable us to perform this kind of calculation, taking into account the presence of small magnetic fields, are under way.

For a better understanding of the relatively small polarization effect $Q_{7\leftarrow 6}^{0|} / Q_{7\leftarrow 6}^{1|}$, it is sufficient to point to the similarity of the avoided crossing for the $\{\alpha\}_6$ and $\{\alpha\}_7$ states for $\Omega = 1$ to that for the $\{\alpha\}_4$ and $\{\alpha\}_5$ states. Once again, a grazing impact is favoured, at slightly higher radial velocities. The smaller crossing radius is bound to lead to smaller cross sections than for the $\{\alpha\}_5 \rightarrow \{\alpha\}_4$ transition, though in itself not by the amount evidenced by the experimental cross sections.

6. Energy dependence and absolute values

6.1. Energy dependence

We have performed measurements of the energy dependence of the $Q_{7\leftarrow 5}^{M_5|}$ and $Q_{4\leftarrow 5}^{M_5|}$ cross sections for $\text{Ne}^{**}\text{-He}$. This has been done, both by varying the magnitude of the primary beam velocity v_1 (by using a 85% He / 15% Ne seeded primary beam) and by varying the direction of v_2 (by scanning the laser beam along the primary beam axis). While primary-beam velocities have been determined through time-of-flight measurements, employing a pseudo-random optical chopper³⁷⁾, at this stage no attempt has been made to resolve collision-induced fluorescence spectra. Here, as elsewhere, velocity-averaged results only are presented, both as to measured (Ne^*) and as to calculated (He) velocity distributions.

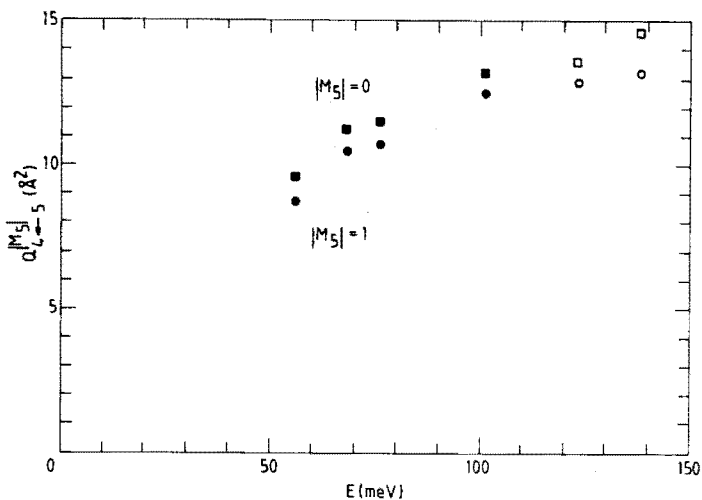


Fig. 18. Energy dependence of the polarized cross sections $Q_{4\leftarrow 5}^{[0]}$ and $Q_{4\leftarrow 5}^{[1]}$, with E the center-of-mass energy. The open points have been obtained by varying the magnitude of the primary-beam velocity v_1 ; the full points by varying the position of the laser beam along the primary-beam axis, resulting in a different direction of v_2 .

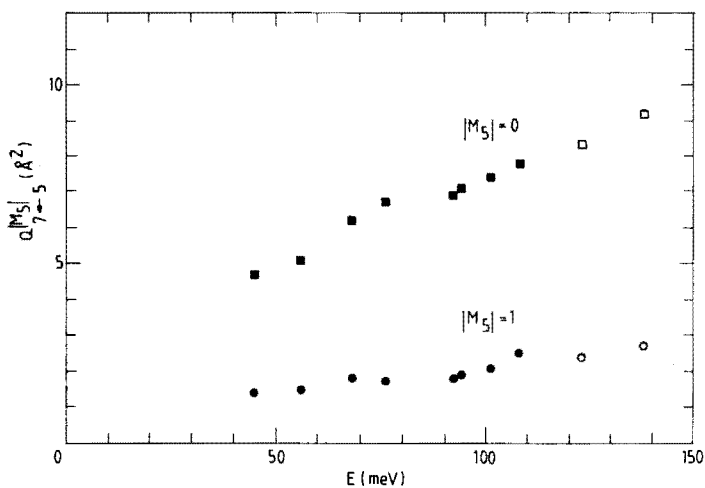


Fig. 19. Energy dependence of the polarized cross sections $Q_{7\leftarrow 5}^{[0]}$ and $Q_{7\leftarrow 5}^{[1]}$. See caption of Fig. 18 for further detail.

The observed energy dependence of the polarised-atom cross sections $Q_{4\leftarrow 5}^{M_5}$ and $Q_{7\leftarrow 5}^{M_5}$ is shown in Figs. 18 and 19. The data points at approximately 60 meV represent the low-end limit of the position-dependent energy variation with the He secondary beam. Likewise, 150 meV is the maximum attainable practical energy with the above seeded primary beam. Errors in the average energy are typically 5%, due to uncertainties in the present laser beam alignment technique.

A detailed discussion of these results on the basis of quantum-mechanical coupled-channels calculations would require a prohibitively large amount of computer-time. An analysis in semiclassical terms⁴⁰⁾ is less demanding in this respect and seems highly appropriate, in view of the pronounced avoided crossings between the adiabatic potentials of Fig. 5.

6.2. Various other transitions

In addition to the polarisation measurements reported above, we have performed a number of exploratory measurements under much less well-defined experimental conditions. Their purpose was to establish the presence or absence, within experimental limits, of various transitions. The range of these measurements was determined by filter availability and dye laser operation. Only order-of-magnitude results at an approximate energy $E = 100$ meV are presented in Table IV. The substantial $\{a\}_5 \rightarrow \{a\}_{10}$ transition probability is at first sight rather surprising, given the large energy distance $\Delta E_{5,10} = 312$ meV. When using the two-level system $\{a\}_9$ state as an initial state, experimental signals are especially large, due to the replacement of the lifepath l_T by the laserbeam width in Eq. (10), allowing detection of smaller cross sections. The $\{a\}_9 \rightarrow \{a\}_6$ transition is an example of this.

Table IV. Order of magnitude of some observed cross sections $Q_{l \leftarrow k}$, at approximate center-of-mass energy $E = 100$ meV. In case of a fluorescence signal below the experimental threshold, an upper limit for the relevant cross section is given. Also shown are calculated unpolarized cross sections. Only for the $\{a\}_5$ [calculations I(a), II(a)] and $\{a\}_6$ [calculations I(b), II(b)] initial states, the collision energy E conforms to the experiment. In some other cases the results of the calculation providing the closest energy-match are given between parentheses.

| Initial state k | | $Q_{l \leftarrow k} (\text{\AA}^2)$ | | | | | |
|-------------------|--|-------------------------------------|--------------------|-----------------------|---------------------|---------------------|--------------------|
| | | Final state l | | | | | |
| k | $E_k(\text{meV})$ | 4 | 5 | 6 | 7 | 8 | 10 |
| 2 | expt calc 100 (67 ^a /67 ^b) | | | <0.1 (0.04 / 0.06) | <0.1 (0.2 / 0.2) | <0.1 (0.0 / 0.1) | |
| 5 | expt calc 100 100 ^a /100 ^b | 12.7 13.8 / 13.9 | * * | 0.8 0.8 / 0.8 | 3.7 3.1 / 3.6 | 0.6 0.4 / 1.1 | 0.3 0.0 / 0.05 |
| 6 | expt calc 100 100 ^c /100 ^d | 0.4 0.1 / 0.2 | 0.4 0.03 / 0.3 | * * | 4.7 5.5 / 5.2 | | <0.1 0.0 / 0.04 |
| 7 | expt calc 100 124 ^c /(181 ^b) | 0.4 0.6 / (2.2) | 0.3 0.7 / (2.0) | 3.2 7.4 / (8.7) | * * | 9.0 8.2 / (10.8) | |
| 8 | expt calc 100 | | | 0.1 | <0.1 | * * | 1.9 |
| 9 | expt calc 100 | | | 0.01 | 0.1 | | 2.5 |

a) Calculation I(a).

b) Calculation II(a).

c) Calculation I(b).

d) Calculation II(b).

When comparing, in Table IV, experimental cross sections with unpolarised quantum-mechanical cross sections $Q_{l \leftarrow k}$ from calculations I(a) I(b), II(a) and II(b), allowances must of course be made for the imperfect energy match of other than the $\{\alpha\}_5 \rightarrow \{\alpha\}_1$ and $\{\alpha\}_6 \rightarrow \{\alpha\}_1$ transitions. The relevant energies have been indicated in the table. On account of the energy-mismatch we have refrained from giving the calculated $Q_{l \leftarrow 8}$ and $Q_{l \leftarrow 9}$ cross section values. Preliminary calculations seem to indicate an inability of coupled-channels calculations with the model potentials of Hennecart and Masnou-Seeuws to predict the considerable $Q_{10 \leftarrow 8}$ and $Q_{10 \leftarrow 9}$ cross sections, while our extended potentials fare somewhat better in this respect. Apart from that, there is rough qualitative agreement between theory and experiment, considering the experimental and computational limitations of the comparison. A similar remark can be made with respect to rate constants available from the literature. Again, a proper comparison awaits semiclassical calculations on the energy dependence of cross sections⁴⁰⁾.

Statistical errors in the experimental data are, on the whole, small for all but the weak transitions. In view of the inherent experimental difficulties, discussed earlier, this speaks well for the design of the apparatus. The overall systematic error of our absolute cross section values we currently estimate at a respectable 30% , laser beam alignment being the main limiting factor. We are working on an automated alignment procedure, that will constitute an definite improvement in this regard³⁷⁾.

The absolute cross section values given here for the $\{\alpha\}_5 \rightarrow \{\alpha\}_7$ and $\{\alpha\}_5 \rightarrow \{\alpha\}_4$ transitions differ somewhat from those cited in an earlier paper¹⁹⁾. This is due almost exclusively to a more recent set of lifetime values⁴¹⁾ having been used in their calculation, different from that used earlier⁴²⁾.

7. Concluding remarks

At the investigated thermal energies, where mainly the long range interactions are probed, quantum-mechanical coupled-channels calculations on the basis of the model potentials of Hennecart and Masnou-Seeuws appear to offer a very satisfactory description of our $\text{Ne}^{**}\text{-He}$ experimental results. In particular, this is true for the transitions within the $\{\alpha\}_{4,5,6,7}$ group of states. For other transitions, which so far have been explored much less intensively, the general trend is reproduced as well. There are indications, that for some of these transitions the inner potential regions, which are not covered by the model potential method, are of importance.

It is possible to obtain a qualitative insight into the mechanisms underlying the coupled-channels and experimental results, by considering the adiabatic potentials calculated from the model potentials. Our present understanding is based on the constraints of symmetry, the occurrence of avoided crossings between the potential curves, and the partial absence of "locking". It seems feasible to develop a fully semiclassical description in terms of Landau-Zener theory. The $\{\alpha\}_{4,5,6,7}$ multiplet is a natural candidate for such an approach. This will be discussed in another paper⁴⁰⁾. The energy-dependence of cross sections deserves more scrutiny than it has received here. We are in the process of perfecting a time-of-flight measurement technique, employing a pseudo-random laser chopper³⁷⁾. When used with seeded beams, and ultimately a hollow cathode arc metastable beam source⁴³⁾, this will enable us to cover a wide energy range in considerable detail. Thus it will become much easier to correlate rate constants cited in literature with our beam experiment results. Even in its present form, however, our crossed-beam apparatus and coupled-channels program, taken together, form an excellent test-bed for interaction potentials and collision mechanisms.

References

- 1 D. Hennecart and F. Masnou-Seeuws, *J. Phys. B* **18**, 657 (1985).
- 2 a) W. Buszert, T. Bregel, R.J. Allan, M.-W. Ruf, and H. Hotop, *Z. Phys. A* **320**, 105 (1985); b) W. Buszert, T. Bregel, J. Ganz, K. Harth, A. Siegel, M.-W. Ruf, H. Hotop and H. Morgner, *J. Phys. (Paris)* **46** C19 (1985).
- 3 M.H. Alexander, T. Orlikowski, and J.E. Straub, *Phys. Rev. A* **28**, 73 (1983).
- 4 G. Nienhuis, *Phys. Rev. A* **26**, 3137 (1982).
- 5 J.G. Kircz, R. Morgenstern, and G. Nienhuis, *Phys. Rev. Lett* **48**, 610 (1982).
- 6 H.A.J. Meyer, H.P. van der Meulen, and R. Morgenstern, *Z. Phys. D* **5**, 299 (1987).
- 7 D. Neuschäfer, M.O. Hale, I.V. Hertel and S.R. Leone, in "Electronic and Atomic Collisions", Eds. D.C. Lorents, W.E. Meyerhof, and J.R. Peterson, Elsevier (1986).
- 8 a) M.O. Hale, I.V. Hertel, and S.R. Leone, *Phys. Rev. Lett.* **53**, 2296 (1984); b) M.O. Hale and S.R. Leone, *Phys. Rev. A* **31**, 103 (1985).
- 9 J.M. Parson and T. Ishikawa, *J. Chem. Phys.* **80**, 3137 (1984)
- 10 A. Bähring, I.V. Hertel, E. Meyer, W. Meyer, N. Spies, and H. Schmidt, *J. Phys. B* **17**, 2859 (1984).
- 11 a) D. Hennecart, *J. Phys. (Paris)* **39**, 1065 (1978); b) D. Hennecart, Ph.D. Thesis, Université de Caen, 1982 (unpublished).
- 12 J.M. Mestdagh, J. Berlande, P. de Pujo, J. Cuvallier, and A. Binet, *Z. Phys. A* **304**, 3 (1982).
- 13 E. Düren, E. Hasselbrink and H. Tischen, *Phys.Rev.Lett.* **50**, 1983 (1983)
- 14 L. Hüwel, J. Maier, and H. Pauly, *J. Chem. Phys.* **76**, 4961 (1982).
- 15 H.J. Yuh and P.J. Dagdigian, *Phys.Rev. A* **28**, 63 (1983).
- 16 a) N.Böwering, M.R. Bruce and J.W. Keto, *J. Chem. Phys.* **84**, 709 (1986); b) N.Böwering, M.R. Bruce and J.W. Keto, *J. Chem. Phys.* **84**, 715 (1986).
- 17 J.K. Kuh and D.W. Setser, *J. Chem. Phys.* **84**, 4304 (1986).
- 18 I.V. Hertel, H. Schmidt, A. Bähring and E. Meyer, *Rep. Prog. Phys.* **48**, 375 (1985).
- 19 M.P.I. Manders, J.P.J. Driessen, H.C.W. Beijerinck and B.J. Verhaar, *Phys.Rev.Lett.* **57**, 1577 (1986); *ibid.*, **57**, 2472 (1986).
- 20 M.J. Webster and M.J. Shaw, *J. Phys. B* **12**, 3521 (1979).
- 21 F.C.M. Coolen, N. van Schaik, R.M.M. Smits, M. Prins, and L.W.G. Steenhuysen, *Physica (Amsterdam)* **93B+C**, 131 (1978).

- 22 R.M.M. Smits, Ph.D. Thesis, Eindhoven University of Technology, 1977 (unpublished).
- 23 R.S.F. Chang and D.W. Setser, *J. Chem. Phys.* 72, 4099 (1980).
- 24 J.S. Cohen and B. Schneider, *J. Chem. Phys.* 61, 3230 (1974).
- 25 S. Iwata, *Chem. Phys.* 37, 251, (1979).
- 26 F. Masnou-Seeuws, M. Philippe and P. Valiron, *Phys. Rev. Lett.* 41, 95 (1978).
- 27 P.J. Dagdigian and M.L. Campbell, *Chem. Rev.* 87, 1 (1987).
- 28 H. Haberland, W. Konz and P. Oesterlin, *J. Phys. B.: Atom. Mol. Phys.* 15, 2969 (1982).
- 29 I. Dabrowski and G. Herzberg, *J. Mol. Spectr.* 73, 183 (1978).
- 30 R.B. Bernstein, "Atom Molecule Collision Theory", Plenum Press, New York and London (1979).
- 31 A.M. Schulte, Ph.D. Thesis, Eindhoven University of Technology (1978) (unpublished).
- 32 J. Raynal in "Computing as a Language of Physics", ed. A.E. Salam, IAEA, Vienna (1972).
- 33 W.J.G. Thijssen, B.J. Verhaar and A.M. Schulte, *Phys. Rev. C* 23, 984 (1981)
- 34 M.J. Verheijen, H.C.W. Beijerinck, L.H.A.M. van Moll, J.P.J. Driessen and N.F. Verster, *J. Phys. E* 17, 904 (1984).
- 35 M.J. Verheijen, H.C.W. Beijerinck and N.F. Verster, *J. Phys. E* 15, 1198 (1982).
- 36 H.C.W. Beijerinck and N.F. Verster, *Physica* 111C, 327 (1981).
- 37 M.P.I. Manders, W.M.J. Ruyten, F. v.d. Beucken, J.P.J. Driessen, W.J.T. Veugelers, P.H. Kramer, E.J.D. Vredenburg, W.B.M. van Hoek, G.J. Sandker, H.C.W. Beijerinck, and B.J. Verhaar, to be published.
- 38 A. Messiah, "Quantum Mechanics", Vol. I+II, North Holland, Amsterdam (1981).
- 39 M.J. Verheijen, H.C.W. Beijerinck and N.F. Verster, *Rev. Sci. Instr.* 56, 62 (1985).
- 40 M.P.I. Manders, E.J.D. Vredenburg, W.B.M. van Hoek, G.J. Sandker, H.C.W. Beijerinck and B.J. Verhaar, to be published.
- 41 P. Hartmetz and H. Schmoranzler, *Phys. Lett.* 93 A, 404 (1983).
- 42 W.L. Wiese, M.W. Smith and B.M. Glennon, "Atomic Transition Probabilities I: Hydrogen through Neon", U.S. Dept. of Commerce, National Bureau of Standards (U.S. GPO, Washington, D.C., 1966).
- 43 P.G.A. Theuws, H.C.W. Beijerinck, D.C. Schram, and N.F. Verster, *J. Phys. E* 15, 573 (1982).

Chapter V.

SEMICLASSICAL ANALYSIS OF POLARISATION EFFECTS IN COLLISION INDUCED
INTRAMULTIPLY MIXING FOR $\text{Ne}^{**}\{(2p)^5(3p)\} + \text{He}$

M.P.I. Manders, W.B.M. van Hoek, E.J.D. Vredenbregt,

G.J. Sandker, H.C.W. Beijerinck and B.J. Verhaar

Physics Department, Eindhoven University of Technology

P.O. Box 513, 5600 MB Eindhoven, The Netherlands

Abstract

We have performed new crossed-beam measurements and quantum-mechanical calculations on transitions between the short-lived $\text{Ne}^{**}\{(2p)^5(3p)\}_k \equiv \{\alpha\}_k$ states with $k = 4,5,6,7$ (Paschen numbering), induced by collisions with ground state He atoms at energies between 70 and 140 meV. The $\{\alpha\}_{4,5,6,7}$ multiplet is distinguished by the presence of several avoided crossings between the adiabatic potentials $V_k^\Omega(R)$ - a sign of strong, localized radial coupling. This has inspired a simple, semiclassical model for the Ne^{**} -He collision process, which has the following ingredients:

straight line trajectories with hard-sphere scattering at the classical turning point R_T ;

rotational coupling for $R > R_L$ and "locking" of the electronic angular momentum J to the internuclear axis for $R \leq R_L$, with R_L the locking radius;

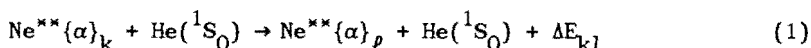
Landau-Zener type curve-crossing transitions near the crossing radius R_C .

This model goes a long way towards explaining the experimental polarization effects, i.e. differences between polarized cross sections $Q_{\ell \leftarrow k}^{|M_k|}$ for the $\{\alpha\}_k \rightarrow \{\alpha\}_\ell$ transition depending on the asymptotic orientation of the total electronic angular momentum J , as specified by the magnetic quantum number M_k . These polarization effects are at times very large. For example, at a center-of-mass collision energy $E \approx 100$ meV, we find $Q_{\ell \leftarrow 5}^{|0|} / Q_{\ell \leftarrow 5}^{|1|} = 0.52$ and 3.5, for $\ell = 6$ and 7, respectively; $Q_{\ell \leftarrow 6}^{|0|} / Q_{\ell \leftarrow 6}^{|1|} = 0.41$ and 1.3, for $\ell = 5$ and 7; and $Q_{\ell \leftarrow 7}^{|0|} / Q_{\ell \leftarrow 7}^{|1|} = 0.08$ and 8.9, for $\ell = 4$ and 5.

1. Introduction

In recent years there has been a rise in the attention paid to inelastic collisions of atoms in short-lived electronically excited states¹⁻¹⁷). A recent review of the field was given by Hertel et al.¹⁸), while the basics of our own work were set out in earlier papers^{19,20}). Excitation by polarized laser prepares the short-lived states in well-defined asymptotic orientations. Strong effects of the orientation on cross-section magnitude have been observed. In many cases, however, a satisfactory explanation of these polarisation effects proves elusive, due to lack of accurate information on coupling potentials for the systems under consideration.

A fundamentally different situation obtains with the inelastic intramultiplet-mixing process



where $\{\alpha\}_j = \{(2p)^5(3p)\}_j$, with j running from 1 to 10 with decreasing energy. Here all three ingredients, necessary for a better understanding, are available: experimental data, potential surface information and the capability to perform fully quantum-mechanical coupled-channels calculations.

First, we have obtained experimental results on polarized-atom inelastic cross sections from a crossed-beam experiment, for a well-defined translational energy and asymptotic orientation of the initial state $\{\alpha\}_k$ ²⁰). Careful design of the crossed-beam apparatus²¹), necessitated by the short lifetimes of the Ne^{**} -states ($\tau \approx 20$ ns) and the small transition cross sections ($Q_{\ell \leftarrow k} \approx 1 \text{ \AA}^2$), has resulted in large signals ($1 \text{ kHz}/\text{\AA}^2$) for the fluorescence from the final state $\{\alpha\}_\ell$) and a relatively low background

(2-15 kHz). Absolute polarized-atom cross sections $Q_{\ell \leftarrow k}^{|M_k|}$ were presented earlier²⁰⁾ for the $\{\alpha\}_5 \rightarrow \{\alpha\}_4$, $\{\alpha\}_6$, $\{\alpha\}_7$ and $\{\alpha\}_6 \rightarrow \{\alpha\}_7$ transitions. Here M_k is the magnetic quantum number of the intrinsic electronic angular momentum \underline{J} along the asymptotic relative velocity \underline{g} , i.e. the z-axis. We observe large polarization effects. Typical results at center-of-mass energy $E \approx 100$ meV are: $Q_{\ell \leftarrow 5}^{|0|}/Q_{\ell \leftarrow 5}^{|1|} = 1.06, 0.52$ and 3.5 for $\ell = 4, 6$ and 7 , respectively.

Secondly, we have at our disposal Ne^{**}-He model potentials^{1,11)}. They have been calculated starting from a three-particle model, in which the system is taken to consist of the Ne^{+(2p)⁵}-core, the e^{-(3p)} valence electron and the He(¹S₀)-target. Thus are obtained, for internuclear distances $R \gtrsim 4.5 a_0$, separate basic potentials $V_{\sigma}^{el}(R)$ and $V_{\pi}^{el}(R)$ for the $\sigma \equiv (|m_{\ell}|_{z'} = 0)$ and $\pi \equiv (|m_{\ell}|_{z'} = 1)$ orientations of the 3p-orbital of the valence electron with respect to the internuclear axis, i.e. the z'-axis. Tentatively extended by us down to $R \gtrsim 2.0 a_0$ ²⁰⁾, and supplemented²⁰⁾ by potentials $V_{\sigma}^{core}(R)$ and $V_{\pi}^{core}(R)$ for the two orientations of the core hole, derived from the spectroscopy of the (NeHe)⁺ ion^{22,23)}, these allow calculation of the matrix elements of the Ne^{**}-He electronic Hamiltonian H_{el} in the atomic $|LSJM_J\rangle$ -basis^{1,11)}. Here L, S, J are the quantum numbers of the electronic orbital, spin and total angular momenta \underline{L} , \underline{S} and \underline{J} , respectively. Diagonalisation of H_{el} then yields the adiabatic eigenstates $|\alpha_{k J_k \Omega_k}(R)\rangle$ and potential curves $V_k^{\Omega}(R)$, where $\Omega_k \equiv |M_k|_{z'}$. The 23 adiabatic potentials are divided into Ω -manifolds. For $\Omega = 0$, the further restraint of reflection symmetry of the molecular states generates distinct + and - classes, each containing 5 states with even and odd J, respectively.

A third instrument for a better understanding are our fully quantum-mechanical coupled-channels calculations, using the above potentials as input²⁰⁾. These are performed in a basis of diabatic functions $|\pi \alpha J \Omega P M_p\rangle$ which, besides being atomic eigenfunctions $|\alpha J \Omega\rangle$, have definite parity π

and well-defined quantum numbers P , $M_{P,z}$ and $\Omega = |M_J|_z = |M_P|_z$, for the \underline{P}^2 , P_z and $P_z = J_z$, operators of the total angular momentum \underline{P} . The time-independent Schrödinger equation for the $\text{Ne}^{**}\text{-He}$ scattering problem then gives rise to a set of at most 18 coupled differential equations for each value of P and parity $\pi = +/- 1$. In this " Ω -diabatic" representation, we have "physical" coupling by the molecular interaction $V_{\text{mol}} = V^{\text{Ne}^{**}\text{-He}}$ and rotational coupling by the operator T_{rot} of rotational nuclear motion. Our coupled-channels code uses a modified Numerov integration method²⁴). We limit the calculation to impact parameters $b \lesssim 15 a_0$, beyond which the non-diagonal matrix-elements of $V^{\text{Ne}^{**}\text{-He}}$ vanish. For a $\text{Ne}^{**}\text{-He}$ collision energy $E = 100 \text{ meV}$ this implies $P \lesssim 100$. A complete calculation with appropriate integration stepsize $\Delta R = 0.02 a_0$ then requires about 2.5 hours on a Burroughs B7900 mainframe computer and yields cross sections, that generally agree well with experiment²⁰).

Unfortunately, by their very nature, the quantum-mechanical calculations constitute essentially a "black box". The link between input (model potentials) and output (cross sections) is rather remote. At this point, an analysis in semiclassical terms, if at all feasible, becomes highly desirable.

Our experiment, in its present form, involves $\text{Ne}^{**} + \text{He}$ collisions at thermal energies $70 \lesssim E(\text{meV}) \lesssim 200$. At these low energies, relative velocities of the colliding atoms are small compared to electron velocities. This implies a quasi-molecular system. Just as the molecular adiabatic electronic eigenfunctions $|\alpha_{k,J_k,\Omega_k}(R)\rangle$ are likely to offer a fair description of the electronic states, so are the adiabatic potentials $V_k^\Omega(R)$ apt to govern the relative motion of the nuclei. A completely adiabatic picture of the collision process of course precludes the possibility of transitions between different states. In general, the molecular electronic

states will still be coupled by nuclear motion. The coupling between adiabatic states is bound to be particularly strong at so-called avoided crossings of the adiabatic potentials. It has long been established²⁵⁾, that the non-adiabatic (radial) coupling at an avoided crossing lends itself particularly well to a semiclassical description. As we shall see, not only do several avoided crossings occur between the $\text{Ne}^{*x}\text{-He}$ adiabatic potentials, but in addition they are limited to the quasi-closed multiplet of $\{\alpha\}_{4,5,6,7}$ states. Under the circumstances, semiclassical theory would appear to provide a natural framework for the discussion of a number of important $\{\alpha\}_k \rightarrow \{\alpha\}_l$ transitions.

In the present paper, our aim is to obtain more insight into the physics involved in the collision, than provided by "black box"-type quantum-mechanical calculations. As to absolute values of inelastic cross sections, the semiclassical approach is somewhat of a standard procedure. However, as an essential extension, we include the prediction of polarisation effects by way of a physically suitable description of rotational coupling.

In section 2 we present new experimental results for the $\{\alpha\}_{4,5,6,7}$ group of states, which allow of a better test of our semiclassical model. In section 3 the basic concepts of semiclassical theory, i.e. the Landau-Zener approach to radial coupling at an avoided crossing and the weighing of rotational coupling against "locking", are discussed and related to the $\text{Ne}^{*x}\text{-He}$ system. This is followed, in section 4, by the description of a semiclassical model for calculating polarized-atom inelastic cross sections, which permits, in combination with experimental results and quantum-mechanical calculations, a "complete" analysis for this system. Finally, in section 5, we offer some concluding remarks.

2. New experimental results

We present new $\text{Ne}^{**}\text{-He}$ measurements on polarisation effects, complementing those reported earlier for the $\{\alpha\}_5 \rightarrow \{\alpha\}_{4,6,7}$ and $\{\alpha\}_6 \rightarrow \{\alpha\}_7$ transitions²⁰⁾. Figures 1-3 and 4-6 show observed cross sections for the $\{\alpha\}_6 \rightarrow \{\alpha\}_{4,5,7}$ and $\{\alpha\}_7 \rightarrow \{\alpha\}_{4,5,6}$ transitions, as a function of the angle β between the laser electric field vector \underline{E} and the asymptotic relative velocity \underline{g} of the collision partners. Center-of-mass energy is approximately $E = 100$ meV for these measurements. The absolute cross section values are estimated to exhibit a systematic error of at most 30%. Table I gives the corresponding single- M_k -state polarized cross sections $Q_{\ell \leftarrow k}^{\beta} |M_k|$. These have been determined from a least-squares fit of the data to a model-function of the general form

$$Q_{\ell \leftarrow k}^{\beta} = \sum_{n=0}^{J_k} C_n^{J_k} \cos 2n\beta \quad (2)$$

In detail²¹⁾,

$$Q_{\ell \leftarrow k}^{\beta} = \sum_{m_k=-J_k}^{J_k} g_{m_k} \sum_{M_k=-J_k}^{J_k} \{d_{m_k M_k}^{J_k}(\beta)\}^2 |M_k| Q_{\ell \leftarrow k} \quad (3)$$

where the rotation matrices or reduced Wigner D-functions $d^{26)}$ transform the initial distribution g_{m_k} over magnetic substates $|\alpha_k J_k m_k\rangle_{\underline{E}}$ to a distribution over substates $|\alpha_k J_k M_k\rangle_{\underline{g}}$. Upon excitation with a linearly polarized laser from the $|^3P_0, J_i = 0\rangle$ metastable state, we have for an $|\alpha_k J_k = 1\rangle$ initial state: $g_{|m_k|=0} = 1$, $g_{|m_k|\neq 0} = 0$. The coefficients in Eq. (2) are

$$C_0^1 = \frac{1}{2} (Q_{\ell \leftarrow k}^{0|} + Q_{\ell \leftarrow k}^{1|}) \quad (4)$$

$$C_1^1 = \frac{1}{2} (Q_{\ell \leftarrow k}^{0|} - Q_{\ell \leftarrow k}^{1|})$$

For $|\alpha_k J_k = 2\rangle$ and $|^3P_2, J_i = 2\rangle$, again using a linearly polarized laser so that $g_{+m_k} = g_{-m_k} = g_{|m_k|}$, we can write

$$C_0^2 = \frac{1}{64} [(22g_0 + 24g_1 + 18g_2)Q_{\ell \leftarrow k}^{0|} + (24g_0 + 64g_1 + 40g_2)Q_{\ell \leftarrow k}^{1|} + (21g_0 + 40g_1 + 70g_2)Q_{\ell \leftarrow k}^{2|}] \quad (5)$$

$$C_1^2 = \frac{1}{64} [(24g_1 - 24g_2)Q_{\ell \leftarrow k}^{0|} + (32g_1 - 32g_2)Q_{\ell \leftarrow k}^{1|} + (-24g_0 - 32g_1 + 56g_2)Q_{\ell \leftarrow k}^{2|}]$$

$$C_2^2 = \frac{1}{64} [(18g_0 - 24g_1 + 6g_2)Q_{\ell \leftarrow k}^{0|} + (-24g_0 + 32g_1 - 8g_2)Q_{\ell \leftarrow k}^{1|} + (6g_0 - 8g_1 + 2g_2)Q_{\ell \leftarrow k}^{2|}]$$

In the present case, as earlier for the $(\{\alpha\}_6, J_6=2)$ initial state²⁰⁾, the time-integrated distribution g_{m_k} over magnetic substates $|\alpha_k J_k m_k\rangle_{\underline{E}}$ in the scattering volume was calculated assuming the absence of a magnetic field, with the result: $g_{|m_k|=0} = 0$, $g_{|m_k|=1} \approx \frac{1}{6}$, $g_{|m_k|=2} \approx \frac{2}{6}$. This leaves some room for error in the $\{\alpha\}_6 \rightarrow \{\alpha\}_\ell$ polarized cross sections.

The measurements disclose large variations, both in cross section magnitude ($Q_{5 \leftarrow 7}^\beta \ll Q_{6 \leftarrow 7}^\beta$) and in polarisation effects ($Q_{5 \leftarrow 7}^{0|}/Q_{5 \leftarrow 7}^{1|} \approx 8$, $Q_{6 \leftarrow 7}^{0|}/Q_{6 \leftarrow 7}^{1|} \approx 0.2$). The cross sections $Q_{\ell \leftarrow 7}^\beta$, where $(\{\alpha\}_7, J_7 = 1)$ is the initial state, closely agree with the $\cos 2\beta$ -dependence of Eq. (2). For the $(\{\alpha\}_6, J_6 = 2)$ initial state, the presence of the higher order $\cos 4\beta$ -term of Eq. (2) is not always immediately apparent (compare e.g. $Q_{7 \leftarrow 6}^\beta$ with $Q_{4 \leftarrow 6}^\beta$). Of course, much depends on the distribution parameters g_{m_6} .

With our coupled-channels code²⁰⁾ we have calculated polarized cross sections $Q_{\ell \leftarrow k}^{M_k}$ for the transitions within the $Ne^{**}\{\alpha\}_{4,5,6,7}$ multiplet, at some different energies within the experimental energy range. The extended

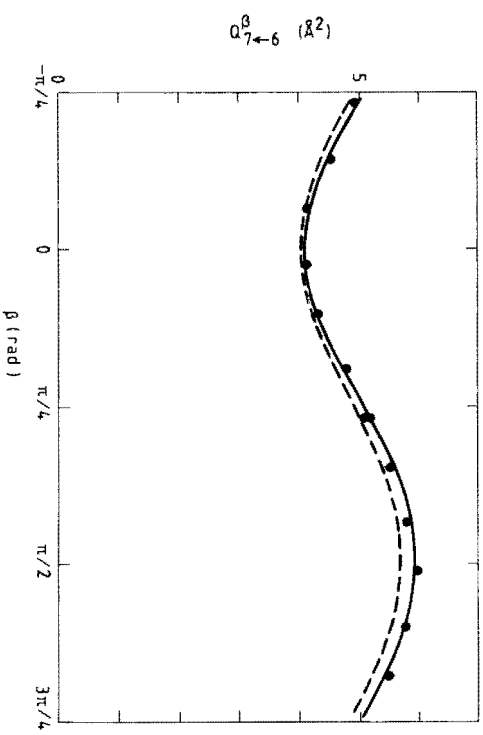
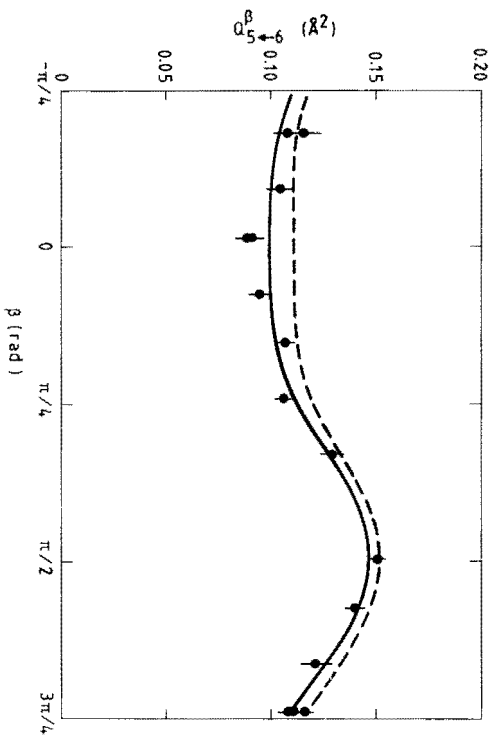
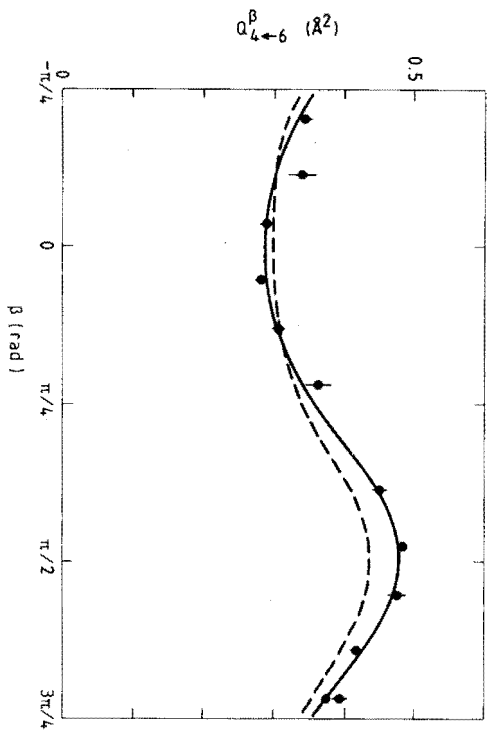


Fig. 1. Experimental results for the observed cross section $Q_{4\leftarrow 6}^{\beta}$, as a function of the angle β between the electric field \underline{E} of the laser and the average relative velocity \underline{g} , at a center-of-mass energy $E_6 \simeq 100$ meV. Statistical errors only have been indicated. The solid line (—) represents a curve fit of the data points according to Eqs. (2) and (5), assuming the absence of a magnetic field. The dashed line (---) is the result of quantum-mechanical calculations with the extended model potentials of Hennecart and Masnou-Seeuws as input. It uses a weighed average of quantum-mechanical cross sections $Q_{4\leftarrow 7}^{|M_7|}$, assuming Gaussian primary- and secondary-beam velocity distributions.

Fig. 2. Experimental results for the observed cross section $Q_{5\leftarrow 6}^{\beta}$ at $E_6 \simeq 100$ meV. See caption of Fig. 1 for further detail.

Fig. 3. Experimental results for the observed cross section $Q_{7\leftarrow 6}^{\beta}$ at $E_6 \simeq 110$ meV. See caption of Fig. 1 for further detail.

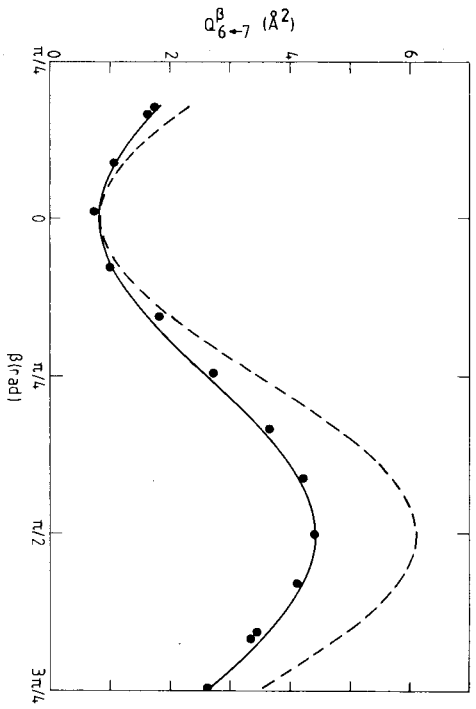
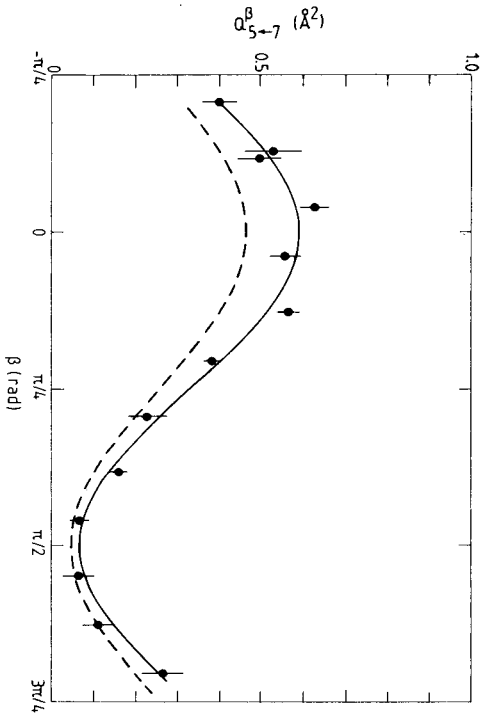
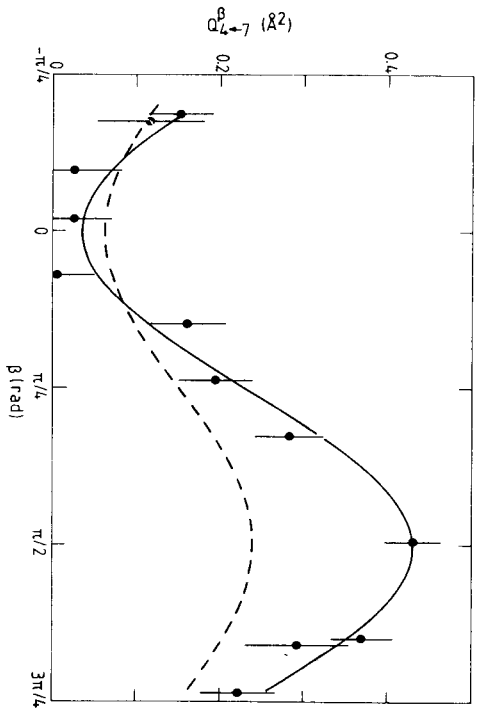


Fig. 4. Experimental results for the observed cross section $Q_{4\leftarrow 7}^{\beta}$ at $E_7 \simeq 95$ meV. The curve fit of the data points (—) is according to Eqs. (2) and (4). This is a highly endothermic transition, with the threshold energy $\Delta E_{47} = 91$ meV close to the average experimental center-of-mass energy. See caption of Fig. 1 for further detail.

Fig. 5. Experimental results for the observed cross section $Q_{5\leftarrow 7}^{\beta}$ at $E_7 \simeq 95$ meV. The threshold energy is $\Delta E_{57} = 81$ meV. See caption of Fig. 4 for further detail.

Fig. 6. Experimental results for the observed cross section $Q_{6\leftarrow 7}^{\beta}$ at $E_7 \simeq 95$ meV. The threshold energy being only $\Delta E_{67} = 24$ meV, averaging over different velocities has only a limited effect. See caption of Fig. 4 for further detail.

Table I. Experimental and quantummechanical polarized cross sections $Q_{\ell \leftarrow k}^{|\mathbf{M}_k|}$, at various center-of-mass energies E of the initial state $\{\alpha\}_k$, together with the polarization effect $Q_{\ell \leftarrow k}^{|0|} / Q_{\ell \leftarrow k}^{|1|}$. The extended potentials, used in the calculations, are identical to those used in Ref. 20. Where indicated, the experimental energy distribution has been taken into account in calculating effective quantum-mechanical cross sections.

| | | Cross Section | | | | | | | | Polarization effect | |
|---------------------------------|----------------------------------|-------------------|------|---|------|---|------|---|------|---|------|
| Initial state $\{\alpha\}_k$ | Final state $\{\alpha\}_\ell$ | E_{cm} (meV) | | $Q_{\ell \leftarrow k}^{ 0 }$ (\AA^2) | | $Q_{\ell \leftarrow k}^{ 1 }$ (\AA^2) | | $Q_{\ell \leftarrow k}^{ 2 }$ (\AA^2) | | $Q_{\ell \leftarrow k}^{ 0 }/Q_{\ell \leftarrow k}^{ 1 }$ | |
| | | QM | EXPT | QM | EXPT | QM | EXPT | QM | EXPT | QM | EXPT |
| $\{\alpha\}_5$ | $\{\alpha\}_4$ | 60 | 60 | 8.9 | 9.6 | 10.1 | 8.7 | * | * | 0.9 | 1.1 |
| | | 100 | 100 | 14.4 | 13.2 | 13.7 | 12.5 | * | * | 1.0 | 1.1 |
| | | 140 | 140 | 16.9 | 14.6 | 16.1 | 13.3 | * | * | 1.1 | 1.1 |
| | $\{\alpha\}_6$ | 60 | 70 | 0.32 | 0.32 | 0.34 | 0.62 | * | * | 0.92 | 0.52 |
| | | 100 | 100 | 0.66 | 0.50 | 0.93 | 0.97 | * | * | 0.71 | 0.52 |
| | | 140 | 140 | 0.77 | 0.75 | 1.61 | 1.27 | * | * | 0.48 | 0.60 |
| | $\{\alpha\}_7$ | 60 | 55 | 5.0 | 5.0 | 1.17 | 1.4 | * | * | 4.3 | 3.6 |
| | | 100 | 100 | 7.1 | 7.0 | 1.91 | 2.0 | * | * | 3.7 | 3.5 |
| | | 140 | 140 | 7.7 | 9.2 | 2.15 | 2.7 | * | * | 3.6 | 3.4 |
| $\{\alpha\}_6$ | $\{\alpha\}_4$ | 100 ^a | 100 | 0.21 | 0.27 | 0.38 | 0.42 | 0.08 | 0.05 | 0.55 | 0.64 |
| | $\{\alpha\}_5$ | 100 ^a | 100 | 0.05 | 0.06 | 0.14 | 0.14 | 0.03 | 0.02 | 0.35 | 0.41 |
| | $\{\alpha\}_7$ | 110 ^a | 110 | 7.8 | 8.3 | 6.0 | 6.3 | 3.1 | 3.1 | 1.3 | 1.3 |
| $\{\alpha\}_7$ | $\{\alpha\}_4$ | 95 ^a | 95 | 0.06 | 0.04 | 0.24 | 0.43 | * | * | 0.27 | 0.08 |
| | | 140 | 140 | 0.43 | 0.44 | 1.3 | 1.3 | * | * | 0.33 | 0.33 |
| | $\{\alpha\}_5$ | 95 ^a | 95 | 0.46 | 0.59 | 0.05 | 0.07 | * | * | 9.3 | 8.9 |
| | | 140 | 140 | 2.4 | 2.6 | 0.30 | 0.37 | * | * | 9.0 | 7.0 |
| | $\{\alpha\}_6$ | 95 ^a | 95 | 0.84 | 0.81 | 6.1 | 4.4 | * | * | 0.14 | 0.18 |
| | | 140 | 140 | 2.1 | 2.0 | 9.7 | 7.2 | * | * | 0.22 | 0.28 |

a) Experimental velocity distribution taken into account

potentials mentioned in section 1, which for $R \geq 4.5 a_0$ are identical to those of Hennecart and Masnou-Seeuws, were used throughout. Otherwise, the calculations are similar to those reported before²⁰). The calculated cross section values $Q_{\ell \leftarrow k}^{|M_k|}$ are compared with those derived from the experiment in Table I. The relevant results for the observed cross sections $Q_{\ell \leftarrow k}^\beta$ (using either Eq. (4) or Eq. (5)) are shown in Figs. 1-3 for the $\{\alpha\}_7 \rightarrow \{\alpha\}_{4,5,6}$ transitions and in Figs. 4-6 for the $\{\alpha\}_6 \rightarrow \{\alpha\}_{4,5,7}$ transitions, together with the experimental results. Agreement between experiment and quantal calculations is observed to be generally good.

For the highly endothermic $\{\alpha\}_7 \rightarrow \{\alpha\}_{4,5}$ and $\{\alpha\}_6 \rightarrow \{\alpha\}_{4,5}$ transitions in particular, it is necessary to convolute the quantum-mechanical cross-section values with the experimental energy distribution. This is because the measurements yield energy-averaged results. The total center-of-mass energy spread is typically $\Delta E/E \simeq 40\%$, as determined by the velocity distribution of the supersonic primary and secondary beams²¹). The strong threshold effect in the $\{\alpha\}_7 \rightarrow \{\alpha\}_{4,5}$ transitions ($\Delta E_{75} = -81$ meV, $\Delta E_{74} = -91$ meV) explains, why the observed averaged cross sections are much larger than the cross sections, which would have been obtained in calculations for the average collision energy. For the $\{\alpha\}_6 \rightarrow \{\alpha\}_{4,5}$ transitions ($\Delta E_{65} = -57$ meV, $\Delta E_{64} = -67$ meV) the threshold effect is less severe. This effect plays a progressively smaller role at the higher energies, at which measurements were performed. For the exothermic transitions, it is generally sufficiently accurate to use the average collision energy in the calculation. In the calculation of effective quantum-mechanical cross sections, generally four or five cross section values were available within the width of the experimental energy distribution. The convolution procedure was carried out while linearly interpolating between these values.

The experiment offers two methods of varying the Ne^{xx}-He collision energy²⁰). First, by scanning the laser beam along the primary-beam axis, the position of the scattering volume with respect to the secondary-beam nozzle can be varied. The resulting change in the direction of the secondary-beam velocity \underline{v}_2 effects both direction and magnitude of the relative velocity \underline{g} . Secondly, the magnitude of the primary-beam velocity \underline{v}_1 can be changed through the use of a seeding agent. We have used a 15% Ne - 85% He seeded primary beam, in addition to a 100% Ne beam.

The observed energy dependence of the $\{a\}_5 \rightarrow \{a\}_{4,6}$ and $\{a\}_7 \rightarrow \{a\}_{5,6}$ cross sections, for which most data are available, is discussed in section 4. Generally speaking, the time-consuming nature of quantum-mechanical coupled-channels calculations is prohibitive, when it comes to simulating the energy-dependence of cross sections. In this respect, the semiclassical calculations of section 4 are much less demanding.

3. Semiclassical model

3.1. Adiabatic representation

To facilitate the discussion, without pretending in any way to provide an overview of semiclassical theory, we now introduce a number of key concepts. The system of nuclei and electrons is described by the wave equation

$$i\hbar \frac{\partial \Psi}{\partial t}(\underline{r}, \underline{R}, t) = H \Psi(\underline{r}, \underline{R}, t) = (H_{el} + T_n) \Psi(\underline{r}, \underline{R}, t) \quad (6a)$$

$$T_n = T_{rad} + T_{rot} \quad (6b)$$

$$H_{el} = H_{at} + V_{mol} \quad (6c)$$

in which T_n is the kinetic-energy operator of nuclear motion, with T_{rad} and T_{rot} its radial and angular components, and H_{el} is the electronic Hamiltonian, split into the atomic part H_{at} of the separate particles and the remaining molecular part V_{mol} . Within the framework of our scattering problem, we are interested in solutions $\Psi(\underline{r}, \underline{R})$ of the time-independent Schrödinger equation, where \underline{r} represents all electronic coordinates and \underline{R} is the internuclear radius vector:

$$(T_n + H_{\text{el}}) \Psi(\underline{r}, \underline{R}) = E \Psi(\underline{r}, \underline{R}) \quad (7)$$

with E the total energy in the center-of-mass system.

Now, a fully quantummechanical treatment takes an evenhanded approach to the general problem of coupled nuclear-electronic motion. The wavefunction $\Psi(\underline{r}, \underline{R})$ is expanded in an orthonormal basis of channel functions, characterized by the collective quantum number i :

$$\Psi(\underline{r}, \underline{R}) = \sum_i \frac{F_i(R)}{R} |\varphi_i(\underline{r}, \underline{R})\rangle \quad (8)$$

The channel functions $|\varphi_i(\underline{r}, \underline{R})\rangle$ have the form

$$|\varphi_i(\underline{r}, \underline{R})\rangle = |\varphi_i(\underline{r}'; R) \chi_i(\hat{R})\rangle \quad (9)$$

where $\hat{R} = \underline{R}/R$ indicates the orientation of \underline{R} , and \underline{r}' represents the electronic coordinates \underline{r}'_j in the body-fixed frame. The electronic functions $|\varphi_i(\underline{r}'; R)\rangle$ depend parametrically on R . Substitution of Eq. (8) into Eq. (7) results in a set of coupled differential equations for the wavefunctions $F_i(R)$ of radial nuclear motion. In a basis of adiabatic eigenfunctions of the electronic Hamiltonian H_{el} , for which we have

$$H_{el} |\varphi_i^{ad}\rangle = \{H_{at} + V_{mol}\} |\varphi_i^{ad}\rangle = V_i(R) |\varphi_i^{ad}\rangle \quad (10)$$

non-adiabatic coupling is caused by T_{rad} and T_{rot} .

The semiclassical approach to Eq. (7) consists of separating the coupled electronic-nuclear motion into electronic motion, treated quantum-mechanically, and nuclear motion, which is now treated classically. Supposing for the moment the latter problem solved, with the classical trajectory $\underline{R} = \underline{R}(t)$ as a result, we are left with the time-dependent electronic Schrödinger equation

$$i\hbar \frac{\partial \psi}{\partial t}(\underline{r}; \underline{R}(t)) = H_{el}(\underline{r}; \underline{R}(t)) \psi(\underline{r}; \underline{R}(t)) \quad (11)$$

where the electronic Hamiltonian depends on the time t through the known quantity \underline{R} .

In the adiabatic representation of Eq. (10), with the expansion

$$\psi(\underline{r}; \underline{R}(t)) = \sum_i a_i(t) |\varphi_i^{ad}(\underline{r}; \underline{R}(t))\rangle \exp\left[-\frac{i}{\hbar} \int^t V_i(\underline{R}(t)) dt\right] \quad (12)$$

non-adiabatic coupling is caused by the time-derivative operator

$$-i\hbar \frac{\partial}{\partial t} = -i\hbar \dot{\underline{R}} \frac{\partial}{\partial \underline{R}} - i\hbar \hat{\underline{R}} \cdot \frac{\partial}{\partial \underline{R}} \quad (13a)$$

Taking into account Eq.(9), we have

$$\frac{\partial}{\partial \underline{R}} \Big|_{\underline{r}=\text{const}} = - \sum_j \frac{\partial}{\partial \hat{r}'_j} \Big|_{\perp} = \frac{1}{i\hbar} \underline{J}_{\perp} \quad (13b)$$

with \perp referring to the component perpendicular to the internuclear z' -axis. As a consequence we have

$$-i\hbar \frac{\partial}{\partial t} = -i\hbar v_R \frac{\partial}{\partial R} - \hat{R} \cdot \hat{J}_\perp \quad (14)$$

Here v_R and $|\hat{R}| = \dot{\Theta} = \omega$ are the radial and angular velocities of nuclear motion respectively, Θ being the angle of the internuclear axis with the space-fixed z-axis, i.e. the polar angle in the collision plane. The operator \hat{J}_\perp is perpendicular to the collision plane. Given that $\hat{J}_\perp = \frac{1}{2}(J_{+,z} + J_{-,z})$, where $J_{+,z}$ and $J_{-,z}$ denote the raising and lowering operators for the azimuthal angular momentum M_{J_z} along the internuclear axis, clearly the terms of Eq. (14) represent radial and rotational non-adiabatic coupling, respectively. In practice, radial coupling will occur mainly between adjacent states k and ℓ within a particular Ω -manifold (and reflection-symmetry class, for $\Omega = 0$). Rotational coupling takes place between different Ω -states for a single k , with $|\Omega - \Omega'| = 1$.

Our task will be to find a suitable semiclassical description for both types of coupling, in addition, of course, to working out a solution to the trajectory problem. The calculation of polarized cross sections $Q_{\ell \leftarrow k}^{|M_k|}$ for the $(\alpha_k J_k M_{k,z}) \rightarrow (\alpha_\ell J_\ell)$ electronic transition calls for a semiclassical transition probability $\mathcal{P}_{\ell \leftarrow k}^{|M_k|}(b)$, where b is the impact parameter. For a given \mathcal{P} , it follows directly that

$$Q_{\ell \leftarrow k}^{|M_k|} = \int_0^\infty 2\pi b \mathcal{P}_{\ell \leftarrow k}^{|M_k|}(b) db \quad (15)$$

Thus, it remains to derive a suitable expression for $\mathcal{P}_{\ell \leftarrow k}^{|M_k|}$.

3.2. Radial coupling

Non-adiabatic radial coupling near an avoided crossing of two adiabatic potential curves has first been described semiclassically by the Landau-Zener-Stückelberg (LZS) theory, which has its origin in 1932²⁷⁻²⁹. In its extended LZS-form, this model allows for interference between different collision paths followed by a particle, as opposed to the Landau-Zener (LZ) model. A survey of LZS-theory is given by Thorson e.a.³⁰. There have been numerous additions and extensions to LZS-theory, notably the inclusion of tunneling effects^{31,32}. At the same time, the application range of previous linear models has been greatly extended by the advent of non-linear models^{32,33}. For our analysis of Ne^{**}-He intra-multiplet mixing, the linear model of Nikitin³¹ has a sufficiently wide application range and offers maximum potential for physical insight.

At the basis of the linear model lies a description of the two-state system near the avoided crossing in terms of only weakly R-dependent diabatic states $|\varphi_k^d\rangle$ and $|\varphi_\ell^d\rangle$. At a large distance from the crossing these must coincide with the adiabatic states $|\varphi_k^{ad}\rangle$ and $|\varphi_\ell^{ad}\rangle$. For the diabatic matrix elements of H_{e1} an approximate expression is adopted, retaining only the linear part of the expansion in terms of $(R-R_C)$, with R_C the crossing point of the diabatic potential curves $H_{kk}(R)$ and $H_{\ell\ell}(R)$:

$$\begin{aligned}
 H_{kk}(R) &= H_C - F_k(R-R_C) \\
 H_{\ell\ell}(R) &= H_C - F_\ell(R-R_C) \\
 H_{k\ell}(R) &= H_{\ell k}(R) = H_{k\ell}(R_C) \equiv H_{k\ell}^\Omega
 \end{aligned}
 \tag{16}$$

where $F_j = -\partial/\partial R H_{jj}(R)|_{R=R_C}$ is the slope of the diabatic potential at R_C . The crossing point R_C can then be identified as the point of minimum

splitting between the adiabatic potentials $V_k^\Omega(R)$ and $V_\ell^\Omega(R)$. The crossing potential H_C is given by

$$H_C = \{V_k^\Omega(R_C) + V_\ell^\Omega(R_C)\} / 2 \quad (17)$$

while for the coupling matrix element $H_{k\ell}^\Omega$ we find

$$H_{k\ell}^\Omega = \{V_k^\Omega(R_C) - V_\ell^\Omega(R_C)\} / 2 \quad (18)$$

This situation is clarified in Fig. 7.

For the total probability $P_{k\ell}^\Omega$ of a transition from one adiabatic potential curve to the other, we cite here the limiting case of the original Landau-Zener formula, obtained under the assumption of uniform motion near the crossing radius R_C :

$$P_{k\ell}^\Omega = 2p_{k\ell}^\Omega (1 - p_{k\ell}^\Omega) \quad (19a)$$

$$p_{k\ell}^\Omega = \exp(-v_{k\ell}^\Omega/v_R) \quad (19b)$$

$$v_{k\ell}^\Omega = 2\pi (H_{k\ell}^\Omega)^2 / \hbar |F_k - F_\ell| \quad (19c)$$

Here v_R is the radial velocity, and $v_{k\ell}^\Omega$ a reference velocity that contains all information on the coupling at the avoided crossing. In the LZ-case, with the crossing radius far from the classical turning point ($R_C \gg R_T$), a transition may occur with single-pass transition probability $p_{k\ell}^\Omega$, both on the incoming and on the outgoing transit. For radial velocities $v_R \ll v_{k\ell}^\Omega$, the original adiabatic curve will be followed both coming in and going out, whereas for $v_R \gg v_{k\ell}^\Omega$, on both occasions a crossing to the other curve will take place. In both instances, the total transition probability $P_{k\ell}^\Omega$ amounts

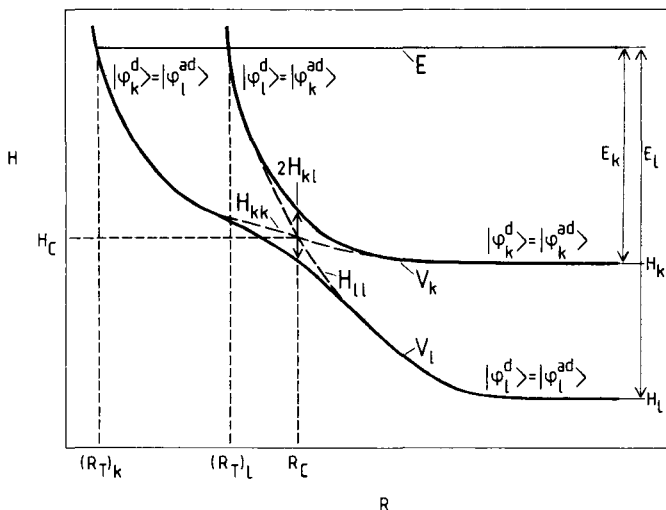


Fig. 7. Schematic picture of an avoided crossing of adiabatic potentials V_k and V_l , with corresponding diabatic potentials H_{kk} and H_{ll} . The crossing parameters of Nikitin's linear model have been indicated, i.e. the crossing point R_C , the crossing energy H_C and the diabatic coupling matrix element H_{kl} . The non-adiabatic transition probability $P_{k\ell}$ is determined by the radial energy at the crossing.

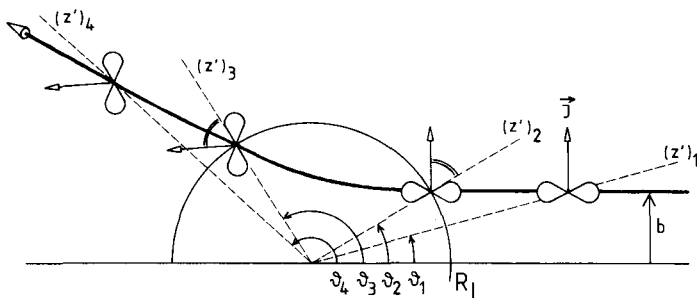


Fig. 8. By introducing a locking radius R_L , we assume the electronic angular momentum J to be space-fixed for $R > R_L$, and locked to the inter-nuclear axis for $R \leq R_L$. Thus, we have purely geometrical Ω -mixing through rotational coupling for $R > R_L$, and Ω -conservation for $R \leq R_L$.

to zero. A net transition is most likely for intermediate velocities $v_R \approx v_{k\ell}$. In particular, the maximum value $P_{k\ell} = 1/2$ is obtained for $v_R = v_{k\ell} / \ln(2)$.

As the classical turning point R_T comes closer to the crossing region ($R_T \lesssim R_C$), interference occurs between incoming and outgoing trajectories. In the general linear model, this is taken into account by postulating constant acceleration by an effective force $F = |F_k F_\ell|^{1/2}$ near the crossing point. The resulting description is equivalent to the quantum-mechanical one³⁴). Quantum-mechanical tunneling (important for $R_T \approx R_C$) is thus simulated, as well. The case of F_k and F_ℓ having a different sign, implying transition over or under a potential barrier near the crossing, will not be considered here.

Depending on the coupling strength, the linear model yields analytical expressions $P_{k\ell}(\epsilon, \beta)$ in certain regions of the (ϵ, β) plane³¹), with

$$\epsilon = \frac{E_C}{2H_{k\ell}} \frac{|F_k - F_\ell|}{|F_k F_\ell|^{1/2}} \tag{20}$$

$$\beta = 4H_{k\ell} \left\{ \frac{\mu H_{k\ell}}{\hbar^2 |F_k F_\ell|^{1/2} |F_k - F_\ell|} \right\}^{1/2}$$

Of the dimensionless parameters ϵ and β , the first characterizes the (radial) kinetic energy $E_C = 1/2 \mu v_R^2$ at the crossing point, the second the non-adiabatic coupling matrix element $H_{k\ell}$. The only region, for which there is no analytical expression for $P_{k\ell}$, is defined by $|\epsilon| \approx 1$, $\beta \approx 1$. However, numerically calculated transition probabilities have been tabulated³⁵).

In practice, the centrifugal potential E_{rot} combines with the adiabatic potentials V_k^Ω to form effective potentials $V_{\text{eff},k}^\Omega(R) = V_k^\Omega(R) + E_{\text{rot}}(R)$. Through $E_{\text{rot}} = 1/2 \mu g^2 b^2 / R^2$, the single-transit and total

transition probabilities therefore depend on the impact parameter b (and, of course, on the relative velocity g), and will hereafter be denoted as $P_{k\ell}^{\Omega}(b)$ and $P_{k\ell}^{\Omega}(b)$, respectively.

3.3. Rotational coupling

For polarized cross sections $Q_{\ell \leftarrow k}^{|\mathbf{M}_k|}$ to be determined from the transition probability $P_{k\ell}^{\Omega}(b)$ of the preceding section (with $\Omega = |\mathbf{M}_k|_z$), it is necessary that the distribution over $M_{k,z}$ states at the crossing radius R_C be known. The development of a distribution $G_k^{M'_{k,z'}}(R)$ from an initial distribution $G_k^{M_{k,z'}}(-\infty) = \delta_{M_{k,z'}, M_k}$ is a matter of non-adiabatic rotational coupling between states $|\alpha_{k k} J_k M_{k,z}\rangle$ and $|\alpha_{k k} J_k M_{k,z} \pm 1\rangle$.

The problem of rotational coupling can be reformulated in compliance with the original LZ-formalism³⁶⁾. The dynamical state model³⁷⁾ even enables one to apply LZS-theory to cases involving both radial and rotational coupling. In the case of a C_s/R^5 adiabatic potential difference, a different general treatment is possible as well³⁸⁾. However, for our $Ne^{*n}-He$ problem, a somewhat simpler approach is both possible and desirable.

Rotational coupling, of course, simply reflects the effect of describing an essentially space-fixed electronic state in a rotating body-fixed coordinate system. However, it is unrealistic to suppose that the electronic angular momentum \mathbf{J} will retain its space-fixed orientation along the entire trajectory. The "mathematical" rotational coupling must at all times compete with the Ω -conserving "physical" coupling that gave rise to the adiabatic potentials $V_k^{\Omega}(R)$. Their relative importance depends on the magnitude of the Ω -splitting

$$\Delta V_k^{\Omega\Omega'}(R) = V_k^\Omega(R) - V_k^{\Omega'}(R) \quad (21)$$

compared to the rotational coupling strength

$$T_{\text{rot}}^{\Omega\Omega'} \simeq \{N(N+1)\}^{1/2} \hbar^2 / \mu R^2 \quad (22)$$

where $|\Omega - \Omega'| = 1$.

There are two limiting cases to be discerned. If the Ω -splitting greatly outweighs the rotational coupling strength, i.e. if $\Delta V_k^{\Omega\Omega'} \gg T_{\text{rot}}^{\Omega\Omega'}$, the internuclear axis serves as the effective quantisation axis and the orientation of the electronic wave function is "locked" to it. For values $\Delta V_k^{\Omega\Omega'} \ll T_{\text{rot}}^{\Omega\Omega'}$, the electronic state observes no angle-dependent forces and remains space-fixed. In a semiclassical context, the inherently problematic transition between these extremes is often considered to occur at a fixed position R_L , the so-called "locking" radius, where the rotational coupling strength equals the Ω -splitting:

$$\Delta V_k^{\Omega\Omega'}(R_L) = f_L \{N(N+1)\}^{1/2} \hbar^2 / \mu R_L^2 \quad (23)$$

For future reference, we have included here a "locking factor" f_L .

More insight into the phenomenon of "locking" than provided by the above can be obtained from classical mechanics. The Ω -splitting $\Delta V^{\Omega\Omega'}$ correlates with an angle-dependent force and thus with a torque, which operates on the spinning top representing the angular momentum \mathbf{J} . The net result of this torque is a precession of \mathbf{J} about the internuclear z' -axis, with angular frequency

$$\omega_{\text{prec}} = \Delta V^{\Omega\Omega'} / \hbar \quad (24)$$

On the other hand, there is the angular velocity of the internuclear axis, due to nuclear motion:

$$\dot{\Theta} = \{N(N+1)\}^{1/2} \hbar/\mu R^2 . \quad (25)$$

If $\omega_{\text{prec}} \gg \dot{\Theta}$, then \underline{J} will precess so rapidly about the internuclear axis as to rotate with it, which implies locking. For $\omega_{\text{prec}} \ll \dot{\Theta}$, \underline{J} is bound to remain space-fixed, since there is hardly time for \underline{J} to precess at all during the internuclear axis' rotation from $\Theta(-\infty) = 0$ to $\Theta(\infty) \lesssim \pi$. Defining the onset of locking by $\Omega_{\text{prec}} = f_L \dot{\Theta}$, we again find Eq. (23).

It is the spinning top image of Eqs. (24) and (25) in particular, which suggests the insertion of a "locking factor" $f_L > 1$ to the right of the equality sign in Eq. (23). For $f_L = 4$, say, we have one full precession of \underline{J} for a typical $\Theta = \pi/2$ rotation of the internuclear axis.

Another approach is based on the principle of energy conservation. In this case, we have to compare the change of energy for a unity change of the quantum numbers Ω and N , i.e.

$$\frac{d}{d\Omega} V^\Omega = V^{\Omega'} \quad (26)$$

and

$$\frac{d}{dN} E_{\text{rot}} = (N+1/2) \hbar^2/\mu R^2 \quad (27)$$

where E_{rot} is the rotational energy. If $\frac{d}{d\Omega} V^\Omega \gg \frac{d}{dN} E_{\text{rot}}$, we expect Ω to be conserved, that is to say locking, since a change in Ω would require an unrealistically large change in N to provide for the necessary change in E_{rot} . Likewise, the condition $\frac{d}{d\Omega} V^\Omega \ll \frac{d}{dN} E_{\text{rot}}$ means that N must remain unchanged and that rotational coupling will act on the space-fixed \underline{J} , changing Ω . With $\frac{d}{d\Omega} V^\Omega = f_L \frac{d}{dN} E_{\text{rot}}$ and writing $(N+1/2) \simeq \{N(N+1)\}^{1/2}$, we once more have Eq. (23).

The simplification, implicit in the concept of a locking radius, has met with considerable success, e.g. in the $\text{Na}^* + \text{Na}^+$ case³⁹). The picture of sudden locking, as illustrated by Fig. 8, is quite appropriate in the present $\text{Ne}^{**}\{\alpha\}_{4,5,6,7} + \text{He}$ context, as will be shown in section 3.5.

Where "locking" pertains, the distribution $G_k^\Omega(R)$ over $|\alpha_k J_k \Omega \equiv |M_k|_z\rangle$ states is bound to remain unchanged. For pure rotational coupling, the effect of a rotation θ_{12} of the internuclear z' -axis between two positions $R_1(t_1)$ and $R_2(t_2)$ can be described in terms of the rotation matrices d^{26}). Given a suitable choice for the x' - and y' -axes, we may write, with $G_k^\mathcal{M}$ the distribution over $\mathcal{M} \equiv M_{k,z}$:

$$G_k^\mathcal{M}(R_2) = \sum_{\mathcal{M}'} \left\{ d_{\mathcal{M} \mathcal{M}'}^{J_k}(\theta_{12}) \right\}^2 G_k^\mathcal{M}(R_1) \quad (28)$$

Thus, for $J = 1$, an initial $\mathcal{M} = 0$ state (represented by $G_k^\mathcal{M}(R_1) = \delta_{\mathcal{M},0}$) will be mixed according to $G_k^1(R_2) = \sin^2 \theta_{12}$ and $G_k^0(R_2) = \cos^2 \theta_{12}$, etc.

3.4. The $\text{Ne}^{**}\text{-He}$ case: avoided crossings

In practice, for $\text{Ne}^{**}\text{-He}$, the various crossing-parameters are determined from figures like Fig. 9 and 10 of the adiabatic potentials, following the guidelines established in section 3.1. The imperfect match to the linear model's assumptions introduces an arbitrary element into the choice of "best" diabatic potentials. Also, the adiabatic potentials themselves, at a given point R_C , are bound to allow of small uncertainties. In view of this, it seems appropriate to allow some small realistic latitude in determining optimum effective diabatic slope parameters, in particular. In this respect we did not think it necessary to include negative potential

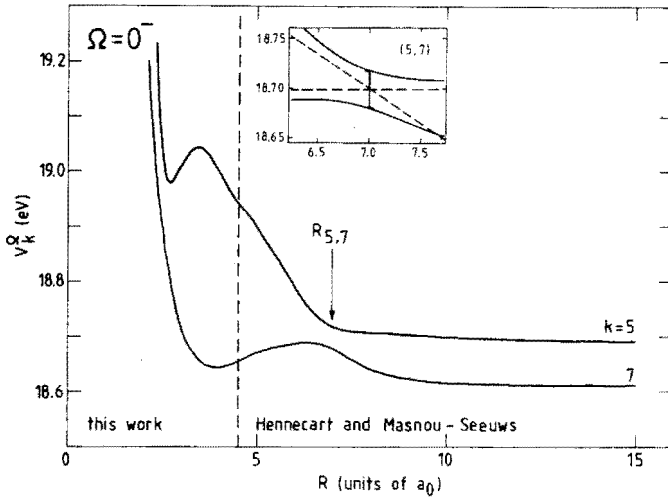


Fig. 9. Adiabatic potential curves $V_k^\Omega(R)$ for $k = 5, 7$ and $\Omega = 0^-$. The arrow points to the position $R_{5,7}$ of the avoided crossing. The insert shows the crossing region in more detail. The diabatic potentials and the coupling matrix element, indicated in the figure, are given in Table II. See Fig. 7 for comparison.

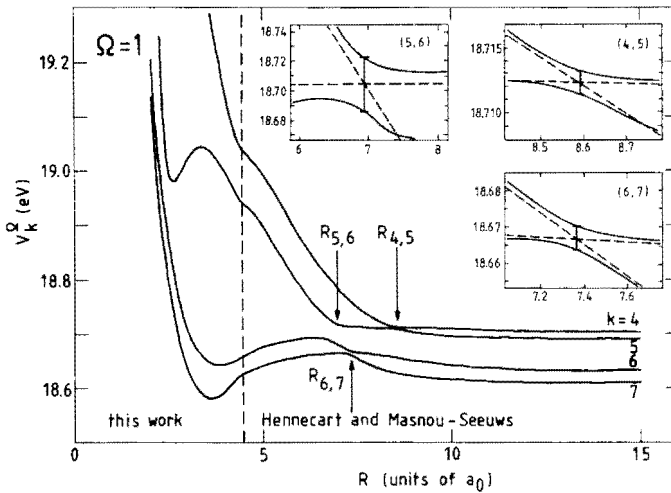


Fig. 10. Adiabatic potential curves $V_k^\Omega(R)$ for $k = 4, 5, 6, 7$ and $\Omega = 1$. The arrows point to the position $R_{k,e}$ of the avoided crossings. See caption of Fig. 9 for further detail.

slopes. What negative slopes can be construed are small, the more so if rotational energy is included. Negative slopes would unnecessarily complicate the radial coupling picture³¹⁾.

The effective crossing parameters, thus determined, are given in Table II. They correspond to the diabatic potentials and coupling matrix elements that are indicated in Figs. 9 and 10. All calculations in the present work have used these values. We expressly point out the effect of reflection symmetry, whereby for $\Omega = 0^-$ only a single (57)-avoided crossing is present, as opposed to the three (45)-, (56)- and (67)-crossings for $\Omega = 1$. Also, it is noteworthy, that the reference velocities $v_{k\ell}$ of the (57)- and (56)-crossings on the one hand, and the (45)- and (67)-crossings on the other, differ by an order of magnitude.

The values of $H_C - H_k$ in Table II indicate how easily the crossing can be reached. For an estimate of the range of impact parameters b contributing to the cross section for a given initial energy E_k , we must compare the rotational energy at the crossing radius R_C with the total kinetic energy available there. If the crossing is to be reached at all, some radial energy must remain, which gives rise to the following condition for the impact parameter b :

$$\left(\frac{b}{R_C}\right)^2 \leq \frac{E_k - (H_C - H_k)}{E_k} \quad (29)$$

For positive values of $(H_C - H_k)$, the range is $b < R_C$. Of course, in terms of the classical turning point R_T , Eq. (29) translates to $R_T(b) \leq R_C$.

A closer view of the radial coupling at and near the various avoided crossings of Table II is offered by Fig. 11 of the radial coupling matrix elements $\langle \alpha_\ell J_\ell \Omega | \partial / \partial R | \alpha_k J_k \Omega \rangle$. In all cases where an avoided crossing of the adiabatic potential curves is present, the corresponding $\partial / \partial R$ -matrix

Table II. Characteristic linear-model parameters for the avoided crossings of the $\{\alpha\}_{4,5,6,7}$ group as shown in Figs 9-10. A broad distinction can be made between crossings with a high and with a low reference velocity v_{kl} . This is instrumental in explaining the observed differences in cross section behavior. For comparison, the asymptotic energy difference ΔE_{kl} is given, as well.

| Crossing (k, l) | Ω | R_C (a_0) | H_{kl} (meV) | F_k (meV/ a_0) | F_l (meV/ a_0) | v_{kl} (m/s) | $H_C - H_k$ (meV) | $H_C - H_l$ (meV) | ΔE_{kl} (meV) | $\delta R_C =$ $H_{kl}/\Delta F$ (a_0) |
|--------------------|----------|--------------------|-------------------|------------------------|------------------------|-------------------|----------------------|----------------------|--------------------------|--|
| 57 | 0^- | 7.0 | 20 | 70 | 0 | 2900 | 6 | 87 | 80.6 | 0.28 |
| 45 | 1 | 8.60 | 0.9 | 21 | 0.6 | 20 | 9 | 19 | 10.7 | 0.05 |
| 56 | 1 | 6.95 | 17.8 | 75 | 0 | 2150 | 11 | 68 | 56.5 | 0.24 |
| 67 | 1 | 7.35 | 3.6 | 42 | 1.9 | 165 | 31 | 55 | 24.1 | 0.09 |

Table III. Position R_{\max} , height $\langle \partial/\partial R \rangle_{\max}$ and width ΔR of the peaks of the radial-coupling matrix elements $\langle \alpha_{\ell} J_{\ell} \Omega | \partial/\partial R | \alpha_k J_k \Omega \rangle$, associated with the avoided crossings of Table II. The peaks are shown in Fig. 11. See caption of that figure.

| Crossing (k, l) | Ω | R_{\max} (a_0) | $\langle \partial/\partial R \rangle_{\max}$ (a_0^{-1}) | ΔR (a_0) |
|--------------------|----------|-------------------------|--|-------------------------|
| 57 | 0^- | 6.95 | 1.0 | 0.95 |
| 45 | 1 | 8.55 | 5.7 | 0.17 |
| 56 | 1 | 6.90 | 1.1 | 0.80 |
| 67 | 1 | 7.35 | 3.5 | 0.27 |

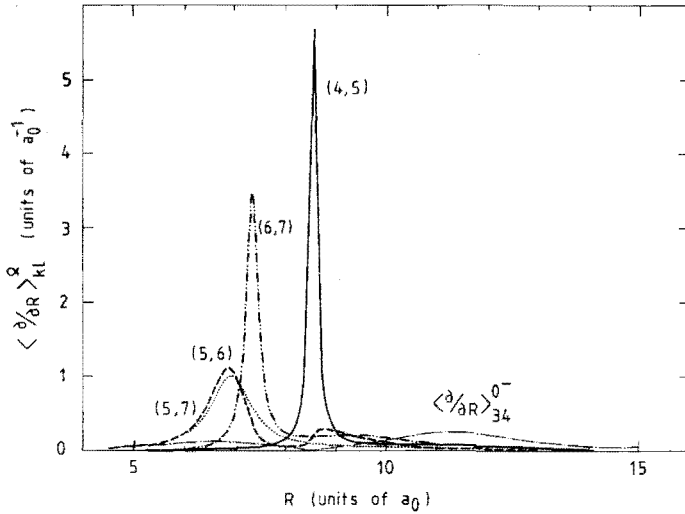


Fig. 11. The radial coupling matrix element $\langle \alpha_l J_l \Omega | \partial/\partial R | \alpha_k J_k \Omega \rangle$ has a sharp peak, if an avoided crossing of the adiabatic potentials $V_k^\Omega(R)$ and $V_\ell^\Omega(R)$ is present. This lies at the basis of our model assumption, that radial coupling is localized at the crossing radius R_C . The matrix element $\langle \alpha_3 J_3 \Omega=0^- | \partial/\partial R | \alpha_4 J_4 \Omega=0^- \rangle$, which is not associated with an avoided crossing and therefore denoted as $\langle \partial/\partial R \rangle_{34}^{0^-}$, extends over a far wider range.

elements display a peak at the crossing radius R_C . This is in contrast with the behaviour of a $\partial/\partial R$ -matrix element in the absence of an avoided crossing, exemplified here by the $\langle \alpha_3 J_3 \Omega=0^- | \partial/\partial R | \alpha_4 J_4 \Omega=0^- \rangle$ matrix element, which is both smaller and extends over a considerably wider range. The peak values and FWHM-widths of the $\partial/\partial R$ -peaks in Fig. 11 are listed in Table III. By comparison, the maximum value of the $\langle \alpha_3 J_3 \Omega=0^- | \partial/\partial R | \alpha_4 J_4 \Omega=0^- \rangle$ matrix element is only $0.25 a_0^{-1}$ which still makes it larger than most matrix elements not associated with an avoided crossing. The width of the widest $\partial/\partial R$ -peaks is roughly of a size with the minimum wavelengths, encountered at R_C for an initial energy $E = 100$ meV. These are obtained for head-on collisions. For the (57)-crossing for $\Omega = 0^-$, $E_5 = 100$ meV yields $\lambda_C \leq 0.97 a_0$. An energy $E_4 = 100$ meV translates, through multiple curve crossings, to $\lambda_C \leq 0.87 a_0$ for the (67)-crossing for $\Omega = 1$. For $E_6 = 100$ meV, we find for this crossing $\lambda_C \leq 1.12 a_0$. This illustrates the localized nature of the avoided crossings.

Comparing Tables II and III, the close relationship between crossing parameters and $\partial/\partial R$ -matrix element characteristics is obvious. The peak positions R_{\max} are seen to coincide with the crossing radii R_C . The order of magnitude of peak-values $\langle \partial/\partial R \rangle_{\max}$ not unexpectedly compares closely to that of the reference velocities $v_{k\ell}$. Lastly, the width of the coupling region $\delta R_C = H_{k\ell}/\Delta F^{31}$) is directly proportional to the peak-width ΔR . In fact, we find approximately $\Delta R \simeq 4\delta R_C$.

3.5. The Ne^{**} -He case: rotational coupling vs locking

In Figs. 12-15 we have plotted the Ω -splitting $\Delta V_k^{\Omega'}$ and the rotational coupling strength $T_{\text{rot}}^{\Omega'}(N)$ as a function of the internuclear distance R . From these figures we can determine the locking radius R_L , as defined by Eq. (23). In principle, R_L depends upon the impact parameter b ,

which is related to the rotational quantum number N by the semiclassical correspondence relation

$$b = (N + \frac{1}{2}) \lambda_k \quad (30)$$

with $\lambda_k = h/\mu g$ the De Broglie wavelength in the incoming channel. For the $\text{Ne}^{*x}\text{-He}$ system, in practical units, Eq. (30) translates to

$$b = 0.149 [a_0] N (E_k/100 \text{ meV})^{-\frac{1}{2}} \quad (31)$$

Equation (23), with "locking factor" $f_L = 1$, yields locking radii $R_L(N)$ which are quite far out, especially for low N -values. In fact, at the present thermal energies, they are larger than even the largest crossing radius R_C of Table II over a considerable part of the range of contributing impact parameters. This would effectively negate the role of rotational coupling in bringing about transitions between states $\{\alpha\}_k$ and $\{\alpha\}_\ell$. It is when postulating a locking factor $f_L \approx 4$ in Eq. (23), that the steep rise of the Ω -splitting with decreasing R enables us to define effective locking radii R_L for the $\{\alpha\}_{4,6,7}$ states, valid for all impact parameters b that contribute to the cross sections of interest. This approach yields the R_L given in Table IV. For the $\{\alpha\}_5$ state, the criterion for locking is met only over a much more limited range of R - and N -values than for the other states. Since the turning point is always quite far out for this state anyway, we have neglected locking for $\{\alpha\}_5$ altogether. With a single exception, explained later, these are the locking radii which have been used in our calculations.

Looking at Table IV, we observe that locking will occur at a rather large internuclear distance $R = 7-8 a_0$ for all states, except perhaps $\{\alpha\}_5$. Even so, comparison with the crossing radii of Table II shows that in all

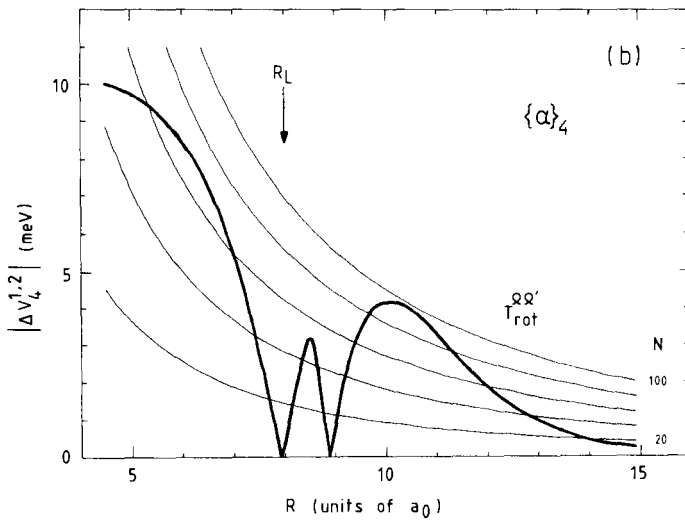
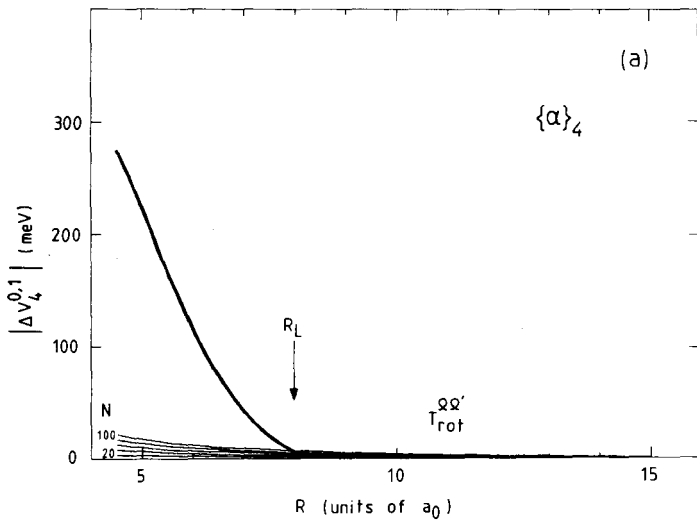


Fig. 12.

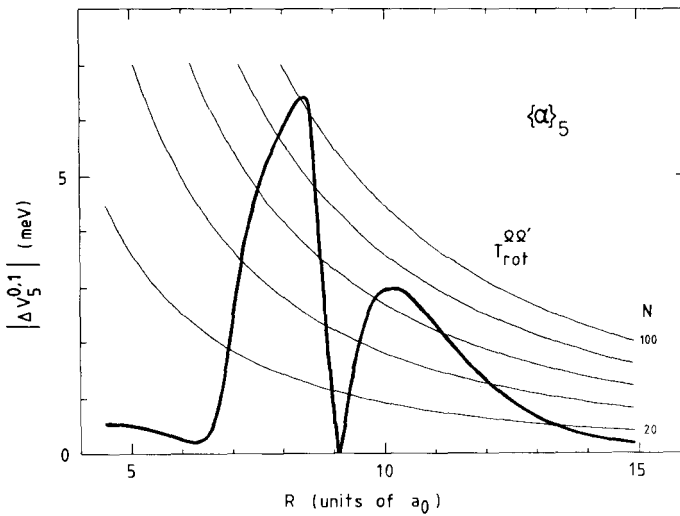


Fig. 13.

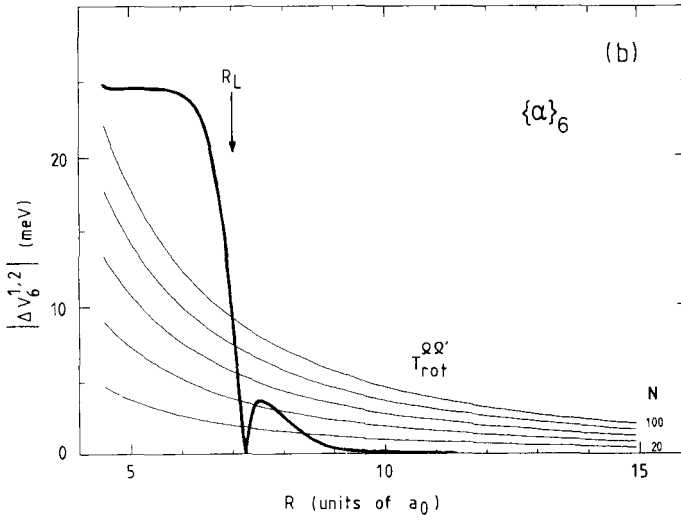
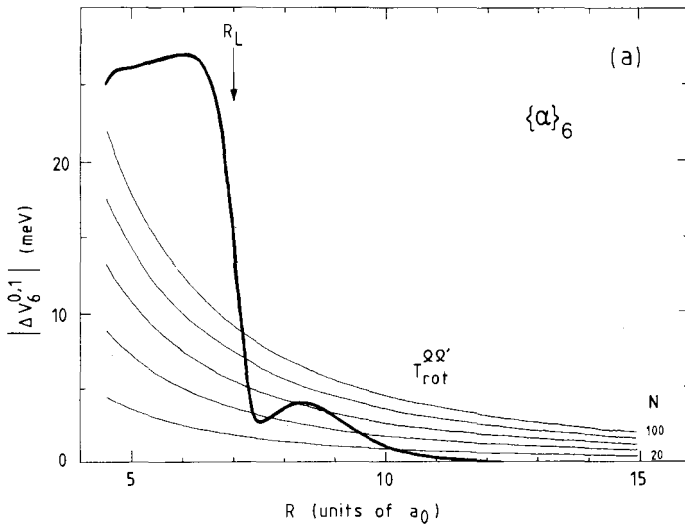


Fig. 14.

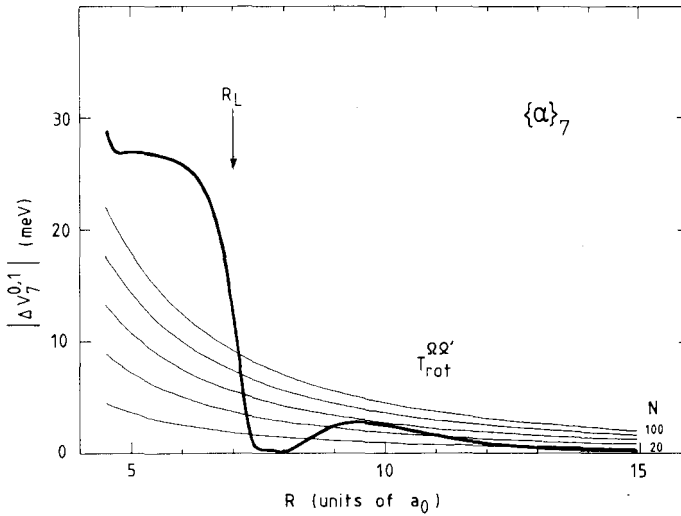


Fig. 15.

Fig. 12. The Ω -splitting $\Delta V_k^{\Omega\Omega'}(R)$ of the adiabatic potentials for $k = 4$ and $\Omega, \Omega' = 0, 1$ (a); $\Omega, \Omega' = 1, 2$ (b). Comparison with the rotational coupling strength $T_{\text{rot}}^{\Omega\Omega'}(R)$, in accordance with Eq. (23), offers a criterion for determining a locking radius R_L . The effective locking radius of Table III coincides with the observed steep rise of the Ω -splitting.

Fig. 13. The Ω -splitting $\Delta V_k^{\Omega\Omega'}(R)$ for $k = 5$ and $\Omega, \Omega' = 0, 1$. Locking would seem to occur intermittently. See caption of Fig. 12 for further detail.

Fig. 14. The Ω -splitting $\Delta V_k^{\Omega\Omega'}(R)$ for $k = 6$ and $\Omega, \Omega' = 0, 1$ (a); $\Omega, \Omega' = 1, 2$ (b). Note the "hump" at large R -values, which makes it hard to define a single effective locking radius R_L . See caption of Fig. 12 for further detail.

Fig. 15. The Ω -splitting $\Delta V_k^{\Omega\Omega'}(R)$ for $k = 7$ and $\Omega, \Omega' = 0, 1$. Once more, it is possible to define an overall locking radius R_L . See caption of Fig. 12 for further detail.

cases rotational coupling will have its Ω -mixing effect, at least up to or even slightly beyond the various avoided crossings. What consequences this has for the $\{a\}_k \rightarrow \{a\}_\ell$ cross sections, will be discussed in detail in section 4.

At higher initial energies than encountered in this paper, there will be locking only for a limited range of impact parameters $b < R_L$. With the Ω -splitting rising steeply at R_L to an approximate value $\Delta V_{k,\max}^{\Omega\Omega'}$, we may perform the following estimate. The energies E_L , for which the locking criterion of Eq. (23), will just barely be met on a trajectory with an impact parameter equal to the locking radii R_L of Table IV, are defined by

$$V_{k,\max}^{\Omega\Omega'} = f_L T_{\text{rot}}^{\Omega\Omega'}(R_L; b=R_L, E=E_L) \quad (35)$$

The values of $\Delta V_{k,\max}^{\Omega\Omega'}$ and the corresponding energy-values are given in Table IV, as well. It may be concluded, that for thermal energies the present concept of a universal locking radius has practical application.

4. Application to the $\{a\}_{4,5,6,7}$ group

4.1. Single- and multiple-curve-crossing model

For the calculation of polarized cross sections $Q_{\ell \leftarrow k}^{|M_k|}$, in accordance with Eq. (15), it remains to combine the concepts of radial coupling and locking and use these with trajectory information in the computation of the total transition probability $\mathcal{P}_{\ell \leftarrow k}^{|M_k|}$.

Table IV. Effective locking radii R_L for the thermal energy range, deduced from the $\{a\}_{4,5,6,7}$ adiabatic potentials, and approximate values $\Delta V_{k,\max}^{\Omega\Omega'}$ of the Ω -splitting at R_L . In addition, the approximate collision energies E_L are given, at which the concept of a universal locking radius for the states in question must break down, as specified by Eq. (35) with a locking factor $f_L = 4$. For $f_L = 1$ the values of E_L would be higher by a factor 16.

| State k | R_L (a_0) | $\Delta V_{k,\max}^{\Omega\Omega'}$ (meV) | E_L (meV) |
|------------|--------------------|--|----------------|
| 4 | 8.0 | 22 ^a | 220 |
| 5 | -- | -- | -- |
| 6 | 7.1 | 26 | 240 |
| 7 | 7.0 | 24 | 210 |

a) Value at $R = 7.5 a_0$.

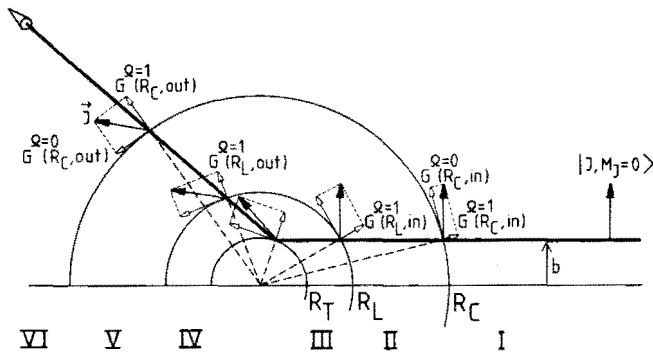


Fig. 16. Overview of the collision process according to the semiclassical model expounded in the text. Indicated are the crossing radius R_C , the locking radius R_L and the turning point R_T . For $R > R_L$, we have rotational coupling; for $R \leq R_L$, locking. At $R = R_C$ a non-adiabatic transition may take place, both on the incoming and on the outgoing trajectories. The latter are assumed straight-lined, with hard-sphere scattering at $R = R_T$. We explicitly point out that, for the distribution $G_k^\Omega(R)$ over Ω -states, we have: $G_k^\Omega(R_C, \text{in}) \neq G_k^\Omega(R_C, \text{out})$, $G_k^\Omega(R_L, \text{in}) = G_k^\Omega(R_L, \text{out})$.

As to trajectories, in a discussion of rotational coupling, knowledge of the orientation of the internuclear z-axis for any given R (but in particular, of course, for $R = R_C$ and $R = R_L$) clearly is indispensable. Classical trajectories are often assumed to be constant-velocity, straight-lined. While assuming straight-line trajectories, a scattering plane can still be defined by in- and outgoing relative velocities for a very small scattering angle³⁹⁾. All the same, curved trajectories have been used in a semiclassical context⁴⁰⁾. In our present model, we will assume scattering from a hard sphere, with radius equal to the (impact-parameter dependent) classical turning point R_T .

Single-curve-crossing model

At the basis of our semiclassical model are a number of approximations and assumptions. Firstly, radial coupling is taken to be strictly localized at the crossing radius R_C . Figure 11 of the $\langle \alpha_\ell J_\ell \Omega | \partial/\partial R | \alpha_k J_k \Omega \rangle$ radial coupling matrix elements lends legitimacy to this assumption, even in the case of the (57)-matrix element which exhibits the least pronounced peak. As in Landau-Zener theory, we distinguish between incoming and outgoing transits of the avoided crossing (thus neglecting interference effects). This permits complete separation of radial and rotational coupling. Secondly, there is assumed to be a sharp transition, at the locking radius R_L , between pure rotational coupling and locking. Justification for this lies in the behaviour of the Ω -splitting of the adiabatic potentials, as shown in Figs. 12-15. Lastly, in the now disconnected issue of particle trajectories, we postulate hard-sphere scattering at the classical turning point R_T . Of course, at the price of additional computational effort the model could easily accommodate both impact-parameter dependent locking radii and more realistic trajectories. This was deemed unnecessary, for the moment, in view of various other simplifications inherent to the model.

In the end, for a transition caused by a single avoided crossing, the collision process is as depicted in Fig. 16, where $R_T < R_L < R_C$. On the straight-line ingoing trajectory at impact parameter b , we have rotational coupling down to R_C , where the distribution $G_k^{\mathcal{M}}(R)$ over magnetic substates $\mathcal{M} \equiv M_{k,z}$, can be determined. At R_C , each substate may cross from the initial $V_k^{\Omega}(R)$ curve to the $V_{\ell}^{\Omega}(R)$ curve, with a transition probability $p_{k\ell}^{|\mathcal{M}|}$. Of course, this implies a probability $(1-p_{k\ell}^{|\mathcal{M}|})$ of following the initial curve. The two fractions are then traced separately, once more undergoing rotational coupling down to their respective locking radii R_L , where the angular momentum becomes body-fixed, so that the distribution remains constant. At the respective classical turning points R_T , hard-sphere scattering takes place. Then, on the outgoing trajectory, the reverse process evolves.

In view of this, the following expression may be written down for the total probability $\mathcal{P}_{\ell \leftarrow k}^{|\mathcal{M}_k|}$ of a transition from the polarized $|\alpha_k J_k M_k\rangle$ state to the $|\alpha_{\ell} J_{\ell}\rangle$ state (the roman numerals denote the various R-regions in Fig. 16):

$$\mathcal{P}_{k\ell}^{M_k}(b) = \sum_{\mathcal{M}=-J_k}^{J_k} g_k^{M_k \mathcal{M}}(\theta_I) p_{k\ell}^{|\mathcal{M}|}(b) \left\{ \sum_{\mathcal{M}'=-J_{\ell}}^{J_{\ell}} g_{\ell}^{\mathcal{M}\mathcal{M}'}(\theta_{II}+\theta_V) [1-p_{k\ell}^{|\mathcal{M}'|}(b)] \right\} \quad (33)$$

$$+ \sum_{\mathcal{M}=-J_k}^{J_k} g_k^{M_k \mathcal{M}}(\theta_I) [1-p_{k\ell}^{|\mathcal{M}|}(b)] \left\{ \sum_{\mathcal{M}'=-J_k}^{J_k} g_k^{\mathcal{M}\mathcal{M}'}(\theta_{II}+\theta_V) p_{k\ell}^{|\mathcal{M}'|}(b) \right\}$$

$$g_k^{\mathcal{M}\mathcal{M}'} = \{d_{\mathcal{M}\mathcal{M}'}^{J_k}\}^2$$

with $\mathcal{M} \equiv M_{k,z}$, or $\mathcal{M} \equiv M_{l,z}$, as appropriate.

In cases where LZ-theory applies, the appropriate formula yields $p_{k\ell}^{|\mathcal{M}|}$ directly. Otherwise, an effective single-pass transition probability $p_{k\ell,\text{eff}}^{|\mathcal{M}|}$ has been introduced, calculated from the averaged total transition probability $P_{k\ell}^{\Omega}(\epsilon, \beta)$ of Nikitin, in accordance with Eq. (19a). In the light of our calculation of total (as opposed to differential) cross sections, there is justification for the omission of interference effects implied by this procedure. Of course, for $R_T \simeq R_C$, interference effects once more are fully accounted for, the rotation between R_C and R_T being negligible under the circumstances. Likewise, there is no limitation on tunneling, since this presupposes $R_T \simeq R_C$ anyway. The straight-line trajectories make for a very simple calculation of rotation angles θ .

Multiple-curve-crossing model

As is plainly evident from Fig. 10, a $\{\alpha\}_k \rightarrow \{\alpha\}_\ell$ transition may have to take place via more than one avoided crossing. Of course, the principles expounded in the previous section still apply. Now, we must keep track of all possible particle trajectories, along different adiabatic potentials, with different locking-radii R_L and turning points R_T . Every relevant route along the various curve crossings consists of non-adiabatic crossings (probability $p_{k\ell}^{|\mathcal{M}|}$) and adiabatic non-crossings (probability $1-p_{k\ell}^{|\mathcal{M}|}$). Keeping track of the distribution over $\mathcal{M} \equiv M_z$ -states at each crossing poses a considerable book-keeping problem. In practice, however, matters may be considerably simplified. Given the relative position of the various avoided crossings and the locking behaviour of the states involved (see Tables II and IV), the interaction between the $\Omega = 0^-$ and $\Omega = 1$ manifolds is bound to be minimal, in the $\text{Ne}^{*x}\text{-He}$ case. Our calculations have therefore been limited to a single Ω -manifold at a time. Otherwise, all effects of rotational coupling have been properly accounted for.

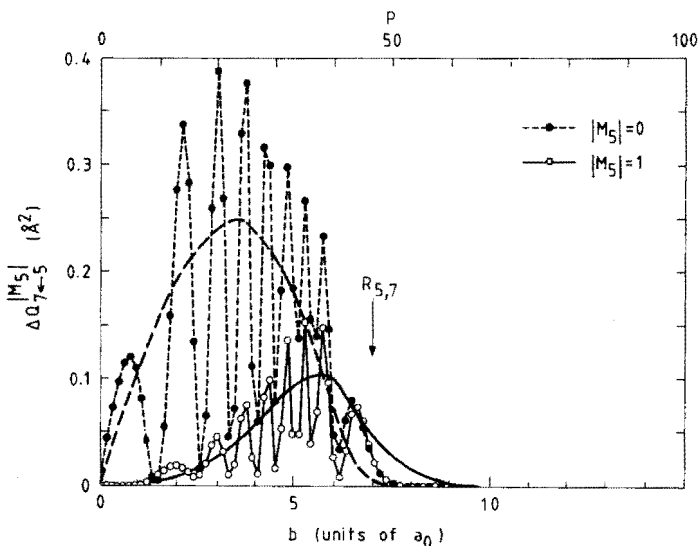


Fig. 17. Semiclassical cross section contributions $dQ_{7\leftarrow 5}^{|M_5|}(b)/db$, as a function of the impact parameter b , at energy $E_5 = 100$ meV. The dashed line (---) represents $|M_5| = 0$, the solid line (—) $|M_5| = 1$. They compare closely with their quantum-mechanical analogues $\Delta Q_{7\leftarrow 5}^{|M_5|}(P)$, indicated by full points (\bullet) for $|M_5| = 0$, and open points (\circ) for $|M_5| = 1$. Fairly small impact parameters are preferred, yielding a large orientation effect. The arrow points to the avoided-crossing position $R_{5,7}$.

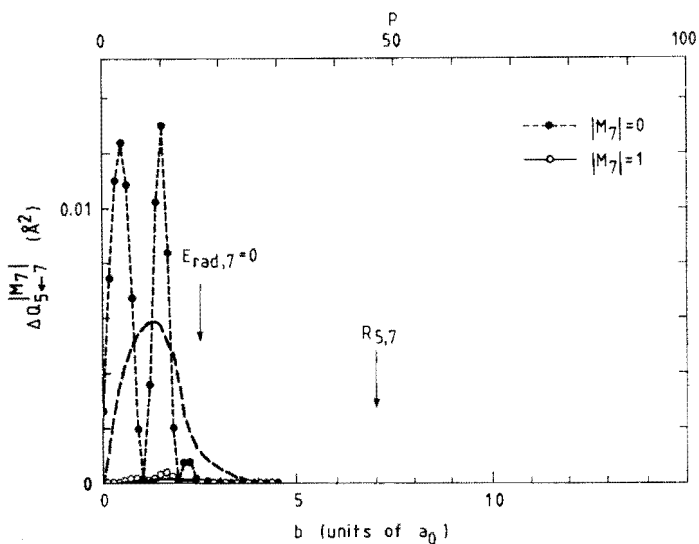


Fig. 18. Semiclassical and quantum-mechanical cross section contributions $dQ_{5\leftarrow 7}^{|M_7|}(b)/db$ and $\Delta Q_{5\leftarrow 7}^{|M_7|}(P)$, at energy $E_7 = 100$ meV. The endothermic nature of the transition dictates a preference for even smaller impact parameters than in the case of the reverse transition of Fig. 17. See caption of Fig. 17 for further detail.

A cross section calculation for a single energy at present takes only about 30 seconds on an AT-compatible microcomputer with numerical co-processor. This contrasts sharply with the 2-3 hours on a Burroughs B7900 mainframe computer, required by every quantum-mechanical calculation²⁰⁾, which translates to 30 to 45 hours on the AT-compatible microcomputer.

4.2. The $\{\alpha\}_5 \leftrightarrow \{\alpha\}_7$ transitions

The $\{\alpha\}_5 \leftrightarrow \{\alpha\}_7$ transitions are governed almost exclusively by the (57)-avoided crossing for $\Omega = 0^-$. The greatly disparate reference velocities of the (45)-, (56)- and (67)-crossings for $\Omega = 1$ make a multiple curve-crossing $\{\alpha\}_5 \leftrightarrow \{\alpha\}_7$ transition unlikely. The high reference velocity $v_{57}^{\Omega=0}$ implies a main cross-section contribution from small impact parameters, where radial velocities are large ("head-on" collisions). Even without locking, the initial Ω orientation will then be largely conserved at the crossing. Hence, the large polarisation effect $Q_{7 \leftarrow 5}^{|0|} \gg Q_{7 \leftarrow 5}^{|1|}$ in the $\{\alpha\}_5 \rightarrow \{\alpha\}_7$ cross sections. With $\{\alpha\}_7$ as initial state, the radial energy at the crossing is less than with $\{\alpha\}_5$. So, the main contribution to the $\{\alpha\}_7 \rightarrow \{\alpha\}_5$ cross section will come from even smaller impact parameters than in the $\{\alpha\}_5 \rightarrow \{\alpha\}_7$ case (Eq. (29)). This translates to both a smaller $\{\alpha\}_7 \rightarrow \{\alpha\}_5$ cross section and a larger polarisation effect.

The above is illustrated by Figs. 17 and 18, which compare semiclassical cross section contributions $dQ_{5 \leftarrow 7}^{|M_k|}(b)/db$ with their quantum-mechanical counterparts $\Delta Q_{5 \leftarrow 7}^{|M_k|}(P)$ at an initial energy $E = 100$ meV. For this, we have made use of the correspondence relation of Eq. (30) and approximated the total angular momentum by $P \simeq N$. Averaging out the interference oscillations in the quantum-mechanical cross-section contributions brings out the excellent agreement with the semiclassical

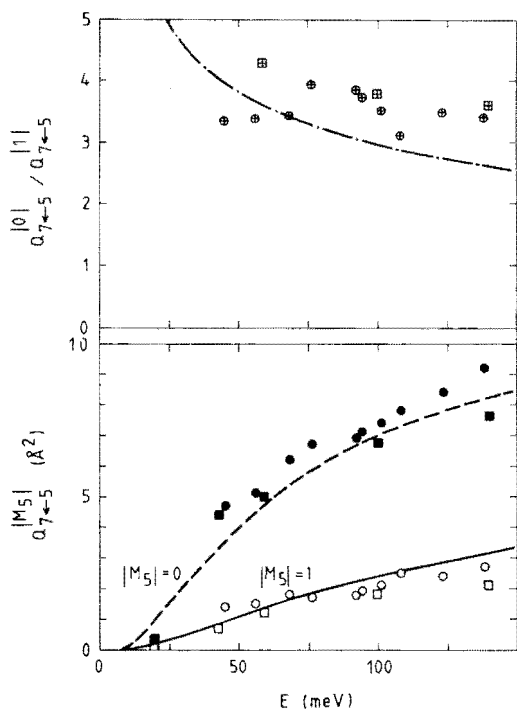


Fig. 19. Energy dependence of the polarized cross sections $Q_{7\leftarrow 5}^{0|}$ and $Q_{7\leftarrow 5}^{1|}$, with E the center-of-mass energy. Full (\bullet) and open (\circ) circles depict the experimental data points, dashed (---) and solid (—) lines the semiclassical results. In addition, three quantum-mechanical cross sections are shown, indicated by full (\blacksquare) and open (\square) quadrangles. (All for $|M_S| = 0$ and 1, respectively.) The corresponding polarisation effect $Q_{7\leftarrow 5}^{0|} / Q_{7\leftarrow 5}^{1|}$ is given as well, in a similar notation. For $E = 43$ meV, the quantum-mechanical polarisation effect has a value of 6.3.

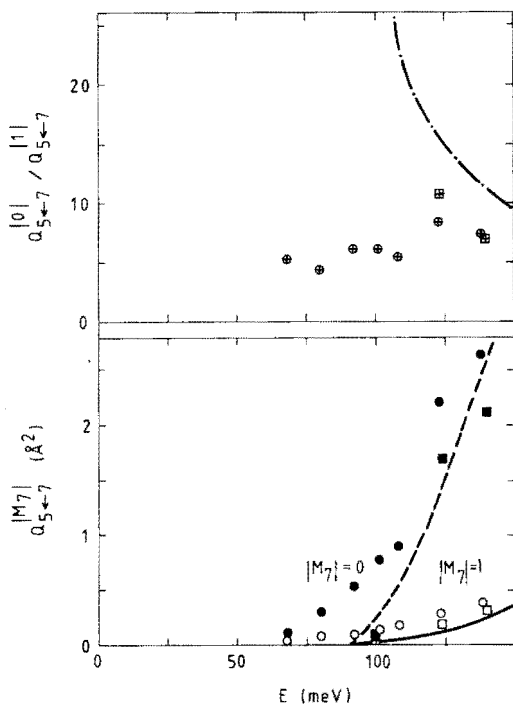


Fig. 20. Energy dependence of the polarized cross sections $Q_{5\leftarrow 7}^{[0]}$ and $Q_{5\leftarrow 7}^{[1]}$. The behavior of the experimental data points near the threshold energy $E = \Delta E_{57} = 91$ meV is strongly influenced by the experimental velocity distribution which, as no data-averaging has been applied here, makes the comparison with the semiclassical and quantum-mechanical cross sections break down. For $E = 100$ meV, the quantum-mechanical polarisation effect has a value of 30! See caption of Fig. 19 for further detail.

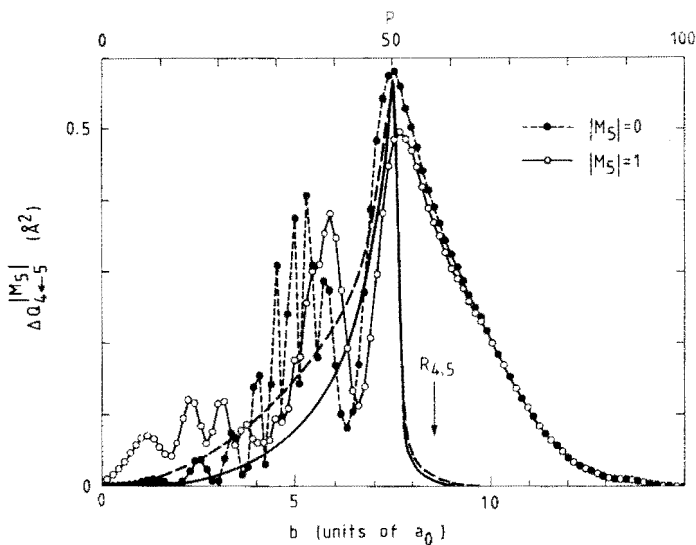


Fig. 21. Semiclassical and quantum-mechanical cross section contributions $dQ_{4 \leftarrow 5}^{M_5}(b)/db$ and $\Delta Q_{4 \leftarrow 5}^{M_5}(P)$, at energy $E_5 = 100$ meV. The preference for intermediate impact parameters combined with the absence of locking on the $\langle \alpha \rangle_5$ -curve, leads to thorough Ω -mixing and almost no overall polarisation effect. The semiclassical cross section contributions are cut off when the turning point passes the crossing radius. The quantum-mechanical large-impact-parameter contributions point to an additional radial-coupling mechanism. See caption of Fig. 17 for further detail.

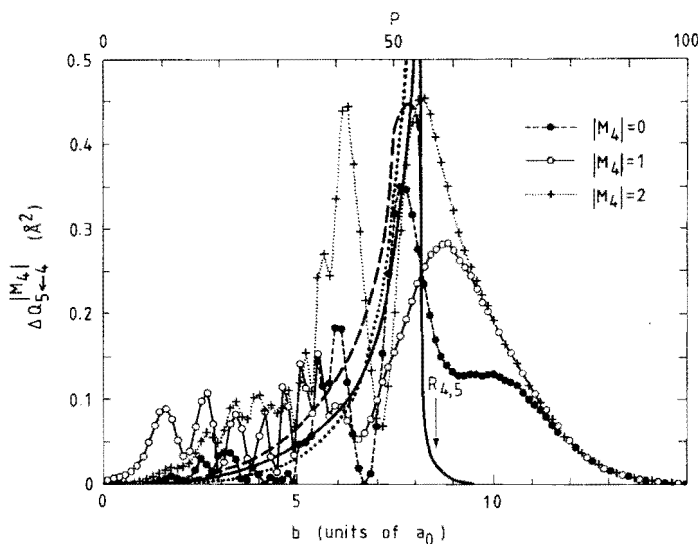


Fig. 22. Semiclassical and quantum-mechanical cross section contributions $dQ_{5 \leftarrow 4}^{M_4}(b)/db$ and $\Delta Q_{5 \leftarrow 4}^{M_4}(P)$, at energy $E_4 = 100$ meV. The similarity to Fig. 21 is not surprising in view of the small energy distance ΔE_{45} . See caption of Fig. 17 for further detail.

results. This holds both for the general behavior, and for the position of the maximum. The preferred "head-on" character of the collision is evident at once.

Figures 19 and 20 show the energy dependence of the semiclassical polarized-atom cross sections $Q_{7\leftarrow 5}^{M_5}$ and $Q_{5\leftarrow 7}^{M_7}$, together with the experimental cross sections. The latter are seen to rise with the energy, as do all cross sections studied in the present paper. The initial rise of the polarisation effect with falling energy reflects the effective Ω -conservation implied by a shift to smaller impact parameters. Agreement between semiclassical theory and experiment is good. The same can be said regarding the results of the quantum-mechanical calculations, performed with our coupled-channels code.

The experimentally observed threshold behavior of the cross sections for endothermic transitions is obscured to a certain extent by the fact that average velocities only are considered here. The calculated energy spread of about $\Delta E \approx 40$ meV, due to the primary- and secondary-beam (Gaussian) velocity distributions and to the spatial extent of the scattering volume²¹⁾, roughly corresponds with the observed transgression of the energy threshold. These convolution effects have not been included here, other than (where necessary) in Table I and Figs. 1-6.

4.3. The $\{\alpha\}_5 \leftrightarrow \{\alpha\}_4$ transitions

The $\{\alpha\}_5 \rightarrow \{\alpha\}_4$ transition is caused in effect by the isolated (45)-avoided crossing for $\Omega = 1$, which has a low reference velocity $v_{45}^{\Omega=1}$. The small radial velocities, required for optimum coupling, imply that at the high-velocity inner (56)-avoided crossing almost always the adiabatic curve is followed. For the favoured larger impact parameters ("glancing" collisions), Ω -mixing up to the crossing point R_C is considerable. The

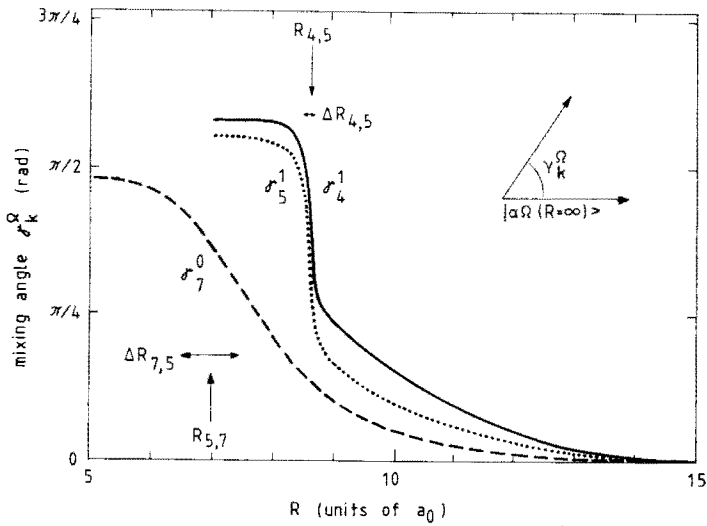


Fig. 23. Development with decreasing R of the mixing-angle $\gamma_k^\Omega(R)$ between adiabatic eigenfunctions $|\alpha_{k,J_k,\Omega_k}^\Omega(R=\infty)\rangle$ and $|\alpha_{k,J_k,\Omega_k}^\Omega(R)\rangle$, with $k=4,5$ for $\Omega=1$, and $k=7$ for $\Omega=0$. For $k=4,5$ the effect of the (45)-avoided crossing is added to by a substantial rotation for large R -values. This reflects additional radial coupling, perhaps of Demkov-type.

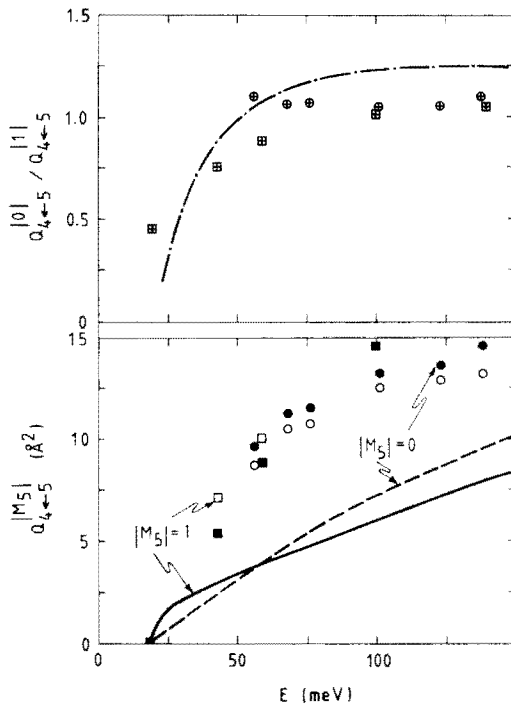


Fig. 24. Energy dependence of the polarized cross sections $Q_{4\leftarrow 5}^{|0\rangle}$ and $Q_{4\leftarrow 5}^{|1\rangle}$. Added radial coupling may explain the discrepancy between semiclassical and quantum-mechanical (and experimental) cross sections. See caption of Fig. 19 for further detail.

absence of locking on the $\{\alpha\}_5$ -curve leads to an even more thorough Ω -mixing and to the virtual absence of a polarisation effect: $Q_{4\leftarrow 5}^{|0\rangle} \approx Q_{4\leftarrow 5}^{|1\rangle}$. The small asymptotic energy difference $\Delta E_{45} = 11$ meV results in calculated cross sections for the endothermic $\{\alpha\}_4 \rightarrow \{\alpha\}_5$ transition, which are only slightly smaller than the $\{\alpha\}_5 \rightarrow \{\alpha\}_4$ cross sections.

The $\{\alpha\}_5 \rightarrow \{\alpha\}_4$ transition is very instructive in several regards. First of all, it is rotational coupling that is largely responsible for the transition. The peculiar nature of the (45)-crossing with its extremely low reference velocity $v_{45}^{\Omega=1} \approx 20$ ms⁻¹, makes the single-transit crossing probability close to unity. For a net transition to take place, rather than two subsequent crossings, rotational coupling is required to generate an $|M_4|_Z \neq 1$ component, which cannot cross again at the second transit. Of course, rotation of the $|M_5|_Z \neq 1$ components at the first transit of the avoided crossing to $|M_5|_Z = 1$ at the second transit, has a similar effect. For this reason, the expected Landau-Zener pattern of a rise and subsequent fall of the cross sections does not materialize. To the $\{\alpha\}_4 \rightarrow \{\alpha\}_5$ crossing, the same reasoning can be applied. With locking radii equal to the crossing radius, we would obtain cross sections $Q_{4\leftarrow 5}^{|M_5|}, Q_{5\leftarrow 4}^{|M_4|} < 1 \text{ \AA}^2$, at $E_5 = 100$ meV. This both confirms the need for a locking factor $f_L \gtrsim 1$ in Eq. (23), and provides a quite accurate upper limit for the locking radii in question. Rotational coupling inside of the inner (56)-avoided crossing turns out to play no part. It is possible to represent this crossing as a simple loss-term on the $\{\alpha\}_5$ -curve, due to radial coupling only.

A second interesting aspect of the $\{\alpha\}_5 \rightarrow \{\alpha\}_4$ transition is evident from Fig. 21, which once more compares semiclassical and quantum-mechanical cross section contributions per impact parameter value, for $E_5 = 100$ meV. Agreement is good, up to the sharp cut off in the semiclassical cross sections that signals the onset of tunneling at the turning point. This behavior, closely paralleled by that for the $\{\alpha\}_4 \rightarrow \{\alpha\}_5$ transition in

Fig. 22, is quite insensitive to the (45)-crossing-parameter values. To account for the quantum-mechanical contributions at large impact parameters, a different radial coupling mechanism seems to be required.

The $\{\alpha\}_5 \rightarrow \{\alpha\}_4$ transition thus appears to be a prime candidate for the tentative demonstration of Demkov coupling⁴¹⁾. This is supported by Fig. 23 of the development of the mixing angle $\gamma_k^\Omega(R)$ between the adiabatic eigenfunctions $|\alpha_k J_k \Omega = 1 (R=\infty)\rangle$ and $|\alpha_k J_k \Omega = 1 (R)\rangle$, for $k = 4, 5$. Ideally, a Landau-Zener type avoided crossing involves a $\pi/2$ rotation of the adiabatic eigenfunctions, while a $\pi/4$ rotation is associated with Demkov-coupling. Whereas obviously neither case applies here with textbook clarity, the influence of the (45)-avoided crossing for $\Omega = 0$ is unmistakable. The sharp transition near the (45)-crossing radius $R_C = 8.6 a_0$ makes the gradual rotation over close to $\pi/4$ in the outer R-regions the more remarkable. Compare this, in the same figure, with the much smaller amount of mixing displayed by the $|\alpha_7 J_7 \Omega = 0 (R)\rangle$ state, in spite of the more diffuse character of the (57)-avoided crossing for $\Omega = 0$.

We must look at Fig. 24, which shows the semiclassically calculated energy dependence of the $Q_{4 \leftarrow 5}^{M_5}$ cross sections, with the above in mind. What differences with the quantum-mechanical cross sections there are, stem mainly from a lack of large-impact-parameter contributions. In our opinion the conclusion is justified that the $\{\alpha\}_5 \rightarrow \{\alpha\}_4$ transition is essentially caused by Demkov-coupling in the outer R-regions and LZ-coupling at R_C .

The quantum-mechanical calculations, in their turn, agree well with the experimental results. Lower energies (and smaller impact parameters) in this case favor the $\Omega = |1|$ cross section, which means a decreasing polarisation effect. As yet, there are no experimental data for the $\{\alpha\}_4 \rightarrow \{\alpha\}_5$ transition.

4.4. The $\{\alpha\}_7 \leftrightarrow \{\alpha\}_6$ transitions

The $\{\alpha\}_7 \leftrightarrow \{\alpha\}_6$ transitions are caused mainly by the (67)-avoided crossing for $\Omega = 1$. It resembles the (45)-crossing in the same Ω -manifold, but has not quite so small a reference velocity. Also, of course, the crossing radius is smaller. Other than for the $\{\alpha\}_5 \leftrightarrow \{\alpha\}_4$ transitions, however, on account of more complete locking in the inner regions there is a remaining orientation effect for the $\{\alpha\}_7$ initial state: $Q_{6\leftarrow 7}^{|1|} > Q_{6\leftarrow 7}^{|0|}$. For the $\{\alpha\}_6$ initial state, the energy at the crossing is larger than for the $\{\alpha\}_7$ state, thereby forcing impact parameters to be larger still ("grazing" collisions). In fact, even a small inversion of the polarisation effect is observed: $Q_{7\leftarrow 6}^{|1|} \lesssim Q_{7\leftarrow 6}^{|0|}$, though, of course, here there is a $Q_{7\leftarrow 6}^{|2|}$ cross section to be taken into account as well ($J_6 = 2$).

For the $\{\alpha\}_7 \rightarrow \{\alpha\}_6$ transition, semiclassical cross section behavior as a function of the impact parameter, at energy $E_7 = 100$ meV, compares favourably with that of the quantum-mechanical cross sections, as may be seen from Fig. 25. Figure 26 for the reverse $\{\alpha\}_6 \rightarrow \{\alpha\}_7$ transition, at $E_6 = 100$ meV, also displays good agreement. The $\{\alpha\}_7 \rightarrow \{\alpha\}_6$ polarisation effect is underestimated, though. Some improvement may be achieved by using a larger effective locking radius for the $\{\alpha\}_7$ state than indicated in Table IV. The larger value, $R_L = 9.0 a_0$, perhaps reflects the slowly rising flank of the Ω -splitting $\Delta V_7^{0,1}$ in Fig. 15. No realistic change in crossing parameters, though, can correct the tendency of the semiclassical cross sections $Q_{6\leftarrow 7}^{|M_6|}$ to decrease prematurely with rising energy (in contrast to the cross section $Q_{4\leftarrow 5}^{|M_5|}$), as shown in Fig. 27. The $\{\alpha\}_6 \rightarrow \{\alpha\}_7$ transition has only been measured at a single energy, so far.

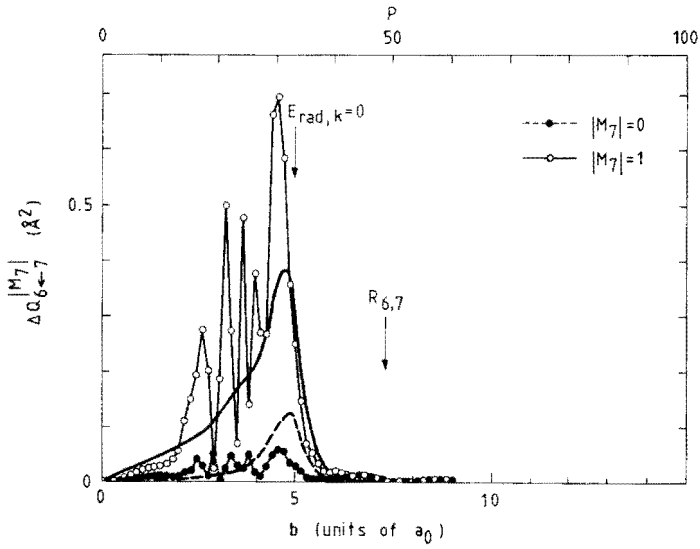


Fig. 25. Semiclassical and quantum-mechanical cross section contributions $dQ_{6\leftarrow 7}^{M_7}(b)/db$ and $\Delta Q_{6\leftarrow 7}^{M_7}(P)$, at energy $E_7 = 100$ meV. See caption of Fig. 17 for further detail.

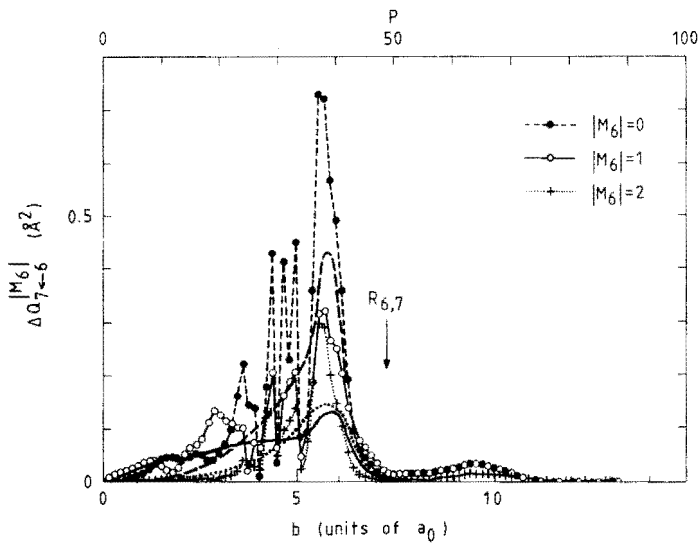


Fig. 26. Semiclassical and quantum-mechanical cross section contributions $dQ_{7\leftarrow 6}^{M_6}(b)/db$ and $\Delta Q_{7\leftarrow 6}^{M_6}(P)$, at energy $E_6 = 100$ meV. See caption of Fig. 17 for further detail.

4.5. The $\{\alpha\}_5 \leftrightarrow \{\alpha\}_6$, $\{\alpha\}_{7,6} \leftrightarrow \{\alpha\}_4$ transitions

Transitions $\{\alpha\}_{4,5} \leftrightarrow \{\alpha\}_{6,7}$ are possible only through multiple curve crossings. The high radial velocities favoured by the inner (56)-crossing imply a dominant contribution from small impact parameters. In view of the locking on all but the $\{\alpha\}_5$ -curve, some polarisation effect is to be expected. For high radial velocities, a single-transit non-adiabatic transition is much more likely at the low-velocity (45)- and (67)-crossings than single-pass adiabatic following. The $\{\alpha\}_4 \rightarrow \{\alpha\}_7$ transition is therefore the most probable, with cross sections comparable even to those for the single-curve-crossing transitions. Once again, we expect more of an orientation effect in the reverse highly endothermic ($\Delta E_{74} = -91$ meV) $\{\alpha\}_7 \rightarrow \{\alpha\}_4$ transition, for the same initial energy. Figure 28, which compares the composition of semiclassical and quantum-mechanical cross sections for the $\{\alpha\}_4 \rightarrow \{\alpha\}_7$ transition, once more at initial-state energy $E_k = 100$ meV, shows them to be in reasonable agreement.

The transitions requiring adiabatic following at one ($\{\alpha\}_4 \leftrightarrow \{\alpha\}_6$ and $\{\alpha\}_5 \leftrightarrow \{\alpha\}_7$) or both ($\{\alpha\}_5 \rightarrow \{\alpha\}_6$) of the (45)- and (67)-crossings are progressively less likely than the $\{\alpha\}_4 \leftrightarrow \{\alpha\}_7$ transitions. This is roughly the behavior displayed by the quantum-mechanical cross sections of Table I. The smaller the cross sections, the sooner our simple semiclassical model may be expected to deviate from quantum-mechanical "reality". Even here, though, qualitative agreement is sometimes maintained, as e.g. for the $\{\alpha\}_6 \rightarrow \{\alpha\}_4$ transition. On the other hand, while e.g. the $\{\alpha\}_5 \rightarrow \{\alpha\}_6$ quantum-mechanical cross sections are small, the semiclassical cross sections are considerably smaller still and cannot be said to present a true picture anymore. Once more, this may indicate radial coupling mechanisms not included in our model. For none of these transitions, experimental energy-dependence data are available.

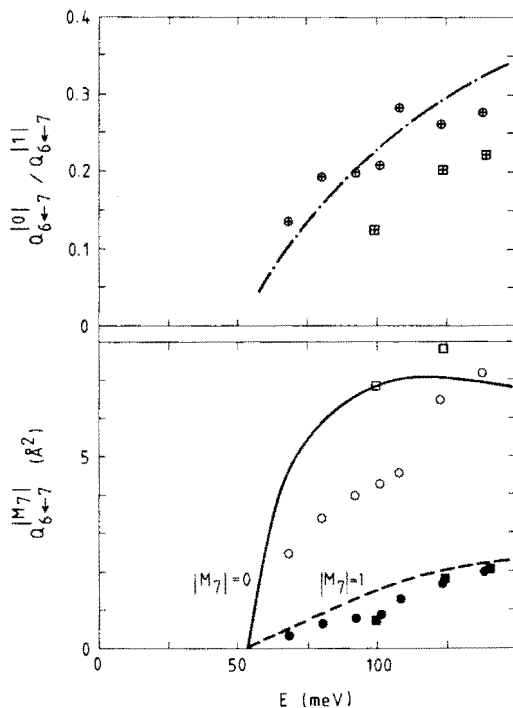


Fig. 27. Energy dependence of the polarized cross sections $Q_{6\leftarrow 7}^{|0\rangle}$ and $Q_{6\leftarrow 7}^{|1\rangle}$. Other than the experimental and quantum-mechanical cross sections, the semiclassical cross sections fall off with rising energy. For $E = 140$ meV, the quantum-mechanical cross section $Q_{6\leftarrow 7}^{|1\rangle}$ has a value of 9.7 \AA^2 . See caption of Fig. 19 for further detail.

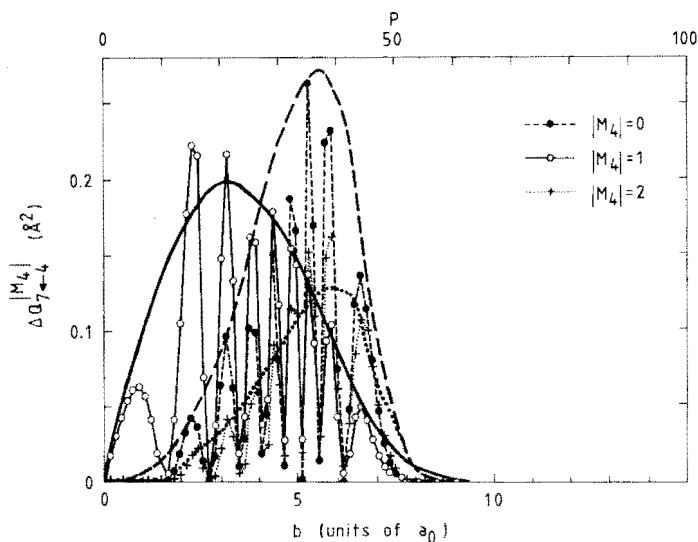


Fig. 28. Semiclassical and quantum-mechanical cross section contributions $dQ_{7\leftarrow 4}^{|M_4\rangle}(b)/db$ and $\Delta Q_{7\leftarrow 4}^{|M_4\rangle}(P)$, at energy $E_4 = 100$ meV. The large crossing probabilities p_{kl} at the outer (45)- and (67)-avoided crossings make this multiple-curve-crossing transition quite likely. Thus the large cross sections. See caption of Fig.17 for further detail.

For the transitions of this subsection and for all transitions discussed earlier, Table V offers a comparison between semiclassical and quantum-mechanical *total* cross sections. Some possible reasons for existing discrepancies have been given above. In general, though, the quantum-mechanical results are qualitatively and often quantitatively reproduced by the calculations with our semiclassical model. We note that by fitting the semiclassical crossing parameters to the cross-section data, still better agreement could have been obtained.

4.6. General conclusions

From the previous case-studies, several general conclusions may be drawn as to cross section magnitude, dominance of impact parameter regions and polarisation effects. First, for two adjacent $\{a\}$ -states, an isolated avoided crossing between the adiabatic potentials will result in large cross sections. This is true when only a single crossing is present, but also when the principal crossing is "isolated" by a second, inner crossing with an entirely different reference-velocity and thus representing only a small loss-term. In comparison with transitions outside the $\{a\}_{4,5,6,7}$ multiplet²⁰⁾, the cross sections that meet the above criterion (i.e. the $\{a\}_5 \leftrightarrow \{a\}_7$, $\{a\}_5 \leftrightarrow \{a\}_4$ and $\{a\}_7 \leftrightarrow \{a\}_6$ cross sections) are indeed relatively large. The same principle, in reverse, holds for the true multiple-curve-crossing transitions. Here, the inner of three crossings determines the preferred velocity. Hence, the $\{a\}_6 \rightarrow \{a\}_4$ cross section is bound to be larger than the $\{a\}_6 \rightarrow \{a\}_5$ cross section.

Exothermic $\{a\}_k \rightarrow \{a\}_\ell$ transitions are seen to yield larger cross sections than their endothermic $\{a\}_\ell \rightarrow \{a\}_k$ counterparts. This is because for a given energy with respect to the initial state, radial energy at the

Table V. Performance of the semiclassical model. Comparison of semiclassical and quantummechanical polarized total cross sections $Q_{\ell+k}^{|\mathbf{M}_k|}$, at center-of-mass energy $E = 100$ meV of the initial state $\{\alpha\}_k$.

| Initial state $\{\alpha\}_k$ | Final state $\{\alpha\}_\ell$ | Cross section $\left\{ Q_{\ell+k}^{ \mathbf{M}_k } \right\}_{SC} : \left\{ Q_{\ell+k}^{ \mathbf{M}_k } \right\}_{QM}$ | | | Polarization effect $\left\{ Q_{\ell+k}^{ 0 } / Q_{\ell+k}^{ 1 } \right\}_{SC}$: $\left\{ Q_{\ell+k}^{ 0 } / Q_{\ell+k}^{ 1 } \right\}_{QM}$ |
|------------------------------|-------------------------------|---|------|-----|--|
| | | $ \mathbf{M}_k $ | | | |
| | | 0 | 1 | 2 | |
| $\{\alpha\}_4$ | $\{\alpha\}_5$ | 1.4 | 1.1 | 0.7 | 1.3 |
| | $\{\alpha\}_6$ | 0.4 | 0.4 | 0.3 | 1.0 |
| | $\{\alpha\}_7$ | 2.6 | 2.1 | 1.8 | 1.2 |
| $\{\alpha\}_5$ | $\{\alpha\}_4$ | 0.8 | 0.8 | * | 1.0 |
| | $\{\alpha\}_6$ | 0.02 | 0.07 | * | 0.3 |
| | $\{\alpha\}_7$ | 1.0 | 1.2 | * | 0.8 |
| $\{\alpha\}_6$ | $\{\alpha\}_4$ | 0.6 | 0.5 | 0.7 | 1.3 |
| | $\{\alpha\}_5$ | 1.0 | 0.2 | 0.8 | 10 |
| | $\{\alpha\}_7$ | 0.8 | 0.7 | 1.3 | 1.2 |
| $\{\alpha\}_7$ | $\{\alpha\}_4$ | 0.2 | 1.1 | * | 0.13 |
| | $\{\alpha\}_5$ | 2.5 | 2.3 | * | 1.1 |
| | $\{\alpha\}_6$ | 1.8 | 1.0 | * | 1.8 |

avoided crossing is larger in the exothermic case. For the transitions under discussion, this is a favorable condition.

Secondly, as to the behavior of cross section contributions as a function of the impact parameter, the expected preference of "high-velocity" crossings for high radial velocities translates directly into a preference for small impact parameters ("head-on" collisions). Likewise, "low-velocity" crossings require "grazing" or, in any case, "glancing" collisions at greater impact parameters.

The occurrence of polarisation effects in $\{\alpha\}_k \rightarrow \{\alpha\}_\ell$ cross sections is determined by the relative importance of impact parameter regions and by the competition between rotational coupling and locking of the electronic angular momentum \mathbf{J} . For head-on collisions ($b \ll R_C$), the orientation of \mathbf{J} remains quite unchanged, irrespective of locking. This holds for both the incoming and outgoing trajectories. Since, for $\text{Ne}^{**}\text{-He}$, avoided crossings are limited to a single Ω -value per transition ($\Omega = 0^-$ or $\Omega = 1$), the preponderance of small impact parameters is equivalent to a large orientation effect. For grazing collisions and large impact parameters ($b \approx R_C$) locking plays no part either (since $R_L \leq R_C$), but the orientation of \mathbf{J} with respect to the internuclear axis undergoes an almost complete "inversion" ($M = 0 \rightarrow \Omega = 1$, $M = \pm 1 \rightarrow \Omega = 0$ for $J = 1$). Again, a large but now opposite orientation effect is expected. For intermediate impact parameters and glancing collisions, strong Ω -mixing generally leads to an averaging out of orientation effects, unless locking occurs along a substantial part of the trajectory.

Lastly, it is worth noting, that rotational coupling inside the crossing radius can play an instrumental role in bringing about a net $\{\alpha\}_k \rightarrow \{\alpha\}_\ell$ transition in the first place. This happens when the single-pass transition probability approaches unity, as in the $\{\alpha\}_4 \leftrightarrow \{\alpha\}_5$ case.

5. Concluding remarks

For the $\text{Ne}^{**}\{\alpha\}_{4,5,6,7}$ group of states, semiclassical considerations are of great help in obtaining insight in the $\text{Ne}^{**} + \text{He}$ intramultiplet-mixing process at thermal energies. Symmetry restraints, Landau-Zener type radial coupling at avoided crossings, and the competition between rotational coupling and locking, are the essential elements of our simple semiclassical model. The semiclassical calculations, not only qualitatively but more often than not quantitatively as well, effectively emulate quantum mechanical coupled-channels calculations (which in turn agree well with experiment).

The combination of crossed-beam experiment, quantum-mechanical coupled-channels calculations and semiclassical analysis presents a picture, of polarisation effects in particular, that is quite remarkable in its completeness. The energy dependence of cross sections still needs to be examined in more detail. It will be worthwhile to investigate the possible inclusion of another kind of radial coupling (e.g. Demkov coupling) into the present model's framework.

In the case of related systems, such as $\text{Ne}^{**}\text{-Ne}$, $\text{Ne}^{**}\text{-H}_2$ or perhaps even $\text{Ne}^{**}\text{-CH}_4$ etc., semiclassical calculations offer a practical way of directly testing the validity of interaction potentials, similar to that for $\text{Ne}^{**}\text{-He}$ but for the changes due to e.g. a different polarizability. The possible merits of this idea are suggested by preliminary $\text{Ne}^{**}\text{-Ne}$ and $\text{Ne}^{**}\text{-H}_2$ measurements, which show cross section behavior for these systems to be quite similar to that for $\text{Ne}^{**}\text{-He}$.

References

- 1 D. Hennecart and F. Masnou-Seeuws, *J. Phys. B* **18**, 657 (1985).
- 2 a) W. Buszert, T. Bregel, R.J. Allan, M. W. Ruf, and H. Hotop, *Z. Phys. A* **320**, 105 (1985); b) W. Buszert, T. Bregel, J. Ganz, K. Harth, A. Siegel, M.-W. Ruf, H. Hotop and H. Morgner, *J. Phys. (Paris)* **46** C1-199 (1985).
- 3 M.H. Alexander, T. Orlikowski, and J.E. Straub, *Phys. Rev. A* **28**, 73 (1983).
- 4 G. Nienhuis, *Phys. Rev. A* **26**, 3137 (1982).
- 5 J.G. Kircz, R. Morgenstern, and G. Nienhuis, *Phys. Rev. Lett* **48**, 610 (1982).
- 6 H.A.J. Meyer, H.P. van der Meulen, and R. Morgenstern, *Z. Phys. D* **5**, 299 (1987).
- 7 D. Neuschäfer, M.O. Hale, I.V. Hertel and S.R. Leone, in "Electronic and Atomic Collisions", Eds. D.C. Lorents, W.E. Meyerhof, and J.R. Peterson, Elsevier (1986).
- 8 a) M.O. Hale, I.V. Hertel, and S.R. Leone, *Phys. Rev. Lett.* **53**, 2296 (1984); b) M.O. Hale and S.R. Leone, *Phys. Rev. A* **31**, 103 (1985).
- 9 J.M. Parson and T. Ishikawa, *J. Chem. Phys.* **80**, 3137 (1984)
- 10 A. Bähring, I.V. Hertel, E. Meyer, W. Meyer, N. Spies, and H. Schmidt, *J. Phys. B* **17**, 2859 (1984).
- 11 a) D. Hennecart, *J. Phys. (Paris)* **39**, 1065 (1978); b) D. Hennecart, Ph.D. Thesis, Université de Caen, 1982 (unpublished).
- 12 J.M. Mestdagh, J. Berlande, P. de Pujo, J. Cuvallier, and A. Binet, *Z. Phys. A* **304**, 3 (1982).
- 13 E. Düren, E. Hasselbrink, and H. Tischen, *Phys. Rev. Lett.* **50**, 1983 (1983)
- 14 L. Hüwel, J. Maier, and H. Pauly, *J. Chem. Phys.* **76**, 4961 (1982).
- 15 H.J. Yuh and P.J. Dagdigian, *Phys.Rev. A* **28**, 63 (1983).
- 16 a) N.Böwering, M.R. Bruce and J.W. Keto, *J. Chem. Phys.* **84**, 709 (1986); b) N.Böwering, M.R. Bruce and J.W. Keto, *J. Chem. Phys.* **84**, 715 (1986).
- 17 J.K. Kuh and D.W. Setser, *J. Chem. Phys.* **84**, 4304 (1986).
- 18 I.V. Hertel, H. Schmidt, A. Bähring and E. Meyer, *Rep. Prog. Phys.* **48**, 375 (1985).
- 19 M.P.I. Manders, J.P.J. Driessen, H.C.W. Beijerinck and B.J. Verhaar, *Phys.Rev.Lett.* **57**, 1577 (1986); *ibid.*, **57**, 2472 (1986).

- 20 M.P.I. Manders, J.P.J. Driessen, H.C.W. Beijerinck and B.J. Verhaar, *Phys. Rev. A*, (1988) accepted for publication.
- 21 M.P.I. Manders, W.M.J. Ruyten, F. v.d. Beucken, J.P.J. Driessen, W.J.T. Veugelers, P.H. Kramer, E.J.D. Vredenburg, W.B.M. van Hoek, G.J. Sandker, H.C.W. Beijerinck and B.J. Verhaar, to be published.
- 22 I. Dabrowski and G. Herzberg, *J. Mol. Spectr.* 73 (1978) 183.
- 23 H. Haberland, W. Konz and P. Oesterlin, *Phys. B: At. Mol Phys.* 15 (1982) 2969.
- 24 J. Raynal, in "Computing as a Language of Physics", ed. A.E. Salam, IAEA, Vienna (1972).
- 25 R.B. Bernstein, "Atom Molecule Collision Theory", Plenum Press, New York and London (1979).
- 26 A. Messiah, "Quantum Mechanics", Vol. I + II, North Holland, Amsterdam (1981).
- 27 L. Landau, *Phys. Z. Sow.* 2 (1932) 46
- 28 C. Zener, *Proc. Roy. Soc. A* 137 (1932) 696
- 29 E.C.G. Stueckelberg, *Helv. Phys. Acta* 5 (1932) 369
- 30 W.R. Thorson, J.B. Delos and S.A. Boorstein, *Phys. Rev. A* 4 (1971) 1052.
- 31 E.E. Nikitin, in "Chemische Elementar Prozesse", Ed. H. Hartmann and J. Heidelberg, Springer Verlag, Berlin, Heidelberg, New York (1968).
- 32 J.B. Delos and W.R. Thorson, *Phys. Rev. A* 6 (1972) 728.
- 33 E.E. Nikitin, *Adv. Quantum Chem.* 5 (1970) 135.
- 34 V.K. Bykhovskii, E.E. Nikitin and M.Ya. Orchinnikova, *JETP* 20 (1965) 500.
- 35 J.B. Delos, *Phys. Rev. A* 9 (1974) 1626.
- 36 A. Russek, *Phys. Rev. A* (1971) 1918.
- 37 H. Nakamura and M. Namiki, *Phys. Rev. A* 24 (1981) 2963.
- 38 J. Grosser, *J. Phys. B: At. Mol. Phys.* 14 (1981) 1449.
- 39 I.V. Hertel, H. Schmidt, A. Bähring and E. Meijer, *Rep. Prog. Phys.* 48 (1985) 375.
- 40 C. Gaussorgues and F. Masnou-Seeuws, *J. Phys. B* 10 (1977) 2125.
- 41 Yu.N. Demkov, *Soviet Phys. JETP* 45 (1963) 1959

Chapter VI.

COLLISION-INDUCED INTRAMULTIPLY MIXING FOR $\text{Ne}^{**} \{(2p)^5(3p)\} + \text{Ne}$:
PRINCIPLES AND PRACTICE OF SYMMETRY EFFECTS

M.P.I. Manders, W. Boom, H.C.W. Beijerinck and B.J. Verhaar

Physics Department, Eindhoven University of Technology,

P.O. Box 513, 5600 MB Eindhoven, The Netherlands

Abstract

We present an extension of the model potential method of $\text{Ne}^{**}\{(2p)^5(3p)\}$ Ne collisions. The role of the electronic inversion symmetry in the core/valence-electron separation for stationary nuclei is examined. This leads to approximate electronic eigenfunctions and corresponding adiabatic potentials. In this, an essential element is the R-dependent mixing of gerade and ungerade core potentials, associated with the R-dependent uncertainty of the valence-electron being located at the Ne^+ -ion or the Ne-atom. Subsequently, nuclear dynamics is included in the approximate wave function and the role of the identity of the nuclei is considered.

With the aim of testing our extended approximate treatment, we also present experimental $^{20}\text{Ne}^{**}\text{-Ne}$ and $^{22}\text{Ne}^{**}\text{-Ne}$ total polarized cross sections $Q_{l \leftarrow k}^{|M_k|}$ for the $\{(2p)^5(3p)\}_k \equiv \{\alpha\}_k \rightarrow \{\alpha\}_l$ transition, with M_k the magnetic quantum number of the electronic angular momentum \underline{J} of the initial $\{\alpha\}_k$ state with respect to the asymptotic relative velocity. Considerable polarization effects have been observed, as well as some interesting differences with earlier $\text{Ne}^{**}\text{-He}$ data, but no significant differences between the results for ^{20}Ne and ^{22}Ne .

Preliminary quantum-mechanical coupled-channel calculations for the $\text{Ne}^{**}\text{-Ne}$ problem, using valence-electron potentials from Hennecart and Masnou-Seeuws and core potentials from Cohen and Schneider as input, allow us to test theory against experiment, a procedure proven successful for $\text{Ne}^{**}\text{-He}$. We distinguish between the two limiting cases of complete and zero mixing of the gerade and ungerade core potentials. Complete mixing gives much better agreement. For example, the experimental polarization effect $Q_{6 \leftarrow 5}^{|0|} / Q_{6 \leftarrow 5}^{|1|} = 2.1$ should be compared to the predictions 1.9 and 0.3 for zero and perfect overlap, respectively. In general, the measure of agreement obtained for complete mixing indicates the relative lack of importance of symmetry effects for the thermal energies investigated.

1. Introduction

In recent years there is a growing interest in the literature for inelastic collisions of atoms in short-lived electronically excited states¹⁾. In line with this development we studied in several earlier papers²⁻⁵⁾ intramultiplet mixing collisions of $\text{Ne}^{**}\{(2p)^5(3p)\}_k \equiv \{\alpha\}_k$ atoms with ground state He atoms. In view of its importance for our work it is of special interest to mention the papers by Hennecart and Masnou-Seeuws on the $\text{Ne}^{**}\text{-He}$ and $\text{Ne}^{**}\text{-Ne}$ systems^{6,7)}. It is the $\text{Ne}^{**}\text{-Ne}$ system that we will deal with in this paper. From a theoretical point of view, we will be able to extend our quantum-mechanical treatment of $\text{Ne}^{**}\text{-He}$ collisions³⁾. In this, the availability of $\text{Ne}^{**}\text{-He}$ potential information both for the valence electron^{6,7)} and for the Ne^+ core⁸⁾ is of decisive importance. As to experimental data, these are provided by our crossed-beam experiment⁴⁾, in the form of total polarized cross sections $Q_{l \leftarrow k}^{|M_k|}$ for the $\text{Ne}^{**}\{\alpha\}_k \rightarrow \{\alpha\}_l$ transition. Here M_k is the magnetic quantum number of the electronic angular momentum J in the initial state $\{\alpha\}_k$ along the asymptotic relative velocity \underline{g} . The special interest of the $\text{Ne}^{**}\text{-Ne}$ collision process is, of course, connected with the possible occurrence of symmetry effects, not present in $\text{Ne}^{**}\text{-He}$ collisions. For the $\text{Ne}^{**}\text{-Ne}$ system this problem has been addressed before, on the basis of total unpolarized cross sections from a bulk experiment^{6,7)}. We finally mention a recent analysis of, mostly elastic, $\text{Ne}^*\{(2p)^5(3s)\}\text{-Ne}$ differential scattering⁹⁾ and an older but very illuminating study of $\text{He}^*\{(1s)(2s)\}\text{-He}$ differential scattering¹⁰⁾.

From the point of view of symmetry¹¹⁻¹³⁾, collisions between noble gas atoms fall into one of three categories, depending on the atomic nuclei. First we have the case of non-identical nuclei with different nuclear charge, as in $\text{Ne}^{**}\text{-He}$ collisions. The second category, connected with

equally-charged non-identical nuclei, implies electron inversion symmetry, e.g. in the $^{22}\text{Ne}^{**}-^{20}\text{Ne}$ collision. Finally, we have the situation of identical nuclei, as for $^{20}\text{Ne}^{**}-^{20}\text{Ne}$, in which case identical-particle symmetry must be considered, in addition. The aim of this paper is to extend the earlier model-potential treatment of $\text{Ne}^{**}\text{-He}$ collisions.

In section 2 we take into account the additional symmetry due to the equality of nuclear charges in finding approximate electronic eigenfunctions for stationary nuclei and corresponding adiabatic eigenvalues. In section 3 we include the nuclear dynamics in the approximate wave function and consider the role of the identity of nuclei. With the ultimate aim of testing our extended approximate treatment, we present in section 4 experimental data for both the $^{22}\text{Ne}^{**}-^{20}\text{Ne}$ and $^{20}\text{Ne}^{**}-^{20}\text{Ne}$ systems. A preliminary comparison of these data with theory is presented in section 5. Finally, section 6 offers some concluding remarks.

Before turning to theory in section 2, however, it is of interest to present a short description of the experiment. The experiment⁵⁾ is of the crossed-beam variety, essential to the study of polarization phenomena. A primary beam of metastable $\text{Ne}^*(^3\text{P}_{0,2})$ atoms is crossed at right angles by a linearly polarized laser beam. The short-lived $\text{Ne}^{**}\{a\}_k$ atoms, produced by optical pumping, will mostly be deexcited through the spontaneous emission of so-called "direct" fluorescence radiation. However, with secondary-beam atoms from a free-jet supersonic expansion passing through the intersection of primary- and laser-beam, some of the $\text{Ne}^{**}\{a\}_k$ atoms undergo a collision-induced transition to the $\text{Ne}^{**}\{a\}_l$ state. This, in turn, spontaneously decays, with its fluorescence radiation designated as "collision-induced" fluorescence. Measuring a single line of both types of fluorescence by means of interference filters yields a criterion for the number of atoms in the k and l states, respectively, and thus for the $\{a\}_k \rightarrow \{a\}_l$ transition

probability. The available data on the secondary-beam density, Ne^{**} -lifetimes and the optical detection efficiency, inter alia, then allow us to arrive at absolute values of total cross sections. Details of this analysis of the experimental signals are given in Ref. 5.

The short lifetimes of the Ne^{**} -states ($\tau \approx 20$ ns) and the small transition cross sections ($Q_{l \leftarrow k} \approx 1 \text{ \AA}^2$) enforce a very compact design of the apparatus, with special care paid to the optical detection system. The result has been a large sensitivity (1 kHz/ \AA^2 for the number of counts per unit of inelastic cross section), as in a bulk experiment. Still, the resolving power of a crossed-beam experiment (associated with a well-defined relative velocity) has been retained. A polarized laser produces a well-defined polarized initial $\{\alpha\}_k$ -state, enabling us to determine total polarized-atom cross sections $Q_{l \leftarrow k}^{|M_k|}$. For Ne^{**} -He we have previously observed large variations in cross section magnitude and polarization effects $Q_{l \leftarrow k}^{|M'_k|} / Q_{l \leftarrow k}^{|M_k|}$ 2-5).

By selective excitation of either the $^{20}\text{Ne}^*$ or the $^{22}\text{Ne}^*$ metastable atoms in the primary beam, we produce short-lived $\text{Ne}^{**}\{\alpha\}_k$ -atoms of a single isotope. Isotope selection of secondary beam Ne-atoms is, of course, impossible. However, the natural abundance of the Ne-isotopes, about 90% ^{20}Ne and 10% ^{22}Ne , ensures that effects related to ^{20}Ne collision partners will be highly predominant.

2. Inversion symmetry in core/valence-electron separation for stationary nuclei

The most essential model assumption in the Hennecart and Masnou-Seeuws approach^{6,7)} to the $\text{Ne}^{**} + \text{He}$ adiabatic electron wave functions is related to the separate role of the 3p valence electron on the one hand and the eleven core electrons on the other. In the case of $\text{Ne}^{**} + \text{Ne}$ this approach needs some modification in connection with inversion symmetry.

Let us write the total 20-electron Hamiltonian in the form

$$H^{el}(1, \dots, 20) = H^C(1, \dots, 19) + H^V(20) + V^{\text{rest}} \quad (1)$$

the 20th electron preserving its identity as the valence electron. The corresponding exchange effects are taken into account only insofar as they are represented in the effective potentials, operating on the valence electron, by which V^{rest} is approximated in a practical scheme in which the present theory is applied.

Eigenfunctions for the $\text{Ne}^+ + \text{Ne}$ core have been obtained by an ab initio method by Cohen and Schneider⁹⁾. For a single asymptotic electronic state we denote them in this subsection by the short-hand notation

$$|\psi^C(1, \dots, 19) \pi_c^e \rangle \quad (2)$$

with the core electronic parity $\pi_c^e = \pm 1$. This brings into focus a basic difference with the $\text{Ne}^{**} + \text{He}$ core problem. Whereas in the relevant core eigenfunctions of the latter problem the ionic part of the core is predominantly located around the Ne nucleus, the $\text{Ne} + \text{He}^+$ adiabatic potentials lying at far higher energies for the internuclear distances considered, here the ionic part is located with equal probability at each of the Ne nuclei in the states with definite parity π_c^e . Assuming the

effective valence electron potential to be similarly inversion-symmetric, would be highly unfavorable energetically, however: the valence electron would not profit sufficiently from the attraction by the ionic part of the core. With that in mind we break the inversion symmetry in the intermediate stage of our treatment. This is a generally accepted procedure in a somewhat different context¹⁴⁾.

Presuming a relatively small separation of the $\pi_c^e = \pm 1$ core eigenvalues at the relevant distances, we introduce the linear combination

$$|\psi_A^c(1, \dots, 19)\rangle = \frac{1}{\sqrt{2}} (|\psi^c \pi_c^e = +1\rangle + |\psi^c \pi_c^e = -1\rangle) \quad (3a)$$

$$|\psi_B^c(1, \dots, 19)\rangle = \frac{1}{\sqrt{2}} (|\psi^c \pi_c^e = +1\rangle - |\psi^c \pi_c^e = -1\rangle) \quad (3b)$$

With a suitable relative phase of the $\pi_c^e = \pm 1$ states, ψ_A^c represents a state in which the ionic part of the core is predominantly at the Ne-nucleus A, while ψ_B^c bears the same relation to Ne-nucleus B.

The assumption of ψ_A^c and ψ_B^c to be approximate core eigenfunctions can be interpreted classically in terms of a time constant for the ionic part to shift among the nuclei, slow compared to the typical time constant associated with the motion of the valence electron. Essentially, we assume the valence electron to "follow" rapidly the slow shift of the ionic part of the core. The intermediate violation of inversion symmetry is restored in a later stage of the calculation.

Each of the states ψ_A^c and ψ_B^c subsequently plays a role analogous to that of a core state in the $\text{Ne}^+ + \text{He}$ system. A corresponding valence electron eigenfunction ψ_A^v or ψ_B^v may be obtained by approximations completely analogous to those introduced in Refs. 6 and 7. We will not enter into the details of such an approach.

Now finally, it is natural to reintroduce the total electron parity π^e as a good quantum number. Consider a Ritz variation procedure to determine optimal linear combinations of the two product states $\psi_A^C \psi_A^V$ and $\psi_B^C \psi_B^V$. The expectation value of $H^C + H^V + V^{\text{rest}}$ of Eq. (1) with the exact interaction V^{rest} , conserving total parity π^e exactly, is clearly stationary for those linear combinations that have definite parity, given by:

$$\frac{1}{\sqrt{2}} (|\psi_A^C \rangle |\psi_A^V \rangle + \pi^e |\psi_B^C \rangle |\psi_B^V \rangle) \quad (4)$$

Note that the overlap of the two terms in this expression vanishes due to

$$\Delta^C \equiv \langle \psi_A^C | \psi_B^C \rangle = 0 \quad (5)$$

on the basis of Eqs. (3a) and (3b), although the corresponding valence electron overlap is different from zero:

$$\Delta^V \equiv \langle \psi_A^V | \psi_B^V \rangle \neq 0 \quad (6)$$

This again stresses the different roles of valence electron and core due to the above-mentioned basic assumption of our approach with respect to the valence-electron and core time scales.

The energy eigenvalues associated with the gerade and ungerade 20-electron states of Eq. (4) are now obtained as follows. We take the expectation value of the Hamiltonian in Eq. (1), including V^{rest} insofar as it operates effectively only on the valence-electron part of the wave function. Using Eq. (5) we thus find the energy value

$$E_o + V_{\pi^e}(R) = E_o + V^V(R) + \frac{1}{2} \{V_g^C(R) + V_u^C(R)\} + \frac{1}{2} \pi^e \Delta^V(R) \{V_g^C(R) - V_u^C(R)\} \quad (7)$$

in which E_0 denotes the energy for $R \rightarrow \infty$, V_g^c and V_u^c are the gerade and ungerade $Ne^+ - Ne$ adiabatic potentials and V^v is the eigenvalue of the valence electron, all taken relative to their value at infinity.

We want to emphasize the R-dependent mixing of the gerade and ungerade core potentials V_g^c and V_u^c . In our picture this is essentially due to the R-dependent uncertainty with respect to the valence electron being located at the Ne^+ ion or at the Ne atom, which causes the valence-electron inversion-overlap integral of Eq. (6) to be unequal to zero.

In contrast to Eq. (7), Hennecart and Masnou-Seeuws^{6,7)} use energy values

$$E_0 + V_{\pi} e(R) = E_0 + V^v(R) + \{V^c(R)\}_{\pi_c} e = \pi e \quad (8)$$

equivalent to ours only for $\Delta^v(R) \equiv 1$. In general, however, $\Delta^v(R) = 1$ is not a good approximation; $\Delta^v(R) = 0$ is much closer to reality.

In a practical application, spin-orbit coupling could be relegated to V^{rest} , together with the residual Coulomb-interaction between valence electron and core. The corresponding valence-electron and core potentials are those of Ref. 6 and Ref. 8, respectively (the latter, we repeat, without spin-orbit interaction). Then V^{rest} can be included again later in the way of Ref. 6.

3. Inversion and identical-nuclei symmetry in Ne^{**}-Ne scattering

We are now ready to tackle the nuclear dynamics part of the problem. We confine ourselves to pointing out the aspects related to inversion and identical-nuclei symmetries, in which the present problem differs from that for Ne^{**} + He in Refs. 3 and 6.

3.1. Inversion symmetry and the coupled-channel equations

The Ne^{**}-Ne scattering problem is governed by the Hamiltonian H^{el} of Eq. (1) and the kinetic energy operator T_n of the nuclei:

$$H = H^{el} + T_n \quad (9)$$

Scattering eigenstates $\psi(\underline{r}, \underline{R})$, where \underline{r} represents all electron coordinates and \underline{R} is the internuclear radius vector, satisfy the time-independent Schrödinger equation

$$H \psi(\underline{r}, \underline{R}) = E \psi(\underline{r}, \underline{R}) \quad (10)$$

with E the total energy in the center-of-mass system. In the coupled-channel approach, we expand $\psi(\underline{r}, \underline{R})$ in terms of a set of orthonormal channel states $|\phi_\kappa\rangle$ with R -dependent coefficients:

$$\psi(\underline{r}, \underline{R}) = \sum_{\kappa} \frac{F_{\kappa}(R)}{R} |\phi_{\kappa}\rangle \quad (11)$$

Each of the channel functions ϕ_{κ} is a combination of an electronic wave function, depending at most parametrically on R (such as functions of the type of Eq. (4)), and an angular function of nuclear motion, depending on

$\hat{R} = \underline{R}/R$. From Eqs. (10) and (11) a set of second-order coupled-channel differential equations is obtained for the radial wave function $F_{\kappa}(R)$ of nuclear motion. The form of these equations depends on the channel functions ϕ_{κ} chosen. A careful choice of the latter, taking into account the symmetries of the system, is called for in order to decouple as far as possible the coupled-channel equations.

In addition to the symmetries for the entire system already present for two non-equal nuclear charges, i.e. rotational symmetry with associated quantum numbers P and M_p and inversion symmetry to which corresponds the total parity π , we now have inversion symmetry for the electronic system with associated quantum number π^e . Contrary to the case of stationary nuclei, considered in section 2, this inversion symmetry is not exact for moving nuclei with different masses, due to the fact that the center-of-charge C does not coincide with the center-of-mass. For our case of $^{22}\text{Ne}-^{20}\text{Ne}$ we shall neglect this effect, however.

It is also useful to include quantum numbers, which are approximately good in particular regions of configuration space. As in Ref. 3, we can select as such either the magnitude $\Omega = |M_J|$ of the total electronic angular momentum projection on the internuclear axis, or the rotational angular momentum quantum number N of the Ne^{**} and Ne nuclei. These two are mutually exclusive. The former is a convenient quantum number at shorter distances, the latter at large distances. One may switch from one basis to the other by a simple transformation using essentially only Clebsch-Gordan coefficients ($J - \Omega \ P \ \Omega | NO \rangle^3$).

Taking the added factor of the electronic parity π^e into account amounts to using Eq. (7) as a starting point, rather than $V(R) = V^V(R) + V^C(R)$ as in the $\text{Ne}^{**}\text{-He}$ case of Refs. 3 and 6. The coupled-channels calculation itself remains essentially unaffected. It is executed in the basis containing Ω . Reference 3 uses basis functions

$$|\phi_{\kappa}\rangle \equiv |\pi\pi^e \alpha_{J\Omega P M_P}\rangle \quad (12)$$

The final result, the S-matrix is calculated in the basis including N, with basis functions

$$|\phi_{\kappa}\rangle \equiv |\pi\pi^e \alpha_{J N P M_P}\rangle \quad (13)$$

Its elements are written as $S_{\lambda\kappa}$ in the following sections.

3.2. Ne^{**} -Ne cross sections for non-identical nuclei

The final step in the treatment of the Ne^{**} -Ne collision process is the calculation of transition cross sections from the S-matrices of the preceding subsection. This is done through the intermediary of the familiar scattering amplitude $f_{\ell k}$. The latter is firmly based in the physical scattering picture of an ingoing plane wave for the initial electronic state $|k\rangle \equiv |\alpha_{J_k M_k}\rangle$ and scattered outgoing spherical waves for all possible final electronic states $|\ell\rangle \equiv |\alpha_{\ell} J_{\ell} M_{\ell}\rangle$. Disregarding electronic inversion symmetry for the moment, we have (as in the Ne^{**} -He case³⁾) the usual asymptotic wave boundary condition

$$|\psi_k\rangle_{k \rightarrow \infty} = e^{i\mathbf{k}_k \cdot \mathbf{R}} |k\rangle + \sum_{\ell} f_{\ell k}(\hat{\mathbf{R}}) \frac{e^{i\mathbf{k}_{\ell} \cdot \mathbf{R}}}{R} |\ell\rangle \quad (14)$$

where \mathbf{k}_k and \mathbf{k}_{ℓ} stand for the (magnitude of the) asymptotic wave vector. As indicated, $f_{\ell k}$ depends on the scattering direction $\hat{\mathbf{R}}$.

By expanding the incoming plane wave $e^{i\mathbf{k}_k \cdot \mathbf{R}}$ in spherical waves, the scattering amplitude $f_{\ell k}$ can be expressed in terms of S-matrix elements $S_{\lambda\kappa}$, where $\lambda = \lambda(\ell)$ and $\kappa = \kappa(k)$, symbolizing the inclusion of the atomic

quantum numbers l and k in the collective channel quantum numbers λ and κ (Eq. (13)). In shorthand notation we thus have

$$f_{\ell k}(\hat{R}) = \sum_{\substack{\lambda(\ell) \\ \kappa(k)}} L_{\lambda\kappa} (S_{\lambda\kappa} - \delta_{\lambda\kappa}) Y_{N_\lambda}^{M_{N_\lambda}}(\hat{R}) \quad (15)$$

with coefficients $L_{\lambda\kappa}$ which need not be specified here (compare Ref. 3). The \hat{R} -dependence of the scattering amplitude is described by the spherical harmonics $Y_{N_\lambda}^{M_{N_\lambda}}(\hat{R})$, which are eigenfunctions of the rotational angular momentum operators N^2 and N_z . Differential cross sections $\sigma_{l \leftarrow k}$ are then given by¹⁵⁾

$$\sigma_{l \leftarrow k}(\hat{R}) = \frac{k_l}{k_k} |f_{lk}(\hat{R})|^2 \quad (16)$$

while, for instance, the total single M_k -state polarized cross sections $Q_{l \leftarrow k}^{M_k}$ of Ref. 3 are calculated from

$$Q_{l \leftarrow k}^{M_k} = \frac{1}{2J_l + 1} \sum_{M_l} \int_{4\pi} \sigma_{l \leftarrow k}(\hat{R}) d\hat{R} \quad (17)$$

In case of equally charged but non-identical Ne-nuclei (e.g. $^{22}\text{Ne}^{**} - ^{20}\text{Ne}$), it is convenient to consider in Eq. (14) electronic states $|k\rangle$ and $|l\rangle$ of definite π^e . Indicating this π^e value explicitly, we have

$$|\psi_k \pi^e\rangle = e^{i\mathbf{k} \cdot \mathbf{R}} |k \pi^e\rangle + \sum_l f_{lk}^{\pi^e}(\hat{R}) \frac{e^{i\mathbf{k}_l \cdot \mathbf{R}}}{R} |l \pi^e\rangle \quad (18)$$

$$f_{lk}(\hat{R}) = \sum_{\substack{\lambda(l) \\ \lambda(k)}} L_{\lambda\kappa} (S_{\lambda\kappa}^{\pi^e} - \delta_{\lambda\kappa}) Y_{N_\lambda}^{M_{N_\lambda}}(\hat{R}) \quad (19)$$

Now, to turn $|\psi_k \pi^e \rangle$ into a physically relevant scattering eigenstate, the excited Ne^{**} -electron cloud is to be associated with the incident direction \hat{k}_k and with the outgoing direction \hat{R} . With a suitable choice of relative phases of $|\psi_k g \rangle$ and $|\psi_k u \rangle$ we thus define the physical scattering state

$$|\psi_k \rangle = \frac{1}{\sqrt{2}} (|\psi_k g \rangle + |\psi_k u \rangle) \quad (20)$$

Working this out, we find

$$\begin{aligned} |\psi_k \rangle = & \lim_{R \rightarrow \infty} e^{i\mathbf{k} \cdot \mathbf{R}} \frac{1}{\sqrt{2}} (|kg \rangle + |ku \rangle) + \\ & + \sum_l f_{lk}^D(\hat{R}) \frac{e^{i\mathbf{k}_l \cdot \mathbf{R}}}{R} \frac{1}{\sqrt{2}} (|lg \rangle + |lu \rangle) \\ & + \sum_l f_{lk}^E(\hat{R}) \frac{e^{i\mathbf{k}_l \cdot \mathbf{R}}}{R} \frac{1}{\sqrt{2}} (|lg \rangle - |lu \rangle) \end{aligned} \quad (21)$$

The first term represents an incoming plane wave where the excitation is with nucleus A. The subsequent terms describe "direct" and "exchange" scattering, where the excitation has remained with A or moved to B during the collision, respectively¹⁰). The direct scattering amplitude f_{lk}^D is given by

$$f_{lk}^D(\hat{R}) = \frac{1}{2} \{ f_{lk}^g(\hat{R}) + f_{lk}^u(\hat{R}) \} \quad (22)$$

and the exchange scattering amplitude f_{lk}^E by

$$f_{lk}^E(\hat{R}) = \frac{1}{2} \{ f_{lk}^g(\hat{R}) - f_{lk}^u(\hat{R}) \} \quad (23)$$

The differential cross sections $\sigma_{l \leftarrow k}^D$ and $\sigma_{l \leftarrow k}^E$ for direct and exchange scattering are given, once more, by Eq. (16). The g/u coherence evident from Eqs. (22) and (23) gives rise to g/u interference.

The detection of any $\text{Ne}^{***}\text{-Ne}$ interference effects hinges on the capability to distinguish experimentally between direct and exchange scattering. While in principle this may be done using the 1800 MHz isotope shift¹⁶⁾ between the fluorescence from like $^{20}\text{Ne}^{***}$ - and $^{22}\text{Ne}^{***}$ -levels, in practice it is impossible. The summed differential cross sections $\sigma_{l \leftarrow k}^{\text{NI}}(\hat{R})$ under conditions of equally-charged but non-identical (NI) nuclei, will exhibit no g/u coherence effects:

$$\begin{aligned} \sigma_{l \leftarrow k}^{\text{NI}}(\hat{R}) &= \sigma_{l \leftarrow k}^{\text{D}}(\hat{R}) + \sigma_{l \leftarrow k}^{\text{E}}(\hat{R}) \\ &= \frac{k_l}{k_k} \left\{ \frac{1}{2} |f_{lk}^{\text{g}}(\hat{R})|^2 + \frac{1}{2} |f_{lk}^{\text{u}}(\hat{R})|^2 \right\} \end{aligned} \quad (24)$$

3.3. $\text{Ne}^{**}\text{-Ne}$ cross sections for identical nuclei

In the case of identical Ne-nuclei, we should symmetrize the physical scattering state of Eqs. (20) and (21) in the nuclei. This leads to the asymptotic form

$$\begin{aligned} |\psi_k \rangle &= \frac{1}{\sqrt{2}} e^{i\mathbf{k}_k \cdot \mathbf{R}} \frac{1}{\sqrt{2}} (|kg \rangle + |ku \rangle) + \frac{1}{\sqrt{2}} e^{-i\mathbf{k}_k \cdot \mathbf{R}} \frac{1}{\sqrt{2}} (|kg \rangle - |ku \rangle) \\ &+ \frac{1}{\sqrt{2}} \sum_l f_{lk}^{\text{D}}(\hat{R}) \frac{e^{i\mathbf{k}_l \cdot \mathbf{R}}}{R} \frac{1}{\sqrt{2}} (|lg \rangle + |lu \rangle) \\ &+ \frac{1}{\sqrt{2}} \sum_l f_{lk}^{\text{D}}(-\hat{R}) \frac{e^{i\mathbf{k}_l \cdot \mathbf{R}}}{R} \frac{1}{\sqrt{2}} (|lg \rangle - |lu \rangle) \\ &+ \frac{1}{\sqrt{2}} \sum_l f_{lk}^{\text{E}}(\hat{R}) \frac{e^{i\mathbf{k}_l \cdot \mathbf{R}}}{R} \frac{1}{\sqrt{2}} (|lg \rangle - |lu \rangle) \\ &+ \frac{1}{\sqrt{2}} \sum_l f_{lk}^{\text{E}}(-\hat{R}) \frac{e^{i\mathbf{k}_l \cdot \mathbf{R}}}{R} \frac{1}{\sqrt{2}} (|lg \rangle + |lu \rangle) \end{aligned} \quad (25)$$

In this wave function all terms correspond to the excited Ne^{***} electron cloud moving in the direction \mathbf{k}_k (plane wave terms) and \hat{R} (spherical

outgoing waves). Note that an exchange of the nuclei leaves the gerade electron states invariant but turns the ungerade states into their opposites.

No detector being able to distinguish the two identical (ID) nuclei, we should sum incoherently over their contributions in Eq. (25) to find the inelastic intensity in a given direction \hat{R} :

$$\begin{aligned} \sigma_{l \leftarrow k}^{\text{ID}}(\hat{R}) &= \frac{1}{2} \frac{k_l}{k_k} |f_{lk}^{\text{D}}(\hat{R}) + f_{lk}^{\text{E}}(-\hat{R})|^2 + \frac{1}{2} \frac{k_l}{k_k} |f_{lk}^{\text{D}}(-\hat{R}') + f_{lk}^{\text{E}}(\hat{R}')|^2_{\hat{R} = -\hat{R}} \\ &= \frac{k_l}{k_k} |f_{lk}^{\text{D}}(\hat{R}) + f_{lk}^{\text{E}}(-\hat{R})|^2 \end{aligned} \quad (26)$$

We thus find a differential cross section $\sigma_{l \leftarrow k}^{\text{ID}}$ for identical nuclei of the previous form of Eq. (16), with the scattering amplitude replaced by the well-known coherent addition¹³⁾

$$f_{lk}^{\text{ID}}(\hat{R}) = f_{lk}^{\text{D}}(\hat{R}) + f_{lk}^{\text{E}}(-\hat{R}) \quad (27)$$

of direct and exchange amplitudes. (Compare this with the incoherent addition in Eq. (24).)

Essentially, direct and exchange scattering have become indistinguishable, where the scattering of the excited Ne^{**} -electron cloud in the \hat{R} -direction is concerned (for exchange scattering, this involves a reversed direction of the internuclear axis). A coherent addition of scattering amplitudes is therefore in order, with the associated D/E interference oscillations. The separate scattering amplitudes f_{lk}^{D} and f_{lk}^{E} are still given by the expressions of Eqs. (22) and (23) for non-identical nuclei, thus giving rise to g/u interference in addition.

In the related case of Ne^*-Ne differential cross sections both types of interference, fast direct/exchange oscillations and slow gerade/ungerade oscillations, have been observed⁹⁾. The gerade/ungerade oscillations can be said to arise from the dissimilar turning points associated with the gerade and ungerade potentials. Since the corresponding gerade/ungerade difference in path length is much less than the skip over the diameter of the molecular system, which semiclassically characterizes the difference between direct and exchange scattering, the faster rate of the direct/exchange oscillations can be readily understood.

We finally note that after symmetrization π and π^e are no longer independent quantum numbers. Rather, since spinless bosons have even nuclear parity $\pi^N = 1$, we have

$$\pi = \pi^N \pi^e = \pi^e \quad (28)$$

This relation supplements the expression $\pi = (-1)^N$, which already applies without symmetrization in the nuclei. Equation (20) is also found as a direct consequence of the direct/exchange interference of Eq. (27). The behavior of the spherical harmonics under inversion,

$$Y_{NM_N}(\hat{-R}) = (-1)^N Y_{NM_N}(\hat{R}) \quad (29)$$

leads to the exclusion of all S-matrix elements with $\pi^e \neq (-1)^N$, i.e. about half the number, from the expression for f_{lk} .

4. Experimental $^{20}\text{Ne}^{**}-^{20}\text{Ne}$ and $^{22}\text{Ne}^{**}-^{20}\text{Ne}$ cross sections

4.1. Experimental conditions

From the experimental point of view, there is no fundamental difference between $\text{Ne}^{**}-\text{Ne}$ measurements and the $\text{Ne}^{**}-\text{He}$ measurements of Ref. 3. However, in the case of $\text{Ne}^{**}-\text{Ne}$ there is the additional interest of a comparison between $^{22}\text{Ne}^{**}-^{20}\text{Ne}$ and $^{20}\text{Ne}^{**}-^{20}\text{Ne}$ cross sections. In this connection there are two aspects to be discussed.

The first of these is related to the relative abundance of the different Ne-isotopes in natural neon¹⁶⁾:

^{20}Ne : 90.92%

^{21}Ne : 0.26%

^{22}Ne : 8.82%

In the metastable beam source, Ne^* -atoms are produced in the same ratio. This means a ten-fold decrease in the density of the short-lived initial state $\text{Ne}^{**}\{\alpha\}_k$ -atoms in the scattering volume, when going from $^{20}\text{Ne}^{**}$ to $^{22}\text{Ne}^{**}$. With the collision-induced fluorescence signals smaller by a factor ten as well, there is a heavy bias in favor of strong transitions as an object of study. Of course, distinguishing between the Ne-isotopes in the secondary beam is impossible. In this regard, the use of neon enriched in ^{22}Ne , for either the primary or the secondary beam, is prohibitively expensive. To indicate the less than absolute purity of the Ne-secondary beam, we will use the symbol $(^{20})\text{Ne}$.

The second aspect is the shift in the optical $\text{Ne}^* \{^3\text{P}_{0,2}\} \rightarrow \text{Ne}^{**} \{\alpha\}_k$ transition frequency ν_{ik} . It is found to be approximately¹⁶⁾

$$\nu_{ik} = {}^{22}\nu_{ik} - {}^{20}\nu_{ik} \simeq 1800 \text{ MHz.}$$

For the laser system¹⁷⁾, finding and maintaining the ${}^{22}\text{Ne}^{**}$ -transition frequency presents no problem.

Of a different order is the practical impossibility to distinguish between direct and exchange scattering on the basis of the isotope shift of the fluorescence radiation measured in our experiment. In view of the related circumstance that the experiment determines total cross sections only, the kind of gerade/ungerade and direct/exchange oscillations, manifest in e.g. the Ne^* -Ne differential cross sections of Ref. 9, are unfortunately out of its province. This makes the present experiment a less than ideal instrument for the study of symmetry effects in Ne^{**} -Ne intra-multiplet mixing collisions. It is the only instrument available, however.

A comparison between (the energy dependence of) Ne^{**} -Ne cross sections on the one hand and Ne^{**} -He and similar cross sections on the other, offers a means of assessing the influence of electronic inversion symmetry on the collision process. Also, any significant differences between ${}^{20}\text{Ne}^{**}$ - ${}^{20}\text{Ne}$ and ${}^{22}\text{Ne}^{**}$ - ${}^{20}\text{Ne}$ cross sections must be attributed to the effects of symmetrization in the nuclei.

4.2. Experimental Cross Sections

We have performed measurements on Ne^{**} -Ne polarisation effects, for a number of $\{\alpha\}_5 \rightarrow \{\alpha\}_1$ and $\{\alpha\}_7 \rightarrow \{\alpha\}_1$ transitions, at various center-of-mass energies. These measurements have been less extensive, as yet, than those for the Ne^{**} -He system²⁻⁵⁾. The supersonic Ne-secondary beam, which

constitutes the only difference between the present measurements and those of Refs. 2-4, has the following characteristics. The velocity distribution peaks at a calculated velocity $v_2 = 780$ m/s. The speed ratio, at reservoir pressure $p_{2,0}^{\text{Ne}} = 160$ Torr, is $S_2 = 6.5$.

Figures 1-3 show observed cross sections for the $^{20}\text{Ne}^{**}-(20)\text{Ne} \{\alpha\}_5 \rightarrow \{\alpha\}_{4,6,7}$ transitions, measured over the full range of the angle β between the laser electric field vector \underline{E} and the asymptotic relative $\text{Ne}^{**}\text{-Ne}$ velocity \underline{g} . For the $\{\alpha\}_5 \rightarrow \{\alpha\}_{4,7}$ transitions, these may be compared directly with their $^{22}\text{Ne}^{**}-(20)\text{Ne}$ counterparts in the same figure. At present no data are available for the $^{22}\text{Ne}^{**}-(20)\text{Ne} \{\alpha\}_5 \rightarrow \{\alpha\}_6$ transition. The average center-of-mass energy is approximately $E = 115$ meV for these measurements. Systematic errors in absolute cross section values may amount to 30%. This applies to the cross sections as a group. Relative accuracy of cross section values is considerably better. The polarisation effects, naturally, exhibit only the experimental statistical errors, which usually are smaller still, except for weak transitions.

Table I gives the single- M_k -state polarized cross sections $Q_{l \leftarrow k}^{\beta}$, derived from a least-squares fit of these data to³⁾

$$Q_{l \leftarrow k}^{\beta} = \frac{1}{2} (Q_{l \leftarrow k}^{0|0} + Q_{l \leftarrow k}^{1|1}) + \frac{1}{2} (Q_{l \leftarrow k}^{0|0} - Q_{l \leftarrow k}^{1|1}) \cos 2\beta \quad (30)$$

Of course, in principle it suffices to measure $Q_{l \leftarrow k}^{\beta}$ of Eq. (30) for $\beta = 0$ and $\beta = \pi/2$ only. This yields $Q_{l \leftarrow k}^{0|0}$ and $Q_{l \leftarrow k}^{1|1}$ directly, faster but with less accuracy. Some of the other data in Table I were collected this way. To allow a comparison with similar $\text{Ne}^{**}\text{-He}$ cross sections^{3,4)}, the latter are shown in Table I, as well.

The $\text{Ne}^{**}\text{-Ne}$ results vary considerably, both as to cross section magnitude ($Q_{4 \leftarrow 5}^{\beta} \gg Q_{6 \leftarrow 5}^{\beta}$) and as to polarization effects ($Q_{7 \leftarrow 5}^{0|0} / Q_{7 \leftarrow 5}^{1|1} \approx 5$, $Q_{6 \leftarrow 7}^{0|0} / Q_{6 \leftarrow 7}^{1|1} \approx 0.20$). This will be discussed later.

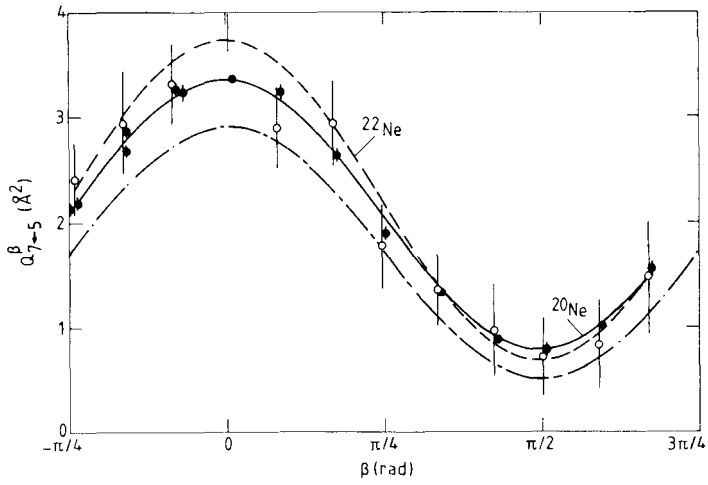
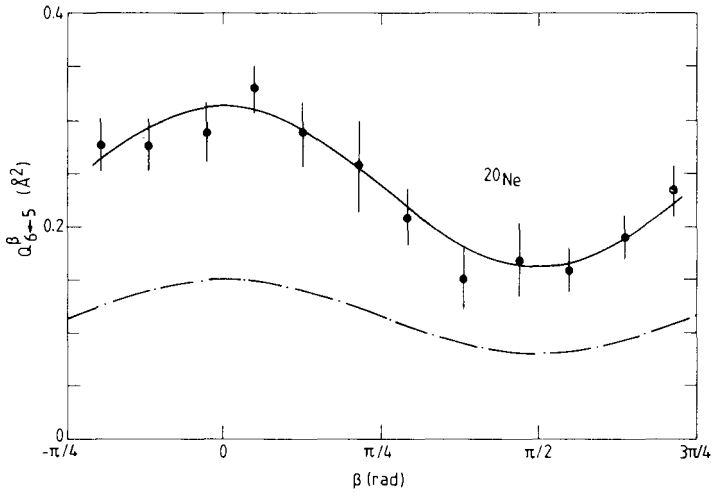
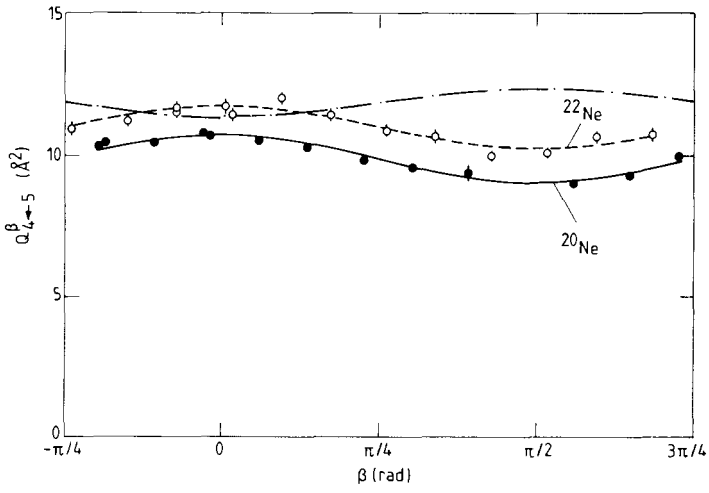


Fig. 1. Experimental results for the observed $^{20}\text{Ne}^{**}(20)\text{Ne}$ and $^{22}\text{Ne}^{**}(20)\text{Ne}$ cross sections Q_{4+5}^{β} , as a function of the angle β between the electric field \underline{E} of the laser and the relative velocity \underline{g} , at a center-of-mass energy $E_{\text{c.m.}} = 120$ meV. Statistical errors only have been indicated. The solid (—) and dashed (---) lines represent a curve fit of the data points to Eq.(30). The dash-dotted line (-·-·-) is the result of a quantum-mechanical calculation with the potentials of Eq. (32) ($[\frac{1}{2}(g+u)]$).

Fig. 2. Experimental results for the observed $^{20}\text{Ne}^{**}(20)\text{Ne}$ cross section Q_{6+5}^{β} . See caption of Fig. 1 for further detail.

Fig. 3. Experimental results for the observed $^{20}\text{Ne}^{**}(20)\text{Ne}$ and $^{22}\text{Ne}^{**}(20)\text{Ne}$ cross section Q_{7+5}^{β} . See caption of Fig. 1 for further detail.

Table I. Experimental $^{20}\text{Ne}^{**}-(^{20})\text{Ne}$ and $^{22}\text{Ne}^{**}-(^{20})\text{Ne}$ polarized cross sections and polarization effects for the $\{\alpha\}_5 \rightarrow \{\alpha\}_{4,6,7}$ and $\{\alpha\}_7 \rightarrow \{\alpha\}_{4,5,6}$ transitions, to be compared with each other and with $^{20}\text{Ne}^{**}\text{-He}$ data.

| Initial state | Final state | E_k (meV) | | | Cross section | | | | | | | | | Polarization effect | | |
|----------------|----------------|------------------|------------------|-----|--|------------------|------|--|------------------|------|---|------------------|------|---------------------|--|--|
| | | | | | $Q_{l \leftarrow k}^{ 0 }$ (\AA^2) | | | $Q_{l \leftarrow k}^{ 1 }$ (\AA^2) | | | $Q_{l \leftarrow k}^{ 0 }/Q_{l \leftarrow k}^{ 1 }$ | | | | | |
| | | ^{20}Ne | ^{22}Ne | He | ^{20}Ne | ^{22}Ne | He | ^{20}Ne | ^{22}Ne | He | ^{20}Ne | ^{22}Ne | He | | | |
| $\{\alpha\}_5$ | $\{\alpha\}_4$ | 115 | 115 | 100 | 10.8 | 11.8 | 13.2 | 9.0 | 10.2 | 12.5 | 1.2 | 1.1 | 1.1 | | | |
| | $\{\alpha\}_6$ | 115 | 115 | 100 | 0.29 | - | 0.50 | 0.14 | - | 0.97 | 2.1 | - | 0.52 | | | |
| | $\{\alpha\}_7$ | 115 | 115 | 100 | 3.3 | 3.6 | 7.0 | 0.77 | 0.66 | 2.0 | 4.2 | 5.4 | 3.5 | | | |
| $\{\alpha\}_7$ | $\{\alpha\}_4$ | 110 | - | 100 | 0.06 | - | 0.05 | 0.35 | - | 0.59 | 0.14 | - | 0.08 | | | |
| | | 135 | - | 140 | 0.09 | - | 0.44 | 0.54 | - | 1.3 | 0.16 | - | 0.33 | | | |
| | $\{\alpha\}_5$ | 110 | - | 100 | 0.40 | - | 0.85 | 0.08 | - | 0.09 | 5.0 | - | 9.0 | | | |
| | | 135 | - | 140 | 0.61 | - | 2.6 | 0.09 | - | 0.37 | 6.6 | - | 7.0 | | | |
| | $\{\alpha\}_6$ | 110 | - | 100 | 0.87 | 0.64 | 0.89 | 3.0 | 3.1 | 4.3 | 0.29 | 0.20 | 0.21 | | | |
| | | 135 | - | 140 | 0.88 | - | 2.0 | 3.3 | - | 7.2 | 0.27 | - | 0.28 | | | |

In addition to the above, more or less extensive cross section measurements have been performed at various other energies, mostly for the $^{20}\text{Ne}^{**}-(20)\text{Ne}$ system. These concern the $\{\alpha\}_5 \rightarrow \{\alpha\}_{4,7}$ and $\{\alpha\}_7 \rightarrow \{\alpha\}_{5,6}$ transitions. Some energy points are available for the $^{22}\text{Ne}^{**}-(20)\text{Ne}$ $\{\alpha\}_7 \rightarrow \{\alpha\}_6$ transition. Both methods by which the experiment allows varying the average $\text{Ne}^{**}\text{-Ne}$ collision energy²⁻⁴⁾ have been employed here. The first of these is scanning the laser beam along the primary-beam axis, which changes the position of the scattering center relative to the secondary-beam velocity v_2 . This affects the relative collision velocity, within limits. A somewhat wider range of collision energies is accessible by seeding the primary beam, e.g. with He. We have used a 15% Ne - 85% He mixture to obtain a higher primary-beam velocity v_1 .

Figures 4-7 show the observed energy dependence of the polarized cross sections $Q_{l \leftarrow k} \frac{|M_{lk}|}{k}$ for the $^{20}\text{Ne}^{**}-(20)\text{Ne}$ transitions mentioned. Of the endothermic $\{\alpha\}_7 \rightarrow \{\alpha\}_{5,6}$ transitions ($\Delta E_{75} = -81$ meV, $\Delta E_{76} = -24$ meV) the former in particular displays a strong threshold effect. For the $\{\alpha\}_5 \rightarrow \{\alpha\}_4$ transition, the decrease in cross-section magnitude with rising energy is in contrast with cross section behavior for the other transitions. These results are compared with $\text{Ne}^{**}\text{-He}$ data below.

Please note, that the $\text{Ne}^{**}\text{-Ne}$ data of Figs. 4-7 partially represent older measurements, performed at various occasions, under varying circumstances. This has caused scaling problems and may well be at the root of e.g. the apparent discrepancy between low- and high-energy values of the $\{\alpha\}_7 \rightarrow \{\alpha\}_6$ cross section in Fig. 7. Even though of lesser quality than the measurements reported for $\text{Ne}^{**}\text{-He}$ in Refs. 3 and 4, the measurements of Figs. 4-7 were thought to be of value nevertheless, because they indicate general trends.

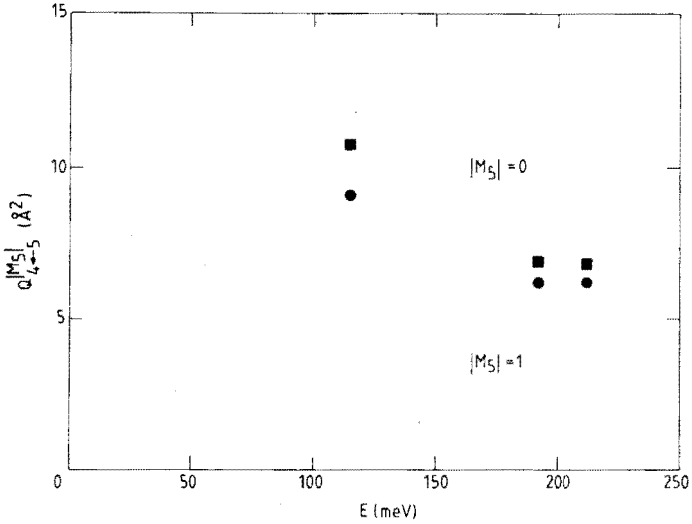


Fig. 4. Energy dependence of the polarized $^{20}\text{Ne}^{**}-(20)\text{Ne}$ cross sections $Q_{4+5}^{[0]}$ and $Q_{4+5}^{[1]}$, with E the center-of-mass energy. The high-energy points have been obtained by using a 15% Ne - 85% He seeded primary beam, the other points with a 100% Ne beam. Additional changes in energy were brought about by varying the position of the laser beam along the primary-beam axis. See the text for further explanation.

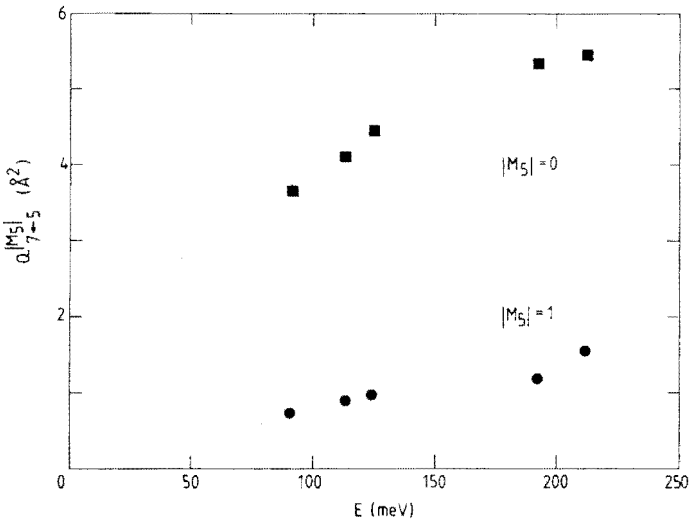


Fig. 5. Energy dependence of the polarized $^{20}\text{Ne}^{**}-(20)\text{Ne}$ cross sections $Q_{7+5}^{[0]}$ and $Q_{7+5}^{[1]}$. See caption of Fig. 4 for further detail.

4.3. Discussion

In general, there is a considerable degree of similarity between the $\text{Ne}^{***}\text{-Ne}$ experimental cross sections and those for $\text{Ne}^{***}\text{-He}$. What trend there is points towards smaller cross sections for $\text{Ne}^{***}\text{-Ne}$, somewhat contrary to expectation. We have seen earlier in the $\text{Ne}^{***}\text{-He}$ case⁴⁾ that cross section behavior for transitions within the $\{\alpha\}_{4,5,6,7}$ group of states can largely be explained in semiclassical terms by considering the avoided crossings present between the relevant adiabatic potentials.

For lack of data on the valence-electron inversion-overlap integral $\Lambda^V(R)$ of Eq. (6), we have considered the adiabatic potentials, calculated with $\Lambda^V = 0$ and $\Lambda^V = 1$, respectively. For $\Lambda^V = 1$, where either gerade or ungerade core potentials are used, the adiabatic potentials are those of Hennecart and Masnou-Seeuws^{6,7)}. We have said already that $\Lambda^V = 0$, which gives the average of gerade and ungerade potentials, should be a better choice. The $\text{Ne}^{***}\text{-Ne}$ adiabatic potentials thus calculated, while presenting a much less clear-cut picture than in the $\text{Ne}^{***}\text{-He}$ case, once more allow a number of avoided crossings to be tentatively identified. These are, in the main, the same as present for $\text{Ne}^{***}\text{-He}$, i.e. between the (5,7) adiabatic potentials for $\Omega = 0^-$, and between the (4,5), (6,7) and (less clearly) the (5,6) adiabatic potentials for $\Omega = 1$. Their characteristics differ somewhat from those for the $\text{Ne}^{***}\text{-He}$ avoided crossings. Nor are they necessarily the same for gerade and ungerade potentials separately, in the case that $\Lambda^V = 1$. This is confirmed by the preliminary coupled-channel calculations of the next section, which use these potentials as input. We note, that the position of the various avoided crossings is shifted to R-values, smaller by typically 10% than those found in the $\text{Ne}^{***}\text{-He}$ case. This is indeed consonant with a decrease in cross section values. Given roughly similar potential-characteristics, the similarity between ${}^{22}\text{Ne}^{***}\text{-}(20)\text{Ne}$ and $\text{Ne}^{***}\text{-He}$ cross sections is not surprising.

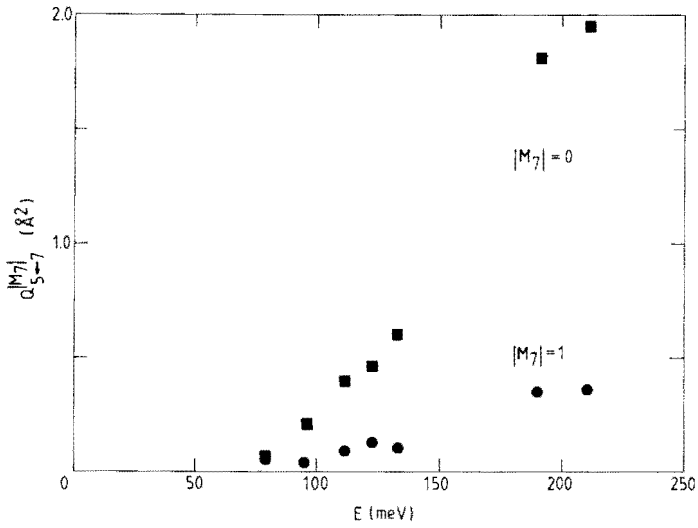


Fig. 6. Energy dependence of the polarized $^{20}\text{Ne}^{**}(20)\text{Ne}$ cross sections $Q_{5+7}^{[0]}$ and $Q_{5+7}^{[1]}$. See caption of Fig. 4 for further detail.

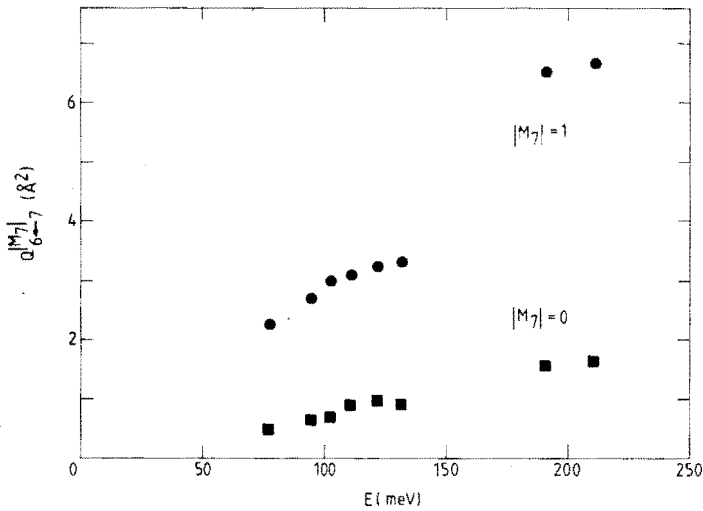


Fig. 7. Energy dependence of the polarized $^{20}\text{Ne}^{**}(20)\text{Ne}$ cross sections $Q_{6+7}^{[0]}$ and $Q_{6+7}^{[1]}$. See caption of Fig. 4 for further detail.

A striking exception to the general likeness of $\text{Ne}^{**}\text{-Ne}$ and $\text{Ne}^{**}\text{-He}$ results is offered by the $\{\alpha\}_5 \rightarrow \{\alpha\}_6$ transition. The polarisation effect is reversed: $Q_{6\leftarrow 5}^{0|0|} / Q_{6\leftarrow 5}^{1|1|} = 2$ and 0.6 for $\text{Ne}^{**}\text{-Ne}$ and $\text{Ne}^{**}\text{-He}$, respectively. In terms of avoided crossings it is worth noting that the (5,6) avoided crossing for $\Omega = 1$ is the inner of three closely positioned crossings to be passed in the $\{\alpha\}_5 \rightarrow \{\alpha\}_6$ transition. As such, and for $\text{Ne}^{**}\text{-Ne}$ even more than for $\text{Ne}^{**}\text{-He}$, this transition is least susceptible to a semiclassical analysis. The decrease of the $\{\alpha\}_5 \rightarrow \{\alpha\}_4$ cross section with energy, different from what is seen for $\text{Ne}^{**}\text{-He}$, represents high-energy, strong-non-adiabatic-coupling Landau-Zener behavior⁴⁾. Its early onset is understandable in view of the extremely small distance between the adiabatic potentials at the (4,5) crossing, which translates directly into a small coupling matrix element H_{45}^4 . A full semiclassical (and quantum-mechanical) analysis is deferred to a future paper.

In any case, at present there appear to be no overwhelming arguments in favor of a dominant role of $^{22}\text{Ne}^{**}\text{-(20)Ne}$ electronic inversion symmetry effects. We must keep in mind, that the gerade/ungerade splitting is expected to become of more importance for smaller internuclear distances than are probed at the present thermal energies. This is, because both the valence-electron inversion-overlap integral Δ^V and the splitting $V_g^C - V_u^C$ of the core potentials in Eq. (7) will increase with decreasing distance R (see Refs. 6 and 8). Future experiments at higher energies will therefore be perhaps more informative in this respect.

As to the comparison between $^{20}\text{Ne}^{**}\text{-(20)Ne}$ and $^{22}\text{Ne}^{**}\text{-(20)Ne}$ cross sections: within the admittedly rather large experimental errors, no differences are observed. This applies both to cross section magnitude and to polarisation effects. For a more definitive conclusion, both better (i.e. longer) and more numerous measurements (of the energy dependence in particular) are needed.

5. Preliminary coupled-channels results

5.1. The coupled-channels calculation

As has been established in section 3, there are no fundamental differences between a coupled-channel calculation for $\text{Ne}^{**}\text{-Ne}$, including electron inversion symmetry, and one for $\text{Ne}^{**}\text{-He}$.

In broad outline, our coupled-channel calculation for $\text{Ne}^{**}\text{-He}$ proceeds as follows³⁾. The coupled equations in the Ω -diabatic representation of Eq. (12) are numerically integrated with a modified Numerov method¹⁸⁾ beyond a point R_1 , where the non-diagonal physical coupling has disappeared. The Ω -diabatic solution vectors $\underline{F}_\kappa(R)$ (with components $|\phi_\lambda\rangle$) at R_1 and $R_1 + \Delta R_1$ are transformed to the N-diabatic representation of Eq. (13). From the asymptotic matching radius R_2 , where the diagonal potentials have vanished too, the uncoupled equations in the N-representation are integrated inward to R_1 . This yields solutions $I_\lambda(R)$ and $O_\lambda(R)$ with asymptotic ingoing- and outgoing-wave behavior, respectively. Finally, the "mathematical" solution vectors $\underline{F}_\kappa(R)$ are combined linearly to "physical" solution vectors \underline{f}_κ , such that

$$(\underline{f}_\kappa)_\lambda = I_\lambda(R) - S_{\lambda\kappa} O_\lambda(R) \quad (31)$$

where S is the desired S-matrix.

At $\text{Ne}^{**}\text{-He}$ energy $E = 100$ meV, a calculation (integration stepsize $\Delta R \gtrsim 0.02 a_0$, total angular momentum $P \leq 100$) typically requires about 3 h on a Burroughs B7900 mainframe computer. For $\text{Ne}^{**}\text{-Ne}$, computing times will be longer still. This is, because we must distinguish between $\pi^e = \pm 1$. Also, the much larger reduced mass implies a smaller De Broglie wavelength, which requires ΔR to be smaller and P larger.

In a time of computational costs being passed on to the individual users, coupled-channel calculations will thus constitute a heavy drain on a group's budget. With this in mind, we have recently adapted our coupled-channel code NEON/COUPLEDCHANNELS for use on a PC-XT/AT compatible micro-computer.

The conversion from B7900 to PC-XT/AT mainly involved restoring all special Burroughs-Fortran implementations in the 3000-lines source text to standard Fortran form. The resulting source text can be compiled with both the Microsoft MS-Fortran 3.20 Compiler and the IBM Professional Fortran 1.0 Compiler. In Pro-Fortran, the code takes about 180 kbyte. About 225 kbyte are required for data storage. The total of 400 kbyte is well within the 640 kbyte limit of PC-XT/AT addressable memory. The Burroughs Fortran code uses single precision reals (48 bytes). For reasons of numerical accuracy, double precision (64 bytes) implementation proved indispensable for PC-use. When using a floating point coprocessor (8087 or 80287, for PC-XT and -AT, respectively), the move from single to double precision carries only about a 10% penalty in computing time. Remarkably, a very considerable reduction is achieved in Pro-Fortran with 2-byte rather than 4-byte integers.

Table II gives the results of a benchmark Ne^{**} -He calculation for various computer/compiler combinations. This calculation involves five of the ten $\text{Ne}^{**} \{ \alpha \}_k$ -states (8 or 9 channels of the 18, depending on parity) for both parities π , at a single value of the total angular momentum quantum number P . On the basis of Table II, the 2 byte integer double precision Pro-Fortran code was selected for use on our PC-AT micro-computers with 80287 coprocessor. It is slower than the original Burroughs-Fortran code on the B7900 mainframe computer by about a factor 15. A 3 hours calculation on the B7900 thus takes about 45 hours on the PC-AT. For a dedicated small computer, this is entirely acceptable, and opens up the prospect of performing many more coupled-channels calculations than would otherwise be possible, at reasonable cost.

Table II. Benchmarks for the coupled-channels program.

| | | Computation time (s) | | |
|---------------------------|-------------------------------------|----------------------|----------------|-----------------------|
| Computer | Conditions | Compiler | | |
| | | Pro- Fortran | MS- Fortran | Burroughs- Fortran |
| XT (8087 coprocessor) | 2-byte integer/ double precision | 549 | 661 | - |
| AT (80287 coprocessor) | 4-byte integer/ single precision | 317 | 211 | - |
| | 2-byte integer/ single precision | 164 | 200 | - |
| | 2-byte integer/ double precision | 186 | 212 | - |
| B7900 | single precision | - | - | 13 |

5.2. Results

We have not yet performed a full $\text{Ne}^{**}\text{-Ne}$ calculation along the lines set out in the preceding subsection, for a number of reasons. The limited amount of computing time available suggested that we concentrate on the $\text{Ne}^{**}\text{-He}$ system. With the advent of a code suitable for PC-AT use this argument has lost most of its weight. Even more telling was the lack of any obvious electron-inversion and particle-symmetry effects in our experimental $\text{Ne}^{**}\text{-Ne}$ cross sections. With regard to the $\text{Ne}^{**}\text{-Ne}$ interaction potentials, the accuracy of the gerade/ungerade core-potentials by Cohen and Schneider⁸⁾, appears to be in some doubt^{6,9)}. Lastly, data on the valence-electron inversion-overlap integral Δ^V of Eq. (6) have never been commonly available (compare Refs. 6 and 7).

We have performed what is basically a $\text{Ne}^{**}\text{-He}$ calculation, using the potentials of Eq. (7) for zero valence-electron overlap $\Delta^V = 0$. This means that there is no distinction between $\pi^e = \pm 1$. In effect, we have

$$V_{\pi^e}(R) = V^V(R) + \frac{1}{2} \{ V_g^C(R) + V_u^C(R) \} \quad (32)$$

This is probably not a bad approximation (see Ref. 7). In addition, we have considered the case of perfect valence-electron overlap $\Delta^V = 1$. That is to say, we have in imitation of Hennecart and Masnou-Seeuws^{6,7)} equated the electron parity π^e with the core parity π_c^e (Eq. (8)):

$$V_{\pi^e}(R) = V^V(R) + \{ V^C(R) \}_{\pi_c^e} = \pi^e \quad (33)$$

It has been stated already in section 3 that this approximation has a less firm basis in reality than that of Eq. (32).

Table III. Comparison between cross sections calculated with $\Delta^V=0$ ($(\frac{1}{2}(g+u))$) and $\Delta^V=1$ ($(\frac{1}{2}(g)+\frac{1}{2}(u))$). Also shown are the cross sections, calculated with gerade and ungerade ($\pi^e = \pi_c^e$) core potentials separately ($[g]$, $[u]$).

| Initial state | | | Final state | | | | | | | | | | | | | | | |
|---------------|----------------|-------|-------------|-----------------------------|------|------|--------------------|-----------------------------|------|------|--------------------|-----------------------------|------|------|--------------------|-----------------------------|------|------|
| | | | $\{a\}_4$ | | | | $\{a\}_5$ | | | | $\{a\}_6$ | | | | $\{a\}_7$ | | | |
| $\{a\}_k$ | E_k (meV) | M_k | $(g+u)/2$ | $\frac{1}{2}g+\frac{1}{2}u$ | g | u | $\frac{1}{2}(g+u)$ | $\frac{1}{2}g+\frac{1}{2}u$ | g | u | $\frac{1}{2}(g+u)$ | $\frac{1}{2}g+\frac{1}{2}u$ | g | u | $\frac{1}{2}(g+u)$ | $\frac{1}{2}g+\frac{1}{2}u$ | g | u |
| $\{a\}_4$ | 114 | 0 | | | | | 6.4 | 6.4 | 5.7 | 7.2 | 0.29 | 0.58 | 0.47 | 0.69 | 0.83 | 0.20 | 0.35 | 0.06 |
| | | 1 | | | | | 6.7 | 6.6 | 6.3 | 6.9 | 0.59 | 0.52 | 0.70 | 0.34 | 1.8 | 0.21 | 0.31 | 0.11 |
| | | 2 | | | | | | 8.2 | 8.4 | 7.2 | 9.7 | 0.15 | 0.23 | 0.30 | 0.17 | 0.42 | 0.11 | 0.20 |
| $\{a\}_5$ | 125 | 0 | 11.3 | 10.1 | 8.2 | 12.0 | | | | | 0.15 | 0.05 | 0.05 | 0.05 | 2.9 | 1.0 | 1.8 | 0.2 |
| | | 1 | 12.3 | 13.2 | 12.0 | 14.5 | | | | | 0.08 | 0.1 | 0.09 | 0.20 | 0.50 | 0.13 | 0.22 | 0.05 |
| $\{a\}_6$ | 182 | 0 | 0.17 | 0.47 | 0.30 | 0.63 | 0.02 | 0.04 | 0.03 | 0.06 | | | | | 6.5 | 3.1 | 4.50 | 1.8 |
| | | 1 | 0.43 | 0.33 | 0.53 | 0.14 | 0.08 | 0.08 | 0.05 | 0.11 | | | | | 4.9 | 4.4 | 7.17 | 1.69 |
| | | 2 | 0.05 | 0.11 | 0.13 | 0.09 | 0.02 | 0.02 | 0.02 | 0.02 | | | | | 3.8 | 5.1 | 9.3 | 0.8 |
| $\{a\}_7$ | 206 | 0 | 0.22 | 0.03 | 0.05 | 0.01 | 1.98 | 0.72 | 1.29 | 0.15 | 2.1 | 1.6 | 2.7 | 0.5 | | | | |
| | | 1 | 1.42 | 0.23 | 0.38 | 0.09 | 0.22 | 0.04 | 0.05 | 0.03 | 9.5 | 9.0 | 15.1 | 2.8 | | | | |

In the calculation of polarized total $\text{Ne}^{***}\text{-Ne}$ cross sections $Q_{l \leftarrow k}^{M_k}$, we have applied Eq. (16) (or Eq. (17), rather) to the $\Delta^V = 0$ case of Eq. (32), and Eq. (24) to the $\Delta^V = 1$ case of Eq. (33). Under the circumstances, we have not taken symmetrization in the Ne-nuclei into explicit account, as in Eq. (26).

For our $\text{Ne}^{***}\text{-Ne}$ calculations we used the valence-electron potentials of Hennecart and Masnou-Seeuws⁶⁾ and the corresponding core potentials of Cohen and Schneider⁸⁾, as set out in the concluding paragraph of section 2. We applied cubic-spline interpolation between the tabulated values from literature. For internuclear distances $R \geq 9 a_0$, the diagonal charge-induced dipole interaction $-C_4/R^4$ was used for the core potentials. Of necessity, a hard wall at $R = 4.5 a_0$ was introduced. This procedure has proven quite successful in the $\text{Ne}^{***}\text{-He}$ case of Ref. 3. The calculations were performed on a PC-AT with numerical coprocessor. With an integration stepsize $\Delta R = 0.015 a_0$ and total angular momentum $P \leq 150$, the computation time for each of the three calculations, denoted by $[\frac{1}{2}(g+u)]$ (Eq. (32)), $[g]$, and $[u]$ (Eq. (33)), was approximately 80 h.

The results of these coupled-channel calculations for the $\{a\}_5 \rightarrow \{a\}_{4,6,7}$ transitions at $\text{Ne}^{***}\text{-Ne}$ energy $E_5 = 125$ meV, and for the $\{a\}_7 \rightarrow \{a\}_{4,5,6}$ transitions at the corresponding energy $E_7 = 206$ meV are shown in Table III. In addition to the cross sections $Q_{l \leftarrow k}^{M_k}$ calculated as explained above ($[\frac{1}{2}(g+u)]$, $\frac{1}{2}[u]+\frac{1}{2}[g]$), this table also gives the cross sections calculated with the gerade and ungerade (core) potentials of Eq. (33) separately ($[g]$, $[u]$). There are considerable differences in outcome between the various calculations. Of course, this is not unexpected for the separately calculated $[u]$ and $[g]$ cross sections. However, there is often also a significant discrepancy between the averaged $\frac{1}{2}[u]+\frac{1}{2}[g]$ cross

Table IV. Experimental and quantum-mechanical $^{20}\text{Ne}^{**}(20)\text{Ne}$ polarized cross sections and polarization effects. The quantum-mechanical results have been calculated with the potentials of Eq. (7) (calculation [$\frac{1}{2}(g+u)$]) and Eq. (8) ($\frac{1}{2}[g]+\frac{1}{2}[u]$), respectively.

| Initial state | Final state | Cross section | | | | | | | | | Polarization effect | | |
|----------------|----------------|-------------------|--------------------|-----------------------------|---|--------------------|-----------------------------|---|--------------------|-----------------------------|---|--------------------|-----------------------------|
| | | $E_k(\text{meV})$ | | | $Q_{l \leftarrow k}^{ 0\rangle} (\text{\AA}^2)$ | | | $Q_{l \leftarrow k}^{ 1\rangle} (\text{\AA}^2)$ | | | $Q_{l \leftarrow k}^{ 0\rangle} / Q_{l \leftarrow k}^{ 1\rangle}$ | | |
| | | EXPT | $\frac{1}{2}(g+u)$ | $\frac{1}{2}g+\frac{1}{2}u$ | EXPT | $\frac{1}{2}(g+u)$ | $\frac{1}{2}g+\frac{1}{2}u$ | EXPT | $\frac{1}{2}(g+u)$ | $\frac{1}{2}g+\frac{1}{2}u$ | EXPT | $\frac{1}{2}(g+u)$ | $\frac{1}{2}g+\frac{1}{2}u$ |
| $\{\alpha\}_5$ | $\{\alpha\}_4$ | 115 | 125 | 125 | 10.8 | 11.3 | 10.1 | 9.0 | 12.3 | 13.2 | 1.2 | 0.9 | 0.8 |
| | $\{\alpha\}_6$ | 115 | 125 | 125 | 0.29 | 0.15 | 0.05 | 0.14 | 0.08 | 0.15 | 2.1 | 1.9 | 0.3 |
| | $\{\alpha\}_7$ | 115 | 125 | 125 | 3.3 | 2.9 | 1.0 | 0.77 | 0.50 | 0.13 | 4.2 | 5.8 | 7.7 |
| $\{\alpha\}_7$ | $\{\alpha\}_4$ | 210 | 206 | 206 | 0.23 | 0.22 | 0.03 | 1.52 | 1.42 | 0.23 | 0.15 | 0.15 | 0.13 |
| | $\{\alpha\}_5$ | 210 | 206 | 206 | 2.1 | 2.0 | 0.7 | 0.26 | 0.22 | 0.04 | 7.7 | 9.0 | 18.0 |
| | $\{\alpha\}_6$ | 210 | 206 | 206 | 1.7 | 2.1 | 1.6 | 6.6 | 9.5 | 9.0 | 0.26 | 0.23 | 0.18 |

sections associated with Eq. (33) and the a priori more realistic [$\frac{1}{2}(g+u)$] cross sections resulting from Eq. (32). The $\{\alpha\}_5 \rightarrow \{\alpha\}_6$ and $\{\alpha\}_7 \rightarrow \{\alpha\}_4$ cross sections provide extreme examples of this.

In Table IV the quantum-mechanical cross section values are compared with the experimental $^{20}\text{Ne}^{**}(20)\text{Ne}$ cross sections of Table I. Judging from the above-mentioned $\{\alpha\}_5 \rightarrow \{\alpha\}_6$ and $\{\alpha\}_7 \rightarrow \{\alpha\}_4$ cross sections in particular, but also e.g. from the $\{\alpha\}_7 \rightarrow \{\alpha\}_5$ cross sections, the superiority of the average potentials of Eq. (32) over those of Eq. (33) is clearly demonstrated. In this respect, the incorrect reversed $Q_{6\leftarrow 5}^{0|0|} / Q_{6\leftarrow 5}^{1|1|}$ polarisation effect for the $\frac{1}{2}[u]+\frac{1}{2}[g]$ calculation is very telling.

Where the average [$\frac{1}{2}(g + u)$] potentials of Eq (32) are concerned, even in a quantitative sense the agreement between experiment and theory is good. For the $\{\alpha\}_5 \rightarrow \{\alpha\}_{4,6,7}$ transitions, the measure of agreement can be judged directly from Figs. 1-3 which show, in addition to the experimental cross sections $Q_{l\leftarrow k}^\beta$, a quantum-mechanical curve calculated in accordance with Eq. (30). At the present thermal energies, these potentials and our calculations obviously constitute an effective combination. We are at present adapting our coupled-channel code, in order to fully incorporate the $\text{Ne}^{**}\text{-Ne}$ symmetry effects of sections 2 and 3.

6. Concluding remarks

We have established a prescription for the calculation of $\text{Ne}^{**}\text{-Ne}$ interaction potentials, taking proper account of electronic inversion symmetry. As ingredients it uses valence-electron potentials and gerade/ungerade core potentials, such as are available from the literature⁽⁶⁻⁸⁾. A special role is played by the valence-electron inversion-overlap integral. A coupled-channel calculation of $\text{Ne}^{**}\text{-Ne}$ cross sections has been shown to present no additional problems, compared to one for $\text{Ne}^{**}\text{-He}^3$.

Experimental verification of calculated results is another matter. Total cross section measurements, while presenting the only viable option for a study of intramultiplet mixing with short-lived atoms, are by definition less sensitive than differential measurements. The present experimental results reveal no significant differences between $^{20}\text{Ne}^{***}(20)\text{Ne}$ and $^{22}\text{Ne}^{***}(20)\text{Ne}$ intramultiplet-mixing cross sections. For the future, more accurate (i.e. much longer) measurements are planned. Any differences between $\text{Ne}^{***}\text{-Ne}$ and $\text{Ne}^{***}\text{-He}$ cross sections behavior are more likely traceable to general potential characteristics rather than to the effects of charge symmetry. This is confirmed by our preliminary coupled-channel calculations, using average potentials without specific regard for electron parity. These yield good agreement with the experimental $\{\alpha\}_5 \rightarrow \{\alpha\}_{4,6,7}$ and $\{\alpha\}_7 \rightarrow \{\alpha\}_{4,5,6}$ polarized cross sections, much better than calculations which equate total and core electron parity.

In future, our $\text{Ne}^{***}\text{-Ne}$ coupled-channel calculations will have to take full account of symmetry, if only to give direction to the experimental search for symmetry effects. Developments to make this possible are under way.

References

1. I.V. Hertel, H. Schmidt, A. Bähring and E. Meyer, Rep. Prog. Phys. **48** (1985) 375
2. M.P.I. Manders, J.P.J. Driessen, H.C.W. Beijerinck and B.J. Verhaar, Phys. Rev. Lett. **57** (1986) 1577; *ibid.*, **57** (1986) 2472
3. M.P.I. Manders, J.P.J. Driessen, H.C.W. Beijerinck and B.J. Verhaar, Phys. Rev. A., (1988) accepted for publication
4. M.P.I. Manders, W.B.M. van Hoek, E.J.D. Vredenburg, G.J. Sandker, H.C.W. Beijerinck and B.J. Verhaar, Phys. Rev. A., submitted for publication
5. M.P.I. Manders, W.M.J. Ruyten, F. v.d. Beucken, J.P.J. Driessen, W.J.T. Veugeliers, P.H. Kramer, E.J.D. Vredenburg, W.B.M. van Hoek, G.J. Sandker, H.C.W. Beijerinck, and B.J. Verhaar, J. Chem Phys., submitted for publication
6. D. Hennecart and F. Masnou-Seeuws, J. Phys. B. **18** (1985) 657
7. D. Hennecart, Ph.D. Thesis, Université de Caen (1982), unpublished
8. J.S. Cohen and B. Schneider, J. Chem. Phys. **61** (1974) 323
9. W. Beyer and H. Haberland, Phys. Rev. A. **29** (1984) 2280
10. R.M. Jordan and P.E. Siska, J. Chem. Phys. **69** (1978) 4634
11. A. Messiah, "Quantum Mechanics", Vol. I + II, North Holland, Amsterdam (1981)
12. M. Tinkham, "Group Theory and Quantum Mechanics", McGraw Hill (1964)
13. N. Austern, "Direct Nuclear Reaction Theories", Wiley, New York (1970)
14. K. Wildermuth and Y.C. Tang, "A Unified Theory of the Nucleus", Academic Press, New York (1977)
15. R.B. Bernstein, "Atom Molecule Collision Theory", Plenum Press, New York and London (1979)
16. V.I. Odintsov, Opt. and Spectr. **18** (1965) 205.
17. M.J. Verheijen, H.C.W. Beijerinck and N.F. Verster, J. Phys. E **15** (1982) 1198
18. J. Raynal, in "Computing as a Language of Physics", ed. A.E. Salam, IAEA, Vienna (1972)

This thesis has dealt mainly with thermal energy collisions of short-lived Ne^{**} -atoms with He and Ne. On the basis of this, the present experiment has proven itself viable. A considerable degree of insight in the intramultiplet mixing process has been obtained. Now that a firm foundation has been established, the time has come to explore in depth.

A first and vital extension of the experimental capability must consist of opening up higher energy ranges $0.5 \text{ eV} < E < 5 \text{ eV}$. For this purpose, a hollow cathode arc primary-beam source¹⁾, of a proven design²⁾, has been installed in the mini-beam apparatus. It will allow probing the inner potential regions. Thus, perhaps, the existence of Ne^{**} -Ne symmetry effects can be demonstrated. In this connection, increased emphasis on time-of-flight measurements may be fruitful.

Of course, this implies renewed attention for a description of the interaction potentials at small distances, which presents a daunting task, requiring maybe outside assistance. In a similar category falls a closer examination of the Ne^{**} -Ne valence-electron inversion-overlap integral. Given this, the corresponding adaptation of the coupled-channel program may be expected to be relatively straightforward.

Where interaction potentials are concerned, an old ideal of "fitting" potentials to experimental data has come closer to realisation with the advent of dedicated microcomputers and a coupled-channel program to run on them. This is still not practical with the present generation of PC-AT computers, equipped with the 80286 processor, but the 80386 processor, faster by a factor 5 or so³⁾, may be another matter.

In view of the semiclassical calculation's much shorter computation time, it can play an important role in providing a preliminary test of likely potentials. The inclusion of realistic (as opposed to straight-line) trajectories, which is a prerequisite for this, is far-advanced⁴⁾. So is a completely general approach to the number of states and crossings to be included in the calculations⁴⁾. Alternative mechanisms of radial coupling will have to be considered as well.

An entirely new area of research is opened up, if Ne^{***} - collision partners other than He and Ne are studied. It has already been mentioned that the noble gases from Ar upwards are susceptible to Penning ionization by Ne^{***}. In preliminary measurements for Ar, Xe, and Kr, Penning ionization is indeed seen to play an important role⁵⁾. While this complicates the intramultiplet mixing picture, it provides a view of Penning ionization itself, different from that offered by the usual total ionization cross section measurements⁶⁾. Of course, direct Penning ionization measurements with short-lived Ne^{***}-atoms other than the two-level system $\{a\}_g$ state⁷⁾ have not yet been realized (but will be in the future⁸⁾). In the mean time, the propensity for Penning ionization, to be deduced from intramultiplet mixing results, can even be simply and directly linked to various impact-parameter regions. This is done by comparing the effect of Penning ionization on intramultiplet-mixing transitions to which different impact-parameter regions contribute⁵⁾. Thus, this approach is comparable to large-angle differential scattering measurements with metastable atoms, which are plagued, however, by very low signal strengths²⁾. With short-lived atoms, no direct differential measurements are possible.

Eventually, of course, Penning ionization must be incorporated into the calculations themselves. Semiclassically, this will require relatively little effort⁴⁾. In principle, the coupled-channel program can be adapted to use complex potentials, as well.

All this calls for, among other things, real $\text{Ne}^{**}\text{-X}$ model potentials similar to those available for $\text{Ne}^{**}\text{-He}$ and $\text{Ne}^{**}\text{-Ne}$ ^{9,10}). These are forthcoming¹¹). Meanwhile, Ar, for which $\text{Ne}^{**}\text{-Ar}$ model potentials are already available¹²), is the prime candidate for a study of this kind.

If collisions of short-lived Ne^{**} -atoms with noble gas atoms other than He and Ne are perturbed by Penning ionization alone, additional processes occur in collisions with molecules. As has been mentioned briefly before, preliminary measurements have been performed with a variety of molecules such as H_2 , CH_4 , N_2 , CO_2 , and N_2O ¹³). The similarity between the results obtained for these molecules and those for the noble gases seems to indicate that the latter may form a convenient starting point for the analysis. Here too, the calculation, by the model potential method¹¹), of zero-order interaction potentials, on the basis of the distinctive polarizability of the molecules, is expected to provide useful insights. Again, Penning ionization is likely to be a major disturbing factor. Rotational excitation and angular momentum coupling, on the other hand, present a complex problem. A first look at the data suggests, that the extent of the anisotropy of the potentials is an important factor in the quenching mechanisms present for molecular systems, which in the case of Penning ionization is by no means unexpected.

Whereas for most alternative ground-state collision partners the scattering problem only becomes more complicated, the reverse will be true with some alternative short-lived atoms. Firstly, for the noble gas atoms R, a rise in mass number is accompanied by a decrease in comparable energy levels. The number of possible collision partners which will not be Penning ionized grows accordingly. In addition, the complete splitting of the

energy levels of the short-lived $R^{**}\{([n-1]p)^5(np)\}$ multiplet between $J_c = 1/2$ and $J_c = 3/2$ core states, e.g. for Kr¹⁴), makes an analysis of the core's role in the interaction much more promising.

The production of metastable noble gas atoms like Ar* and Kr*, in either the thermal beam source¹⁵⁾ or the hollow cathode arc beam source¹⁾, presents no problem. The present efforts spent on diode lasers are to lead to the production of short-lived Ar** and Kr** atoms, among other things.

An interesting new avenue opens up, if for instance diode lasers were used in a two-photon experiment. In particular, it ought to be possible to saturate the $Ne^*(^3P_2) \rightarrow Ne^{**}\{\alpha\}_9$ transition with the dye laser, and subsequently excite the $\{\alpha\}_9$ atoms to one of the near-Rydberg (5s) or (6s) states, using a diode laser. Apart from other interesting characteristics, these states generally have longer lifetimes than the $\{\alpha\}$ -states, which means a (relative) boost in signal strength. Lifetimes are not long enough, however, to spoil alignment, which is vital for polarization measurements. Obviously, this is a long- rather than short-term target.

The future course of the mini-beam project must be set carefully. The above summary of experimental possibilities, demonstrating the clear potential for growth, provides an additional indication of the fundamental soundness of the concept behind the experiment. It must be kept in mind, though, that the aim of the project (and its main strength) has always been its "complete" approach to the subject of intramultiplet mixing. It is important that theory and experiment continue to go hand in hand.

The continuation of the project, as a joint project of the Atomic Collisions and Spectroscopy group and the Theoretical Physics group, which has been approved by the university for another period of four years, ensures that prospects for this are bright.

References

- 1 P.G.A. Theuws, H.C.W. Beijerinck, D.C. Schram, and N.F. Verster, *J. Phys. E* **15** (1982) 573.
- 2 J.P.C. Kroon, A. Cottaar-Haverkorn, and H.C.W. Beijerinck, *Chem. Phys.* **103** (1986) 119.
- 3 R. Grehan, *Byte*, September 1987, 110.
- 4 M.F.M. Janssens, *Int. Rep. TUE, VDF/NO*, (1988) to be published (in Dutch).
- 5 G.J. Sandker, *Int. Rep. TUE, VDF/NO 88-04* (1988) (in Dutch).
- 6 M.J. Verheijen and H.C.W. Beijerinck, *Chem. Phys.* **102** (1986) 225.
- 7 a) J.P.J. Driessen, F.J.M. v.d. Weijer, and H.C.W. Beijerinck, *Conference Proceedings, XIth Int. Symp. on Mol. Beams, Edinburgh 1987* (1987); b) H.C.W. Beijerinck, J.P.J. Driessen, and F.J.M. v.d. Weijer, *Conference Proceedings, 1988 DAMOP/APS Meeting, Baltimore*, to be published.
- 8 J.P.J. Driessen, private communication.
- 9 D. Hennecart and F. Masnou-Seeuws, *J. Phys. B* **18** (1985) 657.
- 10 D. Hennecart, Ph.D. Thesis, Université de Caen (1982), unpublished.
- 11 F. Masnou-Seeuws, private communication.
- 12 a) W. Buszert, T. Bregel, R.J. Allan, M.-W. Ruf, and H. Hotop, *Z. Phys. A* **320** (1985) 105; b) W. Buszert, Ph.D. Thesis, Universität Kaiserslautern (1985), unpublished.
- 13 G.J. Sandker, M.F.M. Janssens, M.P.I. Manders, H.C.W. Beijerinck, and B.J. Verhaar, *Conference Proceedings, Najaarsvergadering 1987 Sectie At. Botsingsfys. en Spectr. NNV, Lunteren* (1987) (in Dutch).
- 14 V. Kaufman and C.J. Humphreys, *J. Opt. Soc. Am.* **59** (1970) 1614
- 15 M.J. Verheijen, H.C.W. Beijerinck, L.H.A.M. van Moll, J.P.J. Driessen and N.F. Verster, *J. Phys. E* **17** (1984) 904.

SUMMARY

This thesis has as its subject intramultiplet mixing collisions of short-lived, electronically excited $\text{Ne}^{**}\{(2p)^5(3p)\} \equiv \{\alpha\}$ atoms with atoms and molecules in the ground state. Electronically excited states play an important role in laser plasma's and gas discharges. The present study was set up and executed as a joint project of the Atomic Collisions and Spectroscopy group and the Theoretical Physics group of the Physics Department of Eindhoven University of Technology.

In Ne^{**} the outer electron occupies a relatively outlying (3p) orbital, as opposed to the closer (3s) orbital of the metastable Ne^* -atom. With an electron so far out, the initial orientation of the electronic Ne^{**} -angular momentum with respect to the initial relative velocity of the collision partners will have a large influence on the outcome of the collision process. Preparing the short-lived atoms in a well-defined initial orientation may thus be expected to bring out strong polarization effects. From these many interesting features of the potential surfaces and collision dynamics of the systems in question can be deduced. This thesis deals primarily with the Ne^{**} -He system, for which the intramultiplet mixing process can be studied in isolation. The Ne^{**} -Ne system, to which the same applies but with the added complication of possible symmetry effects, was studied too.

The short lifetimes of the Ne^{**} -atoms and the small cross sections for intramultiplet mixing made it necessary to construct a novel, very compact crossed-beam apparatus, the "mini-beam apparatus". This enables us to determine absolute total Ne^{**} -X polarized cross sections $Q_{\ell \leftarrow k}^{M_k}$, for the $\{\alpha\}_k \rightarrow \{\alpha\}_\ell$ transition. Here M_k is the magnetic quantum number of the electronic angular momentum J of the initial $\{\alpha\}_k$ state with respect to the asymptotic relative velocity. For the production of the $\{\alpha\}_k$ atoms in a polarized state, a polarized laser is used. The various $\{\alpha\}_k \rightarrow \{\alpha\}_\ell$ transitions are monitored by measuring the fluorescence signals I_k and I_ℓ from the $\{\alpha\}_k$ and $\{\alpha\}_\ell$ levels, respectively. In a completely automated sequence of measurements the ratio I_ℓ/I_k is determined. After extensive calibration of the experiment, we are able to derive from this ratio absolute total cross sections for intramultiplet mixing. Different kinds of measurements yield polarized cross sections, for several transitions, at various energies, and for miscellaneous systems.

Most experimental data have been collected for the $\text{Ne}^{**}\text{-He}$ system, the $\text{Ne}^{**}\text{-Ne}$ system coming second in this respect. Preliminary measurements have been performed with other noble gas atoms and with a selection of molecules. So far, we have only explored the thermal energy region $50 \text{ meV} \lesssim E \lesssim 200 \text{ meV}$. For $\text{Ne}^{**}\text{-He}$ and $\text{Ne}^{**}\text{-Ne}$ we observe strong, interesting polarization effects, with $Q_{\ell \leftarrow k}^{M_k}$ and $Q_{\ell \leftarrow k}^{M_k'}$ differing by more than a factor 10 in extreme cases. With different collision partners, a variety of competing processes tend to quench these polarization effects to some degree. We find no significant differences between the results for $^{20}\text{Ne}^{**}$ and $^{22}\text{Ne}^{**}$. In all this the mini-beam apparatus has proven itself a valuable instrument. The experimental data it produces are the indispensable first ingredient for a better understanding of the intramultiplet mixing process.

With our fully quantum-mechanical coupled-channels program NEON/COUPLED CHANNELS we can calculate theoretical $\text{Ne}^{**}\text{-He}$ intramultiplet mixing cross sections. We use a basis of diabatic functions $|\pi\alpha J\Omega P M_P\rangle$ which, besides being atomic eigenfunctions $|\alpha J\Omega\rangle$, have definite parity π and well-defined quantum-numbers P , $M_{P,Z}$ and $\Omega \equiv |M_J|_Z = |M_P|_Z$, for the \underline{P}^2 , P_Z and $P_Z = J_Z$, operators of the total angular momentum \underline{P} . Here the space-fixed z -axis is along the asymptotic relative velocity, and the body-fixed z' -axis along the internuclear axis. The time-independent Schrödinger equation for the scattering process then gives rise to a set of at most 18 coupled differential equations, for each value of P and parity $\pi = +/-1$. The coupled-channel code uses a modified Numerov integration method. There is no fundamental difference between $\text{Ne}^{**}\text{-He}$ and $\text{Ne}^{**}\text{-Ne}$ coupled-channel calculations, the added electronic inversion symmetry for $\text{Ne}^{**}\text{-Ne}$ notwithstanding. A single coupled-channel calculation for $\text{Ne}^{**}\text{-He}$, at the present thermal energies, requires about 3 hours on the university's Burroughs B7900 mainframe computer. We have converted the code for use on a PC-AT compatible micro-computer, where it is slower by (only) about a factor 15. Like the mini-beam apparatus, the coupled-channel calculations are an effective instrument, and provide a second essential ingredient for our study of intramultiplet mixing.

The third ingredient is theoretical information on interaction potentials and coupling matrix elements, to be linked to the experimental data by coupled-channel calculations. For the $\text{Ne}^{**}\text{-He}$ system, we have model potentials from the literature at our disposal. These have been calculated on the basis of a three-particle model, in which the system is assumed to consist of the $\text{Ne}^+(2p)^5$ core, the $e^-(3p)$ valence electron and the $\text{He}(^1S_0)$ -

target. Thus are obtained, for internuclear distances $R \geq 4.5 a_0$, basic potentials $V_{\sigma}^V(R)$ and $V_{\pi}^V(R)$ for the two orientations of the 3p-orbital of the valence electron with respect to the internuclear axis. Tentatively extended by us down to $R \geq 2.0 a_0$, and supplemented by potentials V_{σ}^C and V_{π}^C for the two orientations of the core hole, these allow calculation of the matrix elements of the $\text{Ne}^{**}\text{-He}$ electronic Hamiltonian in a basis of atomic eigenfunctions.

In the case of $\text{Ne}^{**}\text{-Ne}$ this approach, based on the separate role of the (3p) valence electron, needs some modification in connection with electronic inversion symmetry. For the $\text{Ne}^+\text{-Ne}$ core, ab initio eigenfunctions of definite parity are available. Keeping in mind that similar valence electron symmetry is highly unfavorable energetically, we break inversion symmetry temporarily. Core states are introduced in which the ionic part is predominantly with one or the other of the Ne-nuclei. Then corresponding valence electron eigenfunctions can be obtained, just as in the $\text{Ne}^{**}\text{-He}$ case. Of importance is the extent to which these electron wavefunctions overlap ("inversion-overlap"). Finally the total electron parity π^e is reintroduced. Thus we find basic potentials, similar to those for $\text{Ne}^{**}\text{-He}$, but associated with gerade and ungerade electron states. An essential element in our picture is the R-dependent mixing of gerade and ungerade core potentials, associated with the R-dependent uncertainty of the valence electron being located with the $\text{Ne}^+\text{-ion}$ or Ne-atom . Given these potentials, $\text{Ne}^{**}\text{-Ne}$ coupled-channel calculations proceed along the same lines as those for $\text{Ne}^{**}\text{-He}$. In the ultimate calculation of cross sections, though, differences arise. For $\text{Ne}^{**}\text{-Ne}$, a distinction must be made between the cases of $^{22}\text{Ne}^{**}\text{-}^{20}\text{Ne}$ (inversion symmetry only) and $^{20}\text{Ne}^{**}\text{-}^{20}\text{Ne}$ (symmetry in the nuclei as well).

In the comparison of theory and experiment, our quantum-mechanical coupled-channel calculations with the above $\text{Ne}^{**}\text{-He}$ potentials as input offer a very satisfactory description of $\text{Ne}^{**}\text{-He}$ experimental results. Calculations, postulating a hard wall at internuclear distance $R = 4.5 a_0$, often are successful as well, indicating that at the investigated thermal energies mainly the long range interactions are probed.

For the $\text{Ne}^{**}\text{-Ne}$ system, we have carried out preliminary coupled-channel calculations under the reasonable approximation of zero inversion-overlap for the valence electron. A good agreement with the experimental results is obtained. Of course, this procedure which implies that no distinction is

made between electronic parity $\pi^e = +1$ and -1 , is consonant with the lack of any obvious electron-inversion and particle-symmetry effects in our experimental $\text{Ne}^{**}\text{-Ne}$ cross sections. The alternative extreme of perfect inversion-overlap, implausible on physical grounds, is indeed disqualified by the comparison with experiment.

Unfortunately, the quantum-mechanical calculations constitute something of a "black box". The link between input (model potentials) and output (cross sections) is rather remote. To provide for more physical insight than these calculations offer, we have adopted a complementary semiclassical approach, inspired by the presence of several avoided crossings between the adiabatic potentials for the $\{\alpha\}_{4,5,6,7}$ states. Our simple, semiclassical model for the collision process has the following ingredients: (1) straight-line trajectories with hard-sphere scattering at the classical turning point R_T ; (2) Landau-Zener type curve-crossing transitions at the crossing radius R_C ; (3) rotational coupling, associated with a space-fixed electronic angular momentum J , for $R > R_L$ and "locking" of J to the internuclear axis for $R \leq R_L$, with R_L the locking radius. In particular, we have investigated the transition from rotational coupling to locking. The insight obtained was essential for a semiclassical description of polarized-atom cross section behavior.

This model has been applied to the $\text{Ne}^{**}\text{-He}$ case and goes a long way towards explaining the experimental results for the transitions between the $\{\alpha\}_{4,5,6,7}$ states. The polarization effects in particular are traceable to a combination of symmetry-restraints, rotational-coupling behavior and a transition-related preference for certain impact-parameter regions.

The aim of the present project was to provide a "complete" analysis of the intramultiplet mixing process, for $\text{Ne}^{**}\text{-He}$ and $\text{Ne}^{**}\text{-Ne}$ in particular. In general, with the work described in this thesis — related to the crossed-beam experiment, coupled-channel calculations, model potentials, and a semiclassical analysis — a solid basis for this can be said to have been established.

SAMENVATTING

Dit proefschrift heeft als onderwerp overgangen tussen de toestanden van het kortlevende, elektronisch geëxciteerde $\text{Ne}^{**}\{(2p)^5(3p)\}$ multiplet ("intramultiplet mixing"), teweegebracht door botsingen met atomen en moleculen in de grondtoestand. Elektronisch geëxciteerde toestanden spelen een belangrijke rol in laser-plasma's en gasontladingen. Het huidige onderzoek werd opgezet en uitgevoerd als een gezamenlijk project van de groep Atomaire en Optische Wisselwerkingen en de groep Theoretische Natuurkunde van de afdeling Natuurkunde van de Technische Universiteit Eindhoven.

In Ne^{**} bezet het buitenste electron een betrekkelijk ver naar buiten gelegen (3p) orbitaal, in tegenstelling tot de meer nabije (3s) orbitaal van het metastabiele Ne^{**} -atoom. Bij een zover naar buiten gelegen electron zal de oorspronkelijke oriëntatie van het elektronisch Ne^{**} -impulsmoment met betrekking tot de asymptotische relatieve snelheid van grote invloed zijn op het verloop van het botsingsproces. Preparatie van de kortlevende atomen in een welbepaalde begin-oriëntatie zal dus naar verwachting sterke polarisatie-effecten te zien geven. Daaruit kunnen vele interessante eigenschappen van de potentiaal-oppervlakken en de botsings-dynamica van de systemen in kwestie worden afgeleid. Dit proefschrift houdt zich in de eerste plaats bezig met het Ne^{**} -He systeem, waarvoor boven-genoemd proces van "intramultiplet mixing" afzonderlijk bestudeerd kan worden. Ook het Ne^{**} -Ne systeem, waarvoor hetzelfde geldt, maar met de bijkomende complicatie van mogelijke symmetrie-effecten, is bestudeerd.

De korte levensduur van de Ne^{**} -atomen en de kleine botsingsdoorsneden voor "intramultiplet mixing" maakten het nodig een nieuw, heel compact gekruiste-bundel apparaat te construeren, het "mini-bundel apparaat". Dit stelt ons in staat om voor de $\{\alpha\}_k \rightarrow \{\alpha\}_l$ overgang absolute totale gepolariseerde Ne^{**} -X botsingsdoorsneden $Q_{l \leftarrow k}^{M_k}$ te bepalen. Hierin is M_k het magnetisch quantumgetal van het elektronisch impulsmoment \underline{J} van de $\{\alpha\}_k$ -begin-toestand met betrekking tot de asymptotische relatieve snelheid. Voor het produceren van de $\{\alpha\}_k$ -atomen in een gepolariseerde toestand wordt een gepolariseerde laser gebruikt. De verschillende $\{\alpha\}_k \rightarrow \{\alpha\}_l$ overgangen worden gedetecteerd door de fluorescentie-signalen I_k en I_l van de $\{\alpha\}_k$ - en $\{\alpha\}_l$ -toestanden te meten. In een volledig geautomatiseerde reeks metingen wordt de verhouding I_l/I_k bepaald. Na uitvoerige calibratie van het experiment zijn we in staat om uit deze verhouding absolute totale botsingsdoorsneden af te leiden. Verschillende soorten metingen leveren gepolariseerde botsingsdoorsneden, voor meerdere overgangen, bij verschillende energieën en voor alle mogelijke systemen.

De meeste meetgegevens zijn verzameld voor het $\text{Ne}^{**}\text{-He}$ systeem; het $\text{Ne}^{**}\text{-Ne}$ systeem komt in dit opzicht op de tweede plaats. Voorlopige metingen zijn uitgevoerd met andere edelgas-atomen en met geselecteerde moleculen. Tot dusver hebben we alleen het thermische energiegebied $50 \text{ meV} \lesssim E \lesssim 200 \text{ meV}$ onderzocht. Voor $\text{Ne}^{**}\text{-He}$ en $\text{Ne}^{**}\text{-Ne}$ nemen we sterke, interessante polarisatie-effecten waar, waarbij $Q_{l \leftarrow k}^{|M_k|}$ en $Q_{l \leftarrow k}^{|M_k'|}$ in extreme gevallen meer dan een factor 10 verschillen. Met andere botsingspartners worden deze polarisatie-effecten gewoonlijk meer of minder gedempt door een aantal verschillende concurrerende processen. We vinden geen significante verschillen tussen de resultaten voor $^{20}\text{Ne}^{**}$ en $^{22}\text{Ne}^{**}$. Bij dit alles heeft het mini-bundel apparaat zich een waardevol instrument getoond. De experimentele gegevens die het produceert vormen het onontbeerlijke eerste bestanddeel voor een beter begrip van het proces van "intramultiplet mixing".

Met ons volledig quantum-mechanisch gekoppelde-kanalen programma NEON/COUPLEDCHANNELS kunnen we theoretische $\text{Ne}^{**}\text{-He}$ botsingsdoorsneden berekenen. Wij gebruiken een basis van diabatische functies $|\pi\alpha J \Omega P M_P\rangle$ die atomaire eigenfuncties $|\alpha J \Omega\rangle$ zijn en bovendien een welbepaalde pariteit π hebben en welbepaalde quantumgetallen P , $M_{P,Z}$ en $\Omega \equiv |M_J|_Z = |M_P|_Z$, voor de operatoren \underline{P}^2 , P_Z en $P_{Z'} = J_{Z'}$, van het totaal impulsmoment \underline{P} . De ruimte-vaste z -as ligt hier langs de asymptotische relatieve snelheid, en de lichaamsvaste z' -as langs de internucleaire as. De tijd-onafhankelijke Schrödinger-vergelijking voor het verstrooiingsproces leidt dan tot een stelsel van maximaal 18 gekoppelde differentiaal-vergelijkingen, voor elke waarde van P en de pariteit π . Het gekoppelde-kanalen programma maakt gebruik van een gemodificeerde Numerov-integratiemethode. Er bestaat geen fundamenteel verschil tussen $\text{Ne}^{**}\text{-He}$ en $\text{Ne}^{**}\text{-Ne}$ gekoppelde-kanalen berekeningen, ondanks de extra elektronische inversie-symmetrie voor $\text{Ne}^{**}\text{-Ne}$. Een enkele gekoppelde-kanalen berekening voor $\text{Ne}^{**}\text{-He}$ vergt bij de huidige thermische energieën ongeveer 3 uur op de Burroughs B7900 mainframe computer van de TUE. Wij hebben het programma geschikt gemaakt voor gebruik op een PC-AT compatibele microcomputer, hetgeen (slechts) een factor 15 snelheidsverlies oplevert. Evenals het mini-bundel apparaat vormen de gekoppelde-kanalen berekeningen een effectief hulpmiddel en zijn een tweede essentieel bestanddeel van onze studie van "intramultiplet mixing".

Het derde bestanddeel is theoretische informatie over wisselwerkings-potentialen en koppelmatrix-elementen, waarvoor de gekoppelde-kanalen berekeningen de schakel met het experiment vormen. Voor het $\text{Ne}^{**}\text{-He}$ systeem hebben we de beschikking over model-potentialen uit de literatuur. Deze

zijn berekend op basis van een drie-deeltjes model, waarin het systeem wordt geacht te bestaan uit de $\text{Ne}^+(2p)^5$ -romp, het $e^-(3p)$ valentie-electron en het $\text{He}(^1S_0)$ -atoom. Zo worden voor internucleaire afstanden $R \geq 4.5 a_0$ basispotentialen V_σ^V en V_π^V verkregen voor de beide oriëntaties van de $3p$ -orbitaal van het valentie-electron ten opzichte van de inter-nucleaire as. Door ons bij wijze van proef uitgebreid tot $R \geq 2.0 a_0$ en aangevuld met potentialen V_σ^C en V_π^C voor de twee oriëntaties van het romp-gat, maken deze potentialen de berekening mogelijk van de matrix-elementen van de $\text{Ne}^{**}\text{-He}$ elektronen-Hamiltoniaan in een basis van atomaire eigenfuncties.

In het geval van $\text{Ne}^{**}\text{-Ne}$ behoeft deze benadering, gebaseerd op de aparte rol van het $(3p)$ valentie-electron, enige aanpassing in verband met de elektronische inversie-symmetrie. Voor de $\text{Ne}^{**}\text{-Ne}$ romp zijn ab-initio eigenfuncties van zekere pariteit beschikbaar. In gedachten houdend dat soortgelijke symmetrie voor het valentie-electron energetisch hoogst ongunstig is, verbreken wij tijdelijk de inversie-symmetrie. We voeren romp-toestanden in waarin het ion-deel zich hoofdzakelijk bij één van de twee kernen bevindt. Overeenkomstige eigenfuncties van het valentie-electron kunnen dan worden verkregen als in het $\text{Ne}^{**}\text{-He}$ geval. Van belang is de mate waarin deze electron-golffuncties elkaar overlappen ("inversie-overlap").

Tenslotte wordt opnieuw de totale electronen-pariteit π^e ingevoerd. Zo vinden we basispotentialen, analoog aan die voor $\text{Ne}^{**}\text{-He}$, maar geassocieerd met gerade en ungerade electron-toestanden. Een essentieel element van het gevormde beeld is de R -afhankelijke menging van gerade en ungerade romp-potentialen, die samenhangt met de R -afhankelijke onzekerheid in de locatie van het valentie-electron: bij het Ne^+ -ion of bij het Ne -atoom. Gegeven deze potentialen, gaan gekoppelde-kanalen berekeningen voor $\text{Ne}^{**}\text{-Ne}$ op dezelfde wijze in hun werk als die voor $\text{Ne}^{**}\text{-He}$. Bij de uiteindelijke berekening van botsingsdoorsneden treden echter verschillen op. Voor $\text{Ne}^{**}\text{-Ne}$ moet onderscheid worden gemaakt tussen het geval van $^{22}\text{Ne}^{**}\text{-}^{20}\text{Ne}$ (alleen inversie-symmetrie) en dat van $^{22}\text{Ne}^{**}\text{-}^{20}\text{Ne}$ (tevens symmetrie in de kernen).

Vergelijken we theorie en experiment, dan geven onze quantum-mechanische gekoppelde-kanalen berekeningen met genoemde $\text{Ne}^{**}\text{-He}$ potentialen als invoer een uiterst bevredigende beschrijving van de $\text{Ne}^{**}\text{-He}$ resultaten. Berekeningen die een harde wand op internucleaire afstand $R = 4.5 a_0$ postuleren voldoen vaak ook goed, wat erop duidt dat bij de onderzochte thermische energieën vooral de lange-dracht wisselwerkingen worden gespeeld.

Voor het $\text{Ne}^{**}\text{-Ne}$ systeem hebben we voorlopige gekoppelde-kanalen berekeningen uitgevoerd onder de redelijke benadering van ontbrekende inversie-overlap voor het valentie-electron. Zo wordt goede overeenstemming met de experimentele resultaten verkregen. Deze procedure, die inhoudt dat geen onderscheid wordt gemaakt tussen electronen-pariteit $\pi^e = +1$ en -1 , is natuurlijk in overeenstemming met het gebrek aan duidelijke electronen-inversie- en deeltjes-symmetrie effecten in onze experimentele $\text{Ne}^{**}\text{-Ne}$ botsingsdoorsneden. Het alternatieve extreem van volledige inversie-overlap, dat onwaarschijnlijk is op fysische gronden, blijkt inderdaad bij vergelijking met het experiment niet te voldoen.

Helaas vormen de quantum-mechanische berekeningen een soort "black box". Het verband tussen invoer (model potentialen) en uitvoer (botsingsdoorsneden) is tamelijk vluchtig. Om meer fysisch inzicht te verkrijgen dan deze berekeningen bieden, zijn wij overgegaan tot een complementaire semi-klassieke aanpak, geïnspireerd door de aanwezigheid van meerdere "avoided crossings" tussen de adiabatische potentiaal-curven voor de $\{\alpha\}_{4,5,6,7}$ toestanden. Ons eenvoudige, semiklassieke model voor het botsingsproces heeft de volgende elementen: (1) rechte banen met harde bol-verstrooiing bij het klassieke omkeerpunt R_T ; (2) Landau-Zener-achtige overgangen tussen potentiaal-curven bij de "crossing"-straal R_C ; (3) rotatiekoppeling bij ruimtevast electronisch impulsmoment \underline{J} voor $R > R_L$ en "locking" van \underline{J} aan de internucleaire as voor $R \leq R_L$, met R_L de "locking"-straal. In het bijzonder is de overgang van rotatiekoppeling naar "locking" onderzocht. Het zo verworven inzicht was van wezenlijk belang voor een semiklassieke beschrijving van het gedrag van gepolariseerde botsingsdoorsneden.

Dit model is toegepast op het $\text{Ne}^{**}\text{-He}$ geval en biedt een verregaande verklaring van de experimentele resultaten voor de overgangen tussen de $\{\alpha\}_{4,5,6,7}$ toestanden. Met name de polarisatie-effecten zijn te herleiden tot een combinatie van symmetrie-beperkingen, rotatiekoppelings-gedrag en een overgangsgebonden voorkeur voor zekere botsingsparameters.

Het huidige project had tot doel een "complete" analyse van het proces van "intramultiplet-mixing", met name voor $\text{Ne}^{**}\text{-He}$ en $\text{Ne}^{**}\text{-Ne}$. In het algemeen kan men zeggen dat met het in dit proefschrift beschreven werk — betrekking hebbend op het gekruiste-bundel experiment, gekoppelde-kanalen berekeningen, model-potentialen, en een semiklassieke analyse — daarvoor een solide basis is geschapen.

DANKWOORD

Ik dank de promotoren, Herman Beijerinck en Boudewijn Verhaar. Verder alle leden en studenten van de groepen Atomaire en Optische Wisselwerkingen en Theoretische Natuurkunde, met wie ik in de afgelopen vier jaren heb samengewerkt. Erkentelijk ben ik ook hen, die hebben bijgedragen aan het gereed maken van dit proefschrift.

Bij naam noemen zal ik alleen de studenten, die op een of andere manier rechtstreeks bij het onderzoek betrokken waren. In chronologische volgorde: de afstudeerders Wim Ruyten (die speciale vermelding verdient vanwege zijn werk aan het ontwerp van de opstelling), Jean Martens, Jan Driessen, Edgar Vredembregt, Ad van Gerven, Marco van Hoek, GertJan Sandker en Matt Janssens; de stagiairs Frank v.d. Beucken, Richard van Amen, Wim Veugelers, Ad v.d. Kieboom, Joris Sparla, Leon Blokker, Pieter Kramer, Pascal Bloemen, Peter Koerseman, Carolien de Graaf en Wim Boom.

CURRICULUM VITAE

23 augustus 1953 geboren te Eindhoven

| | |
|-------------------------|--|
| 1965-1971: | Gymnasium β St. Oelbertgymnasium te Oosterhout |
| 1971-1975, 1980-1983 | Studie Technische Natuurkunde Technische Hogeschool Eindhoven |
| 1984-1988: | Promotie-onderzoek Technische Universiteit Eindhoven |

STELLINGEN

behorend bij het proefschrift
COLLISION-INDUCED INTRAMULTIPLY MIXING
FOR THE Ne^{**}{(2p)⁵(3p)} + He or Ne SYSTEM

door

M.P.I. Manders

Eindhoven, 17 mei 1988

I

De impulsmoment-koppelingsschema's, die in dit proefschrift worden gebruikt voor de beschrijving van de verstrooiing van Ne^{**} aan He, zijn analoog aan die voor de verstrooiing van een deeltje aan een axiaal-symmetrische starre rotator, ondanks de zeer verschillende fysische betekenis van de overeenkomstige quantumgetallen.

A.M. Schulte, proefschrift TH Eindhoven (1978).

II

Een aanzienlijke Ω -opsplitsing tussen moleculaire potentialen leidt in het algemeen alleen in combinatie met een zekere mate van "locking" tot polarisatie-effecten. Dit verklaart waarom bij Penning-ionisatie van Ar door $\text{Ne}^{**}\{(2p)^5(3p)\}$ in het thermische energiegebied wél een polarisatie-effect wordt waargenomen en in het superthermische energiegebied niet.

J.P.J. Driessen, TU Eindhoven, wordt gepubliceerd.

III

Doordat voor de zware edelgassen het totale impulsmoment van de romp een goed quantumgetal is, laat de bevolking van het metastabiele 3P_0 niveau zich niet door optisch pompen vergroten.

F.T.M. v.d. Berg et al., Chem. Phys. 115 (1987) 359.

IV

De ionisatie van waterstof-atomen in elektrische microgolfvelden is, ook in de klassieke beschrijving, geen chaotisch proces in de strikte zin des woords.

P.M. Koch, in "Fundamental Aspects of Quantum Theory", red. V. Gorini en A. Frigerio (Plenum, London, 1986).

V

Het is opmerkelijk dat het bij quantum-optische experimenten vaak grote voordelen heeft juist geen licht maar deeltjes te detecteren.

R.J. Cook, Opt. Commun. 35 (1980) 347;

J.P.C. Kroon et al., Phys. Rev. A 31 (1985) 3724.

VI

De komst van (goedkope) laserdiodes als alternatief voor (dure) dyelasers zal in de komende jaren een revolutie in de atomaire botsingsfysica en de spectroscopie teweegbrengen.

VII

Door in de ontwerpfase een experiment op papier geheel door te rekenen heeft men de beste garantie dat niet in de meetfase tijdrovende en dure correcties in het ontwerp zullen moeten worden aangebracht.

VIII

Tot de optimalisering van een experiment moet ook het bevorderen van werk-omstandigheden worden gerekend, waarbij de experimentator zich wel bevindt.

IX

De ontwikkelingen, die zich op het gebied van computer-hardware voordoen, plaatsen de toekomstige rol van centrale universiteits-rekenfaciliteiten in een geheel nieuw daglicht.

X

Rekenen met een computer-programma zonder dat men er een idee van heeft hoe het werkt, is als duiken in water waarvan men niet weet hoe diep het is.

XI

Nu de compact disc een geluidsgetrouwe weergave zonder ruis mogelijk maakt, mag van musici verwacht worden dat zij tijdens een opname extra zorgvuldigheid betrachten bij het vermijden van bijgeluiden.